The Pennsylvania State University

The Graduate School

Department of Mechanical and Nuclear Engineering

THE EFFECT OF STRESS STATE ON ZIRCONIUM HYDRIDE REORIENTATION

A Dissertation in

Nuclear Engineering

by

Mahmut Nedim Cinbiz

Submitted in Partial Fulfillment
of the Requirements
for the Degree of

Doctor of Philosophy,

December 2015

The dissertation of Mahmut Nedim Cinbiz was reviewed and approved* by the following:

Arthur T. Motta
Professor of Nuclear Engineering and Materials Science and Engineering
Chair of Nuclear Engineering Program
Dissertation Advisor
Chair of Committee

Donald A. Koss
Professor Emeritus of Materials Science and Engineering

Kenan Unlu
Director of the Radiation Science and Engineering Center
Professor of Nuclear Engineering

Clifford J. Lissenden
Professor of Engineering Science and Mechanics

Michael Billone
Manager of Irradiation Performance Section in Nuclear Engineering, Argonne National Laboratory
Special Member

Karen Thole
Department Head of Mechanical and Nuclear Engineering Department,
Professor of Mechanical Engineering

*Signatures are on file in the Graduate School

ABSTRACT

Prior to storage in a dry-cask facility, spent nuclear fuel must undergo a vacuum drying cycle during which the spent fuel rods are heated up to elevated temperatures of $\leq 400°C$ to remove moisture the canisters within the cask. As temperature increases during heating, some of the hydride particles within the cladding dissolve while the internal gas pressure in fuel rods increases generating multi-axial hoop and axial stresses in the closed-end thin-walled cladding tubes. As cool-down starts, the hydrogen in solid solution precipitates as hydride platelets, and if the multi-axial stresses are sufficiently large, the precipitating hydrides *reorient* from their initial circumferential orientation to radial orientation. Radial hydrides can severely embrittle the spent nuclear fuel cladding at low temperature in response to hoop stress loading.

Because the cladding can experience a range of stress states during the thermo-mechanical treatment induced during vacuum drying, this study has investigated the effect of stress state on the process of hydride reorientation during controlled thermo-mechanical treatments utilizing the combination of in situ X-ray diffraction and novel mechanical testing analyzed by the combination of metallography and finite element analysis. The study used cold worked and stress relieved Zircaloy-4 sheet containing approx. 180 wt. ppm hydrogen as its material basis. The failure behavior of this material containing radial hydrides was also studied over a range of temperatures. Finally, samples from reactor-irradiated cladding tubes were examined by X-ray diffraction using synchrotron radiation.

To reveal the stress state effect on hydride reorientation, the critical threshold stress to reorient hydrides was determined by designing novel mechanical test samples which produce a range of stress states from uniaxial to “near-equibiaxial” tension when a load is applied. The threshold stress was determined after thermo-mechanical treatments by correlating the finite element stress-state results with the spatial distribution of hydride microstructures observed within

the optical micrographs for each sample. Experiments showed that the hydride reorientation was enhanced as the stress biaxiality increased. The threshold stress decreased from 150 MPa to 80 MPa when stress biaxiality ratio increased from uniaxial tension to near-equibiaxial tension. This behavior was also predicted by classical nucleation theory based on the Gibbs free energy of transformation being assisted by the far-field stress.

An analysis of in situ X-ray diffraction data obtained during a thermo-mechanical cycle typical of vacuum drying showed a complex lattice-spacing behavior of the hydride phase during the dissolution and precipitation. The in-plane hydrides showed bilinear lattice expansion during heating with the intrinsic thermal expansion rate of the hydrides being observed only at elevated temperatures as they dissolve. For radial hydrides that precipitate during cooling under stress, the spacing of the close-packed {111} planes oriented normal to the maximum applied stress was permanently higher than the corresponding {111} plane spacing in the other directions. This behavior is believed to be a result of a complex stress state within the precipitating plate-like hydrides that induces a strain component within the hydrides *normal* to its "plate" face (i.e., the applied stress direction) that exceeds the lattice spacing strains in the other directions. During heat-up, the lattice spacing of these same "plate" planes actually contract due to the reversion of the stress state within the plate-like hydrides as they dissolve.

The presence of radial hydrides and their connectivity with in-plane hydrides was shown to increase the ductile-to-brittle transition temperature during tensile testing. This behavior can be understood in terms of the role of radial hydrides in promoting the initiation of a long crack that subsequently propagates under fracture mechanics conditions. Finally, the d-spacing of irradiated Zircaloy-4 and M5 cladding tubes was measured at room temperature and compared to that of un-irradiated samples.

TABLE OF CONTENTS

LIST OF FIGURES

LIST OF TABLES

ACKNOWLEDGEMENTS

I would like to thank my advisers Dr. Arthur Motta and Dr. Donald Koss for their help and guidance during my PhD study which was a learning experience in many aspects of research. I also would like to thank Dr. Koss' priceless efforts to develop my experimental and theoretical understanding. I also would like to point out very productive meetings with Dr. Koss at Wegmans.

I would like to thank Dr. Michael Billone, Dr. Cliff Lissenden, and Dr. Kenan Unlu for their insights and recommendations as members of my dissertation committee. I would also like to acknowledge Harold Scott for financial support of Nuclear Regulatory Commission.

I am thankful to Dr. Michael Billone and his colleagues at Argonne National Laboratory for furnishing cladding tube materials for experiments. I would like to thank Jonathan Almer and Jun-Sang Park for their help during conducting experiments at Advanced Photon Source.

I would like to thank David Shelleman to provide mechanical apparatus for thermo-mechanical treatments and tension tests throughout the project. I would like to thank Ken Biddle and his colleagues at machine shop for their specimen and mechanical equipment manufacturing.

Finally, I would like to thank my parents for their patience and support. I also would like to thank my brother and his wife for encouraging me and keeping my motivation.

1 INTRODUCTION AND BACKGROUND

1.1 Zirconium Based-Alloys for Nuclear Fuel Cladding Tube Material

Zirconium-based alloys are being used as the fuel cladding tubes that encapsulate the uranium dioxide fuel (UO_2) in light water reactors (LWRs). Zirconium-based alloys have low thermal neutron absorption cross-section which improves neutron economy [1]. Zirconium-based alloys are also resistant to high temperature corrosion and are mechanically stable under neutron irradiation at the high operating temperatures and pressures of LWRs. These properties are important to the performance of the LWR as the cladding constitutes the principal physical barrier between the fission gases released by the fuel and the coolant water.

Zirconium has a hexagonal closed-packed (HCP) crystal structure with a c/a ratio of 1.594 at temperatures below 865°C, which means that in this temperature range the zirconium crystal exhibits anisotropic properties. At 865°C, an allotropic phase transformation occurs causing a transformation from the HCP crystal structure (α phase) to a body-centered cubic (BCC) crystal structure (β-phase).

Zirconium is alloyed with other elements such as iron (Fe), tin (Sn), chromium (Cr), oxygen (O), nickel (Ni), and niobium (Nb) to improve corrosion resistance and mechanical properties [2-5]. The chemical compositions of selected zirconium-based alloys are shown in Table 1-1. Each alloy type is developed to operate in a certain environment for a specific reactor type. For instance, Zircaloy-2 is utilized as cladding material in boiling water reactors (BWRs) and as structural material in heavy water reactors (CANDU). Zircaloy-2 contains dispersed intermetallic precipitates of $Zr(Fe,Cr)_2$ and $Zr(Fe,Ni)_2$ in the HCP α-zirconium matrix [2]. Tin (Sn) and oxygen (O) found in solid solution in the α-Zr matrix help stabilize the α-zirconium phase and improve its mechanical strength [6].

Zircaloy-4 fuel cladding was developed for use in pressurized water reactors (PWRs), and unlike Zircaloy-2, it contains only $Zr(Fe,Cr)_2$ particles, as an increased Fe content replaces nickel, which was associated with increased hydrogen pickup. In general, the manufacturing process of Zircaloy-4 tubes includes quenching from high temperatures in the β phase field, subsequent hot extrusion, and cold pilgering with intermediate annealing steps, and final stress relieving. The final product is in the cold worked stress relieved condition (CWSR) [6]. The plastic deformation during the pilgering process reduces the tube wall thickness and increases the flow stress because of work hardening. This cold working also creates a textured microstructure within the cladding tube such that the c-axes of the zirconium grains are preferentially oriented normal to the tube surface, and tilted 30-40° from tube radial direction [7]. The presence of the crystallographic texture causes anisotropic deformation behavior due to irradiation creep and growth in the radial, axial, and circumferential orientations. Furthermore, as a result of cold work, the grains tend to be elongated in the axial orientation such that as-fabricated CWSR Zircaloy-4 consists of elongated pancake shaped grains with an average length of 5-10 μm [8].

Replacing Zircaloy-4, modern zirconium alloys, such as ZIRLO and M5, are now preferentially used in PWRs. Both of these alloys include niobium which stabilizes the β phase and improves the corrosion behavior [1]. Similar to Zircaloy-4, ZIRLO, also contains tin as well as a small amount of iron. On the other hand, M5 is a binary alloy of zirconium 1% niobium. Both ZIRLO AND M5 exhibit crystallographic textures similar to Zircaloy-4. While ZIRLO is typically used in CWSR condition, M5 has a re-crystallized grain microstructure [9].

Another common zirconium-based alloy is Zr-2.5Nb, which is used as pressure tube material in heavy water reactors (CANDU). Like M5 and ZIRLO, Zr-2.5Nb contains additions of oxygen and niobium to improve corrosion behavior and mechanical strength. The main difference between Zr-2.5Nb and M5 or ZIRLO is the texture. In Zr-2.5Nb, the c-axes of the α-zirconium grains are aligned parallel to the axial direction and perpendicular to the radial direction because of differences in the tube reduction process [7].

Table 1-1 Alloying elements of selected zirconium alloys in current use in the nuclear industry

Alloys	**Reactor**	**Elements [wt. percent]**					
		Sn	**Fe**	**Cr**	**O**	**Ni**	**Nb**
Zircaloy-4	PWR	1.2-1.7	0.18-0.24	0.07-0.13	1000-1400 [wt. ppm]	N/A	N/A
Zircaloy-2	BWR, CANDU	1.43-1.45	0.13-0.14	0.1	1260-1440 [wt. ppm]	0.05	N/A
Zr-2.5Nb	CANDU	N/A	N/A	N/A	0.09-0.15	N/A	2.4-2.8
ZIRLO	PWR	0.96	0.1	N/A	1430 [wt. ppm]	N/A	0.99
M5	PWR	N/A	N/A	N/A	1250 [wt. ppm]	N/A	1.0

1.2 Environmental Degradation of Nuclear Fuel Cladding

During operation in a nuclear reactor the cladding tubes are concurrently subjected to various degradation driving forces such as radiation damage from the intense particle flux, waterside corrosion of the cladding and hydrogen pickup, stresses induced by pellet-cladding interaction and other possible degradation mechanisms, including grid-to-rod fretting and CRUD-induced localized corrosion. Since the cladding is subjected to a very aggressive environment during operation, the integrity of fuel cladding tube has to be ensured from the beginning of the nuclear power plant's operation, including all steps (pool storage, dry-cask storage, and transportation), to final disposal.

The combination of pellet-clad interaction, which is defined as the mechanical interaction between the UO_2 fuel pellet and the Zircaloy cladding, and chemical attack from fission products within the

environment (especially iodine) can cause stress-corrosion cracking of the cladding. The mechanical interaction is caused by UO_2 swelling which results in friction between pellet and cladding. Radial cracks in the pellet, induced by the temperature gradient in the UO_2 pellet, cause fission products to accumulate in localized regions at which chemical attack of the cladding occurs. Thus, both frictional loading and an environmentally induced deterioration of mechanical properties can cause crack initiation, and subsequently crack growth at slow rates within the cladding [10, 11].

Radiation damage is caused by the displacement of the atoms in the cladding material from their lattice positions by the incoming neutron flux. This process creates a vacancy and a self-interstitial atom pair, i.e. Frenkel pairs. The evolution of those Frenkel pairs causes microstructural changes in the cladding such as solute atom segregation, second-phase-particle amorphization, dislocation loop formation, and dissolution or precipitation of second phase, which cause changes in microstructure leading to hardening, embrittlement, and deformation of the cladding. Thus, the mechanical response of the cladding is degraded. Also, the radiation damage can assist other degradation mechanisms such as stress-corrosion cracking and waterside corrosion [9].

Water side corrosion of the nuclear fuel cladding involves the formation of a zirconium oxide layer at the high operation temperatures in nuclear reactors and is a result of an oxidation reaction of zirconium and water as shown in Equation (1.1). Due to the oxidation reaction, a ZrO_2 layer forms and grows on the cladding outer surface. The mechanisms of oxide formation and growth are complex involving a wide range of multi-scale physical phenomena including electrical charge balance, vacancy-ion transport, crystal structure, crystallographic orientation (texture), initial microstructure of the cladding, alloying elements, residual stresses at the metal-oxide interfaces, waterside chemistry and others (like galvanic properties of cladding and structural metals in the reactor core) [12]. In general, uniform corrosion is the main degradation concern in PWRs and nodular corrosion in BWRs. One of the drawbacks of oxidation is the decrease of the heat transfer properties from cladding to coolant. In addition, the oxide spalling causes material loss and can promotes hydride blister formation [13].

$$Zr + 2H_2O \rightarrow ZrO_2 + 2H_2 \quad (1.1)$$

As shown in Equation (1.1), the other product of water-side corrosion reaction is hydrogen which can be picked-up by the cladding. Also, radiolysis of water under neutron and gamma irradiation, Equation (1.2), produces hydrogen which also may contributes to the hydrogen pick-up [1] in the following manner:

$$H_2O \xrightarrow{n,\gamma} H^+ + OH^- \quad (1.2)$$

The extent of hydrogen pick-up depends on many parameters such as oxide layer thickness, second phase particles, alloying elements, water chemistry, and most importantly the type of the zirconium-based alloy (as listed in Table 1-1) [12]. For instance, the hydrogen pick-up fraction of Zircaloy-4 and ZIRLO is high whereas Zr-2.5Nb is drastically lower than Zircaloy-4 and ZIRLO [14]. The hydrogen picked up by cladding can be either found in solid solution in the HCP zirconium matrix (depending on terminal solid solubility of dissolution at a specific temperature) or in the form of hydride precipitates if the terminal solid solubility limit is exceeded [15-17]. For example, during operation of a PWR, up to 120 wt. ppm of hydrogen is in solid solution due to the terminal solid solubility of dissolution at the cladding tube operating temperature of 350°C [17] and any additional hydrogen precipitates as zirconium hydride platelets in the cladding that are brittle at low temperatures [18].

1.3 Dry Cask Storage/Transportation of the Spent Fuel Cladding

The spent fuel rods that are initially in wet-storage can be removed from the spent fuel pool to be stored in dry-casks containers. In general, the decay heat of fuel rods is removed by either inert gas or air cooling such that the maximum clad temperature will not exceed 400°C in dry-cask storage facilities [19].

Cladding integrity must be assured in dry-cask storage to ensure fuel retrievability. Spent fuel rods may contain a high level of hydrogen content and a hydride microstructure that may degrade cladding mechanical response. The postulated failure mechanisms for cladding are creep, stress corrosion cracking

(SCC), and hydrogen-induced defects such as delayed hydride cracking (DHC), and hydride embrittlement [20, 21].

Delayed hydride cracking involves the hydrogen diffusion under the high triaxial stresses near the crack tip region. When the hydrogen solubility limit is reached on a local scale near the crack tip, hydrides can precipitate and subsequently cracks, thus extending the main crack into a region low in hydrogen content at which point, the crack arrests. The stress field of the arrested crack then attracts more hydrogen, and the process repeats with discontinuous crack growth occurring until the crack becomes critical in length as dictated by the cladding fracture toughness. Thus, DHC is a time-dependent sub-critical crack growth. For dry cask storage conditions, the stress intensity at a crack tip is estimated under conservative conditions as 3-3.5 MPa$\sqrt{m}$, which is below the critical stress intensity to propagate crack in the presence of hydrogen in Zircaloy cladding. Thus, DHC is not likely to happen during dry-cask storage [20].

The most likely cause of cladding failure in dry-cask storage conditions is hydride embrittlement as a result of unfavorable hydride microstructures in the zirconium–based claddings. Possible in homogenous hydride microstructures after reactor operation are hydride rim, hydride blister, and circumferentially oriented hydride platelets, such as shown in Figure 1-1a. In general, the hydride formation can reduce the fracture resistance of the material and directly affects the ductile-to-brittle-transition temperature of the cladding (DBTT) [18]. Hydride rim and blister formation can reduce the ductility of cladding without affecting the DBTT while circumferentially oriented hydrides have less effect on ductility. During drying and storage circumferential hydrides can change their orientation and form radially oriented hydrides, as shown in Figure 1-1b. These radial hydrides drastically decrease the DBTT, causing severe loss of ductility and rupture at low strains. Except for radial hydride embrittlement, the failure mechanisms can be mitigated by controlling the temperature during transportation. Because of the potentially large decrease in DBTT, radial hydride-induced embrittlement is of special concern during dry storage of the spent nuclear fuel rods.

Radial hydride embrittlement can affect cladding failure during dry-cask storage and transportation processes even at elevated temperatures [18, 22]. For instance, when hydrides are aligned through the thickness of the cladding (radial hydrides) as shown in Figure 1-1b, the DBTT increases up to 150°C, and a crack initiation and growth process may occur with very small plastic deformation[18] Thus radial hydride formation can result in a decrease of the DBTT and "brittle-like" failure.

The formation of a radial hydride microstructure occurs if during cool-down the hydrides precipitate under a sufficient tensile hoop stress from a drying cycle in which the cladding experiences sufficiently high temperatures to dissolve part or all of the hydrogen present in the cladding. Such a re-oriented hydride microstructure can happen under the vacuum-drying conditions of spent fuel rods. During wet storage after fuel removal from reactor, most hydrides are oriented circumferentially such that the hydride platelet faces are parallel to the circumferential direction of the cladding tube (i.e., the hoop direction) and perpendicular to the radial direction of the cladding, as shown in Figure 1-1a.

For dry-cask storage or transportation after wet storage, the moisture on the cladding outer surface has to be removed by heating the cladding to ≤ 400°C (with the decay heat of fuel rods) and then cooling-down to storage/transportation temperatures in a process called "vacuum-drying". At the high temperatures achieved during the vacuum-drying process, up to 200 wt. ppm hydrides can dissolve and fill gases (He during fabrication) and gaseous fission products internally pressurize the cladding and creating a hoop stress as the spent fuel rods are heated up. During cool-down, hydrides start to precipitate under stress (at a temperature determined by terminal solid solubility of precipitation [17]). However the presence of a sufficient level of hoop tension stress can change the initial circumferential orientation of the hydrides into a radial orientation ("radial" hydrides) [22].

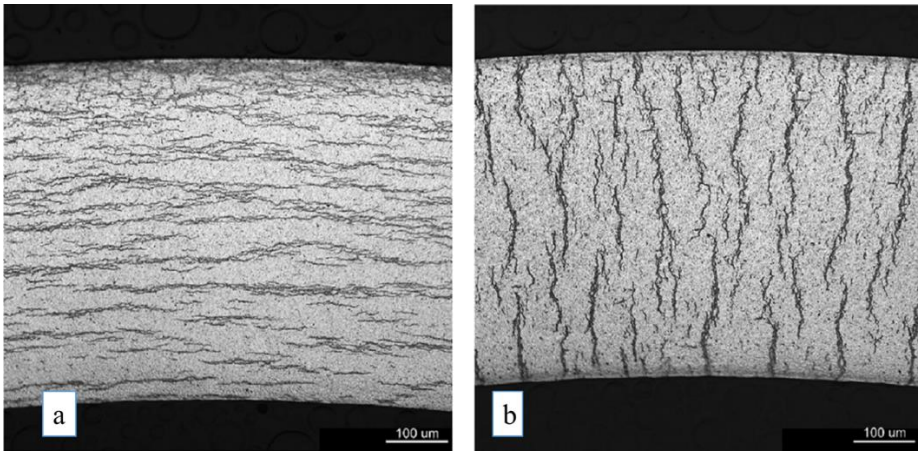

Figure 1-1 Hydride platelets orientations (a) initial circumferential hydride microstructure (b) through thickness (radial) hydride microstructure after thermo-mechanical treatment such as vacuum drying [23].

1.4 Zirconium Hydride Phases and Possible Hydride Microstructures in Nuclear Fuel Cladding during Reactor Operation

1.4.1 Zirconium Hydride Phases

In the open literature, two stable (δ, ε) and one metastable (γ) hydride phases are reported, as shown in the zirconium-hydrogen phase diagram in Figure 1-2 [24-27]. The basic properties of these phases are listed in Table 1-2. The different hydride phases have different degrees of hydrogen occupancy at the two available (preferred) interstitial sites, and this behavior causes different volumetric strains for each phase, stoichiometry, and crystal structure. For γ-hydrides, only half of the two available interstitial sites are occupied by hydrogen which results in a stoichiometry coefficient of 1. On the other hand for δ-hydrides, hydrogen occupies more than half of the two interstitial sites, which yields a stoichiometry coefficient in the range of 1.31 to 1.7 with an equilibrium value of 1.5. For ε-hydride phase, hydrogen occupies almost all the available interstitial sites, which means the ε-hydride stoichiometry is in the range of 1.7 to 2 [6, 28, 29]. Unlike δ-hydrides which have face centered cubic (FCC) crystal structure, both the ε- and γ- hydride phases have face-centered-tetragonal (FCT) crystal structure and are formed by shear transformations that

the ε-hydride is formed as a result of δ → ε reaction; and γ- hydride is formed as a result of H + Zr → γ reaction. Although both the ε- and γ- hydride phases have the same crystal structure, the c/a ratio of γ-hydride is greater than 1 (≈1.08) whereas c/a ratio of ε-hydrides is less than 1 (≈0.95) [6, 26, 28, 30].

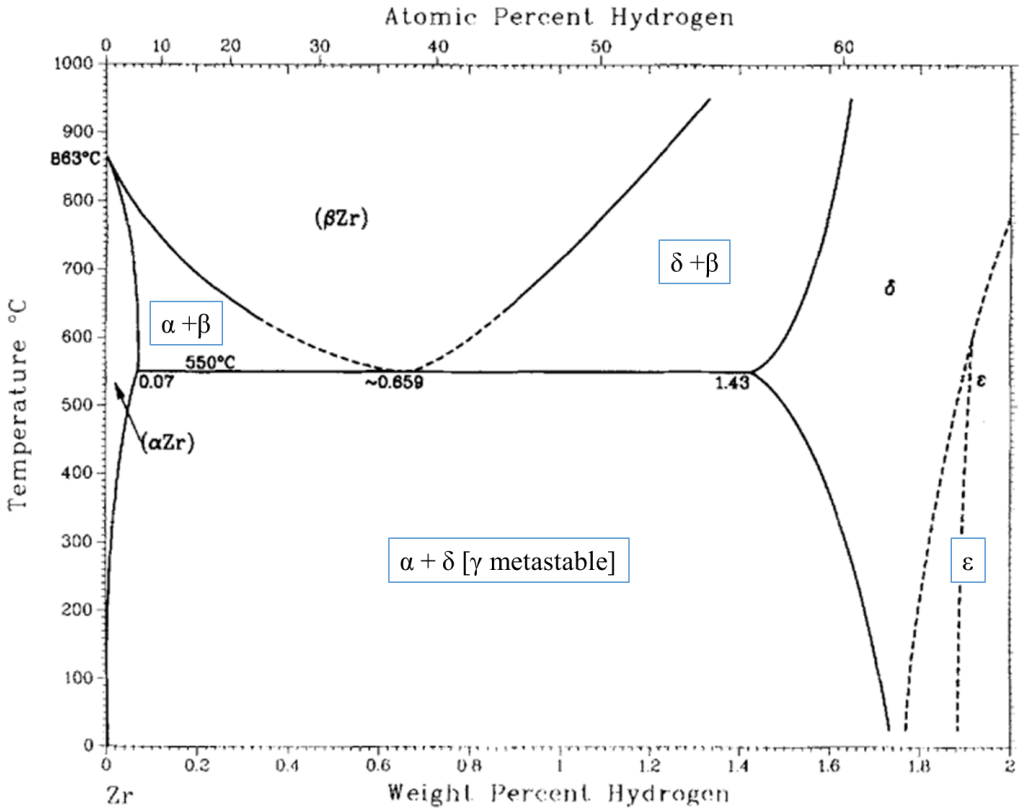

Figure 1-2 Zirconium-hydrogen (Zr-H) phase diagram [24, 25, 31-33]

Table 1-2 The properties of hydride phases observed in zirconium and zirconium-based alloys.

Hydride Phase	**Stoichiometry ZrH_r**	**Crystal Structure**	**Orientation Relationship**	**Lattice Parameters at 25°C [nm]**	**Type of Transformation**	**Morphology**
δ	1.31 to 1.71	FCC, CaF_2	δ{111}//α(002)	a=0.4777	H+Zr→ δ, Nucleation and Growth at slow cooling rates	Platelet
ε	1.71 to 2	FCT		a=0.4888 c=0.457 c/a<1	δ → ε, Martensitic, Twinning	Straight bands with sub-bands
γ	1	FCT	γ {111}//α(002)	a=0.4617 c=0.4888 c/a>1	H + Zr → γ, Bainite-type transformation; Re-distribution of Hydrogen atoms by martensitic shear	Needle-like

The δ to ε-hydride transformation happens at high hydrogen contents greater than 10000 wt. ppm with the ε phase being formed by a martensitic transformation involving twinning at both δ-ε and ε-ε boundaries[26]. The resultant ε-hydride microstructure consists of long straight bands with sub-bands of ε phase as shown in Figure 1-3. However, the ε-hydride forms only at very high hydrogen contents not likely to occur during operation. It is however possible to observe ε phase in the cladding during hydride rim formation at hydrogen contents greater than 3000 wt. ppm (0.3 % wt.) [27].

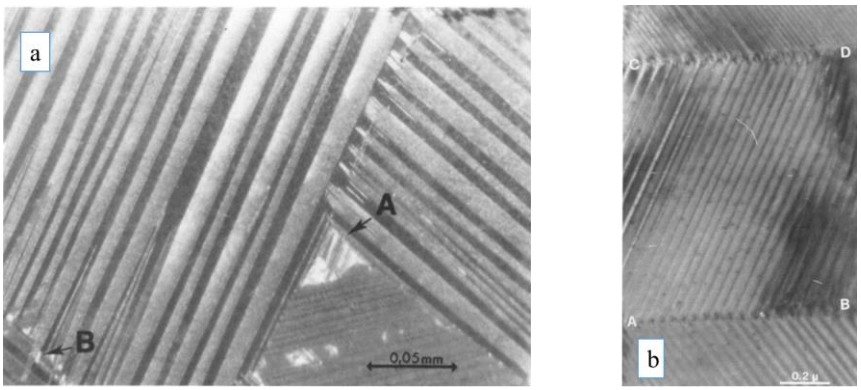

Figure 1-3 ε-hydride microstructure (a) shows the straight band structure at low magnification by optical and (b) shows the sub-band structure at high magnification by TEM[26]

The formation of γ-hydrides involves rapid diffusion of hydrogen atoms to localized regions by shearing of α-zirconium lattice both perpendicular to and parallel to the invariant-plane strain plane of α-(002) [28, 29, 34, 35]. The γ-hydrides have an orientation relationship of γ-{111}// α-(002) with α-zirconium with a volumetric misfit of 12.3% [36-38]. The misfit is relieved by shear (plastic relaxation) and confined by anisotropic dilatational transformation strains, as shown in Table 1-3 [35, 37, 39]. The γ-hydrides (needle-like) have been observed in α-zirconium as a result of quenching, which create hydrogen super saturations higher than 500 wt. ppm [29, 35, 40]. Inter-granular γ-hydrides were also observed at lower super saturations [41].

Table 1-3 Dilatational and volumetric misfit strains of γ- and δ- hydrides

Misfit Strains [%]	**Direction**	**γ-hydrides**	**δ-hydrides**
ε_1^T	[0001]	5.70	7.20
ε_2^T	$[11\bar{2}0]$	0.551	4.58
ε_3^T	$[1\bar{1}00]$	5.64	4.58
Volumetric Strain [%]			
$(V_{hyd} - V_{\alpha Zr})/V_{\alpha Zr}$		12.3	17.2

The γ-hydride phase is reported to be metastable. The γ phase formation has been observed in the high purity of zirconium crystals at various cooling rates and zirconium-based alloys after quenching or cool-down with cooling rates greater than 10°C/min [29, 41-45]. Cann et al. stated that as the purity of zirconium increased, the γ phase formation was increasingly promoted such that the γ phase became an equilibrium phase [43]. They also determined that the accommodation energy of δ-hydride becomes smaller than the accommodation energy of γ-hydride when oxygen content is greater than 1000 wt. ppm (similar to commercial alloys). Lanzani et al. also provided supporting data for the reported effect of purity by testing hydride precipitation in Zircaloy-4. For nuclear fuel cladding such as Zircaloy-4, δ-hydrides were the only observed phase. As the purity of zirconium decreased, the γ phase become more favorable [45].

The δ-hydrides are the equilibrium phase normally observed in nuclear grade zirconium-based alloys of Zircaloy-2 and -4, and Zr-2.5Nb in nuclear reactor operating conditions. The δ-hydrides, unlike ε- and γ- hydrides, are usually formed by diffusion-controlled phase transformation at low hydride super saturation and under conditions of mostly heterogeneous nucleation of inter-granular (grain boundary) precipitates [29, 44, 46, 47]. At cooling rates less than 2-3°C/min, most of the δ-hydrides precipitate at grain boundaries and fewer intra-granular hydrides are observed [29, 44]. For cooling rates higher than 3°C/min (but still lower than 10°C/min), the ratio of intra-granular hydride to inter-granular is high, depending on the alloy, cooling rate, and hydrogen content [29, 41, 44]. Furthermore, the δ-hydride internal structure also depends on cooling rate such that for low cooling rates, high dislocation densities within inter-granular hydrides are observed, whereas for intra-granular hydrides precipitate at intermediate cooling rates (greater than 3°C/min less than 10°C/min), fine internal twinning has been observed within these hydrides [29, 41].

The most common δ-hydride shape is platelets, observed for both intra- and inter-granular hydrides. For intra-granular hydrides, lattice matching of hydride and zirconium matrix is preferred to reduce the strain energy, and the orientation relationship between the close-packed planes of the hydride and matrix is δ-{111}// α-(002), which is similar to γ-hydrides in a zirconium matrix. For inter-granular hydrides, the

grain boundary energy promotes hydride nucleation at grain boundaries [46, 48]. Furthermore, δ-hydrides also tend to precipitate on grains that have basal planes parallel to the grain boundary by lattice matching of closed-packed planes such that δ-{111}// α-(002), to minimize not only the grain boundary energy but also the elastic strain energy and interphase boundary energy [46, 48].

The "macroscopic" hydrides (see Figure 1-1) observed in optical micrographs are usually the collection of much smaller "microscopic hydride" platelets as shown in Figure 1-4a and b. In general, length of these microscopic hydrides (both intra- and inter- granular) are measured mostly in a range of 200-1000 nm [38]. The stacking of the smaller hydride, in particular circumferentially oriented, platelets results in all apparent "macroscopic" hydride platelet orientation (habit plane) of $[10\bar{1}7]$ [38, 49]. The hydride platelets shown in Figure 1-4a likely nucleated at the grain boundary initially close to the triple junction because of high grain boundary energy and growth into the zirconium matrix; thus, dislocation field around the hydride is observed due to plastic relaxation (accommodation) because the transformation (misfit) strain has not been able to accommodate all the strain energy elastically. Figure 1-4b shows that the hydride platelet nucleated nearby the grain boundary that is parallel to one of neighboring grain's (002) planes; thereby hydride platelet orients itself to keep the closed-packed orientation relationship between zirconium and hydride, and other hydride platelet precipitates almost parallel to the grain boundary hydride by minimizing its transformation energy; thus a stacking orientation of hydrides has been observed.

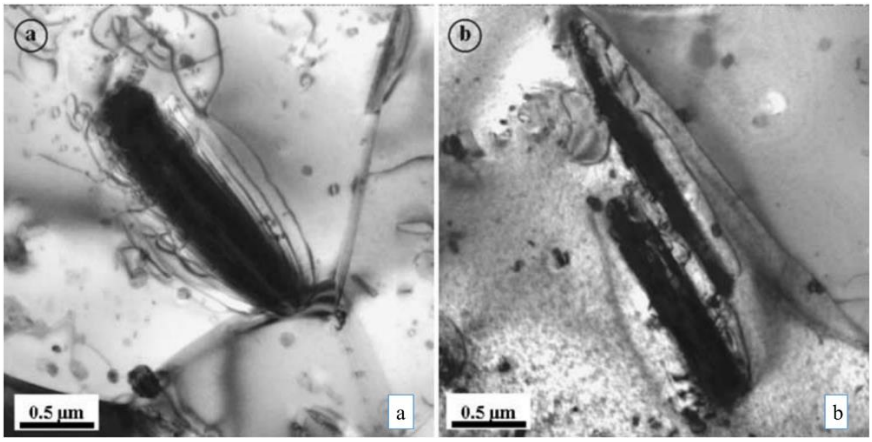

Figure 1-4 Microscopic inter-granular hydrides in furnace cooled sample. (a) hydride precipitate perpendicular to a grain boundary; (b) hydride precipitates along the grain boundary [49]

1.4.2 Possible Zirconium Hydride Microstructures in Nuclear Fuel Cladding

As described previously, during reactor operation the hydrides can be in the form of different hydride microstructures such as a hydride rim, a blister, and uniformly distributed circumferential/radial hydride platelets. A hydride rim is formed due to a temperature gradient in the cladding causing the cladding outer surface temperature to be lower than the inner surface temperature during nuclear power reactor operation. Therefore, the terminal solid solubility is first exceeded near the outer surface of the cladding. As a result, hydrogen precipitates as hydride platelets that accumulate as a continuous layer of separate circumferential hydride platelets, the ensemble of which constitutes the hydride rim (see Figure 1-5a) [27]. If oxide layer spallation occurs on the outer surface of the cladding, lens shaped solid hydrides, hydride blisters, can be formed on cladding outer surface as shown in Figure 1-5b [50].

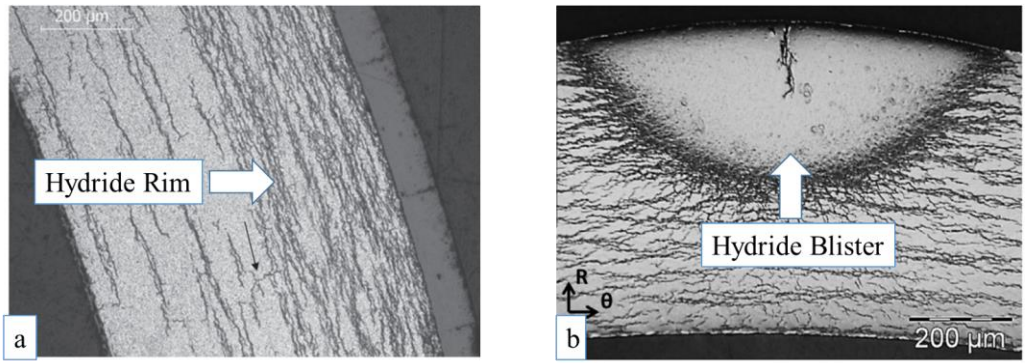

Figure 1-5 (a) Hydride rim formation in the nuclear fuel cladding tube [18] and (b) hydride blister formation on the cladding surface [51]

1.5 Zirconium Hydride Dissolution and Precipitation

The hydrogen solubility in zirconium determines the amount of hydrogen that is in solid solution or precipitated in zirconium or zirconium-based alloy as a function of temperature. At a given temperature, the terminal solid solubility of dissolution describes the maximum hydrogen concentration in solid solution during dissolution and the terminal solid solubility of precipitation is the maximum hydrogen concentration that can precipitate in the matrix during precipitation process. Differential scanning calorimetry (DSC) is a commonly used technique for solubility determination because of its sensitivity to low hydrogen contents and being non-destructive test [17, 52-59]. DSC is based on the measurement of the peak temperature and enthalpy of the thermally isolated hydrided Zircaloy sample and the reference non-hydrided sample at the same time. The enthalpy change is caused by phase transformations or dissolution and precipitation of hydrides.

In addition to DSC, in situ high energy X-ray diffraction (XRD) can also be used for the determination of TSS_d and TSS_p because hydride dissolution and precipitation can be followed as it happens [34, 60-63]. The precipitation and dissolution temperatures can be determined by the appearance or disappearance of the hydride diffraction peak as a function of temperature. It is also possible to detect the d-spacing evolution of zirconium as a function of temperature (in a manner similar to the dilatometry

technique). Figure 1-6 shows the terminal solid solubility of dissolution and precipitation data for Zircaloy-4 as measured by DSC, XRD, and other techniques.

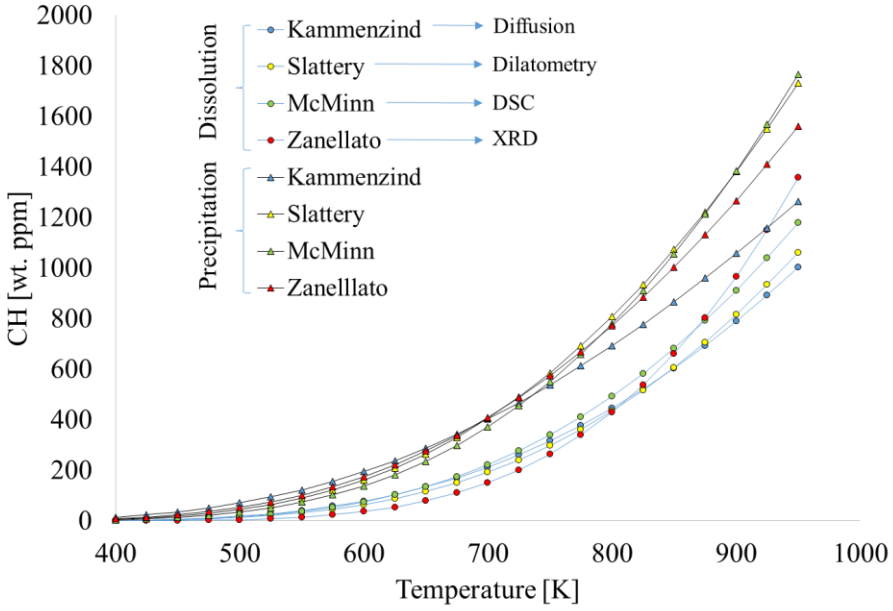

Figure 1-6 Plots of selected dissolution and precipitation data for Zircaloy-4, showing the hysteresis between dissolution and precipitation from Kammenzind [64], Slattery [65], McMinn [17], and Zanellato [62]

Generally, the solubility curves can be written as an Arrhenius type equation [15, 65-67] as shown in Equation (1.3)

$$C_H(\text{wt. ppm}) = A \exp(-\frac{B}{RT}) \quad (1.3)$$

where C_H is the hydrogen concentration in solid solution, wt. ppm, A is the pre-exponential constant, R is the gas constant, T is the temperature, and B is the activation energy of the specific process considered such as dissolution or precipitation. The terms A and B depend on the type of transformation (γ-, δ-, and ε-hydride dissolution or precipitation), stoichiometry of the hydrides, and thermal history of the material. B also depends on the elastic and plastic self-strain accommodation energies.

For the equilibrium dissolution process, B is equal to the heat of solution, ΔH_s, of hydrides in the saturated zirconium matrix. Then, the equilibrium concentration of hydrogen, C_{TSS}, is written as:

$$C_{TSS}(\text{wt. ppm}) = A \exp(-\frac{\Delta H_s}{RT}) \tag{1.4}$$

According to the dissolution and precipitation theory based on accommodation energies, hydrides and matrix both accommodate elastic (w_{el}) and plastic strain energies (w_p) during precipitation. During precipitation, the strain caused by the volumetric accommodation of the hydrides in zirconium matrix; i.e. the volumetric strain is relaxed by elastic strain energy until the critical precipitate size is reached. Thus, the elastic strain energy depends on the elastic properties of matrix (bulk modulus) and hydrides and the anisotropic transformation strains within hydrides. After a critical size of hydride precipitate is exceeded the precipitate accommodates the remaining part of the volumetric strain by punching-out dislocations; i.e. the plastic relaxation. Thus, the plastic strain energy is determined by flow properties of the matrix and the size of the plastic region around hydride precipitate.

During dissolution part of the accommodated elastic strain energy is recovered and the plastic strain energy is not if dislocations are not annealed out. Thus, the remaining part of elastic (w_{el}^r) and the plastic strain (w_p) energies contribute to the dissolution process and the terminal solid solubility of dissolution is written as shown in (1.5) [68], and B in Equation (1.3) is written as $(\Delta H_s - w_{el}^r + w_p)$ for dissolution:

$$C_{TSSd}(\text{wt. ppm}) = A \exp\left(-\frac{\Delta H_s}{RT}\right) \exp(\frac{w_{el}^r - w_p}{RT}) \tag{1.5}$$

As stated previously, for hydride precipitation, there are two distinct stages based on the critical precipitate size for dislocation generation, i.e. plastic deformation of the matrix (and/or the hydride) that affect the terminal solid solubility of precipitation. The first stage is the initial hydride nucleation. At this stage only the elastic strain energy, w_{el}^t, needs to be accommodated in hydride and matrix because the

hydride size is smaller than the critical size to initiate plastic relaxation [69]. In this case, the terminal solid solubility is written as in Equation (1.6) [52, 54, 69, 70].

$$C_{TSSp}(\text{wt. ppm}) = A \exp\left(-\frac{\Delta H_s}{RT}\right) \exp\left(\frac{w_{el}^{t}}{RT}\right) \quad (1.6)$$

As a result, B in Equation (1.3) is equal to $\Delta H_s - w_{el}^{t}$ for the initial stage of the hydride precipitation reference. After size of the hydride size exceeds the critical size to create dislocations in the matrix, the plastic accommodation energy also affects the solubility. Hence, the terminal solid solubility for precipitation as follows [52, 54, 69, 70]:

$$C_{TSSp}(\text{wt. ppm}) = A \exp\left(-\frac{\Delta H_s}{RT}\right) \exp\left(\frac{w_{el}^{r} + w_p}{RT}\right) \quad (1.7)$$

The term B in Equation (1.3) is now equal to $(\Delta H_s - w_{el}^{r} - w_p)$ for the hydride growth stage of the precipitation. The difference between the energy requirements for dissolution and precipitation is $-2w_p$. Because of the presence of the term $-2w_p$, the terminal solubility of dissolution and precipitation curves are not same. As a result, that difference yields different terminal solid solubility values causing a "hysteresis" on the solvus [71].

The plastic accommodation energy strongly depends on the yield strength of hydride and matrix and the plastic zone around the hydride. Thus, the plastic accommodation depends on the thermal history of the cladding, alloying elements, matrix microstructure, and texture.

Since, the elastic accommodation energy is governed by elastic properties of the hydrides and zirconium to zirconium hydride anisotropic transformation strain (or misfit). The misfit ($\varepsilon_{[hkl]}^{T}$) at corresponding inter-atomic planes, in general, is written in terms of d-spacing:

$$\varepsilon_{[hkl]}^{T} = \frac{d_H - d_\alpha}{d_\alpha} \quad (1.8)$$

where [hkl] is the misfit direction, d_H is the hydride d-spacing in the misfit direction, and d_α is the zirconium d-spacing in the misfit direction. Since the transformation strains are governed by the lattice spacing of the hydride and matrix [71-73], the next section briefly addresses the lattice parameters and thermo-mechanical properties of hydrides and Zircaloy-4.

1.6 Thermo-mechanical Properties of Zircaloy-4 and Zirconium Hydrides

In Chapter 1.5, the importance of transformation strains and thermo-mechanical properties are discussed in terms of the hysteresis of hydride dissolution and precipitation. The transformation strains of hydrides depend on the lattice parameters of both α-zirconium and δ-hydrides. The lattice parameters as measured by X-ray diffraction studies are shown in Equations from (1.9) to (1.12) for the temperature dependent single crystal α-zirconium and δ-hydrides[74]. The lattice parameters of α-zirconium phase are

$$a(\text{nm}) = 0.322849 + 1.457\ 10^{-6}\text{T} + 3.37\ 10^{-10}\text{T}^2 - 1.64\ 10^{-13}\text{T}^3 \quad (1.9)$$

$$c(\text{nm}) = 0.513956 + 2.562\ 10^{-6}\text{T} + 1.936\ 10^{-9}\text{T}^2 - 2.45\ 10^{-13}\text{T}^3 \quad (1.10)$$

For δ-hydride lattice parameter, Kempter determined the lattice parameter of δ-hydrides using powder diffraction X-ray analysis of solid hydrides obtaining the relation shown in Equation (1.11)[75].

$$a(\text{nm}) = 0.477872 + 1.716\ 10^{-7}\text{T} + 3.24\ 10^{-9}\text{T}^2 \quad (1.11)$$

However, the lattice parameter of δ-hydrides also depends on the stoichiometry ratio, r_H, in the range of 1.31 to 1.7. Performing X-ray diffraction experiments of hydrided samples, Yamanaka et al. have estimated the δ-hydride lattice parameter as a function of both temperature and stoichiometry as given in

Equation (1.12) [74]. Yamanaka's lattice parameter at room temperature predicts numbers similar to those are reported by Kempter [75].

$$a(\mathrm{nm}) = 0.4706 + 4.382\ 10^{-3} r_H + (T - 25)\{2.475\ 10^{-6} + 6.28\ 10^{-6} r_H + 5.8281\ 10^{-8} r_H^2\} \quad (1.12)$$

1.6.1 Thermal Expansion Coefficients of α-Zirconium, Zircaloy-4 and δ-Zirconium Hydride

The determination of the thermal expansion coefficient of CWSR Zircaloy-4 is based on single crystal zirconium thermal expansion coefficients, as listed in Table 1-4 by MATPRO [76].

Table 1-4 The single crystal α-zirconium thermal expansion coefficients which are selected in literature

Thermal Expansion (10^{-6} °C^{-1})	**[002]**	**[100]**
Cheadle [77]	10.40	6.30
Lloyd [78]	9.21	5.14
Barrow [34]	8.19	5.08
Zanellato [62]	7.62	5.77
Skinner [79]	10.80	5.50

The thermal expansion coefficient calculation of Zircaloy plate is estimated as 7.10 x 10^{-6} /°C in the transverse direction (TD) of plate and 5.41 x 10^{-6} /°C in the rolling direction (RD) [80]. The thermal expansion coefficient of Zircaloy-4 sheet material has been determined to be 6.2 x 10^{-6} /°C in the transverse direction and 5.6 x 10^{-6} /°C in the rolling direction. Hence, the thermal expansion coefficient of Zircaloy-4 is in the range of 5 to 7.5 x 10^{-6} °C^{-1}, depending on the specimen direction.

For δ-hydrides, the thermal expansion coefficient data are controversial. Early studies were performed using solid δ- zirconium hydride samples with hydrogen weight percent (wt.) of 1.6-1.8. Kempter determined the thermal expansion coefficient of δ-hydrides by dilatometry for bulk samples with hydrides as 2.56-2.98 x 10^{-6} /°C, but those data may have been affected by cracks [75]. Beck's estimation of the δ-hydride thermal expansion coefficient, based on X-ray diffraction data, was 14.2 x 10^{-6} /°C[81]. A relatively recent study done by Yamanaka et al. predicts the thermal expansion coefficient of δ-hydrides in a range of 25-30 x 10^{-6} /°C [74] which is at least 5-times greater than Kempter's value. Thus, there is great variability in the open literature that we will discuss in the current work.

1.6.2 Mechanical Properties of Zircaloy-4 and Zirconium Hydrides

MATPRO provides the following values for the temperature dependence of the Young's modulus, shear modulus and Poisson's ratio ν of Zircaloy-4 [82]:

$$E = 1.236\ 10^{11} - 6.222\ 10^{7}T\ [Pa] \quad (1.13)$$

$$G = 4.591\ 10^{11} - 2.464\ 10^{7}T\ [Pa] \quad (1.14)$$

$$\nu = \frac{E}{2G} - 1 \quad (1.15)$$

Selected data of the temperature dependent flow (yield) stresses and strain/strain rate hardening exponents for Zircaloy-4 material are listed in

Table 1-5.

Table 1-5 shows that the flow behavior of plate and sheet materials are similar but slightly different than that of tube material flow in CWSR conditions. This difference is likely caused by the differences of the strain ellipse during reduction process of sheets and tubes. For room temperature, the flow stress is estimated to be in the range of 530-590 MPa and the strength coefficient in the range of 610-715 MPa. Furthermore, high temperature predictions on flow behavior of Zircaloy-4 are also more or less similar for

sheet, plate, and tube samples. Considering the sheet material used in this study that is also used by Raynaud, Pierron, and Colas, the flow stress and strain hardening exponent values in

Table 1-5 are appropriate for our study [8], [50], and [83].

Table 1-5 Selected plastic behavior parameters for tubes and plate/sheet geometries that are related to this study. Yield stress,σ_y and strength coefficient, K, are in MPa. Strain hardening exponent is unitless

	Pierron[50]			Raynaud[8]			Flanagan[84]			Link[85]			MATPRO[80]		
	Zircaloy-4 Sheet						**Zircaloy-4 Plate**			**Zircaloy-4 Tube**			**Model**		
T[°C]	σ_y	K	n	σ_y	K	n	σ_y	K	n	σ_y	K	n	σ_y	K	n
Circumferential Direction Data for Tubes/ Transverse Direction for Plate/Sheet															
25	573	610	0.01	575	647	0.018	533	715	0.052	590	914	0.068	-	1066	0.114
300	318	394	0.03	315	585	0.032	334	425	0.041	350	375	0.059	-	684	0.099
375	-	-	-	290	375	0.027	-	-	-	-	-	-	-	-	-
Axial Direction Data for Tubes/ Rolling Direction for Plate/Sheet															
25	489	-	0.1	485	829	0.09	352	250	0.042	-	-	-	-	-	-
300	-	-	-	273	478	0.077	-	-	-	-	-	-	-	-	-
375	-	-	-	250	405	0.053	-	-	-	-	-	-	-	-	-

The determination of δ-hydride mechanical properties is not a straight forward procedure, and a review is in Puls' book [23]. The resonant frequency technique determines the elastic constant of hydrides as 98 GPa over a temperature range of 27 to 250°C using pure zirconium and Zr-2.5Nb samples. Contrary to the resonant frequency method, Figure 1-7 shows that the traveling wave velocity technique predicts the δ-hydride elastic modulus to be in the range of 125-135 GPa and δ-hydride shear modulus to be in the range of 47.5 to 52.5 GPa as the hydride stoichiometry changes from 1.47 to 1.66 in pure zirconium samples[74]. Since the travelling wave is a common technique to determine elastic properties. The elastic modulus of hydrides are assumed to be in the range of 125 to 135 GPa.

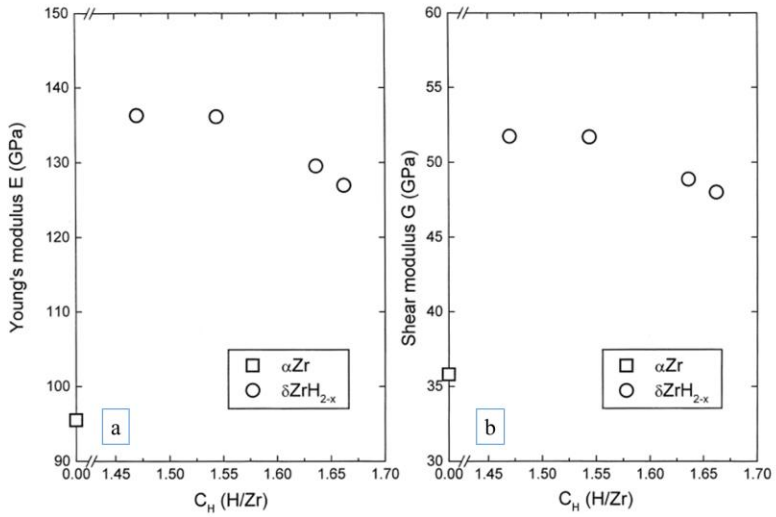

Figure 1-7 The hydrogen stoichiometry dependent (a) elastic and (b) shear modulus of hydrides [74].

The yield strength of hydrides as a function of temperature is shown in Figure 1-8.The yield strength of δ-hydrides decreases from 600 MPa to 50 MPa as the temperature increases from 25 to 400°C. At low temperatures, the hydride yield stress is higher than the matrix yield stress, but as temperature increases, it becomes lower than the yield stress of the matrix.

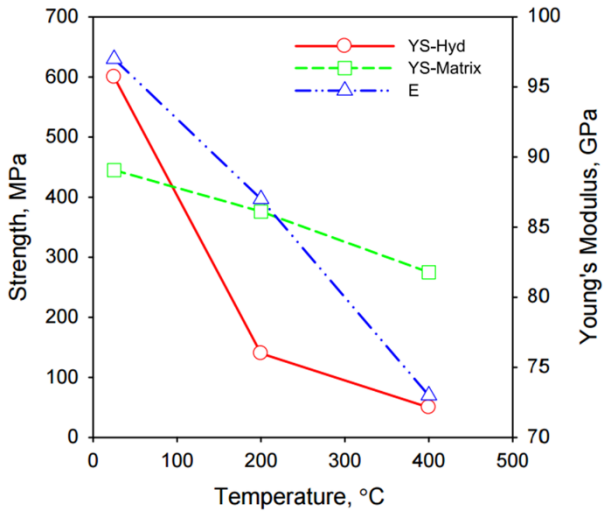

Figure 1-8 Temperature dependent hydride and zirconium matrix yield strengths [86].

1.7 The Hydride Induced Failure Behavior of Zirconium Alloys

As shown in several previous studies the failure behavior of zirconium-based cladding is affected by the hydrogen content, hydride microstructure (circumferential and/or radial hydride platelets and formation of hydride rim), temperature, and stress biaxiality (from uniaxial to equibiaxial) [87-89]. The presence of hydrides may degrade the ductility (fracture strain) and lower crack growth resistance (fracture toughness to initiate the crack growth) [13, 87, 90-96].

Zirconium alloys, in general, retain good ductility when the hydrides present maintain the circumferential orientation. However, there is a stress state effect, such that increasing the stress biaxiality deteriorates the ductility of recrystallized Zircaloy cladding as stress state changes from uniaxial to biaxial tension as shown Figure 1-9 [93, 97].

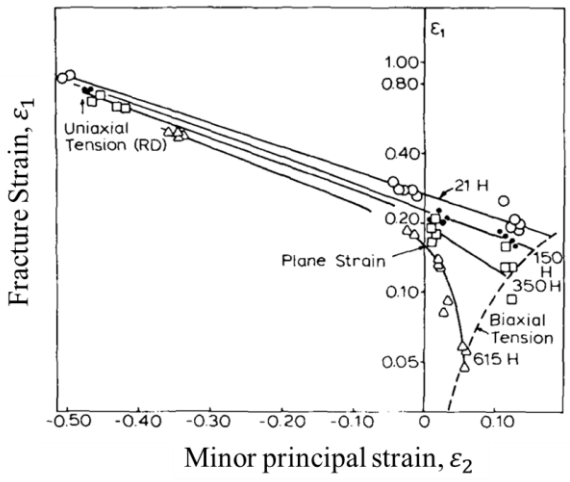

Figure 1-9 Fracture limit diagram for zircaloy-2 at hydrogen contents of 21, 150, 350, and 615wt. ppm [93].

As shown in Figure 1-10, the presence of circumferential hydrides can also lower the fracture toughness such that $J_Q(K_Q)$ values decrease rapidly as hydrogen content increases from [98, 99]. Usually complete loss of ductility with circumferential hydrides and brittle-like failure occurs only at high hydrogen contents and low temperatures. At high temperatures, some ductility is maintained [90, 100].

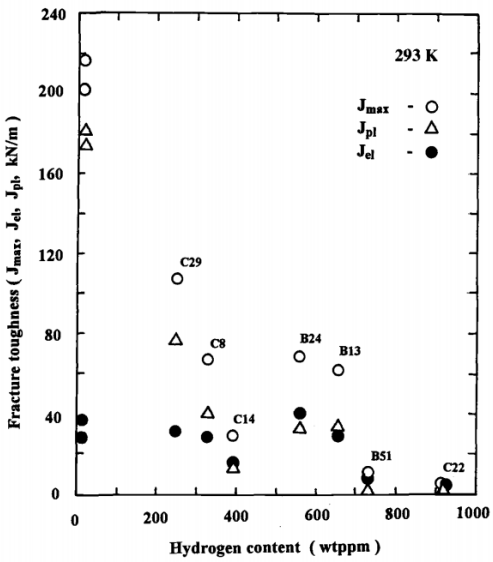

Figure 1-10 J_I-integral values for maximum load point (J_{max}) and its elastic (J_{el}), and plastic components (J_{pl}) for Zircaloy-2 cladding tubes [98].

The presence of radial hydrides can drastically decrease the fracture resistance of zirconium based alloys. For example, Raynaud et al. determined the fracture toughness (stress intensity to induce crack growth) for mixed (both circumferential and radial) and radial hydride regions as 23-28 MPa$\sqrt{m}$ (mixed hydrides) and 10-15 MPa$\sqrt{m}$ (radial hydrides), respectively [101]. This drastic change in fracture toughness is caused by hydride reorientation from circumferential (in-plane) to radial (out-of-plane). Moreover, Billone shows that as the radial hydride continuity factor (a measure of radial and circumferential hydrides' continuity through the thickness that is explained in Chapter 3) increases, the ductility (that is offset-strain at failure for ring compression tests) decreases and brittle-like rupture occurs at elevated temperature approaching 200°C as shown in Figure 1-11 [18].

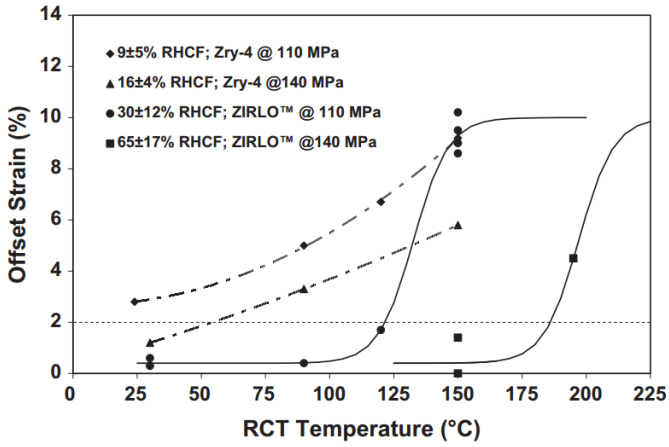

Figure 1-11 Offset-strain (measure of ductility) as a function of ring compression test temperature[18].

To conclude, radial hydride precipitation is especially deleterious to the cladding mechanical response because it can cause brittle-like fracture to occur at low hydrogen contents and high temperatures. Also, resistance to crack growth is lowered when radial hydrides are present; this effect can lead to sustained load cracking behavior and decreased fracture toughness. Thus, radial hydride formation is critical to the safe performance of spent fuel rods during dry-storage and transportation conditions for industry.

1.8 Zirconium Hydride Reorientation

As described in Chapters 1.3 and 1.7, radial hydride formation can drastically increase the susceptibility of cladding failure under spent fuel storage and transportation. Hydride reorientation can occur during the vacuum drying process of spent fuel rods. A typical vacuum drying process involves a thermal treatment such that the cladding is heated to temperatures of 400-450°C to remove moisture, held at the high temperature for a fixed time, and then cooled-down at slow rates of about 1°C/min to the cask-storage operating temperature. The hydrides dissolve during heating, and upon cooling the hydrides precipitate under stress. If the hoop stress exceeds a critical stress for hydride reorientation, hydrogen precipitates as radial hydrides, instead of circumferential hydrides.

To prevent hydride reorientation, the NRC places limitations on the vacuum drying process. For low burn-up fuel, the amount of hydrogen in the cladding remains low due to the relatively short residence time of fuel rods in the reactor, so that, brittle-like failure is unlikely. Consequently, there is no well-defined drying procedure for low burn up fuel. However, high burn-up fuel has higher hydrogen contents as a result of long residence time in nuclear reactor, and there is an increased susceptibility to brittle-like fracture of spent fuel rods with the presence of radial hydrides as described in Chapter 1.7. In order to avoid radial hydride precipitation, the hoop stress which is caused by internal gases at high temperature, is limited to 80 MPa by the maximum cladding operating temperature of 400 °C for vacuum-drying by NRC [19].

In the open literature, radial hydride precipitation in zirconium-based alloys has been studied extensively as a function of intrinsic and extrinsic parameters [22, 38, 60, 102-116]. Intrinsic parameters, result from the manufacturing process such as grain size and shape, grain boundary structure, amount of cold work, texture (basal pole intensity distribution), and alloy content. Other parameters such as temperature, heating/cooling rates, number of thermo-mechanical cycles and internal pressure (the source of the hoop stress) are extrinsic parameters and can be controlled during vacuum drying. Previous studies have investigated the effects of those parameters, both intrinsic and extrinsic, on radial hydride fraction and threshold stress determination. These studies are usually based on optical microscopy examination of the hydrides and the calculation of stress at specific locations where circumferential to radial hydride transition occurs. The hydride microstructure has been usually quantified by parameters such as the radial hydride orientation fraction (F_n), radial hydride fraction, and radial hydride continuity factor [22, 105, 108]. The hydride orientation factor is defined as the ratio of hydrides that are oriented perpendicular to the circumferential direction to total hydrides as shown in Equation (1-16).

$$F_n(\theta - 90°) = \frac{\#\text{ of hydrides oriented within } \theta - 90°}{\#\text{ of hydrides oriented within } 0° - 90°} \quad (1\text{-}16)$$

where $F_n(\theta - 90°)$ is the hydride orientation factor and θ is the angle between circumferential direction and hydride platelet edge direction.

The F_n is based on the ratio of number of radial hydrides to the total number of hydrides [117] and is accurate description of radial hydrides especially at low hydrogen contents when radial to circumferential hydride lengths are comparable. However, at high hydrogen contents, the hydride orientation factor accuracy decreases since circumferential and radial hydride lengths can differ significantly without any change in hydride orientation factor.

The radial hydride fraction (RHF) is defined as the ratio of the total length of radially oriented hydrides to the total length of hydrides at any orientation as shown in Equation (1-17) [8, 83]. Similar to the hydride orientation factor, the angle θ represents the angle between the circumferential direction and the hydride edge direction. Including the length of hydrides, the radial hydride fraction accurately represents the hydride microstructure for any hydrogen contents.

$$RHF_\theta = \frac{\text{Sum of the hydride lengths oriented within } \theta - 90°}{\text{Total length of hydrides at any orientation}} \quad (1\text{-}17)$$

where θ is the right angle between the circumferential (hoop) direction and the macroscopic hydride platelet normal; for instance, the θ angle for radial hydrides will be 90°. Another parameter that can represent the hydride microstructure is the radial hydride continuity factor (RHCF), defined as the ratio of the maximum length of the continuous radial and circumferential hydrides in a 150 μm-segment of the cladding divided by the cladding thickness [18].

Table 1-6 shows various metrics for defining the hydride microstructure and the threshold stress criterion to initiate hydride reorientation. These metrics are based on optical examinations of samples to determine the values of F_n, RHF, and RHCF. In this study, the hydride microstructure is characterized by the RHF. As shown in Table 1-6, the determination of the threshold stress for the onset of radial hydride precipitation has been performed utilizing the different metrics for radial hydride microstructure. For instance, Chu et al. and Sakamoto et al. have determined the threshold stress for a value of F_n hydride orientation factor ($\theta > 50°$) greater than 5%. Daum et al. and Singh et al. determined threshold stresses for hydride reorientation based on the half-thickness methodology which defines the threshold stress as the stress at which 50% of the thickness of the specimen contains radial hydrides. In their studies, the radial hydride microstructure is not uniform because of non-uniform loading through the thickness. In this study, flat Zircaloy-4 sheet material is utilized such that these through-thickness stress variations do not exist. As described in Chapter 2, a RHF value of about 1% is used to determine the onset of radial hydride precipitation.

Table 1-6 Metrics used to characterize the radial hydride microstructure and the criterion for threshold stress

Reference	**Metric for Hydride Microstructure Examination**	**Criterion for Threshold Stress**
Marshall[118]	F_n , radial F_n>48°	-
Louthan & Marshall[103]	F_n, circumferential: 0°<θ<40° radial: 50°<θ<90°	-
Bai[116]	F_n, circumferential: 0°<θ<30° radial: 30°<θ<90°	Low limit: Onset of radial hydride precipitation High limit: complete reorientation
Hardie[106]	F_n, circumferential: 0°<θ<40° radial: 50°<θ<90°	Onset of radial hydride precipitation
Chu et al..[109]	F_n, circumferential: 0°<θ<40° radial: 40°<θ<90°	F_n > 5%
Daum et al.[119]	-	Half-thickness
Singh et al..[120]	-	Half-thickness and Area compensation
Sakamoto et al..[110]	F_n, radial F_n>40° or 45°	F_n > 5%
Alam et al..[114]	F_n, radial: ±30° from radial axis of cladding, circumferential: ±30° from circumferential axis of cladding	-
Raynaud et al..[8]	RHF θ >45°	-
Aomi et al..[22]	F_n, radial F_n>40° or 45°	-
Colas et al..[60]	RHF, radial: θ>45° circumferential: θ<45°	RHF>10% or onset of radial hydride precipitation
Desquines et al..[111]	F_n, circumferential: 0°<θ<40° radial: 50°<θ<90°	Onset of radial hydride precipitation
Valance et al..[121]	F_n, radial: θ< 45°	-
Cha et al.. [122]	F_n, circumferential: 0°<θ<40° radial: 50°<θ<90°	-
This study	RHF: θ>45° circumferential: θ<45°	RHF>5° or 10° or onset of radial hydride precipitation

1.8.1 Sample geometries for hydride reorientation studies

In the literature, hydride reorientation has been investigated using different types of sample geometries and loading conditions, as shown in Figure 1-12. All of these geometries create difficulties in analyzing the threshold stress for hydride reorientation. For example, flattened tube samples, either uniform gauge section or tapered, have residual stresses due to the flattening process after machining. If such samples are used an accurate estimation of residual stresses is important to estimate radial hydride precipitation conditions. The ring stretch samples, such as shown in Figure 1-12c and d, may involve frictional stresses on the sample inner surface if not properly lubricated and these stresses can change the net stress causing any observed effect, and the bending stresses can also exists. For the test specimens shown in Figure 1-12a-d and g, the stress level changes along the outer surface and through the thickness of the specimens, such that detailed analytical or computational tools are required to predict the stress distributions.

Internally pressurized closed-end tube samples induce hoop tension and minor axial tension creating similar loading conditions to those seen in vacuum-drying under pure internal pressure conditions; no pellet-cladding interaction can be accounted for. However tests using the geometry require a considerable amount of material and many tests to obtain a range of applied stresses in order to determine the onset of hydride reorientation. Such tests also cause failure at the weakest spot, so if there is variation in hydride content or microstructure, the test can be vitiated.

Uniaxial tension testing of sheet samples provides a constant stress distribution through the thickness. If such a specimen is tapered, it also provides a range of threshold stress values along the loading direction. Thus, tapered uniaxial tension samples provide accurate results for hydride reorientation but are limited to the uniaxial tension stress state.

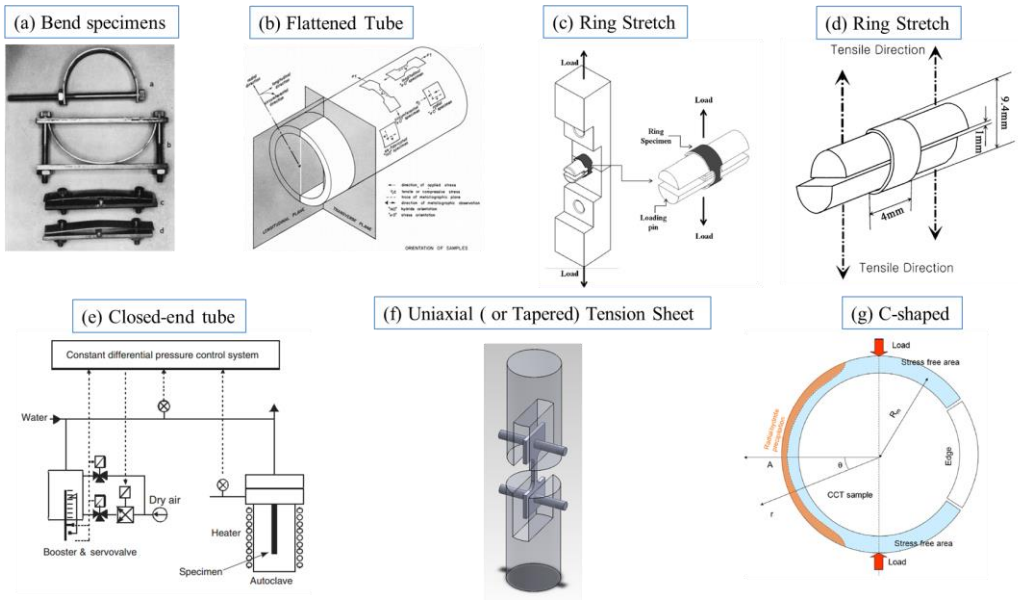

Figure 1-12 Sample types that were used during thermo-mechanical treatments for radial hydride precipitation. Pictures were taken from studies as follows (a) [103] (b) [105] (c) [122] (d) [123] (e) [109] (f) This study (g) [111]

1.8.2 The Effect of intrinsic and extrinsic parameters on hydride reorientation

As stated above, radial hydride precipitation under remote tensile stress is a strong function of cladding microstructural parameters related to the fabrication and thermo-mechanical treatment parameters. Table 1-7 lists the hydride reorientation conditions including type of samples, hydrogen content range, thermo-mechanical treatments, and threshold stresses as determined by the metrics shown in Table 1-6.

Table 1-7 Hydride reorientation thermo-mechanical treatment parameters and predicted threshold stresses from literature.

Reference	**Samples**	**Hydrogen [wt. ppm]**	**Thermo-mechanical treatment**	**Threshold stress**
Louthan[103]	Tensile samples from Zircaloy-2 and -4 tubes	20-200	Tmax=400°C, Tmin=25°C, Cooling rate=1, # of cycles=1	Drawn tube=69 MPa Rolled=103 MPa
Marshall[118]	Tensile samples from Zircaloy-2 and -4tube	50	Tmax=350°C, Tmin=25°C, Annealed at 350 °C for 16hr Cooling rate=1, # of cycles=1	Cold-reduced=82 MPa Hot reduced<82 MPa,
Kearns[105]	Tensile samples from Zircaloy-2 and -4 plate and tube (flattened)	150	Tmax=400°C, Tmin=25 °C, Annealed at 350 °C for 16 hr Cooling rate=1.5, # of cycles=1	Stress was 138 MPa and constant for all tests.
Hardie[106]	Tensile samples from Zr2.5%Nb tube (flattened and tapered) and flattened quadrant	50-300	Tmax=400°C, Tmin=100 °C, Cooling rates=0.17-1.3, # of cycles=1. Annealing at 400 °C was performed for 1, 24, and 1000h	Tapered=100 MPa Flattened=80-100 MPa from inner diameter Flattened=25-50 MPa from outer diameter
Sakamoto[110]	Tensile tapered samples from recrystallized zircaloy-2 sheet at different textures	61-668	Tmax=355(or 290)°C, Tmin=(or 150)160°C, Annealed at 350°C for 16hr Cooling rate=1, # of cycles=5	80MPa
Singh[86]	Tensile samples from Zr2.5%Nb tube (flattened and tapered)	32 and 73	Tmax=400-100°C, Tmin=25°C, Annealed at 300, 400, and 500 prior to reorientation treatment Cooling rate=1, # of cycles=1	140-238 MPa
Singh[113]	Tensile samples from Zr2.5%Nb tube (flattened and tapered)	100	Tmax=350-100°C, Tmin=25°C, Annealed at 400 and 500 prior to reorientation treatment Cooling rate=1, # of cycles=1	Function of temperature $\sigma_{th} = 827.5 - 1.12T$
Kese[124]	Ring stretch samples from Zircaloy tube		Tmax=425°C, Tmin=25°C, Annealed at 500 prior to reorientation treatment Cooling rate<1, # of cycles=1	140-160 MPa (Adequate radial hydride fraction)

Cha[122]	Ring stretch samples from Zr-Nb alloy	250-500	Tmax=400°C, Tmin=25°C, Cooling rates=8, 2, and 0.3 °C/min, # of cycles=1	From micro graphs 80-100 MPa
Chu[109]	Internally-pressurized closed-end tube samples of Zircaloy-4	130-600	Tmax=400°C, Tmin=25°C, Cooling rates=1 °C/min, # of cycles=1-12	
Bai[116]	Uniaxial tension, sheet samples of Zircaloy-4	1250	Tmax=400°C, Tmin=25°C, Cooling rates= 1.4 °C/min, # of cycles=1	Low limit=180 MPa (onset) High limit=240 (complete)
Aomi[22]	Internally-pressurized closed-end tube samples of irradiated Zircaloy-2 and -4, ZIRLO		Tmax=300 °C, Tmin=25 °C, Cooling rates=0.5°C/min, # of cycles=-1	70 MPa (average) 80-100 MPa for Zircaloy-4 60 for ZIRLO
Colas[83]	Uniaxial tension sheet samples of Zircaloy-4	192	Tmax=400°C, Tmin=150°C, Cooling rates=1 °C/min, # of cycles=-1	160-200 MPa
Alam[114]	Ring stretch tube and internally pressurized samples of Zircaloy-2	250-750	Tmax=400°C, Tmin=25 °C, Cooling rates=0.5 °C/min, # of cycles=-1	70 MPa for 250 wt. ppm 140MPa for 560 65 MPa for internally-pressurized
Daum[119]	Ring stretch tube samples of unirradiated and irradiated, Zircaloy-4	350-650	Tmax=400°C, Tmin=25 °C, Cooling rates<2 °C/min, # of cycles=-1	85 MPa for both irradiated and un-irradiated
Desquines[111]	C-shape sample, pinch loading	53-540	Tmax=350 and 450°C, Tmin=25°C, Cooling rates=0.4 °C/min, # of cycles=-1	Low limit=23-80 MPa High Limit=120-186 MPa

1.8.2.1 Effect of intrinsic parameters on radial hydride precipitation

Hydride reorientation is related to *intrinsic* cladding properties that result from alloying and the fabrication history. Early studies on hydride reorientation focused on the effect of the manufacturing history of cladding [103, 105]. Kearns investigated the effect of texture, cold work, and grain size on hydride reorientation while keeping the tensile stress constant (138 MPa). Utilizing plate and tubular samples at different textures and fabrication histories [105], he found that crystallographic texture did not have a strong effect on the hydride reorientation as cold-work and grain size. Kearns observed that increasing either the amount of cold work or decreasing grain size increased radial hydride precipitation, as depicted in Figure 1-13.

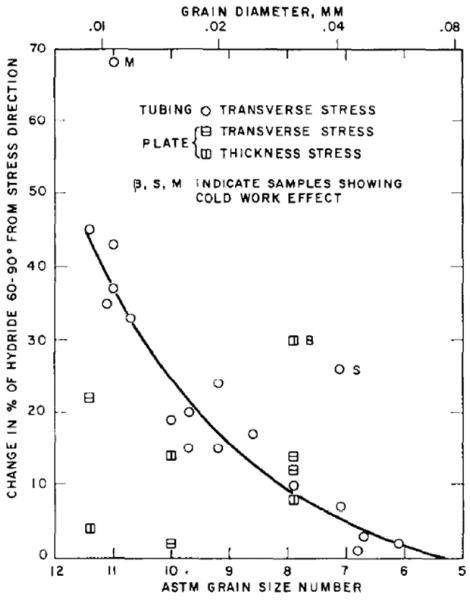

Figure 1-13 The effect of grain size on hydride reorientation

The effect of texture on radial hydride precipitation was also investigated by Sakamoto and Nakatsuka [110]. In order to simulate the texture effect, they utilized recrystallized Zircaloy-2 sheet material and machined tapered uniaxial tension samples in four different tensile directions relative to the sheet rolling direction. As the angle between the tensile load axis and the rolling direction of sheet increased, the radial orientation factor (F_n) for radial hydrides increased, which indicated that as the basal

pole intensity decreased from rolling direction to transverse direction, the number of observed radial hydrides increased. Also, Kumar observed that the hydride precipitation at grain boundaries which have basal plane parallel to tensile stress direction was more favorable than precipitation at the grain boundaries without parallel basal planes to tensile stress direction [46].

Bai et al. examined hydride reorientation in Zircaloy-4 samples with three different microstructures (stress-relieved (SRA), recrystallized (RX), and β-treated compared (β-treated)) that experienced the same thermo-mechanical treatment with maximum temperature of 400°C, cooling rate of 1.4 °C/min [116]. The threshold stresses, defined for onset of hydride precipitation and for complete hydride precipitation, were as follows: 180 and 240 MPa for SRA, 95 and 170 MPa for RX, and 187 MPa for β-treated.

Summarizing the above studies, the major observations related to the effect of intrinsic parameters on hydride precipitation are;

i- The effect of cold work and grain size is greater than that of texture; an increase in cold-work or a decrease in grain size results in higher radial hydride precipitation.

ii- Fabrication history drastically affects the susceptibility of radial hydride precipitation in Zircaloy-based alloys due to microstructural change. Such as the threshold stress is higher for stress relieved annealed (SRA) and lower for recrystallized (RX) material.

iii- Grain boundary precipitation is favored, especially if the grain boundary is aligned with the tensile stress axis.

1.8.2.2 Literature review of extrinsic parameters on radial hydride precipitation

The effect *extrinsic* parameters on hydride precipitation have been investigated comprehensively, such as the maximum temperature, cooling rates, number of cycles, hydrogen content, tensile stress levels, because of development of vacuum-drying process and regulatory limitations [22, 102, 103, 105, 108-110, 125]. From a practical point view, the prediction of the threshold stress as a function of thermal treatments and loading conditions is essential for vacuum-drying conditions. For laboratory studies, the thermal cycles

consist of heating to the maximum temperature ($T_{max.}$), annealing at T_{max} under zero stress, applying a stress, and subsequently cooling down to T_{min} with a stress applied.

In general, the heating rate has little effect on hydride reorientation. Annealing prior to a hydride reorientation treatment at maximum temperatures greater than 440-500°C may cause partial recovery around hydride platelets[121] and a reduction of hydrides-associated dislocation networks[120]. Additionally, Hardie did not observe any effect of dwelling at maximum temperature of 300 to 400°C on hydride reorientation on the value of the threshold stress for Zr2.5%Nb cladding as shown in Figure 1-14[106].

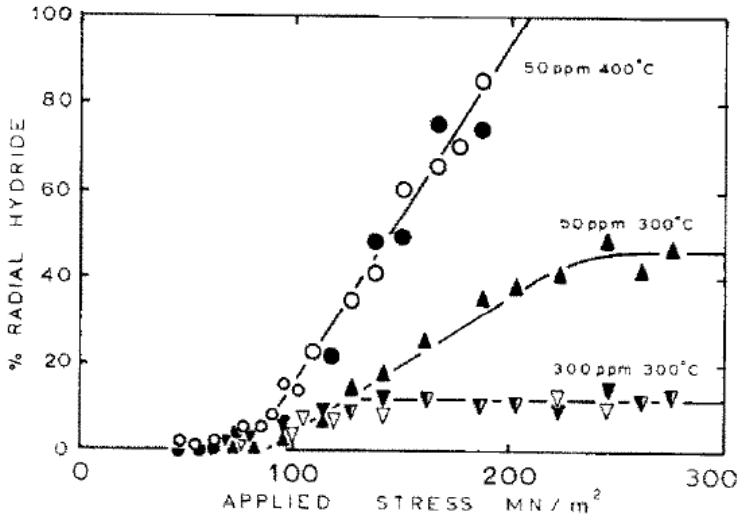

Figure 1-14 Stress orientation of hydrides in Zr-2.5%Nb samples containing 50 to 300 wt. ppm of hydrogen. Open symbols for 1-hr holding and solids are for 24-hr holding at annealing temperatures of 300 and 400 °C[106].

The effect of cooling rate on hydride precipitation and reorientation when cooled under stress has been investigated by many researchers [83, 109, 111, 122] who observed that as the cooling rate decreases radial hydride precipitation is promoted. Figure 1-15 shows several optical micrographs which indicate that radial hydride precipitation is enhanced as either the stress increases or the cooling rate decreases. However, only partial hydride reorientation was observed for the samples shown in Figure 1-15 as the maximum temperature (400^0C) did not dissolve all the hydrides (250 wt. ppm hydrogen was present). Thus,

residual hydrides may have acted as favorable sites for nucleation of both circumferential and radial hydrides.

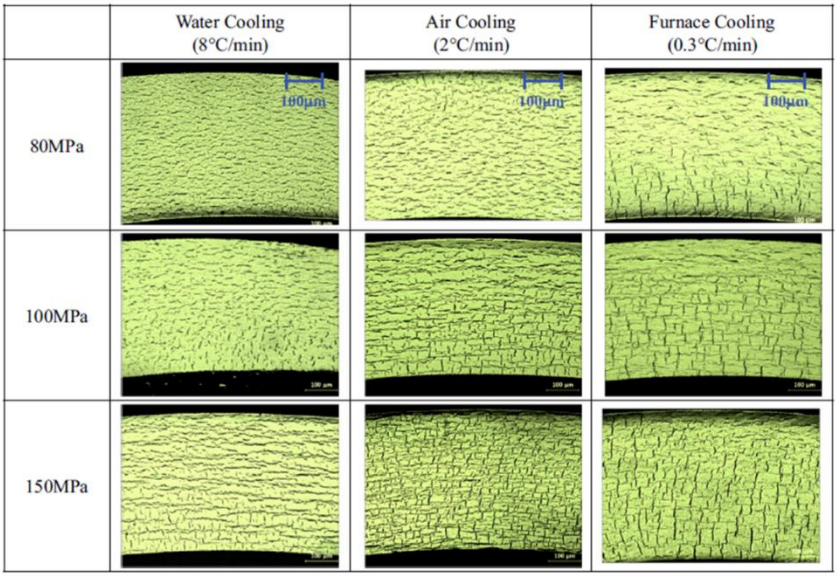

Figure 1-15 The hydride microstructure at different stress levels for water, air, and furnace cooling. Samples has 250 wt. ppm of hydrogen and maximum temperature was 400°C [122].

From the foregoing it is clear that hydride reorientation is a complex phenomenon that involves many factors from fabrication history to thermo-mechanical treatment parameters. In order to interpret the joint effect of all of those factors, a mathematical model should be developed to include not only the many factors but also the scale of the effects. The next section describes modelling efforts of radial hydride precipitation.

1.8.3 Summary of thermodynamics based models for hydride reorientation

Thermodynamic models that describe radial hydride precipitation were developed based on the Gibbs free energy of transformation associated with the nucleation of hydride precipitates. Ells [108] developed a model to predict the radial hydride fraction based on the radial hydride nucleation rate as follows;

$$R_\sigma = R_0 \exp\left(\frac{V_c \delta \sigma \omega}{kT}\right) \tag{1.18}$$

where R_σ is the ratio of radial hydrides to total number of hydrides, R_0 is the ratio of radial hydrides to the total number of hydrides prior to thermo-mechanical treatment, V_c is the volume of hydride nucleus, δ is the linear strain of the lattice in the direction of the applied stress due to second-phase particle, σ is the applied stress, ω (=$\cos^2(\beta)$) is a parameter related to the concentration of basal poles parallel to the stress direction, β is the angle between the stress direction and the normal to the hydride platelet surface, k is Boltzmann's constant, and T is temperature [108]. In addition, Hardie correlated experimental data using Equation (1.18) in this model, obtaining good agreement between data and theory [106].

Puls [68] modified Equation (1.18) by including the effect of external stresses and related the number of hydrides precipitated under zero stress, N_H^o to that at under a tensile-stress, N_k^σ as follows;

$$N_k^\sigma = N_H^o \exp\left(-\frac{PV_H}{kT} + \frac{V_{hyd}\sigma_{ij}e_{ij}^T}{xkT}\right) \tag{1.19}$$

where P is the hydrostatic stress, V_H is the molar volume of hydrogen in zirconium matrix, V_{hyd} is the molar volume of hydrides, x is the stoichiometry coefficient, σ_{ij} are the components of the far-field stress field, e_{ij}^T are the components of the misfit strain of hydrides in zirconium matrix, and $\sigma_{ij}e_{ij}^T$ is the total strain energy ($\sigma_{11}e_{11}^T + \sigma_{12}e_{12}^T + \cdots + \sigma_{32}e_{32}^T + \sigma_{33}e_{33}^T$). The subscript k= C or R represents the circumferential hydrides (C) that are precipitated under external stresses and radial hydrides (R) that are precipitated under the same external stresses. Therefore, the radial hydride fraction was written as;

$$n = \frac{N_R^\sigma}{N_R^\sigma + N_C^\sigma} = \frac{1}{1 + \exp(\Delta(\sigma_{ij}e_{ij}^T)_{R-C})} \tag{1.20}$$

where the term $\Delta(\sigma_{ij}e_{ij}^{T})_{R-C}$ is the strain energy difference of radial and circumferential hydrides caused by external stress field. Equation (1.20) was modified by Chu under the assumption that the radial hydride fractions (n) is less than 2% for all as-hydrided samples and written in terms of the undercooling, ΔT and the major uniaxial tension stress, σ, as follows;

$$n = \frac{1}{1 + 49\exp(-\frac{D\sigma}{(\Delta T)^3 T})} \tag{1.21}$$

where D is constant. Finally, Chu et al. created the circumferential-to-radial hydride transition map as shown in Figure 1-16 by utilizing both the experimental data and model in Equation (1.21). In that map, samples with radial hydride fractions below 5% are considered as samples with no hydride reorientation.

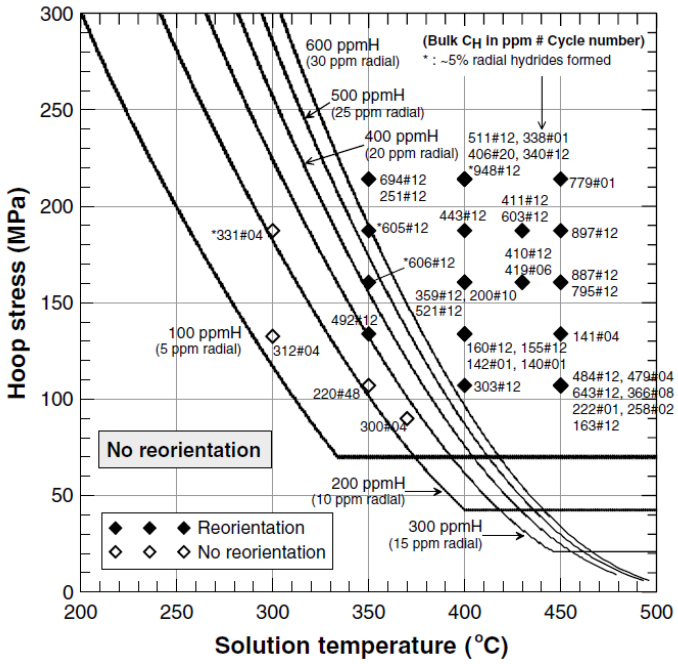

Figure 1-16 The hydride reorientation map as a function of solution temperature and hoop stress. Solid line curves were calculated by Equation (1.21)

A comprehensive thermodynamic analysis of hydride precipitation was developed by Qin et al. [48, 126]. They modified the Ells, and Puls, model equations for both intra- and inter- granular hydrides including the possible platelet shapes, and obtained a criterion for the radial hydride precipitation and the relation for threshold stress shown in Equations (1.22) and (1.24);

$$-\Delta G_{chem} - \frac{xV_H}{3V_{hyd}}(\sigma_1) - \left(\sigma_1^A e_1^T\right) > \Delta G_{strain} \tag{1.22}$$

$$\sigma_r = (\Delta G_{strain} - \Delta G_{chem})/(-\frac{xV_H}{3V_{hyd}} + e_1^T) \tag{1.23}$$

where σ_r is the value of the threshold stress for uniaxial tension loading, ΔG_{chem} is the chemical free energy of transformation for radial hydrides per unit volume, the hydride stoichiometry x is 1.6 for delta hydrides, V_{hyd} is the zirconium hydride molar volume, V_H is the molar volume of hydrogen, the major and minor principal stresses, e_1^T and e_2^T are transformation strains in the major and minor strain orientations, σ_1 and σ_2 are major and minor principal stresses, and ΔG_{strain} the internal strain energy of hydride precipitation per unit volume.

A straight forward extension of Equation (1.23) to a multi-axial stress state is to include the minor stress to determine the threshold stress at biaxial stress states rather than uniaxial tension. In this case, the threshold stress under biaxial stress state should take the following form:

$$\sigma_r = (\Delta G_{strain} - \Delta G_{chem} - (\frac{xV_H}{3V_{hyd}} + e_2^T)\,\sigma_2\,)/(\frac{xV_H}{3V_{hyd}} + e_1^T) \tag{1.24}$$

Thus, Equation (1.24) predicts an effect of minor stress such that increasing stress biaxiality should decrease the threshold stress for hydride reorientation. Testing this prediction is one of the primary goals of this study.

1.8.4 The effect of stress state on hydride reorientation

The threshold stress data for hydride reorientation in Zircaloy-4 were determined in several studies using uniaxial tension loading and multi-axial loading characterized by internal pressurization of a tube specimen as listed in Table 1-7. Aomi et al. [22] performed hydride reorientation tests on nuclear power reactor irradiated Zircaloy-4 cladding tubes with burnup levels of 39 and 48 GWd/t. Samples were internally pressurized, heated up to 300 °C, and then cooled to 25 °C under stress. The threshold stress for hydride reorientation was estimated as 100-115 MPa for hydride reorientation. Another study by Daum [119] also determined the threshold stress for hydride reorientation for both irradiated and unirradiated cladding tubes that had been heated up to 400°C and cooled under ring stretch tension was 85 MPa. The stress state in this work may have been near plane strain.

Chu [109] performed various tests on internally pressurized unirradiated Zircaloy-4 tubes with varying number of thermo-mechanical cycles from 1 to 12. The samples were heated up to 400 °C, annealed for 2hr, then cooled down to 150°C at a rate of 1°C/min. The threshold stress of 70-100 MPa was observed. These results can be compared to the uniaxial tension threshold-stress results of Colas (160-200 MPa) and Bai (180 MPa), as shown in Table 1-8.

Taken together, the above results strongly suggest that there is an effect of the minor principal stress and stress biaxiality on the threshold stress, consistent with the predictions of Equation (1.24) and the thermodynamic analyses of hydride precipitation. Although the experimental data are from different studies involving different hydrogen contents, somewhat different thermal-mechanical histories, including both sheet and tube specimens, the threshold stress data suggest a stress state effect such that the threshold stress is higher under uniaxial tension compared to a multi-axial state of stress associated with internal pressure, as would be expected from Equation (1.24), which means that both the major and minor principal stresses appear to have an effect on radial hydride nucleation. Thus a systematic investigation of the stress biaxiality effect on radial hydride precipitation is necessary in order to establish a more complete hydride precipitation model for future code developments.

Table 1-8 Selected literature data of the threshold stress for the threshold stress for hydride reorientation in CWSR Zircaloy-4

	Zircaloy-4 Samples	**Origin of Hoop Stress**	**Threshold Stress [MPa]**	**Expected Stress State**
Aomi[22]	Tubes, irradiated	Internal pressure	115	Plane-strain
Daum[127]	Tubes, irradiated	Ring stretch test	85	Near Plane-strain
Chu[109]	Tube, unirradiated, as received	Internal Pressure	70-100	Plane Strain
Bai[116]	Sheet, unirradiated, as received	Uniaxial tension	180	Uniaxial Tension
Colas[60]	Sheet, unirradiated, as received	Uniaxial tension	160-200	Uniaxial Tension

1.9 High Energy X-ray Diffraction by Synchrotron Radiation of Hydride Precipitation

In order to establish a model for hydride precipitation, the structural transformation of the hydride phase needs to be understood in terms of dissolution-precipitation temperatures, mechanical deformation during transformation, and misfit strains. A complete mathematical model for both radial and circumferential hydride precipitation must account for the lattice spacing behavior and associated stress states within the hydrides (both circumferential and radial) as nucleation and growth happens.

In-situ high energy X-ray diffraction experiments can be used to acquire a range of structural data in the major principal stress and minor principal stress directions at the same time. The hydride volume fraction (from the hydride X-ray diffraction peak intensities), the strains acting on the hydrides during precipitation (from the d-spacing variation of particular hydride planes), and the size of the hydrides (from a detailed analysis of peak broadening) can be obtained from in situ high energy X-ray diffraction

experiments [60, 62]. Thus, the mechanical and thermal strains within hydrides can be related to stress and stress-state during a structural transformation of hydrides.

There have been a few structural studies that indicate an anisotropic strain state within circumferential hydrides forming in Zircaloy-4. For instance, Santisteban et al. performed high energy X-ray diffraction tests on Zircaloy-4 to estimate the strain variation between δ-{111} planes that were oriented perpendicular to the radial direction of cladding and those of oriented perpendicular to the circumferential direction [63]. The results showed that the lattice parameter of δ-hydrides obtained from hydride planes that are perpendicular to the radial direction are higher than that of obtained from other orientations, and the hydrides were compressed by the matrix which creates anisotropic stresses and strains within the hydrides. Alvarez et al. [115] also showed that the hydride lattice spacing behavior was complex under an applied far-field stress when radial hydrides formed (see Figure 1-17). The d-spacing showed bi-linear behavior during heat-up in some cases but not in others. Also, a surprising d-spacing decrease upon heating was observed in one case. Thus, complicated d-spacing behavior has been shown to result during hydride dissolution and precipitation.

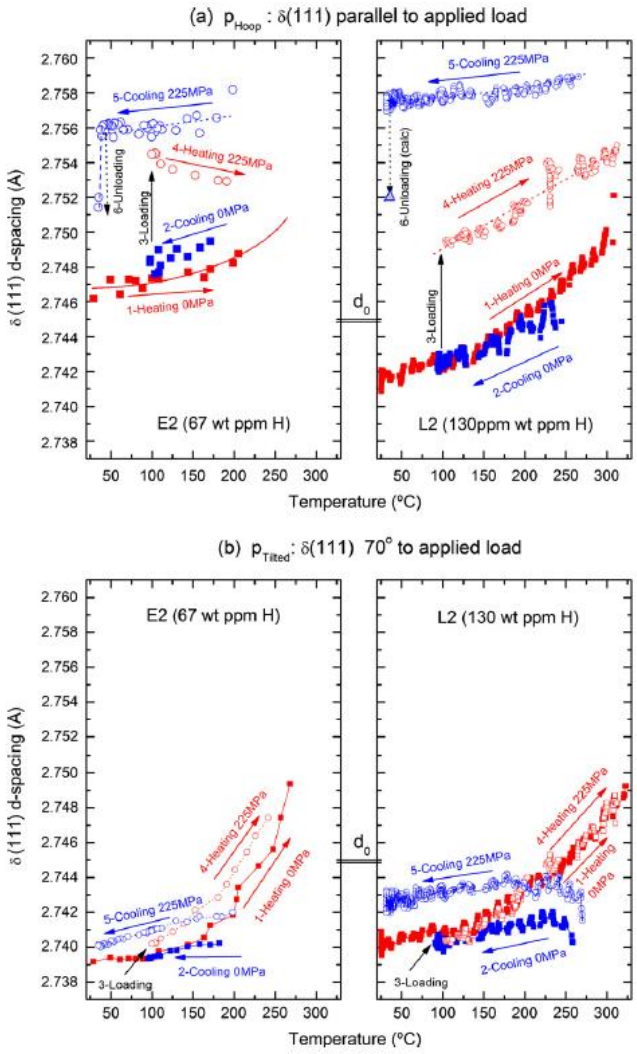

Figure 1-17 d-spacing behavior of δ hydride {111} planes for both (a) stress applied and (b) no-stress-applied directions during hydride reorientation treatments. No stress applied at 1st cycle, stress was applied at the 2nd cycle heat-up and samples were cooled down under stress, and sample was un-loaded [115].

Colas et al. performed systematic experiments to understand the hydride reorientation process in terms of strain evolution for both the zirconium and hydride phases [60]. Uniaxial tension samples were utilized, and stress was applied only during cool-down. While cooling, the strain in α-zirconium decreased at a rate of its thermal expansion, and when the stress was removed, the d-spacings before and after the heating and cooling stages matched as shown in Figure 1-18a and b. However, the radial hydride d-spacing, as shown in Figure 1-19a, had permanent strain that was higher than the initial circumferential hydride d-spacing in the direction of the far-field stress of these uniaxial tension specimens. In the transverse direction

of the specimen (in which in this case there was no applied far-field stress), the hydride d-spacing were matched with their initial and final values. Thus, the radial hydrides, in general, were under very complex stress state; the lattice planes parallel to platelet face appear to be under relative tension compared to those planes parallel to the platelet edge when stress was removed.

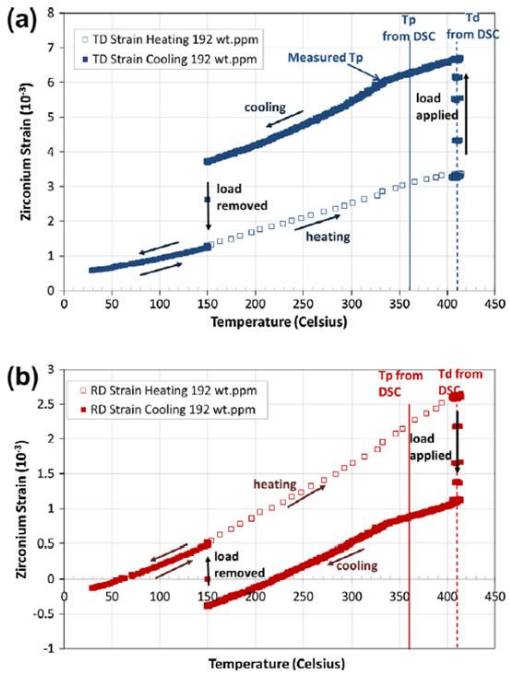

Figure 1-18 α-Zirconium strain evolution during heating without stress and cooling under tensile stress (a) Stress-applied direction (b) no-stress-applied direction [60].

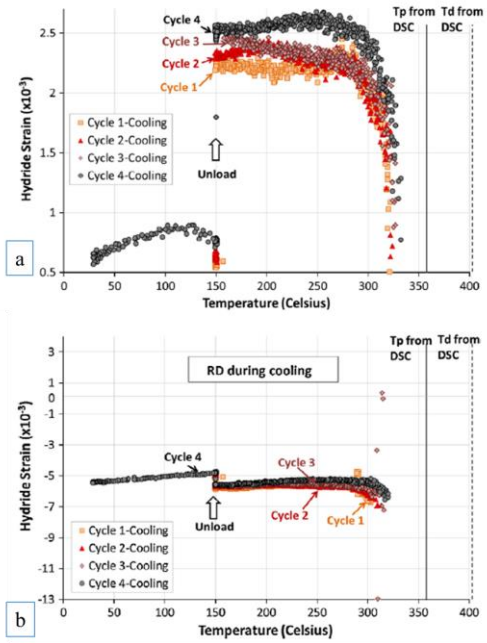

Figure 1-19 Hydride strain evolution during thermo-mechanical treatment. All cool-downs were under no load. Sample with 192 wt. ppm of hydrogen was 5-cycle treated. (a) stress-applied direction (corresponds to the hoop tension for cladding tubes) (b) no-stress-applied direction(radial direction for cladding tubes) [60].

To conclude, although the hydride dissolution and precipitation behavior is crucial to determining hydride reorientation and many studies have been performed, the complexity of the phenomena has led to the fact that the hydride reorientation mechanisms, especially the role of the secondary stress, has not been elucidated. In particular the thermodynamic estimations of precipitation behavior that utilize elastoplastic strain energies should include the interaction of a multi-axial stress state with the complex transformation strains associated with hydride precipitation. In this study we will investigate the hydride reorientation process by designing special samples that induce well defined states of stress that span a range of biaxiality, from uniaxial tension to plane strain and equibiaxial tension. The study is further enhanced by performing in situ measurements of hydride dissolution and precipitation under stress and following both hydride volume fraction and the d-spacing of both the hydride and matrix phases. These results are rationalized with a thermodynamic based model.

1.10 Motivation of the Study

As described in previous sections, hydride reorientation as a result of vacuum drying of spent fuel rods can drastically decrease their ductility and fracture resistance. Degradation of mechanical behavior increases the risk of cladding failure during spent fuel handling and/or dry-cask transportation, so that radial hydride formation should be avoided during vacuum drying.

While the formulations in the models have been developed and used for uniaxial tension conditions, the actual loading conditions of spent nuclear fuel rods during vacuum-drying result in multi-axial stresses within the cladding such that a secondary stress component exists, causing a biaxial stress state($\sigma_2/\sigma_1 > 0$). There has been no systematic study of the effect of a biaxial stress state on hydride re-orientation.

As stated in Section 1.8.4, according to classical precipitate nucleation theory, a far-field stress state should affect hydride precipitation in zirconium-base alloys due to the work done by the stress components in affecting (a) the free energy change of the hydrogen in solution as influenced by hydrostatic stress and (b) the strain energy of the transformation as caused by the misfit between α-zirconium and δ-hydride phases. The latter term depends on the transformation strains which in the case of δ-hydrides have several components, are anisotropic, and quite large, placing the precipitate into hydrostatic compression. Thus, at stress states in which a secondary stress is present($\sigma_2/\sigma_1 > 0$), the secondary stress (σ_2) affects both the hydrostatic work and the strain energy of transformation such that the threshold stress is affected, as shown in Equation 1.18. Thus, the existence of a second tensile stress component during hydride precipitation should affect the threshold stress level in the tensile axis direction (σ_1).

Although most studies have investigated radial hydride precipitation under uniaxial tension, the expected loading conditions during vacuum-drying cause biaxial stress states ($\sigma_2/\sigma_1 > 0$) that differ from the uniaxial tension($\sigma_2/\sigma_1 = 0$). While some experimental studies utilized internally-pressurized tubes that more closely represent the stress state during vacuum-drying, there has been no systematic study of the relationship between the threshold stress and stress state, despite the implication of theory that there should

be an effect of a minor stress on the threshold stress. A close inspection of the threshold data presented in Table 1.10 shows that there appears to be an effect of stress state on radial hydride precipitation in CWSR Zircaloy-4.

This study is divided into two major parts. In the first part, the effect of stress state on the threshold stress for hydride reorientation is studied using novel mechanical testing procedures, metallographic examinations of thermo-mechanical treated samples, and finite element analyses. These results, which show an effect of multi-axial stress state on the threshold stress, are analyzed using a thermo-mechanical model for hydride precipitation that utilizes an analysis of the X-ray diffraction data that are generated in the second part of this study.

For the second part of this study, the results of high energy X-ray diffraction experiments will be analyzed to predict transformation strains at the onset of hydride precipitation temperature as the phase transformations occur, or "in situ". To estimate the transformation strains during phase transformation under tensile stress at relevant stress states, pre-hydrided samples are subjected to heating and cooling cycles while acquiring X-ray diffraction patterns continuously. Using the diffraction intensities and angles of the acquired diffraction patterns, the dissolution and precipitation temperatures of hydrides at various stress and stress states will be determined. Using the misfit strain formulations based on atomic radii method under hard sphere assumption of atoms, the transformation strains involved in the strain energy term of the thermodynamics model are calculated at relevant stress and stress state at the onset of precipitation.

By performing experimental studies with novel sample designs, the effect of stress state on threshold stress will be established for the first time, with results consistent with the predictions of a thermodynamics model for hydride reorientation base on the Gibbs free energy of transformation. An ultimate goal of this study is to provide a robust predictive model that takes into account the effects of anisotropic transformation strains for radial hydride precipitation in zirconium based alloys subjected to a range of far-field stress states and experiencing thermo-mechanical treatments.

2 MATERIALS AND EXPERIMENTAL PROCEDURES

2.1 Materials

In this study, three different materials were used, all of which were initially fabricated in the cold worked stress relieved condition (CWSR): Zircaloy-4 sheet, irradiated Zircaloy-4 tube, and irradiated M5 cladding tube. The Zircaloy-4 sheet material was provided by Teledyne Wah-Chang and was utilized in developing and conducting hydride reorientation tests, in situ synchrotron radiation experiments, and tension tests. The Zircaloy-4 sheet material had a nominal thickness of 0.670 mm and was the same material used in previous studies [60, 94], in which it was shown that the texture was similar to that of Zircaloy-4 cladding tube material. The average grain size in this material was approximately 6 μm x 4.5 μm x 3 μm [94], and the initial hydrogen content of the as-received material was measured as ~20 wt. ppm [8]. All samples were machined with the loading direction along the transverse orientation of the sheet to simulate the tensile stresses present when the cladding tube material is subjected to internal pressure. The irradiated Zircaloy-4 and M5 cladding tube materials were used exclusively in synchrotron radiation X-ray diffraction experiments (see Chapter 4). Both materials were furnished by M. Billone from Argonne National Laboratory (ANL). The Zircaloy-4 was irradiated in the H.B. Robinson reactor to a burn up of approximately 67 GWd/t and contained an average hydrogen concentration of 270 wt. ppm. The M5 material was irradiated to burnups in the range of 63 to 70 GWd/t and had hydrogen contents below 100 wt. ppm, as described later.

2.2 Hydrogen Charging System, Hydride Reorientation Apparatus, and Metallography

The Zircaloy-4 sheet material was hydrogen charged by a gaseous diffusion process, as shown in Figure 2-1. In this procedure, a hydrogen-argon gas mixture (12.5% H_2 and 87.5% Ar) was introduced into the chamber (initially in vacuum at 13.33 μPa) containing the cold-worked specimen at 500ºC.

Prior to insertion in the furnace, the native oxide layer (which is an effective barrier to hydrogen ingress) was removed using an acid solution of 10 parts of nitric acid (HNO_3), 10 parts of distilled water (H_2O) and 1 part of hydrofluoric acid (HF). Following this removal the specimen was immediately coated with a 20-nm thick nickel layer to prevent the native oxide from reforming by exposure to air. Upon insertion in the chamber the sample was maintained at 500°C for 2 hours to allow the hydrogen to diffuse through the specimen thickness and to achieve a homogenous distribution. The hydriding heat treatment also represented a stress relief anneal which was performed while hydrogen charging.

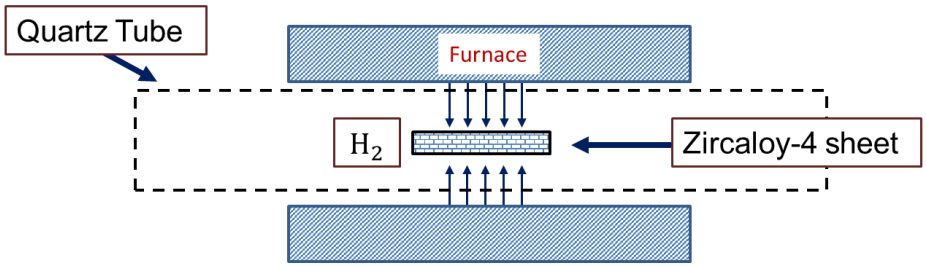

Figure 2-1 Schematic of the hydrogen charging system.

To verify that the desired hydrogen concentrations were attained, they were determined using hot vacuum extraction by Luvak Inc. in Boylston, MA. The examinations were performed on samples taken from the ends of the test specimen. The hydride microstructure was also examined using optical microscopy and electron microscopy, as described in the following paragraphs.

2.2.1 Characterization of hydride microstructure

In order to reveal the hydride microstructure, samples were first cold mounted in epoxy and sequentially ground subsequently with 180, 320 (or 400), 800 grit papers at a very low or no force condition. Then, samples were lightly swab etched in a solution of 10 parts of distilled water (H_2O), 10 parts of nitric acid (HNO_3), and 1 part of hydrofluoric acid (HF) in volume to reveal the hydrides [128]. This same procedure was applied for samples taken from all orientations.

After etching, samples were examined by optical microscopy using a Zeiss inverted light microscope to determine the radial hydride fraction and the threshold stress for radial hydride reorientation. Examples of such optical examinations are shown in Figure 2-2. In order to characterize the hydride morphology in greater detail, some of the hydride microstructures were further examined using an FEI Philips XL-20 scanning electron microscope (SEM) as shown in Figure 2-2c.

In order to investigate the failure behavior of the mechanically tested samples, fracture surfaces were characterized using both SEM and optical profilometry in addition to the optical microscopy. Using secondary electrons allow detailed examination of the fracture surface topography.

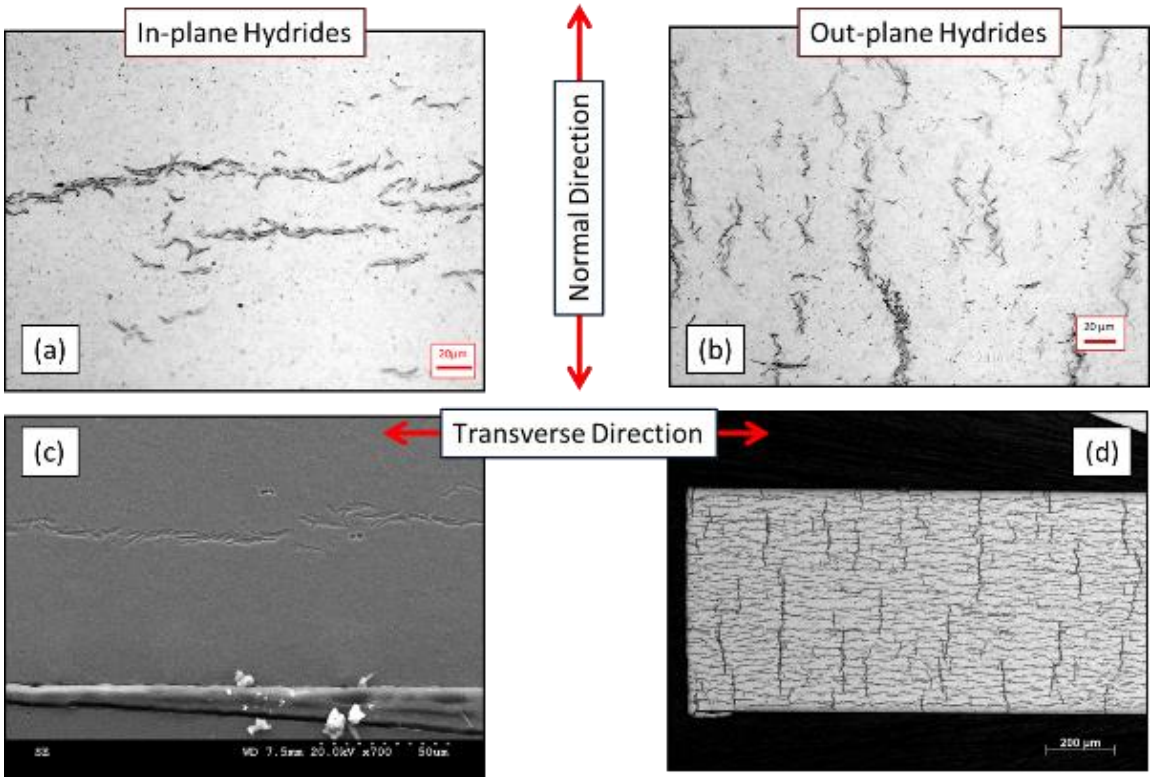

Figure 2-2 Examples of hydride microstructures which are observed in this study; (a) and (c) represent the circumferential (in-plane) hydride microstructure, (b) shows the radial hydride microstructure in the sample which is 2-cycle thermo-mechanically treated, and (d) shows the mixed hydride microstructure in the sample that contained 220 wt. ppm of hydrogen.

A few fracture surfaces were also examined using optical profilometry, which is a surface metrology technique that examines the surface topography by splitting a light beam into two paths by means

of a beam splitter. One path directs onto the surface of the specimen, while the other one reflects from a reference mirror. Reflections from both surfaces are recombined with an array detector, and this recombination results in interference pattern which contains topographic information of the sample surface. Therefore, this technique enables the determination of fracture surface roughness, which can be related to the radial hydride continuity factor on the fracture surface. Figure 2-3 shows examples of both SEM and of the optical profilometry images of the same fracture surface in which the detailed facet structure caused by radial hydride fracture is evident. As shown the optical profilometry provides height information between hydride facets.

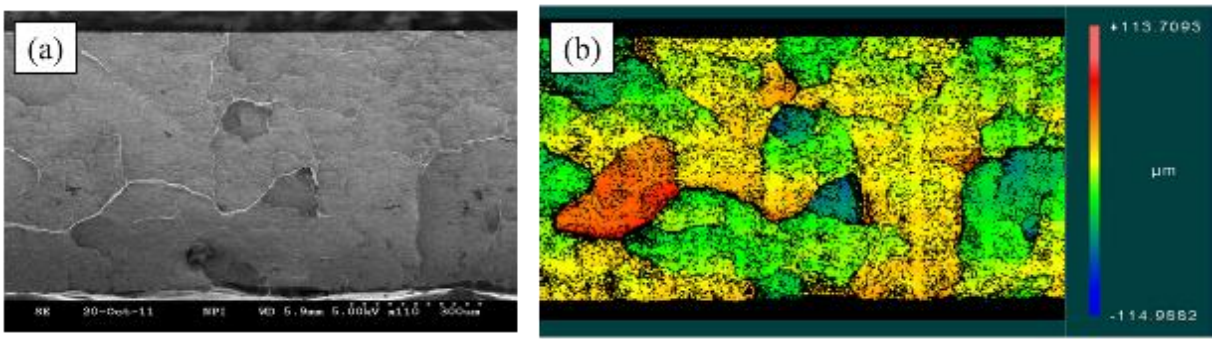

Figure 2-3 Fracture surfaces of a sample with 180 wt. ppm of hydrogen and a radial hydride fraction (RHF) =1. The sample was tested at 125°C and failed in a brittle manner. (a) SEM image of the fracture surface, while (b) depicts the fracture surface of the same area as imaged by optical profilometry.

A hydride reorientation apparatus was designed in order to reorient the hydrides. This apparatus consists of a clam shell furnace and a loading frame to impose controlled thermo-mechanical cycles (TMT) on the samples, as shown in Figure 2-4. As will be discussed later in detail, the samples were heated up to the temperature at which all hydrides dissolved and then cooled under an applied hoop stress created by the dead weight shown to create an out-of-plane (radial) hydride microstructure.

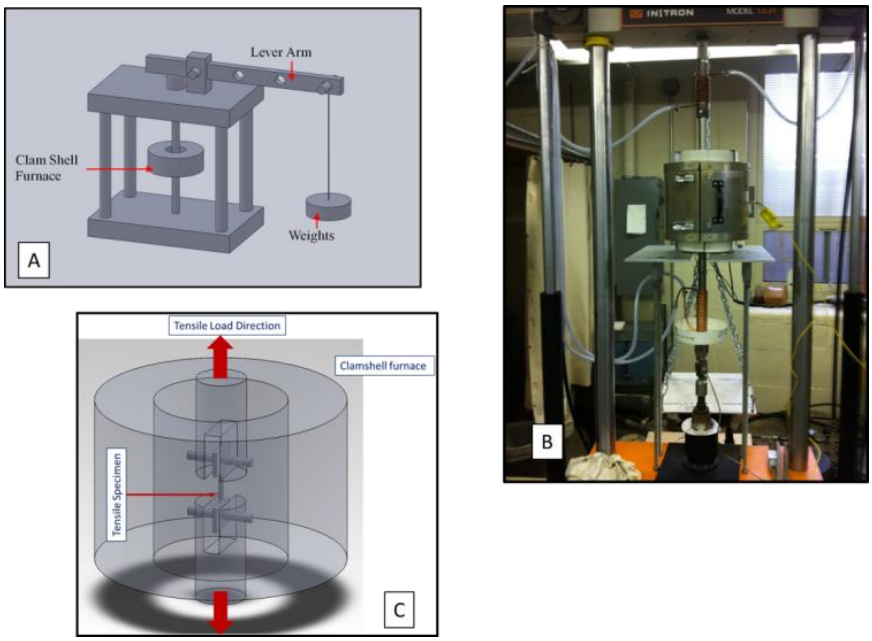

Figure 2-4(a) The radial hydride treatment apparatus; the load is transmitted by a lever arm to the sample from weights. Image (b) shows the arrangement of the furnace, loading train, thermocouples and cooling system, and (c) shows the specimen and the load train orientation in clamshell furnace.

2.3 Sample Design and Finite Element Analysis

2.3.1 Deformation behavior

Hydride reorientation occurs under stresses which are in the elastic regime. The mechanical behavior of the material is determined by utilizing the uniaxial tensile samples with a 4:1 ratio of length to width as specified in the ASTM procedure [129]. The samples are subjected to a tensile load under constant crosshead speed of 0.1 mm/min and tested at: 25, 200, 300, 400, and 450°C. Temperature dependent mechanical properties determined in various previous studies performed at Penn State are shown in Table 2-1. The table shows the yield stress, hardening exponent, and %EL. The yield stress values are consistent with the MATPRO [130] for un-irradiated CWSR Zircaloy-4.

Table 2-1 Summary of the mechanical properties of the Zircaloy-4 samples in this study and other studies. The sheet material utilized in this study is the same sheet material used by Colas[83], Raynaud[8], and Pierron[50] in their work, Link[131] measured yield stress values in tubular samples and Flanagan[84] estimated mechanical properties by compression tests of Zircaloy-4 samples. Temperature is in °c and yield stress (σ_y) is in MPa.

	This study			**Colas[83]**	**Raynaud[8]**			**Pierron[50]**			**Link[131]**		**Flanagan[84]**	
	Sheet										**Tube**		**Cube**	
T	σ_y	n	%EL	σ_y	σ_y	n	%EL	σ_y	n	%EL	σ_y	n	σ_y	n
25	600.0	0.014	17	625	575	0.018	17	573	0.01	19	590	0.068	496	0.059
200	425.0	0.025	14											
300	362.5	0.023	12		315	0.032	20	318	0.03	16	350	0.059	370	0.099
375					290	0.027	22							
400	262.0	0.022	42	330										
425	187.5	0.051	33											
450	180			240										

To simulate the hydride reorientation conditions present in the cladding tube geometry, which used sheet Zircaloy-4, tensile specimens were machined along their long-transverse direction corresponding to the hoop direction of the cladding tube. The three types of samples as shown in Figure 2-5 were designed and used: (a) tapered uniaxial tension, (b) “plane-strain” tension, (c) “near-equibiaxial” tension. These samples were tested to determine the threshold stresses for radial hydride precipitation and the hydride d-spacing as a function of radial hydride fraction using X-ray diffraction.

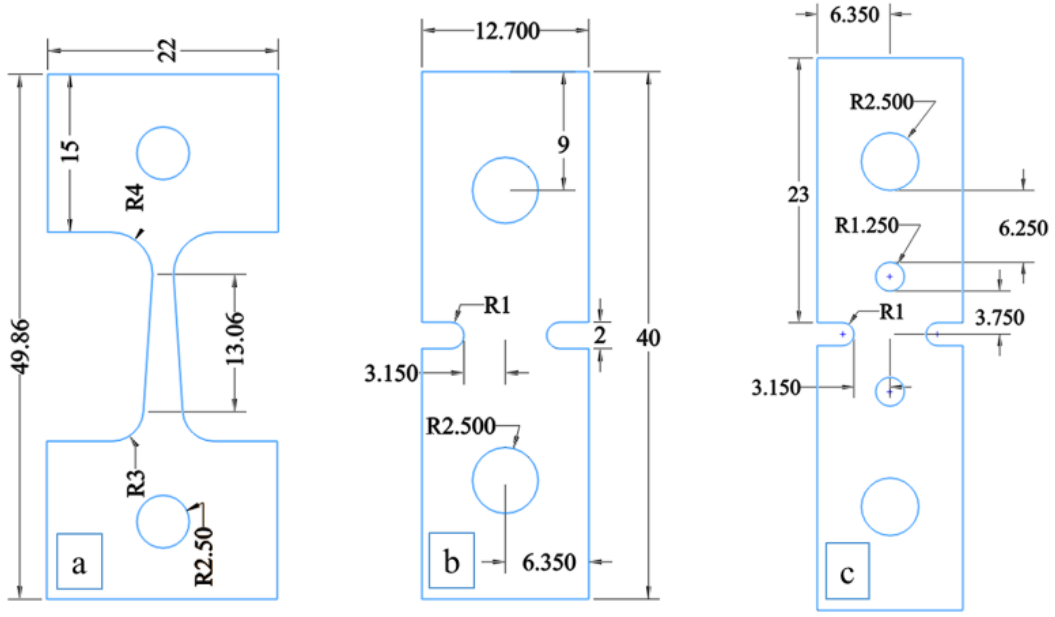

Figure 2-5 Mechanical test specimen designs (a) Tapered uniaxial tension (b) Double-edge notched "plane-strain" tension, and (c) Double-edge notched "near-equibiaxial tension" sample.

A- Uniaxial Tension Samples

The uniaxial tension specimen (see Figure 2-5) design with uniform thickness and taper were based on a previous study by Pierron et al. [129]. In order to create a uniform strain along the gauge length, a 4:1 length to width ratio was used. The tapered uniaxial tension sample as shown in Figure 2-5 is designed to create a 40% decrease in applied stress from the widest section to the narrowest section. For instance, when the applied stress is 213 MPa at the widest part of the gauge section, it is 127 MPa at the narrowest part of the gauge section. The tapered uniaxial tension configuration enables the determination of the threshold stress for hydride reorientation under a uniaxial state of stress by correlating the hydride microstructure (as viewed in the optical micrographs) with the local value of the tensile stress.

B- Double-edge Notched Samples: "Plane-strain" Tension

The second type of the mechanical test sample was the "plane-strain" tension sample. The plane-strain tension stress state was imposed using a variant of the double-edge notched Penn State plane-strain

specimen (see Figure 2-5) [13, 87]. The stress state in this specimen can be described by the resulting stress biaxiality ratio, $\frac{\sigma_2}{\sigma_1}$, where σ_1 is the major principal stress and σ_2 is the minor principal stress.

Because of the more complex stress distribution for the samples with higher degree of biaxiality, it was necessary to perform finite element analysis to determine the stress and stress state distributions within the gauge sections of the samples. Finite element analyzes have been performed using ANSYS, a finite element model of "plane-strain" tension is also shown in Figure 2-6. The finite element models for all double-edge notched samples including the "near-equibiaxial" tension models involve elements that are defined in curvilinear coordinate system to capture geometrical entities such as holes and notches accurately. The triangular elements used in analyzes are high order elements that contain 7 nodes (3 at the triangle corners, 3 at the triangle edge centers, and 1 at the centroid of the triangle) for shape function formulations. Elements also support the non-linear mechanical behavior such that the plasticity modeling is available. Noting, for finite element problems such as plasticity, high strain rate, fracture mechanics, or melting simulations solution should proceed by load steps to capture mechanical behavior accurately; the ANSYS software enables this feature automatically when non-linear elements are used.

The two-dimensional finite element computations of the sample stress distributions assume (i) plane stress through the thickness, (ii) mechanical specimen properties at 400 °C (which corresponds to the highest temperature applied during drying operations), and (iii) isotropic mechanical properties. Because of the notch, local stresses can exceed the yield stress of the material and cause a plastically deformed region as determined by the equivalent stress at yielding. The mechanical response of the Zircaloy-4 sheet in the plastic regime is described by power law hardening law as follows

$$\sigma = K\varepsilon_p^n \tag{2.1}$$

where *K* (approximately 375 MPa at 400 °C) is the strength coefficient, n (0.025 at 400 °C) is the strain hardening coefficient, and ε_p is the plastic strain.

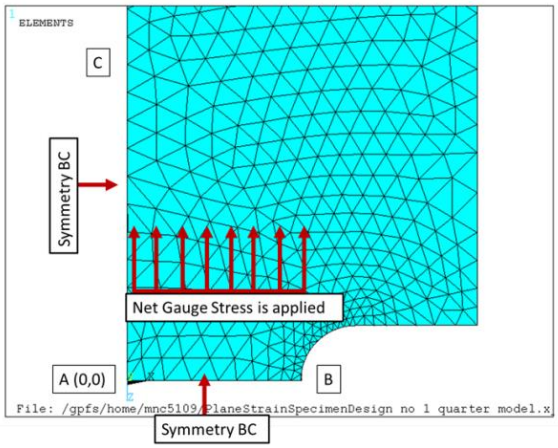

Figure 2-6 Finite element model of the plane-strain specimen: point A is the center of the specimen, and point B represents the edge of the notch.

The calculated σ_1, σ_2, and σ_{eq} $(= \sqrt{\sigma_1^2 + \sigma_2^2})$ along the A-B section in Figure 2-6 are shown in Figure 2-7. Finite element analysis of the "plane-strain" tension sample in the elastic region shows that the stress biaxiality ratio along the gauge width of the specimen decreases from about 0.57 to 0 from points A to B in Figure 2-6. This result indicates a near plane-strain stress state ($\sigma_2/\sigma_1 = 0.57$) in the middle of the specimen and uniaxial tension ($\sigma_2/\sigma_1 = 0$) conditions near the notch. Also, it should be noted that a stress concentration is created near the notch. As a result, as shown in Figure 2-7, if the applied load is sufficiently high, the stress level near the notch may exceed the yield stress (315 MPa) at 400°C while the central region of the specimen remains elastic. Thus, while most of the specimen deforms elastically, a small plastic zone is created near the notch under these loading conditions (which were used to re-orient the hydrides).

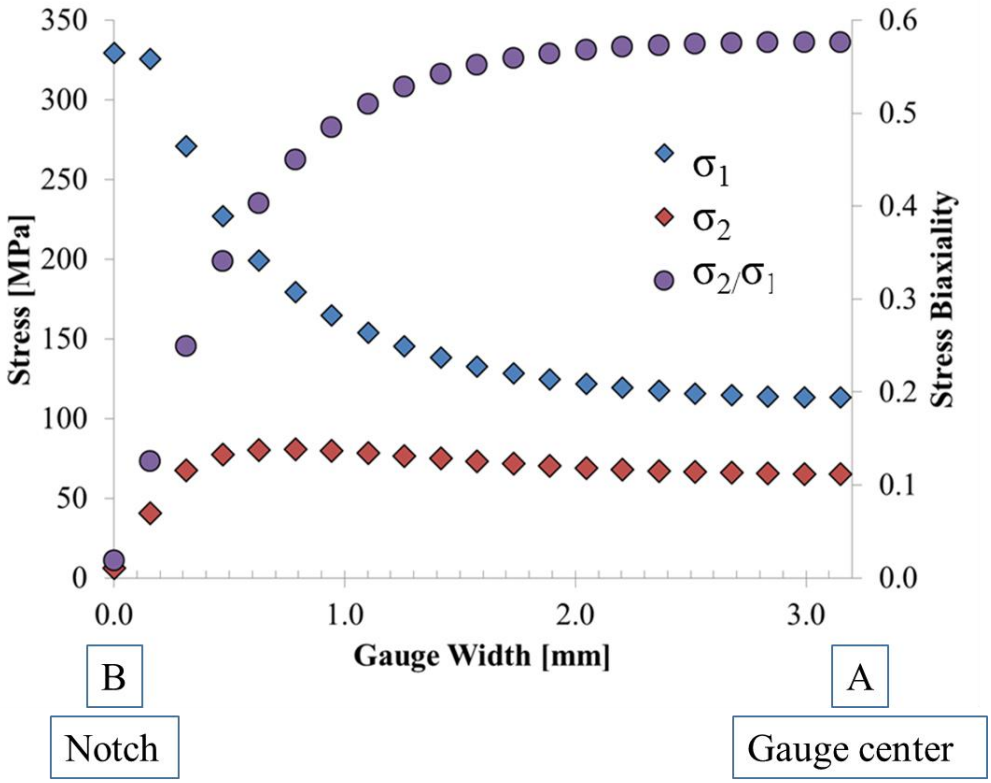

Figure 2-7 Stresses and stress biaxiality distribution along the gauge width (section A-B in Figure 2-6) of the "plane strain" specimen for applied net gauge section stresses of 180MPa. The σ_1 is the major principal stress, σ_2 is the minor principal stress, and σ_2/σ_1 is the stress biaxiality ratio.

C- Double-edge Notched Samples: "Near-equibiaxial" Tension

In order to investigate the sensitivity of hydride reorientation to stress states with stress biaxiality ratios greater than the "plane-strain" tension condition of $\sigma_1/\sigma_2 = 0.5$, a specimen was designed which creates near-equibiaxial stress state ($\sigma_1/\sigma_2 = 0.9$) (see Figure 2-5c). The specimen is essentially a modification of the "plane-strain" tension specimen with the important addition of two "stress state" holes that modify the stress distribution within the specimen.

Figure 2-8 shows the principal stress distribution in this specimen design along both the gauge width and the gauge length when a net gauge section stress of 210 MPa is applied. The notches and the holes create a complex stress state within the sample such that a near equibiaxial stress state $\sigma_1/\sigma_2 = 0.9$ is achieved at the center of the specimen sample; see Figure 2-8c. The central section of the gauge region has

a stress state biaxiality ratio σ_1/σ_2 that ranges between 0.8 and 0.9, while a similar stress biaxiality behavior is also predicted along a line between the centers of the stress state holes as shown in Figure 2-8d. In addition, Figure 2-8b shows that there is an extensive region in which the major principal stress is nearly constant while the minor principal stress is decreasing.

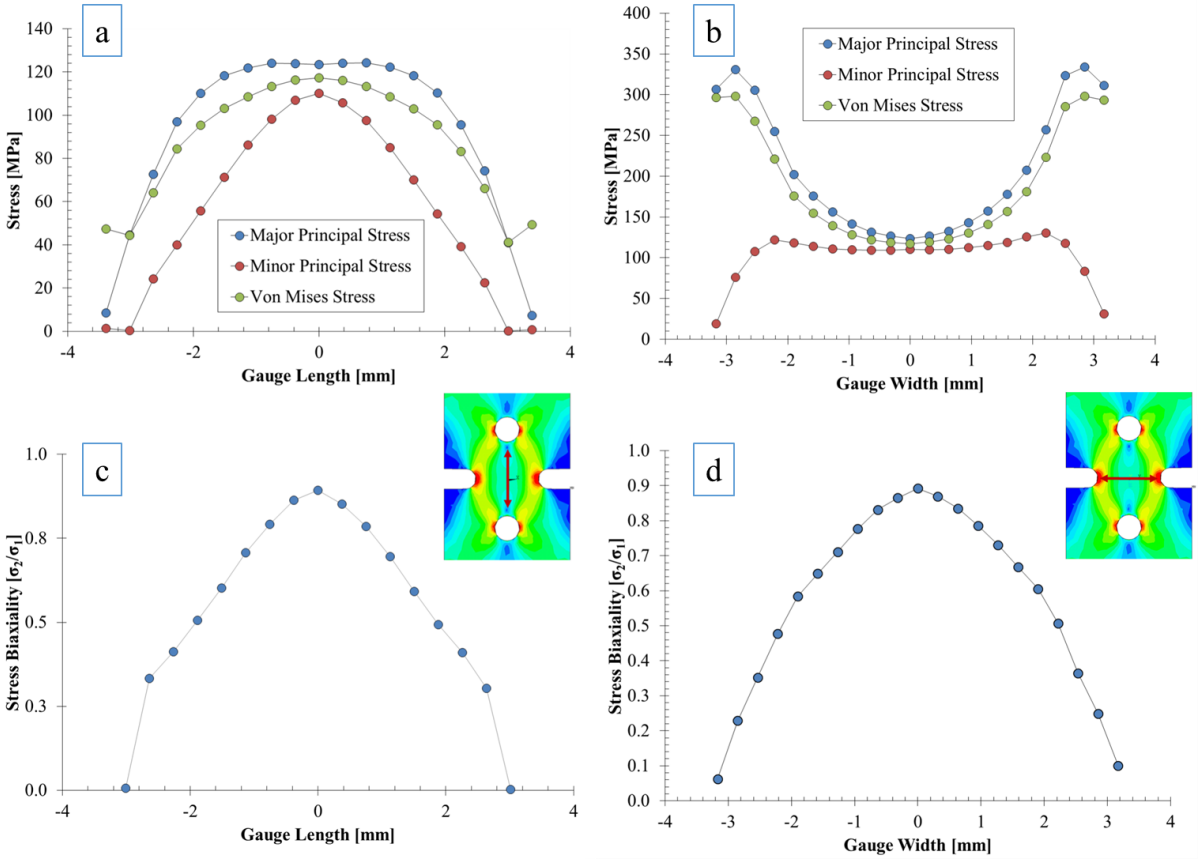

Figure 2-8 The mechanical response of the "near-equibiaxial" sample when the applied net gauge section is 210MPa (far-field stress is 104MPa). In (a) and (b), the major and minor principal stress distributions and the equivalent stress distribution are shown. In (c) and (d), the stress biaxiality ratio along the gauge width and gauge length are shown. The gauge width is defined from notch to notch, and the gauge length is defined as the distance from one hole to another. Plane stress is assumed, such that $\sigma_3 \approx 0$.

In summary, by utilizing a combination of uniaxial, “plane-strain”, and near-equibiaxial tension samples and by examining the extent of hydride reorientation for specific locations in a range of specimen geometries, the effect of stress state on hydride reorientation can be systematically investigated. Importantly, since a range of stress states exists within a single double-edge notched specimen, the effect of stress state can also be examined under well controlled conditions in which all the locations have identical thermo-mechanical histories and the same hydrogen content. This type of sample geometry and detailed finite element analysis allow the investigation of the specific effect stress state on hydride reorientation, using both ex situ and in situ experiments. The latter are described in the next section.

2.4 Synchrotron Radiation Experiments

The Advanced Photon Source (APS) at Argonne National Lab (ANL) is a third-generation synchrotron-radiation source with high brilliance. In the beamline (1-ID-C), it is possible to use high X-ray energies so that relatively thick samples can be examined in transmission mode. In addition, the 1-ID-C has a mechanical loading frame and a furnace capable of taking the sample to high temperature, as well as a fast acquisition image plate that allows frequent recording of the diffraction patterns. These features allow X-ray diffraction data to be continuously collected at specific locations by scanning the beam (about 100 x 100 μm) over the entire gauge section. Acquiring data at different locations in the gauge section allows to monitoring of the evolution of various hydride and matrix peaks in regions subjected to different degree of stress biaxiality. By analyzing the diffraction peaks obtained from various locations within a specimen containing notches, the effect of multiaxial stress state and the degree of stress biaxiality on radial hydride precipitation can be studied in detail

The experimental set up at beamline 1-ID-C is shown in Figure 2-9. The incoming X-ray beam with an average energy of 80 keV penetrates through the sample (about 670 μm), generating X-ray diffraction rings, both from the Zircaloy matrix and from any hydride phases that may be present. The rings are associated with diffraction rings from specific crystallographic planes of particular phases. By

integrating the rings either over their full circumference, or over arcs (cake) aligned with the loading direction (TD) or normal to it (RD), it is possible to obtain separate information on diffracting planes in the two different orientations [132, 133]. X-ray diffraction patterns from material containing different fractions of in-plane versus out-of-plane hydrides were obtained. The analysis of these diffraction patterns may allow us to identify characteristics of the patterns obtained from both types of hydrides so that hydride reorientation can be followed in situ.

A tapered uniaxial tension sample with an evolving microstructure, from circumferential to radial hydrides as a function of stress was examined at room temperature to distinguish the diffraction signals from radial and circumferential hydrides. Double-edge notched samples with both "plane-strain" and "near equibiaxial" geometries were examined using in situ synchrotron radiation X-ray diffraction while dissolution and precipitation was happening. Because the X-ray spot was small (100x100μm), it was possible to translate the beam to different locations within the sample in order to obtain signals from different regions with specific stress states as determined by finite element analysis.

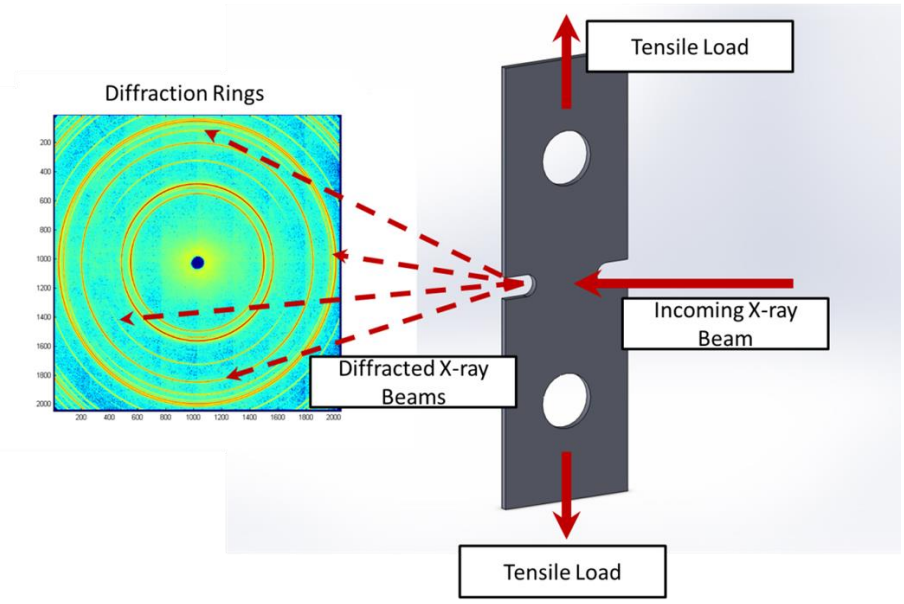

Figure 2-9 An illustration of experimental setup at the 1-ID-C beam line

The X-ray diffraction ring data were acquired using a 2D detector and integrated over different angular arcs. Integration of the diffraction pattern along the areas to obtain intensity vs two-theta plots (see Figure 2-10c), which can be performed over 360° (whole ring), are performed for both TD (load applied direction) and RD (non-load applied direction), as shown in Figure 2-10. The peaks were indexed and fitted using GSAS [134], MATLAB (codes provided by J. Almer and Jun-Sang Park at APS), and manually Peak Fit software. The d-spacings, FWHM, and intensities of both Zirconium and hydride phases were calculated during hydride dissolution and precipitation. For GSAS peak fit analyses; the obtained X-ray signatures during hydride dissolution and precipitation are cut according to the 2θ regions of interest after integration; those cut portions of the X-ray patterns are converted into GSAS format by the MATLAB code provided by J. Almer, and peaks are fitted by pseudo Voigt functions. The same procedure is applied to the MATLAB peak fit. Different than the GSAS and MATLAB fit procedures, the complete X-ray signatures are fitted manually by Peak Fit program using Pearson 7 Area fit functions.

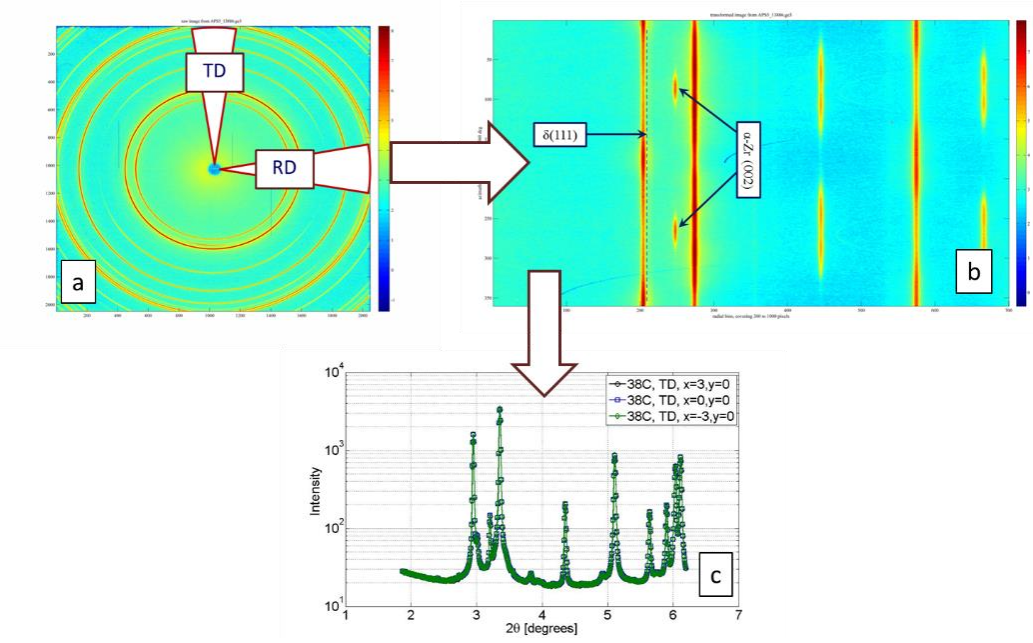

Figure 2-10 The X-ray diffraction data analysis procedure: (a) the Debye rings (b) 2D mapping of the diffraction rings. (c) integrated X-ray diffraction pattern of the samples

2.5 X-ray Diffraction Experiments of Irradiated Cladding Samples

To investigate the effect of irradiation on hydride reorientation, samples were prepared by M. Billone at ANL, which underwent irradiation and subsequent thermo-mechanical treatments as described in Chapter 3. The irradiated cladding samples were prepared at Argonne under the supervision of M. Billone by cutting small slices of irradiated Zircaloy-4 at H.B. Robinson with neutron fluence of 14 10^{25} neutrons/m^2 at 55000 hours [135] and irradiated M5 cladding tube material from North Anna with neutron fluence of 14-16 10^{25} neutrons/m^2 which is estimated from the ZIRLO cladding in the same reactor [136] from which the inner and outer cladding surface oxide layers were removed by grinding and polishing. Metallography was performed on etched sister samples to characterize the hydride microstructures. The hydride microstructures of the Zircaloy-4 sample with 270 wt. ppm of hydrogen are shown in Figure 2-11. The hydrogen contents of the irradiated M5 cladding are listed in Table 4-6 in Chapter 4. The M5 samples were subjected to a prior 1-cycle thermomechanical treatment to create different radial hydride continuity factors as shown in Chapter 4.8 before being examined in the synchrotron to achieve various degrees of hydride reorientation.

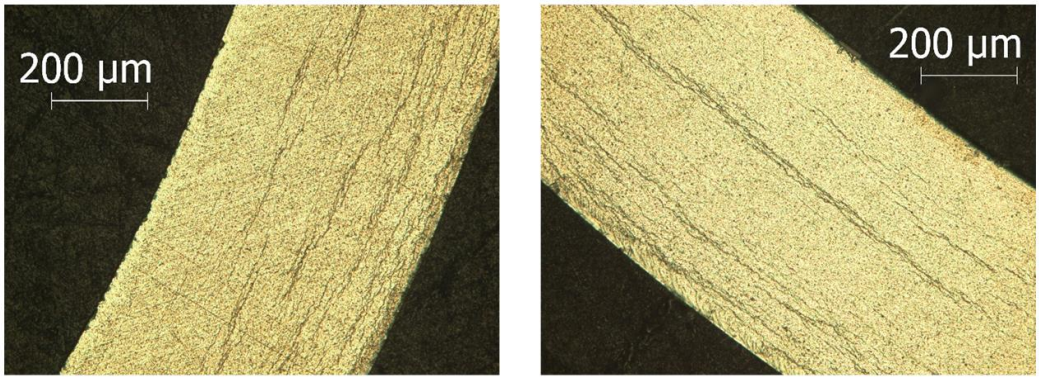

Figure 2-11 Hydride microstructure of irradiated Zircaloy-4 sample (a) at 4 o'clock (b) at 8 o'clock locations (from T. Burtseva and M. Billone)

In order to examine these samples at APS, in collaboration with the safety officers at APS, a sample holder was designed for this experiment to help ensure that no contamination or release of radioactivity occurred during the experiment. The holder confines the 1/3 ring samples both Zircaloy-4 and M5, and keeps them stationary in a double-containment system with two layers of Kapton tape, transparent to X-rays (see Figure 2-12b). Outside the Kapton containment, the dose rates for the samples were measured as 0.2-0.5 mR/h at one foot for gamma only and 0.4-1 mR/h at one foot for both gamma and beta; these dose rates are well below the APS limitations of 5 mR/h at one foot.

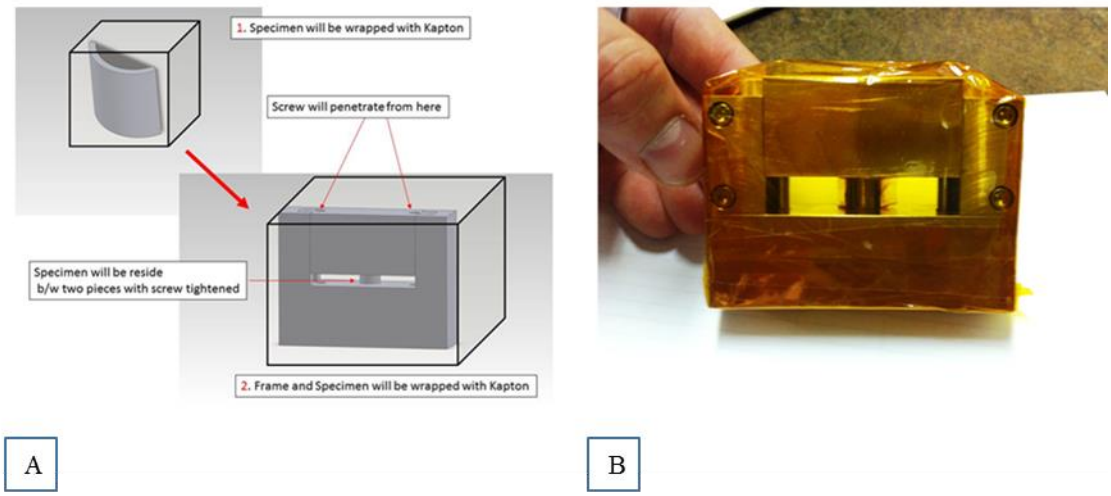

Figure 2-12 (a) Schematic illustration and (b) physical installment of the radioactive samples in two layers of Kapton.

2.6 Mechanical Tests of Hydrided Zircaloy-4 Samples

Hydride reorientation degrades the mechanical properties of the cladding material. Therefore, mechanical tests were performed to quantify the failure behavior of cladding material

with various radial hydride microstructures. Mechanical tests were performed at various temperatures in a range of 25°C to 200°C with a strain rate of 10^{-3} s^{-1} [87] using uniaxial tension samples with various degree of radial hydride fractions. Prior to mechanical testing, the surface of each sample was marked using a Vickers's hardness indenter to form a square array of hardness indentations spaced 1 mm apart (see Figure 2-13) to allow the strain measurements. The distances between two adjacent indents were measured using a traveling microscope. Measurements of the spacing between hardness indentations allows strains near the fracture surface to be calculated according to Equation (2.2).

$$\varepsilon = \ln\left(\frac{l_A + l_B}{l_{10}}\right) \tag{2.2}$$

where ε is the strain between two adjacent markers, l_A and l_B are the distances from the hardness marker to the fracture surface as shown in Figure 2-13, and l_{10} is the initial spacing between two adjacent markers.

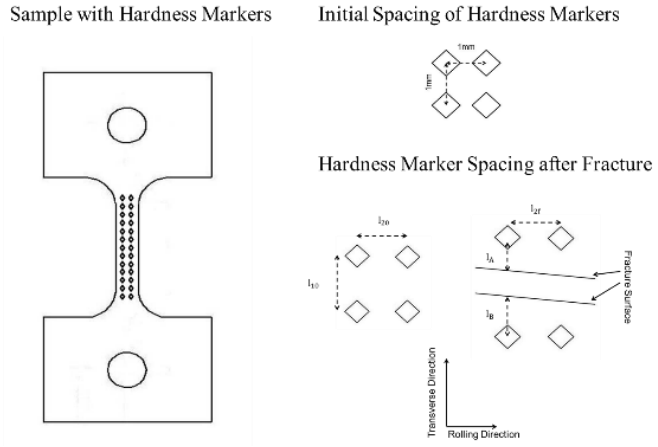

Figure 2-13 Micro hardness indentation distribution on the mechanical test sample surface.

3 THE EFFECT OF STRESS STATE ON HYDRIDE REORIENTATION AND FAILURE BEHAVIOR

This chapter describes the hydride reorientation phenomenon and its effects on the failure behavior of nuclear fuel cladding material, utilizing unirradiated Zircaloy-4 sheet as a model material. At first, the effect of thermo-mechanical treatment on hydride reorientation is investigated for uniaxial tension samples. The effect of stress state on hydride reorientation is studied because the spent fuel cladding is under a multiaxial stress state during vacuum drying and during spent fuel dry-cask storage, and during subsequent transportation as described in Chapter 1. Finally, the failure process of the Zircaloy-4 containing radial hydrides is described on the basis of the ductile-to-brittle transition temperature and associated fracture mechanics behavior.

3.1 Zirconium Hydride Microstructure

This study focuses on the mechanisms of hydride reorientation from its normal in-plane ("circumferential") orientation to the out-of-plane ("radial") orientation in CWSR Zircaloy-4 sheet subjected to a heat treatment which involves dissolution of hydrides completely while heating and precipitation of hydrogen as hydrides while cooling under an applied tensile stress. In order to understand the hydride reorientation mechanisms, proper metrics should be defined to characterize the circumferential and radial hydride microstructures. The degree of hydride reorientation as a result of a thermo-mechanical treatment is characterized by the radial hydride fraction (RHF) as defined in Equation (1-17)

The determination of RHF includes labeling the hydrides and recording the lengths and the angles of hydrides. The hydride angle is estimated with respect to the edge of the sample (transverse direction) as shown in Figure 3-1. Hydrides which have an angle of 45° and greater to the edge of

the sample are denoted radial hydrides. In this study, the RHF is calculated within 600 x 200 μm^2 rectangular regions that represent the hydride microstructure, as shown in Figure 3-1.

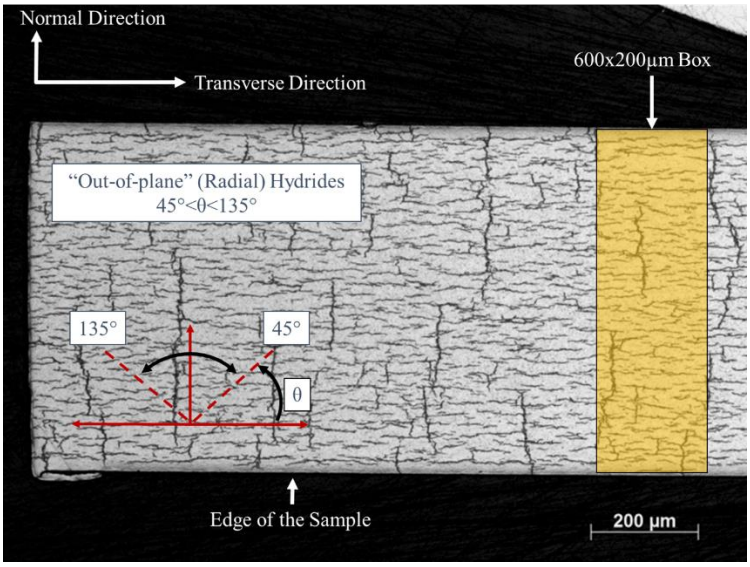

Figure 3-1 A typical hydride microstructure picture illustrating the determination of in-plane and out-plane hydrides and the selected rectangular regions.

In this procedure, one basic issue is the separation of radial hydrides and circumferential hydrides from each other. In low magnification micrographs, both out-of-plane (radial) and in-plane (circumferential) hydrides appear as a connected single hydride, as shown in Figure 3-2. The accurate representation of the RHF by proper assessment of those parameters is essential to depict the hydride microstructure resulting from a given thermo-mechanical treatment. To systematically measure the radial hydride fraction and hydride lengths in a consistent manner, the magnification of the micrographs used was kept constant at 10x.

Figure 3-2 depicts examples of zirconium hydride microstructures with radial hydride fractions of 0, 0.5, and 1 at a constant magnification of 10x. Figure 3-2a shows hydride precipitates oriented within the plane of the sheet specimen, aligned in the transverse direction of the Zircaloy-4 sheet material (analogous to circumferential hydrides in the hoop direction in a cladding tube).

For this microstructure the RHF is zero. These in-plane hydrides are denoted "circumferential" hydrides in this study. For this specific sample, which was hydrided to 180 wt. ppm hydrogen, the circumferential hydride lengths were determined to be in the range of 100 to 1000 μm.

As stated previously, after a thermo-mechanical treatment such as vacuum-drying of spent fuel rods, circumferential hydrides can dissolve at high temperature and change their orientation when re-precipitating upon cooling under stress form radial hydrides whose faces are perpendicular to the applied stress, typically the hoop orientation of a cladding tube. In the present study, "out-of-plane" hydrides oriented in the transverse direction of the Zircaloy-4 sheet, as shown in Figure 3-2b and c, correspond to radial hydrides of cladding and are denoted as such. Figure 3-2b shows a mixed hydride microstructure (both "circumferential" and "radial") after a 1-cycle thermo-mechanical treatment of a sample (180 wt. ppm of hydrogen). The sample was heated up to 400 °C with a rate of 1°C/min, kept at elevated temperature for 1hr, and then cooled down to 150 °C with a rate of 1°C/min under an applied stress level of 225 MPa. For this sample, the radial hydride fraction was estimated to be 0.5. The determination of hydride lengths from the micrograph showed no long circumferential hydrides (such as in Figure 3-2a). In this mixed hydride microstructure, circumferential and radial hydride lengths were estimated to be in the range of 100-500 μm. Figure 3-2c shows a completely reoriented hydride microstructure in a sample with 180 wt. ppm that was subjected to only 4-cycle treatment with the same heating and cooling parameters of the sample in Figure 3-2a. The radial hydride fraction for this sample was evaluated as 1 and the hydride lengths were within a range of 50-500 μm.

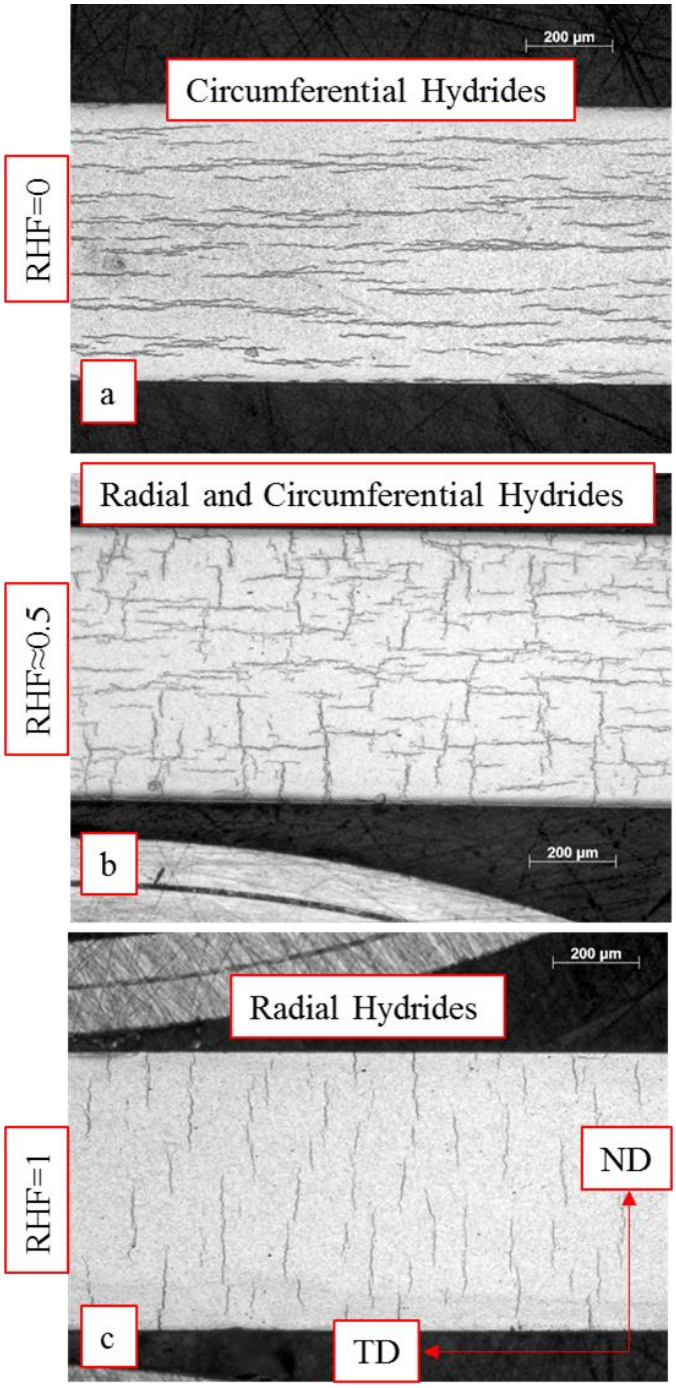

Figure 3-2 Hydride microstructures observed at low magnification in this study in samples with 180 wt. ppm H and cooling under 225 MPa hoop stress (a) shows the hydride microstructure of as hydrided material (RHF=0), (b) shows the hydride microstructure with RHF=0.5 as a result of 1-cycle thermo-mechanical treatment of a sample, and (c) depicts hydride microstructure with RHF=1 as a result of 4-cycle thermo-mechanical treatment.

While the evaluation of the radial hydride fraction and hydride microstructure from the low magnification micrographs of samples will be used to relate the hydride microstructure to subsequent failure behavior of the samples, the details of the hydride microstructure are actually more complex than appear in low magnification. For the same sample shown in Figure 3-2a with RHF = 0, the high (50x) magnification picture (see Figure 3-3a) shows that "single" circumferential hydrides at low magnification are actually a collection of smaller hydrides platelets stacked as a "deck of cards" parallel on the circumferential-axial plane of the material.

The microscopic picture of radial hydrides shown in Figure 3-3 is actually constituted of randomly oriented and even smaller hydride platelets with radial hydride fractions of 0.5 and 1. Thus, a collection of hydride platelets consisting of small platelets is defined as a "circumferential hydride" when the "collection" (or "macroscopic hydride when viewed at low magnifications of equal and less than 10X) is aligned in the plane of the sheet and more or less parallel to it. On the other hand, a collection of small hydride platelets is defined as a "radial hydride" when smaller hydrides are stacked in the radial direction normal to the plane of the sheet specimens, constituting a macroscopic hydride.

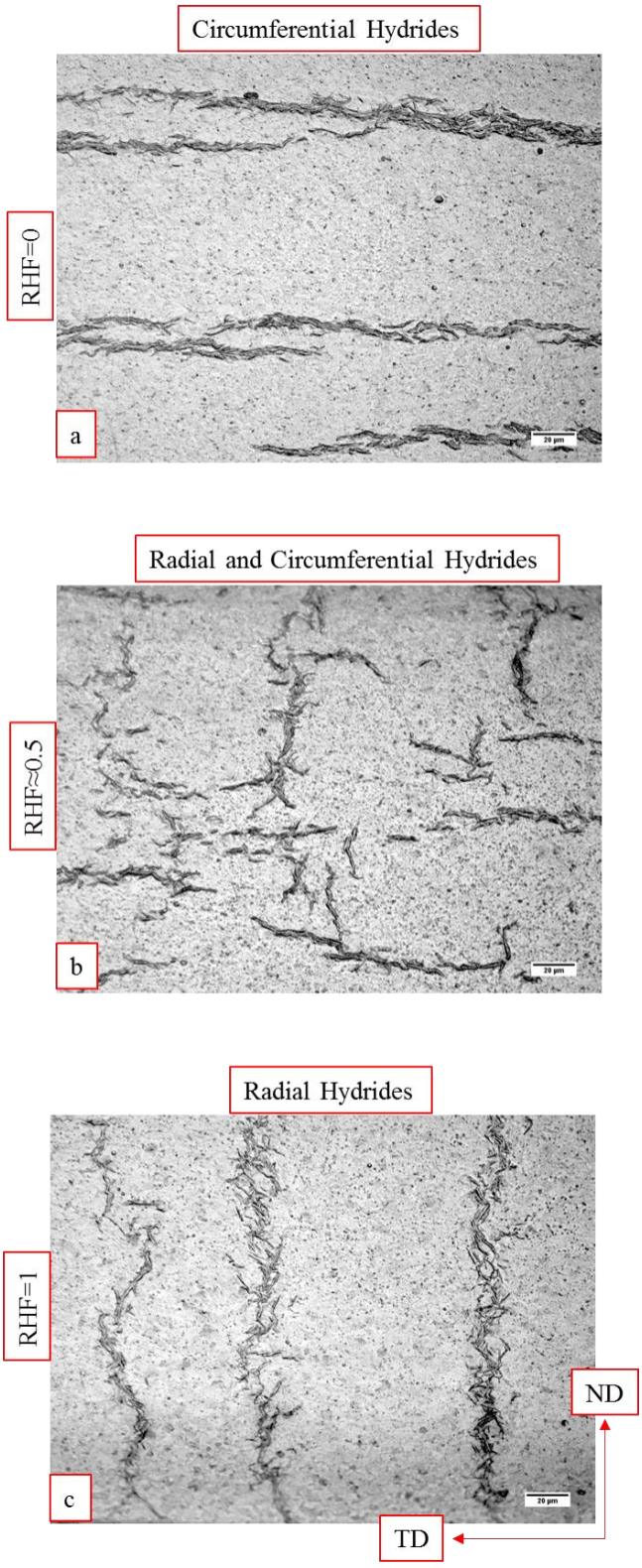

Figure 3-3 High magnification micrographs of “circumferential”, “mixed”, and “radial” hydrides.

3.2 Zirconium Hydride Reorientation

As described in Chapter 1, both intrinsic and extrinsic parameters affect radial hydride precipitation in Zircaloy-4 during vacuum drying of spent nuclear fuel rods. Because the integrity of spent nuclear fuel rod should be maintained after its removal from the core during drying, storage, and transportation, the determination of the effects of these extrinsic parameters on hydride microstructure is essential. Importantly, radial hydrides present in the cladding after vacuum drying and storage can severely reduce cladding ductility by causing through thickness crack initiation and growth which in turn can cause cladding failure at low strains [94]. The result is a significant increase in the ductile-to-brittle transition temperature of the cladding [18]. Therefore, it is crucial to understand radial hydride precipitation as a basis for establishing safety margins for spent fuel rods during dry-cask storage and/or transportation.

In this study, the thermo-mechanical cycles for hydride reorientation were based on the simulation of the bounding vacuum drying operation of spent nuclear rods. To establish a mechanistic understanding of the process of hydride reorientation and microstructure, uniaxial tension samples were subjected to various thermo-mechanical treatments. In order to ensure that all hydrogen was dissolved in the matrix, the maximum temperature in this study was higher than the NRC limitation for high burnup fuel [137].

The first step of the thermo-mechanical cycles for hydride reorientation is the heating of the hydrided specimen up to 450°C, so that the hydrides were completely dissolved in the Zircaloy-4 matrix for the level of hydrogen in the samples (< 200 wt. ppm). To homogenize the hydrogen distribution, the samples were kept at 450°C for 1-hr. After a dwell time, the samples were cooled down to 150°C, such that almost all hydrogen was precipitated, at the cooling rates of 0.2 and 1°C/min. In order to promote radial hydrides precipitation, stress was applied to the sample during

cool down when the temperature reached 400°C while hydrogen was still in solution in Zircaloy-4.

Note that, in general, the internal pressure in a cladding tube decreases as temperature decreases during cool down, which would cause a decrease in the hoop stress as temperature decreased. However, in this study the applied tensile stress was kept constant during cooling, with the idea that such a stress application schedule would provide a conservative baseline for hydride reorientation. Finally, the specimens were kept at 150°C for 1hr, and then the applied stress was removed. Thus, the heat-up, dwell at 450°C, cool-down under stress below 400°C, and dwell at 150°C constituted one thermo-mechanical cycle. All samples were examined using optical metallography after the thermo-mechanical treatments to determine the RHF.

Figure 3-4 shows the effect of cooling rate and of the number of cycles on the resulting hydride microstructures, viewed at low magnification. The hydride lengths were measured using program called ImageJ software [138]. The uniaxial tension sample with 198 wt. ppm of hydrogen, shown in Figure 3-4a, was subjected to a 1-cycle treatment using a slow cooling rate (0.2°C/min). As shown in Figure 3-4a, the final hydride microstructure consisted of large macroscopic radial hydrides (RHF = 1.0). The maximum hydride length was 620 μm, the minimum length was 137 μm, and the average length was 315 μm. While the specimen in Figure 3-4b was also subjected to a 1-cycle heat treatment, its cooling rate was higher (1°C/min). The resulting microstructure consisted of relatively smaller mixed radial and circumferential hydrides. For circumferential hydrides, the maximum length as viewed on this macroscopic basis was determined to be 316 μm, the minimum length was 83 μm, and the average length was 192 μm in Figure 3-4b. However, the corresponding length-values for the radial hydrides were on average 114 μm, the maximum was 222 μm, and the minimum length was 62 μm.

The macroscopic hydride length decreases with increasing cooling rate. Low cooling rates resulted in larger hydrides (up to 620 μm), while higher cooling rates resulted in smaller hydrides (up to 200 μm). This difference in hydride lengths is generally explained by the characteristics of the nucleation and growth rates. While precipitation is occurring, although hydride nucleation and growth occur concurrently, their rates vary with undercooling. As the undercooling increases, the driving force for nucleation (and consequently the nucleation rate) increases. Thus a high cooling rate tends to favor nucleation of new particles relative to the growth of existing ones. While the growth rate decreases due to diffusion issues, the high nucleation rate results in many small particles, rather than a few large ones. Thus, larger hydrides were observed in the samples with low cooling rate, and smaller hydrides were observed in the samples with high cooling rate.

On the other hand, Figure 3-4c shows the hydride microstructure of a specimen with 160 wt. ppm of hydrogen after a 4-cycle treatment with a cooling rate of 1°C/min. As a result of thermo-mechanical treatment with an increased number of cycles, the microstructure consisted only of radial hydrides (RHF = 1). The maximum length of the radial hydrides was estimated as 299 μm, the average length was 183 μm, and the minimum length was 91. μm these values are somewhat larger than those for material undergoing a single cycle heat treatment. It is also clear that the hydrides are more closely aligned, leading to a high continuity factor.

The increase in RHF with increasing number of cycles is a result of greater selectivity among hydrogen atoms to precipitate into a radial hydride rather than circumferential. As the material cools there is a competition between radial and circumferential hydrides for hydrogen atoms. The applied stress creates a bias for radial hydrides but the selection is not perfect in the first cycles. With increasing number of cycles (or decreasing cooling rates) the hydrogen atoms have greater opportunity to precipitate as radial hydrides rather than circumferential, thus increasing the RHF. The connectivity also increases because of an increasing degree of sympathetic hydride nucleation.

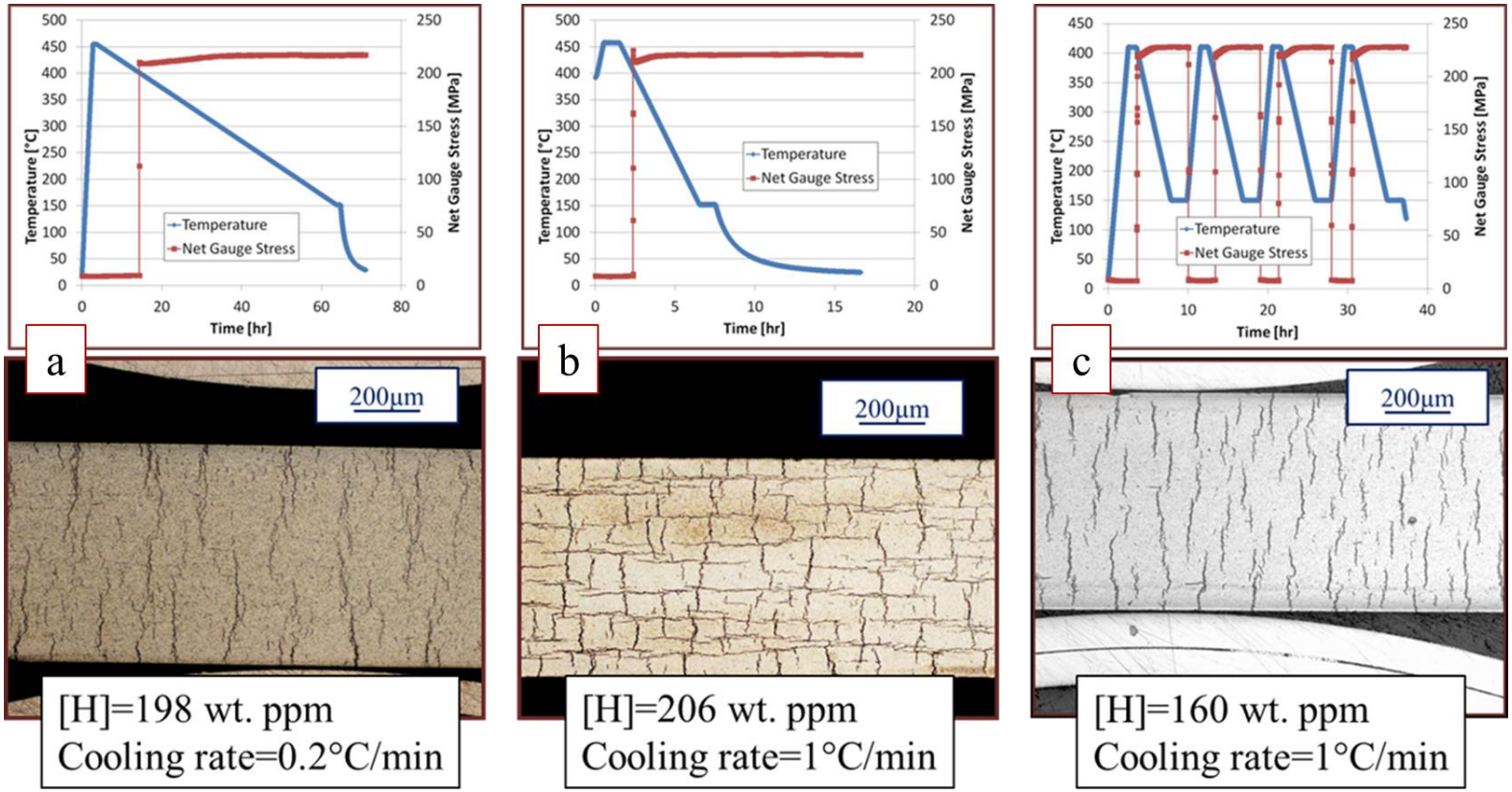

Figure 3-4 Comparison of resulting hydride microstructures as a result of different thermo-mechanical treatments of uniaxial tension samples. Samples were subjected to 225 MPa to initiate radial hydride nucleation

The precipitation of hydrides also creates a dislocation debris that facilitates the precipitation of hydrides in the same orientation. This has been termed the memory effect. The dislocations remain even hydrides are dissolved at high temperatures that are lower than recrystallization temperature of the Zircaloy-4; this depicts only partial plastic recovery happens while annealing. Then, the remaining dislocations help to accommodate the strain energy during successive hydride precipitation. To demonstrate the memory effect for radial hydride precipitation, a companion test was performed as follows: a uniaxial tension sample with 180wt. ppm of hydrogen was subjected to a 2-cycle treatment with a cooling rate of 1°C/min as shown in Figure 3-5. The first cycle of the treatment was similar to the previously described thermo-mechanical treatments (shown in Figure 3-4b) and it should have resulted in a RHF = 0.1-0.12. However, during the 2nd cool down step of the treatment, the stress was not applied to the sample in this case, which means that radial hydride precipitation had the benefit of an applied stress only during the 1st cycle cool-down not but not for the 2nd cycle cool-down. After the 2nd cycle, radial hydride precipitation (RHF=0.1-0.12) was observed even though there was no applied tensile stress during cooling down. This result indicates that radial hydride nucleation sites that were created during the first cycle remained active during the 2nd cycle despite the absence of the applied stress normally required to precipitate radial hydrides.

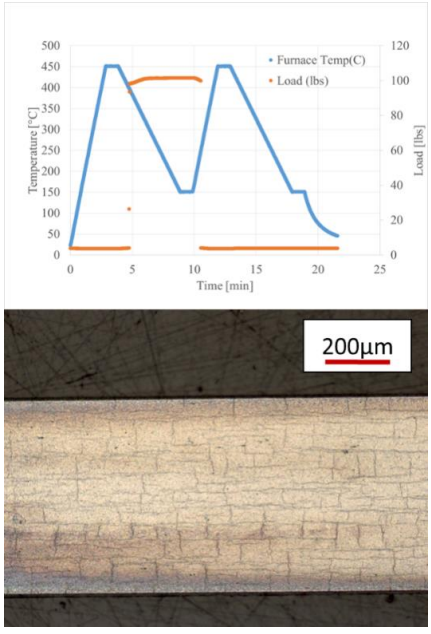

Figure 3-5 The hydride microstructure of a sample after a 2-cycle thermo-mechanical treatment with no load during the 2nd cycle.

3.3 The Effect of Stress Biaxiality on the Zirconium Hydride Reorientation

In the previous section, of the influence of cooling rates and number of cycles on hydride precipitation under tensile stress was addressed. Another important characteristic is the critical ("threshold") stress required to initiate radial hydride precipitation in the cladding. The internal pressure during vacuum drying causes the cladding tubes to be under multiaxial stresses in which a secondary stress (axial stress) component is present in addition to major stress (hoop stress). The purpose of this aspect of the research is to investigate the effect of such multiaxial stress states on the critical threshold stress to form radial hydrides.

To investigate the effect of stress state on the radial hydride precipitation, the following procedure was used. Special double-edge notched specimens were designed to induce various stress biaxialities in the range of uniaxial tension ($\sigma_2/\ \sigma_1 = 0$) to "near-equibiaxial" ($\sigma_2/\ \sigma_1 = 0.8$) within the specimens; see Chapter 2 for details. Using finite element analysis to identify the stress states at specific locations within these specimens and characterizing the hydride microstructure at the same locations, it was possible to obtain values of the threshold stress for radial hydride precipitation for a range of multiaxial stresses. These data were then combined with threshold stress value for hydride reorientation in tapered uniaxial tensile specimens in order to determine the dependence of the threshold stress on stress state for the range of stress biaxialities from uniaxial tension ($\sigma_2/\ \sigma_1 = 0$) to "near-equibiaxial" tension ($\sigma_2/\ \sigma_1 = 0.8$). The Zircaloy-4 sheet samples used to investigate the effect of stress biaxiality contained approximately 180 wt. ppm of hydrogen and were subjected to the 2-cycle thermo-mechanical treatment illustrated in the Figure 3-6.

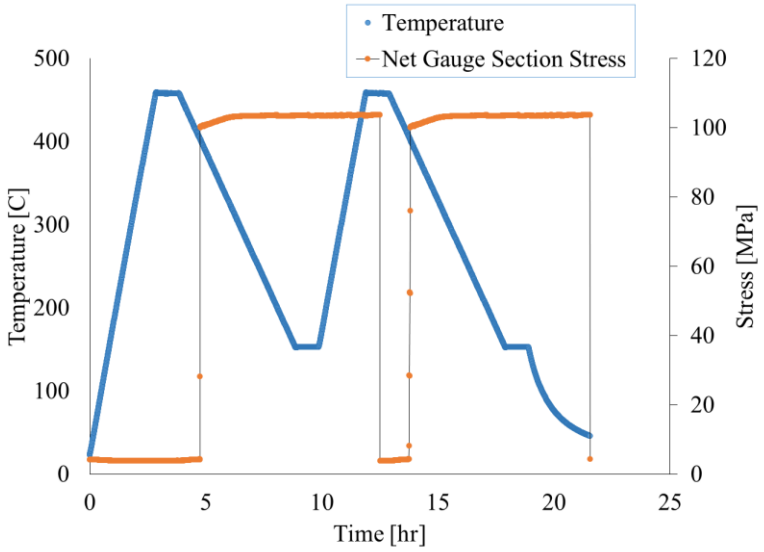

Figure 3-6 Thermo-mechanical treatment used to estimate the threshold stress for hydride reorientation. The maximum temperature is 450°C, the heating rate is 5°C/min, and the cooling rate is 1°C/min.

Figure 3-7 shows the evolution of the hydride microstructure from in-plane hydrides to radial hydrides in a tapered uniaxial tension sample after the thermo-mechanical treatment shown in Fig. 3.6. Because of the taper, the tensile stresses change along the length of the sample during cooling under applied stress as shown in Figure 3-7. As seen in Figure 3-7, the transition from in-plane to out-of-plane hydrides occurs at a tensile stress of about 155 MPa along the length of the tapered specimen. Above 177 MPa, the radial hydride fraction approaches 1, whereas the radial hydride fraction is equal to zero at stress levels below 145 MPa. An analysis of this specimen and other similar samples indicates that for the Zircaloy-4 material used in this study, the threshold stress for hydride reorientation under a uniaxial tension stress state is 155 ± 10 MPa.

For CWSR Zircaloy-4, threshold stresses have been reported between 80 MPa and 200 MPa for uniaxial tension [83, 116, 119]. The present threshold stress values (155 ± 10 MPa) for uniaxial tension stress state are in good agreement with the results of Colas (160 MPa) [83] who used the same Zircaloy-4 sheet material used in this study. In addition, Bai [116] also reported a threshold stress for reorientation of 187 MPa in cold-worked stress-relieved Zircaloy-4 sheet material. However, Daum [119] estimated a threshold stress of 80 MPa for both irradiated

and un-irradiated fuel cladding tubes. The reasons of this difference in threshold stress values are not clear, but one possibility could be the differences in the microstructure of the test samples.

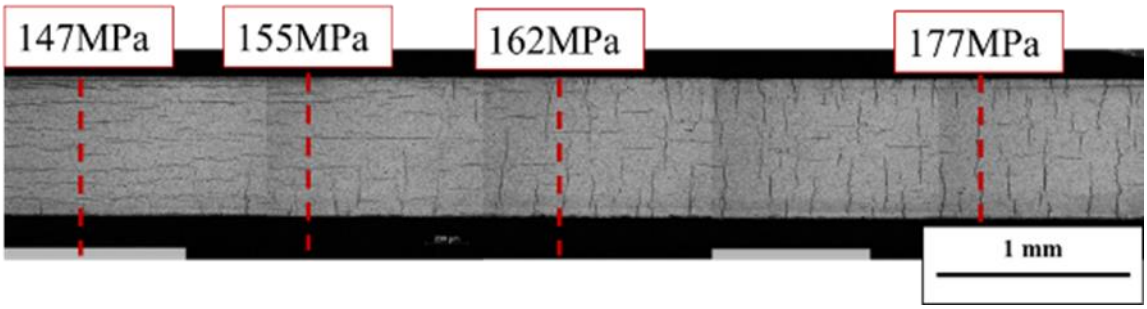

Figure 3-7 Hydride microstructure of a tapered uniaxial tension sample after the 2-cycle thermo-mechanical treatment. The threshold stress for hydride reorientation is approximately 155 MPa.

As mentioned before, hydride reorientation behavior under multiaxial stress states ($\sigma_2/\sigma_1>0$) was assessed using a combination of metallographic examination of double-edge notched specimens and finite element analysis of the test geometry. In this geometry the "radial" hydrides appear on the top surface of the sample after etching. Figure 3-8 depicts both the radial hydride microstructure in the double-edge notch tension sample and the stress biaxiality ratio (σ_2/σ_1) plot from the center of the specimen to the notch tip. The hydride microstructure in Figure 3-8 was observed on the normal plane that contains the transverse and rolling directions of the sheet specimen. If the macroscopic hydrides are viewed as platelets with a face plane, then the in-plane hydrides are oriented with their "face" planes parallel to the flat surface of the sheet specimen shown in Figure 3-7. Thus, etching will not reveal the in-plane hydrides in a micrograph as oriented in Figure 3-8. However, radial hydrides will have face planes oriented perpendicular to the sheet surface, and after etching, the edges of radial hydride platelets are clearly visible in Figure 3-8.

As shown in Chapter 2, for the specimen shown in Figure 3-8, finite element calculation shows that the stress biaxiality ratio at the notch is equal to 0 (uniaxial tension), but increasing rapidly with distance from the notch such that $\sigma_2/\sigma_1=0.57$ near the center of the gauge section (corresponding to internally pressurized thin tube conditions) under the elastic conditions of the analysis shown in Figure 3-8. At other locations such as near the notch but above or below the minimum width section, the state of stress is near uniaxial tension, i.e. $\sigma_2/\sigma_1=0$.

A detailed examination of the radial hydride microstructures such as in the Figure 3-8 shows that the threshold stresses for hydride reorientation (major principal stress, σ_1) near the gauge center, where the stress biaxiality is high ($\sigma_2/\ \sigma_1$=0.5), are lower (115 MPa) than the threshold stresses (155 MPa) observed in the tapered uniaxial tension ($\sigma_2/\ \sigma_1$=0) sample in Figure 3-7. Thus, increasing the degree of stress biaxiality decreases the threshold stress for radial hydride formation.

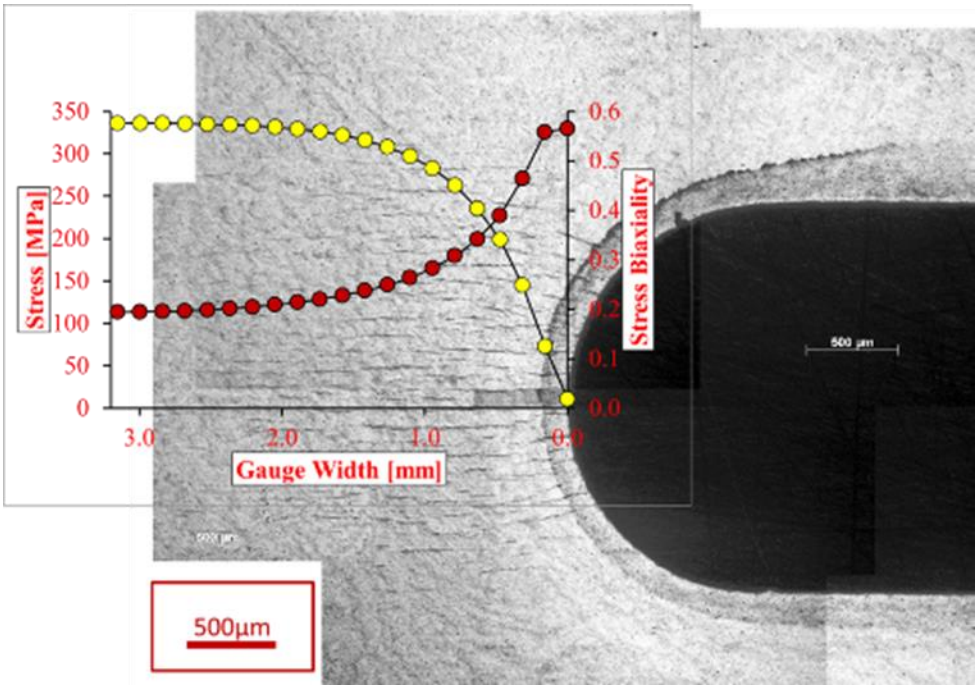

Figure 3-8 The radial hydride microstructure, major principal stress (red, left axis) and stress biaxiality ratios ($\sigma_2/\ \sigma_1$) (yellow points, right axis) across the gauge section of a double edge notch tensile sample containing 180 wt. ppm of hydrogen and subjected to a 2-cycle thermo-mechanical treatment. At the high applied load in this test, radial hydrides are visible even in the uniaxial tensile region near the notch.

The "near-equibiaxial" tension specimen (described in Chapter 2) was used to examine the decrease in the threshold stress at high biaxiality stress ratio. For the specimen depicted in Figure 3-9, the stress state very near the notches is close to uniaxial tension, similar to the double edge-notched specimen in Figure 3-8. However, the presence of the "stress state" holes in Figure 3-8 changes the local stress state in the specimen center to near equibiaxial tension ($\sigma_2/\ \sigma_1$=0.83). As shown in Figure 3-9a, radial hydride precipitation does not occur within a strip of material near the edges of sample where the major principal stress falls below the threshold value for

reorientation in uniaxial tension. In addition, above and below the stress state holes there are regions where the maximum principal stress decreases to such a low level that radial hydrides do not form. In contrast, there is a wide region showing radial hydrides near the center of the specimen where the maximum normal stress is above a minimum value in the range of about 75 MPa, as calculated by finite element analysis, with a high stress biaxiality ratio of 0.83 as shown in Figure 3-9b and where radial hydrides are present. In addition, in all cases the radial hydrides are oriented normal to the maximum principal stress direction as illustrated in Figure 3-9c.

A careful examination of the equibiaxial samples shows that at high stress biaxiality ratios of 0.83 the threshold stress decreases to 75 MPa. This value is significantly lower than the value of 115 MPa for the threshold stress in near plane strain tension when $\sigma_2/\ \sigma_1 = 0.5$. Thus, the threshold stress for radial hydride precipitation decreases from 115 MPa to 70 MPa as the stress biaxiality ratio increases from 0.5 to 0.87.

The results indicate that a determination of the threshold stress for hydride reorientation needs to take into account the degree of the stress biaxiality imposed on the samples by the applied stress. Thus, it is important to know the stress state of the cladding while cooling down under tensile stress during vacuum-drying in order to make an accurate prediction of the threshold stress for hydride reorientation.

.

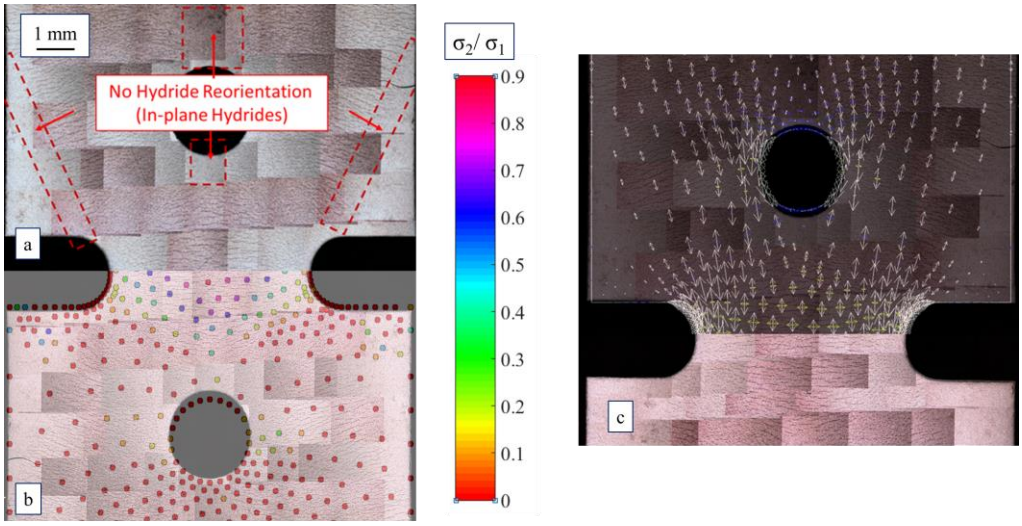

Figure 3-9 Hydride microstructure within an equibiaxial tension sample with 180±15 wt. ppm of hydrogen and (b) the stress biaxiality ratio distribution (σ_1/σ_2) estimated by finite element analysis (FEA) in the sample where 210MPa of net gauge section stress was applied.(c) The principal stress directions mapped on the hydride microstructure within the "equibiaxial" sample after 2-cycle thermo-mechanical treatment. White arrows represent the direction and magnitudes of the maximum principal stresses and the yellow arrows those of the minor principal stresses.

The overall effect of the stress biaxiality on the threshold stress for hydride reorientation is depicted in Figure 3-10. By plotting the threshold stress (as determined by the maximum principal stress) to cause hydride reorientation as a function of the stress biaxiality ratio, as shown in Figure 3-10, the decrease in the threshold stress as stress biaxiality increases is clearly seen. The data for this figure were obtained by examining in detail the regions in each sample that were under a given stress biaxiality ratio and locating where hydride reorientation no longer occurs; the maximum principal stress becomes the threshold stress. It is notable that although several sample designs were used (each with a range of biaxiality ratios), such that the resulting data are indicated by different symbols (see labels), the data are consistent among the sample design, i.e. a given stress biaxiality corresponds to a critical stress independent from the sample design.

For the double-edge notched tensile specimens, the average threshold stress at locations under a uniaxial stress state is 155 ± 10 MPa. This value is similar to results obtained directly from tapered uniaxial tension samples (155 MPa). Thus, there is good agreement in the threshold stress-

values under uniaxial tension for the three types of samples used, supporting the validity of the data obtained from double-edge notched samples.

The value of the threshold stress for a stress biaxiality ratio of 0.5 is 115 ±7 MPa; this biaxiality ratio corresponds to the expected stress state in an internally pressurized tube. In the literature, the threshold stresses for internally pressurized tube samples tested under similar conditions range from 70 MPa to 115 MPa [22, 109]. Thus, the threshold stress of 115 MPa in this study is at the high limit of the unirradiated internally pressurized tube test data.

In summary, a comparison of the uniaxial tension and multiaxial tension data shows that the radial hydride precipitation is enhanced by the higher level of secondary stress present in multiaxial stress states such that the minimum principal stress required for hydride reorientation decreases linearly with increasing biaxiality ratio as shown in Figure 3-10.

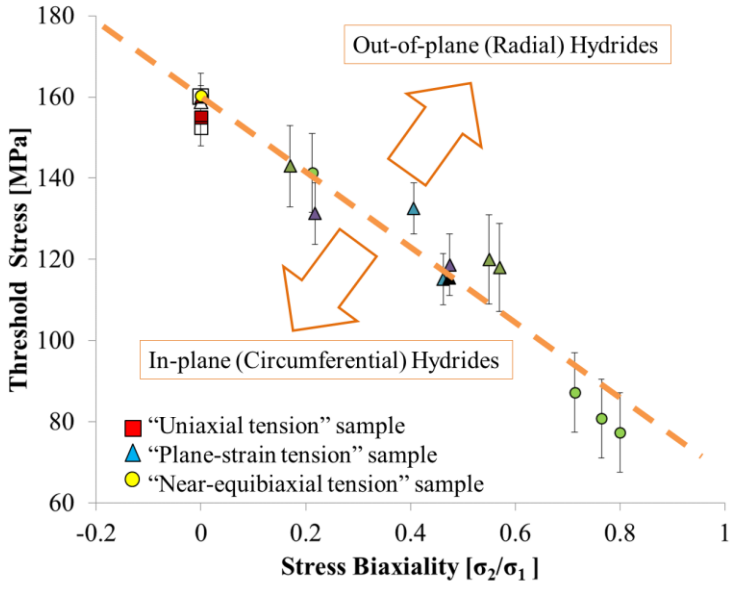

Figure 3-10 Threshold stress (major principal stress) for the onset of radial hydride formation, as a function of stress biaxiality. The specimens contained ≈180 wt. ppm of hydrogen and were subjected to a 2-cycle thermo-mechanical treatment with a maximum temperature of 450°C. Each data point represents the average of 3 to 5 measurements. Different colors indicate different individual samples and different symbols indicate different states of stress.

3.4 An Analysis of the Influence of Stress State on the Threshold Stress

In order to understand the conditions of radial hydride precipitation under tensile stress, Ells [108] and then Puls [68] developed a thermodynamics model based on early studies of Sauthoff [139]. Basically, these models predict the critical energy for the nucleation of hydrides under an external stress field. Importantly, the models recognize the interaction between the external tensile stress field and the hydride transformation strain in assisting hydride nucleation.

Puls' analysis was extended in a study done by Qin et al. [48] who determined the radial hydride precipitation criteria by including the possible precipitate shapes under tensile stress. Based on these analyses, the radial hydride precipitation criterion including the effect of stress state can be written as;

$$-\Delta G_{chem} - \frac{xV_H}{3V_{hyd}}(\sigma_1 + \sigma_2) - (\sigma_1 e_1^T + \sigma_2 e_1^T) > \Delta G_{strain} \tag{3.1}$$

where ΔG_{chem} is the chemical free energy of transformation for radial hydrides per unit volume, energy the hydride stoichiometry x is 1.6 for delta hydrides, V_{hyd} is the zirconium hydride molar volume (16.3 x 10^{-6} m^3/ mol), V_H is the molar volume of hydrogen (1.67 x $10^{-6}$$m^3$/mol), e_1^T (0.077) and e_2^T (0.057) [126, 140] are transformation strains in the major and minor strain orientations, σ_1 and σ_2 are major and minor principal stresses, and ΔG_{strain} the internal strain energy of hydride precipitation per unit volume. Re-writing the inequality as Equation (3.2) establishes a relation for the threshold stress to initiate the radial hydride precipitation $(\sigma_1)_{th}$ as a function of the minor principal stress (σ_2):

$$(\sigma_1)_{th} = \frac{(\Delta G_{\text{strain}} - \Delta G_{\text{chem}}) - (\frac{xV_H}{3V_{hyd}} + e_2^T)\sigma_2}{\frac{xV_H}{3V_{hyd}} + e_1^T} \tag{3.2}$$

The derivative of Equation (3.2) relative to the minor principal stress is:

$$\frac{\partial \sigma_{th}}{\partial \sigma_2^A} = -\frac{(e_2^T + \frac{xV_H}{3V_{hyd}})}{(e_1^T + \frac{xV_H}{3V_{hyd}})} \tag{3.3}$$

Equation (3.3) predicts the rate of change of the threshold stress (σ_{th}) as a function of minor principal stress (σ_2). Importantly, it predicts a linear relationship between σ_{th} and σ_2 such that the slope of the threshold stress versus minor stress data can be estimated if the following variables are known: the transformation strains e_1^T and e_2^T, the hydride molar volume V_{hyd}, and the molar volume of hydrogen in solution V_H.

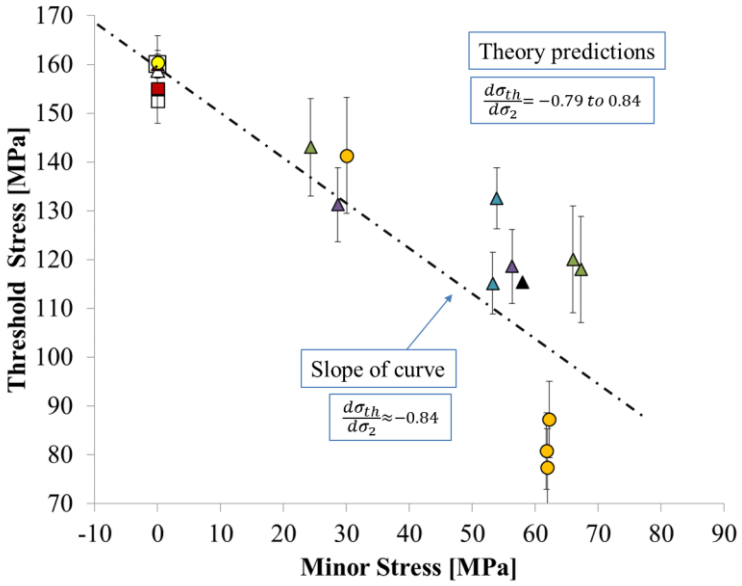

Figure 3-11 The threshold stress to reorient hydrides as a function of minor principal stress with a comparison of the experimental observations with theoretical predictions from Equation (3.3)

Figure 3-11 depicts the effect of minor principal stress on the critical stress for hydride reorientation with both experimental data from the current study and calculated using Equation (3.3). The experimental data exhibits an approximately linear decrease in the critical stress to

reorient hydrides as the minor principal stress increases, which is well predicted by Equation (3.3). A linear fit of the experimental data in Figure 3-11 indicates that the slope of threshold stress as a function of minor stress is -0.84, which is in the range of the theoretical predictions of Equation (3.3), as discussed in the following paragraph.

Table 3-1 also summarizes the transformation strains from the literature and the slope predictions by the Equation (3.3); the slope depends on the magnitude of the anisotropic transformation strains ($e_1^T \neq e_2^T = e_3^T$). An analysis for hydride nucleation in zirconium by Perovic [141] suggests $e_1^T = 0.17$ and $e_2^T = 0.00$, in which case the predicted slope is -0.25 compared to the value of $d\sigma_{th}/d\sigma_2 = -0.84$ which was experimentally calculated. The slope is calculated as -0.80 from Carpenter's predictions of anisotropic transformation strains that are $e_1^T = 0.072$ and $e_2^T = 0.046$ [40]. A TEM study which investigates the interfacial strains of Zircaloy-2 matrix-hydride precipitate by Barrow et al. [142] estimates $e_1^T = 0.055$ and $e_2^T = 0.031$. The resultant slope from his transformation strains is -0.79 which is close to the experimentally obtained slope $d\sigma_{th}/d\sigma_2 = -0.84$; a more detailed analysis by Singh [140] includes a non-zero e_2^T component such that $e_1^T = 0.077$ and $e_2^T = 0.052$ at the nucleation temperature of 294°C for δ-hydride in α-zirconium for a specific hydrogen content. According to those transformation strains from Singh's study, the slope is calculated as -0.81, which is very close to the experimental prediction of the slope.

Table 3-1 The hydride transformation (misfit) strains from literature data and the slope estimations by Equation (3.3)

	Dilatational misfit	**Secondary misfit**	**The slope**
	e_1^T	e_2^T	$d\sigma_{th}/d\sigma_2$
Perovic [141]	0.17	0	-0.25
Carpenter [40]	0.072	0.046	-0.80
Singh [140]	0.077	0.031	-0.81
Barrow [142]	0.055	0.031	-0.79

Carpenter's and Singh's analyses are based on the closed-packed plane orientation relationship of δ-{111} parallel to α-(002) and volumetric accommodation of stress-free, isotropic, and cubic FCC (without distortion) δ-hydride crystal into the anisotropic HCP α-zirconium crystal by atomic radii method. It is stated that the anisotropy of the misfit is caused entirely by the anisotropy of the α-zirconium crystal, and it is independent of the relative orientation of the hydride. With the exception of Barrow's experimental result [142], the above analyses estimate the transformation strains by using atomic radii method under the hard sphere assumption based on single crystal α-zirconium lattice parameters.

However, the d-spacing of hydrides, in particular for circumferential hydrides, shows difference to the α-zirconium materials axis such as normal (radial for tubes) and transverse (hoop) directions, please see Table 4-4 in Chapter 4.6. Thus, the misfit estimation, in particular for circumferential hydrides that are embedded in CWSR zirconium matrix, only shows the maximum possible transformation strains due to the accommodation of misfit; the actual transformation strains in CWSR Zircaloy-4 should be lower due to the grain boundaries, stacking faults, and dislocation structure. Thus, the Carpenter's and Singh's misfit strains are not applicable to the circumferential hydrides.

As will be discussed in Section 4.6, when only the radial hydride microstructure is present, the hydride {111} d-spacing in the normal direction, that is 2.751Å, (ND) which gets closer to hydride {111} d-spacing in the transverse direction, that is 2.759Å, (TD, the stress applied direction), please see Table 4-4. Thereby, the d-spacing difference at normal and transverse directions for radial hydrides can be thought as similar. Thus, the same procedure of the transformation strain calculation based on atomic radii could be applied to the radial hydrides only. Noting cautiously again, for circumferential hydrides, the d-spacing difference between ND (2.763Å) and TD (2.754Å) is more significant than the radial hydrides. Thus, the Singh's procedure will fail in case of circumferential hydrides because the importance of the orientation relationship constraint increases. The correct lattice parameters of hydrides must be involved in the analysis by involving the effects of grain boundary and dislocations on hydride nucleation.

3.5 Calculation of the transformation strain using Carpenter's [40]and Singh's studies [140]

3.5.1 Calculation of dilatational misfit strains using the formal definition of misfit at room temperature

As discussed previously, the Carpenter's and Singh's misfit strain analyses have limitations when atomic radii method is used. Thus, it is essential to include misfit strain calculation by the formal definition of misfit strain using the d-spacings of hydrides and matrix as:

$$\varepsilon_{[hkl]} = \frac{d_H - d_\alpha}{d_\alpha} \tag{3.4}$$

where $\varepsilon_{[hkl]}$ is the misfit (transformation strain) at relevant direction due to the orientation relationship d_H and d_α are the d-spacing of corresponding planes in hydride and α-zirconium matrix. Hence, the dilatation transformation strain (e_1^T) can be directly written as:

$$e_1^T = \frac{d_{\delta 111} - d_{\alpha 002}}{d_{\alpha 002}} \tag{3.5}$$

where $d_{\delta 111}$ is the d-spacing of hydride in <111> direction (closed packed direction) and $d_{\alpha 002}$ is the d-spacing of α-zirconium in <002> direction (normal to the basal plane). Equation (3.5) is based on the closed packed plane orientation relationship of δ-hydride {111} plane parallel to α-zirconium (002) plane. On the other hand, the second component of misfit can be calculated by considering the corresponding planes that are perpendicular to the δ-{111} or α-(002) which is δ-$(2\bar{2}0)$ or δ-{220} and α-{100}. Thus the minor transformation strain is written as:

$$e_1^T = \frac{d_{\delta 2\bar{2}0} - d_{\alpha 100}}{d_{\alpha 100}} \tag{3.6}$$

The Equations (3.5) and (3.6) describes the amount of strain that is accommodated as a result of hydride precipitation. For Singh's procedure, the stress-free conditions yields that the hydride lattice spacing is unique, that is the powder diffraction value, and the transformation strain calculated at stress-free hydride crystal represents the maximum misfit if the hydride crystal ideally fit into zirconium crystal which is basically valid for homogenous nucleation of hydrides. Actually, hydride precipitation initiates at grain boundaries, stacking-faults, or dislocations for CWSR Zircaloy-4 material. Thus, the expected transformation strain that accommodates the volume difference caused by fitting the hydride in matrix could be lesser than the stress-free misfit strains.

As mentioned above such a misfit calculations is valid only if the orientation relationship described above is maintained in the reoriented hydride. As described in Chapter 3.5, the d-spacings

of the δ-hydrides and α-zirconium obtained by high energy X-ray diffraction are shown in Table 3-2.

Table 3-2 d-spacing data of both α-Zirconium and δ-hydrides at room temperature

	d-spacing [Å]
Zirconium α(002)	2.5859
In-plane (circumferential) hydrides δ{111}	2.763
Out-of-plane (radial) hydrides δ{111}	2.759

By using the d-spacings as shown in Table 3-2, Equation (3.5) indicates that the dilatational transformation strains at room temperature in the orientation normal to the hydride platelet are

e_1^T = 0.0685 for circumferential hydrides and

e_1^T = 0.0669 for radial hydrides.

These room temperature values, which are obtained by the X-ray diffraction experiments, are similar to Carpenter's value (0.072) but smaller than the e_1^T = 0.077 which was estimated at 300°C by Singh et al. based on the lattice parameters of stress-free pure α-zirconium single crystal. However, the lattice parameters of CWSR Zircaloy-4 alloy differ from those of pure α zirconium because of cold-work and because of the presence of alloying elements. Importantly, the d-spacing of δ-$(2\bar{2}0)$ was not fittable because of its low intensity and convolution with α-zirconium peak. So, the minor transformation strain could not be calculated.

3.5.2 Transformation strain calculation by atomic radii method at room temperature

The room temperature slope calculation $d\sigma_{th}/d\sigma_1$ based on Carpenter's calculations under hard sphere assumption at room temperature and Barrow's TEM results of Zircaloy-2 may not be accurate for the present study in which precipitation occurs at elevated temperatures. A study

performed by Singh et. al. does provide transformation strain estimates at the hydride precipitation temperature, which should be a better representation of our study than the room temperature estimations.

The Singh model calculations are based on the hydride platelet having an orientation relationship along its face of {111}//(002). While this orientation relationship (and indeed the platelet morphology) may be valid for the intergranular circumferential hydrides only. In addition, the Singh et al. values may not accurately represent the hydrided CWSR polycrystalline Zircaloy-4 alloy, since the hydride and zirconium lattice parameters do not match with lattice parameters of the single crystal.

In addition to calculating the e_1^T transformation strain directly from the d-spacings of δ-{111} hydride and α-(002) zirconium, the e_1^T and $e_2^T = e_3^T$ transformation strains can also be calculated by using the atomic radii under the hard sphere assumption, following Carpenter's and Singh's studies. The transformation strains are calculated by determining the atomic radii of α-zirconium on the a-axis and c-axis. The transformation strain estimation along the c-axis gives e_1^T and the transformation strain estimation along the a-axis results in e_2^T. In the hard sphere assumption, α-zirconium atoms, having HCP lattice structure, are modeled as ellipsoids because of the c/a ratio (<1.633).

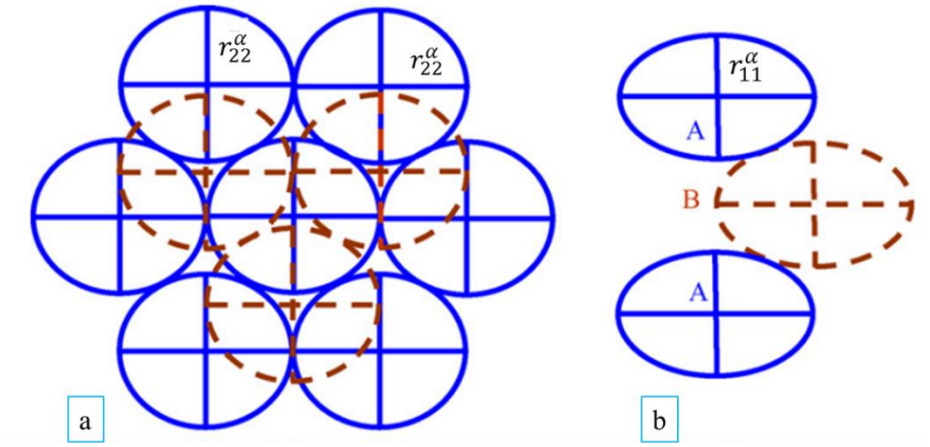

Figure 3-12 Singh's illustration of packing sequence of α-zirconium [140] (a) Basal plane (002) view (b) Prismatic (100) plane view, $\mathbf{r_{11}}$ represents the radius along the closed-packed direction and $\mathbf{r_{22}}$ represents the radius perpendicular to the closed-packed direction. (Illustration was modified)

The atomic radii of the zirconium atoms for directions may then be written as $r_{11} = \sqrt{3/32}\, c^{\alpha-Zr}$ and $r_{22} = a^{\alpha-Zr}/2$, where, c and a are the lattice parameters of the α-zirconium. The lattice parameters of α-zirconium are obtained from in situ X-ray experiments, and for such a calculation, the experimentally obtained d-spacings of α-(002), α-{100,} and δ-{111} in Table 3-3 are used.

Table 3-3 The calculated values of lattice parameters and atomic radii of hydride and zirconium phases. Calculations were based on experimental values of d-spacings

Lattice Parameters [Å]	In-plane hydrides	Out-of-plane hydrides
a of α-zirconium	3.2304	3.2307
c of α-zirconium	5.1718	5.1718
a of δ-hydrides	4.7857	4.7787
r^{δ}	1.6920	1.6895
r_{11}^{α}	1.6152	1.6154
r_{22}^{α}	1.5835	1.5835

For the zirconium atoms within the cubic (FCC) δ-hydrides, a hard-sphere modeling of the atoms means that the atom radius is 1/4 of the face diagonal. It then follows that the atomic radii of the zirconium atoms within the hydrides may be expressed as $r^{\delta} = a^{\delta}\sqrt{2}/4$, where a^{δ} is the lattice parameter of the δ-hydride. The transformation strains and the volume change can be written as [40, 140]:

$$e_1^T = \frac{r^{\delta} - r_{11}^{\alpha}}{r_{11}^{\alpha}} \tag{3.7}$$

$$e_2^T = e_3^T = \frac{r^{\delta} - r_{22}^{\alpha}}{r_{22}^{\alpha}} \tag{3.8}$$

$$\frac{\Delta V}{V} = \frac{\left(V_{hyd} - V_{Zr}\right)}{V_{Zr}} = \frac{(r^{\delta})^3 - (r_{22})^2 r_{11}}{(r_{22})^2 r_{11}} \tag{3.9}$$

Based on the experimentally obtained d-spacings of α-zirconium (002) and δ-hydride {100} in Table 3-2, Equations (3.7) and (3.8) predict the transformation strains to be as follows:

e_1^T = 0.0685 and $e_2^T = e_3^T$ =0.0475 for the circumferential hydrides

and e_1^T = 0.0669 and $e_2^T = e_3^T$= 0.0459 for the radial hydrides.

These results show identical e_1^T-values (e_1^T = 0.0685 for circumferential hydrides and e_1^T = 0.0669 for radial hydrides) calculated from either the atomic radii method or directly from the experimentally determined d-spacings in Table 3-1. Such agreement supports the ellipsoidal assumption for the zirconium atom radii utilized by Carpenter [40] and Singh [140]. Moreover,

the volume change as shown in Equation (B-4) for circumferential hydrides is also calculated as 17.25%, which is similar to that determined by Carpenter as 17.20% [40]. Finally, the small differences in e_i^T-values between the circumferential and radial hydrides may be due to experimental error.

If the transformation strains thus calculated are inserted into Equation 3.4, it is found that the dependence of the threshold stress on the minor stress in Figure 3-11 is $d\sigma_{th}/d\sigma_1 = -0.83$ for circumferential hydrides and $d\sigma_{th}/d\sigma_1 = -0.83$ for radial hydrides. Both values are similar to each other and consistent with the slope $d\sigma_{th}/d\sigma_1 \approx -0.84$ obtained from the linear fitting of the experimental results in Figure 3-11.

3.6 Variation of transformation strains with temperature and transformation strain predictions at hydride precipitation temperature

The transformation or misfit strains calculated above are based on lattice spacing data that are determined at room temperature. However, hydride precipitation occurs at elevated temperatures with the onset of precipitation occurring at approx. 310-320°C for a hydrogen content of ~ 180 wt. ppm. As described in Chapter 4, in situ X-ray diffraction experiments can be used to determine the d-spacings of α-zirconium and δ-hydrides as a function of temperature during hydride precipitation at elevated temperatures. The data are based on samples subjected to three to five thermo-mechanical cycles designed to simulate the vacuum-drying of cladding tubes as described in Chapter 4.

The samples were oriented such that the transverse (TD) and rolling (RD) directions of the sample were perpendicular to the in-coming X-ray beam. At the beginning of the thermo-mechanical treatments, the macroscopic hydride platelet faces in the RT plane (normal to the N direction and therefore perpendicular to the incident beam) and has the characteristic “in-plane”

hydride microstructure. Because of this orientation of the in-plane hydride platelets the diffraction geometry did not allow to obtain diffraction patterns from δ-{111} planes parallel to the hydride platelet faces. As a result the dilatational transformation strains for circumferential hydrides were not calculated. After hydride reorientation, it is possible to regard the macroscopic hydride platelet faces as being normal to the transverse direction. This allowed the dilatational transformation strain to be calculated for reoriented hydride macroscopic "platelets", again if one considers the hydrides in Figure 3.3 to be a single platelet instead of a jumble of smaller hydrides.

Figure 3-13 depicts the evolution of the radial hydride transformation strain components both normal to the apparent face of the hydride (Figure 3-12a) and to the apparent edge of the hydride (Figure 3-12b) for the 2nd cycle cool-down and 3rd cycle heat-up. During 2nd cycle cool-down, a tensile stress of 150 MPa was applied at 375°C while the hydrogen was still in solid solution. Radial hydride precipitation initiated at approximately 320°C, and continued as the temperature continued to decrease down to 150°C. The transformation strains increase with decreasing temperature at a rate of about -12 10^{-6}/°C for e_1^T and -5 10^{-6}/°C for e_2^T. At the onset of precipitation, transformation strains are $e_1^T \approx 0.063$ and $e_2^T \approx 0.043$. As temperature decreases to 150°C, the transformation strains increased to $e_1^T \approx 0.065$ and $e_2^T \approx 0.044$. The extrapolation of the data in Figure 3-12a to room temperature predicts $e_1^T \approx 0.067$, which is identical to the value (0.0669) calculated earlier from the data in Table 3.1. The extrapolated room temperature value of $e_2^T \approx 0.045$ is close to the transformation strain component calculated earlier for hydrides at room temperature ($e_2^T \approx 0.046$). The data in Figure 3-12a indicates that there was no change in the transformation strain value of e_1^T after the removal of the tensile stress at 150°C. It is possible to understand this behavior occurs if it is assumed that the radial hydride is a platelet in which the α-(002) and hydride δ-{111} planes were subjected to similar strains owing to their similar elastic moduli at 25°C (Zircaloy-4, 104 GPa [80] and 110-120 GPa for hydrides [74]). However, the e_2^T decreased from 0.044 to 0.043 after stress removal.

The decrease in the value of e_2^T upon the removal of the load in Figure 3-12b is puzzling. The degree of elastic anisotropy is sufficiently small in Zircaloy-4 [82] such that the same behavior observed in Figure 3-13a would also be expected in Figure 3-13b. At this time, this difference between the two behaviors upon load removal (i.e., Figure 3-13a vs. Figure 3-13b) is not understood. Maybe this different behavior is related to the effect of the minor strain on precipitation.

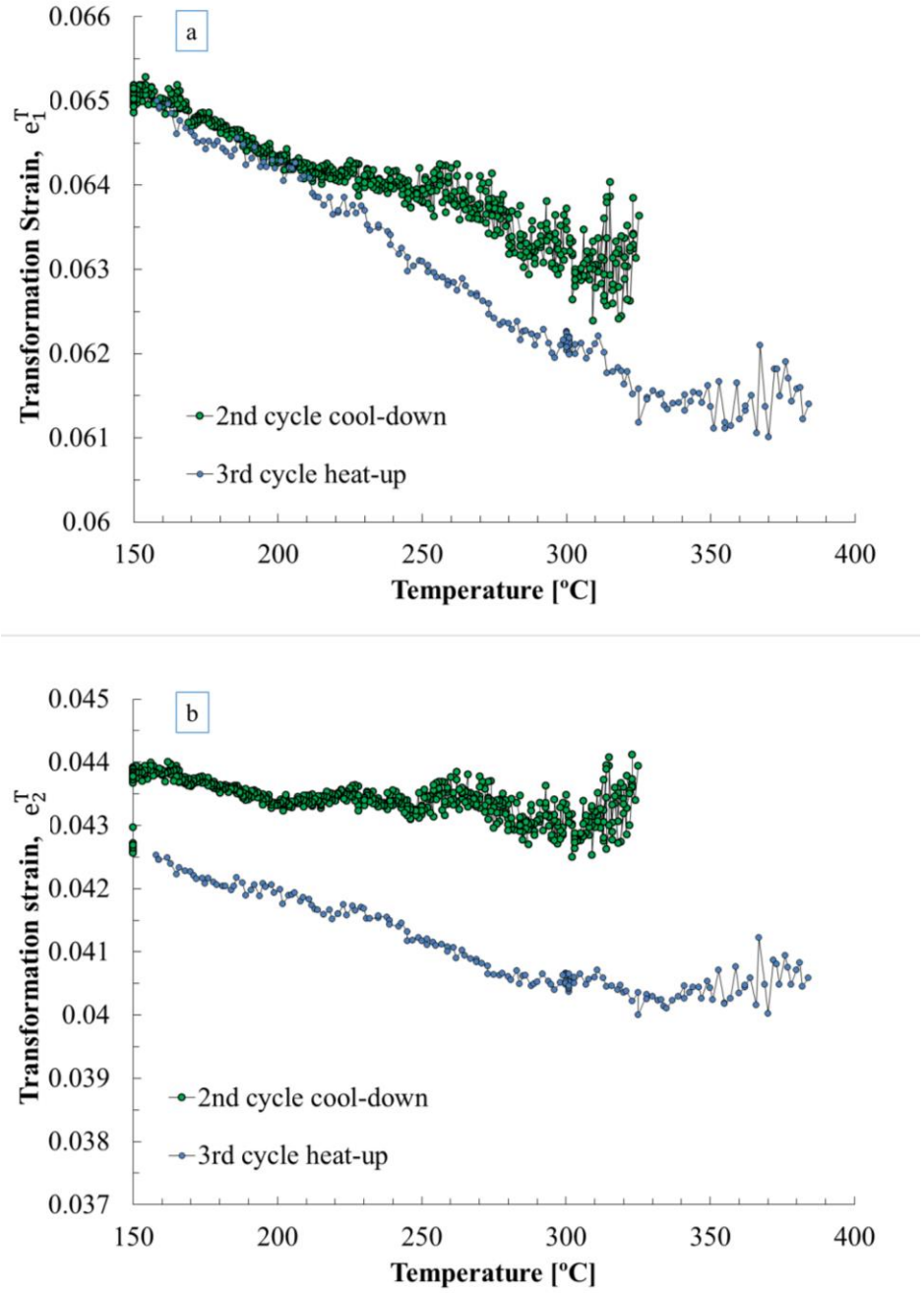

Figure 3-13 (a) The evolution of dilatational transformation strain, $\boldsymbol{\varepsilon_1^T}$, (strain normal to δ-{111}//α-(002) for radial hydrides) during dissolution and precipitation of "radial" hydrides. (b) The evolution of second transformation strain, $\boldsymbol{\varepsilon_2^T}$, (strain parallel to δ-{111}//α-(002) for radial hydrides). The sample was 5-cycle thermo-mechanically treated. For the 2nd and 3rd cycle heat-ups, no tensile stress applied. For the 2nd cycle cool-down tensile stress of 150MPa is applied to the sample. During 2nd cycle heat-up, circumferential hydrides are present. For the 2nd cycle cool-down and 3rd cycle heat-up, only radial hydrides are present.

For the 3rd cycle heat-up, the transformation strain of e_1^T decreased from 0.065 to 0.0615 in a linear manner as temperature increased from 150 °C to 320 °C with a rate of -15 10^{-6} /°C again. For temperatures above 320°C up to the dissolution temperature of 390 °C, the transformation strain (0.0615) varies less. Also, similar behavior was obtained for the transformation strain of e_1^T that decreased from 0.044 to 0.041 in a linear manner as temperature increased from 150 to 320°C with a rate of about -14 10^{-6} /°C.

The increase in transformation strains with decreasing temperatures as the hydrides precipitate and grow may be qualitatively understood by recognizing the implications of the stress state within the plate-like hydrides as they cool. As will be discussed in detail in the diffraction section of this thesis, because of their shape and structure, the hydrides experience a state of hydrostatic compression such that the in-plane stresses exceed that stress normal to the face plane of the hydride [39, 86]. Furthermore, the extent to which the in-plane stresses exceed the stress normal to the hydride-face plane depends on the difference between the yield stresses of the hydride as compared to that of the matrix; and that difference depends on temperature. As the hydrides become harder with decreasing temperature i.e, the $d\sigma_y/dT$ as the temperature decreases is bigger for the hydride than the matrix, the analysis predicts that increasing in-plane stresses within the hydride cause an increase of e_1^T with decreasing temperature, and that behavior is observed in Figure 3-13b. Conversely, the Singh et al. analysis shows that upon precipitate dissolution, a stress reversal (compressive to tensile) occurs near the edge of the hydride platelet such that local tension within the matrix enhances the decrease of e_1^T with increasing temperature for the dissolving precipitates [86]; this effect contributes to the more rapid decrease of e_1^T with temperature upon heating. Thus, de_1^T/dT= -12 x 10^{-6} /°C on cooling/precipitation, but de_1^T/dT = -21 x 10^{-6} /°C upon heating/dissolution.

The effect of the minor principal stress can be predicted from classical nucleation theory based on the balance of the Gibbs free energies and the effect of far-field stresses in assisting hydride precipitation. The sensitivity of the threshold stress to the minor stress (i.e., $d\sigma_{th}/d\sigma_2$) depends on the magnitudes of the transformation strain components for radial hydride precipitation. If it is assumed that the reoriented hydrides are single platelets normal to the stress (TD) then theoretically predicted values of e_1^T and e_2^T from literature yield $d\sigma_{th}/d\sigma_2$ values that are similar to that found experimentally. Further confirmation of that agreement was found by analyzing x-ray diffraction data in the present study to determine directly the values of e_1^T and e_2^T. These values, which are somewhat smaller than those previously determined theoretically, result in predicting that at the onset of radial hydride precipitation, the effect of the minor stress on the threshold stress for radial hydride formation is $d\sigma_{th}/d\sigma_2 = -0.84$ which is identical to the experimentally obtained slope of $d\sigma_{th}/d\sigma_2 = -0.84$.

3.7 The Effect of Radial Hydrides on Failure Processes of Zircaloy-4

This section describes the effect of radial hydrides on the failure of the Zircaloy-4 in terms of the ductile-to-brittle transition temperature (DBTT) and its associated causes. An understanding of the failure mechanisms of the present unirradiated Zircaloy-4 material containing radial hydrides should relate to the potential failure of irradiated cladding material during dry-cask storage and cask transportation conditions. In addition, a micromechanical understanding can also help the future development of predictive modeling of failure conditions during cask transportation.

3.7.1 Failure Processes with the Existence of Radial Hydrides

Uniaxial dog-bone unirradiated Zircaloy-4 sheet samples hydrided to levels from 150 to 252 wt. ppm and with different degrees of radial hydrides (0<RHF<0.8) were tested at different temperatures and the ductility (as measured by the total elongation in the gauge section) measured. Figure 3-14 shows the total ductility, as measured by the total elongation in the gauge section at failure as a function of temperature for dog-bone samples such as shown in Figure 2-13, and for samples that had been hydrided to 180 wt. ppm for various values of the RHF. As the RHF increases the cladding mechanical behavior degrades. This is reflected as the ductile-to-brittle transition temperature (DBTT) increase, as shown in Figure 3-14. For instance, samples with only circumferential hydrides are ductile at room temperature. However, when the radial hydride fraction is greater than 0.8, the hydrided Zircaloy-4 is brittle at room temperature, and the ductile to brittle transition temperature increases to 125°C.

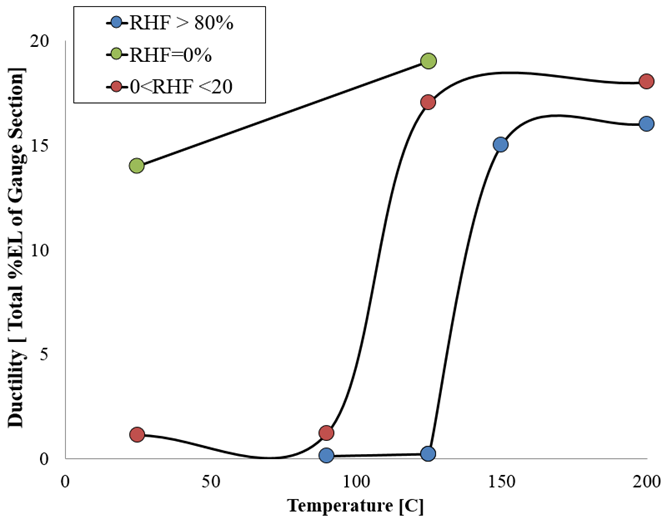

Figure 3-14 The ductile to brittle transition behavior of Zircaloy-4 (RHF represents the radial hydride fraction). Hydrogen concentrations vary from 23 to 170 wt. ppm for samples with no radial hydrides, 160 to 226 wt. ppm for samples with RHF>80%, and184 to 252 wt. ppm for samples with RHF<20%.

At temperatures above the DBTT, ductile fracture of hydrided cladding material can be understood in terms of damage accumulation near hydrides. In the case of cladding with only circumferential hydrides or with a low radial hydride fraction, the process of damage accumulation occurs as follows: voids are initiated at hydrides (often after considerable plastic strain), strain-induced void growth/linking develops, and finally specimen rupture occurs as a result of void coalescence [8]. This type of damage accumulation results in ductile behavior if the cladding is above its ductile to brittle transition temperature as shown in Figure 3-15.

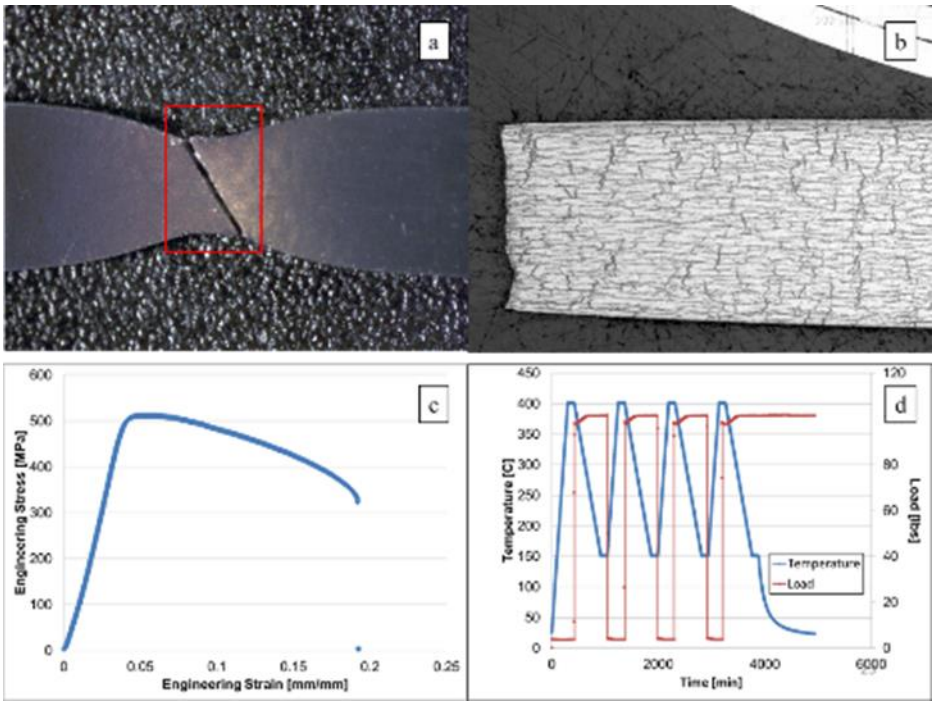

Figure 3-15 (a) The ductile fracture behavior of a sample with 252 wt. ppm of hydrogen and RHF of 0.13 and tested at 125°C. (b) Hydride microstructure of the sample near the fracture surface. (c) Engineering stress and strain curve of this sample showing ductile failure. (d) The 4-cycle radial hydride treatment which creates mixed circumferential and radial hydride microstructure prior to mechanical testing of the sample. Since the terminal solid solubility at the maximum temperature of 400°C is 180 wt. ppm, the hydrides were not completely dissolved during treatment.

The fracture process changes below or near the DBTT when radial hydrides are present. At temperatures just above the DBTT, although radial hydrides can induce cracks at low strains

even though the matrix surrounding the hydride is still ductile (as shown in Figure 3-16), measurable ductility at failure can still be observed in the material.

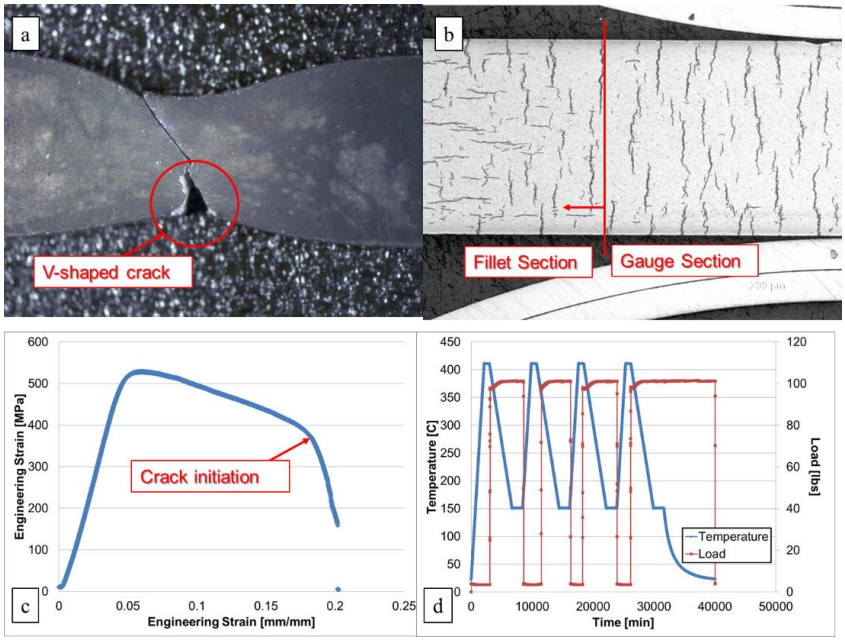

Figure 3-16 The fracture behavior of a sample with 160 wt. ppm of hydrogen and RHF of 1 and tested at 150°C. (b) Radial hydride microstructure near the fracture surface. (c) Engineering stress and strain curve of the sample showing ductile behavior, although the sample failed at low strain. (d) The 4-cycle radial hydride treatment that created the radial hydride microstructure.

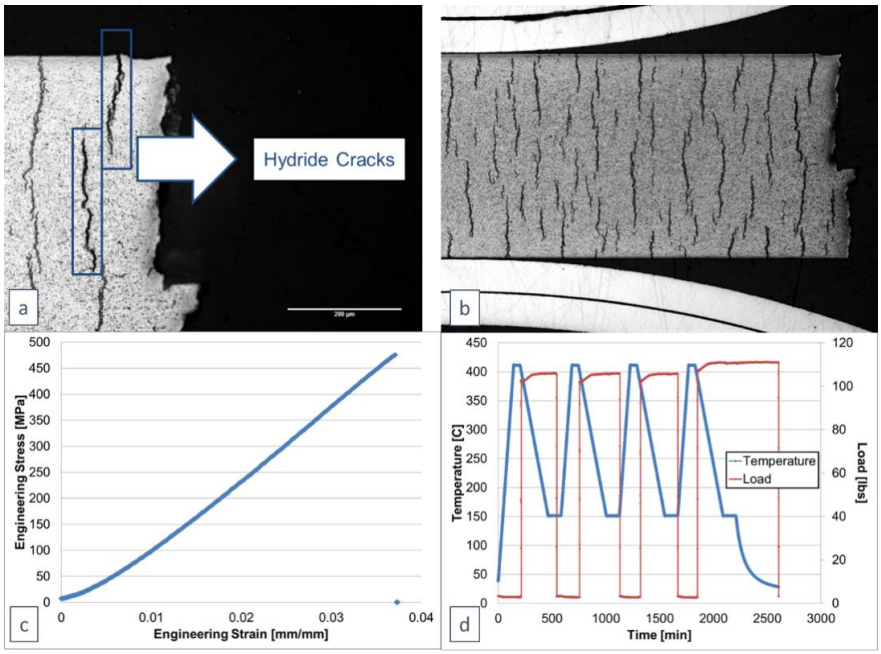

Figure 3-17 (a) The fracture behavior of a sample with 162 wt. ppm of hydrogen, a RHF of 1.0, and tested at 125°C. (b) Radial hydride microstructure near the fracture surface. (c) Engineering stress and strain curve of the sample showing "brittle-like" failure (before yielding), and (d) The 4-cycle radial hydride treatment that created the radial hydride microstructure.

In contrast, as shown in Figure 3-17, a specimen with 80% radial hydrides tested at 125°C (below DBTT for the given hydrogen content) failed in a "brittle manner". Fracture now occurs due to crack initiation and crack growth with little macroscopic ductility; the stress-strain response in Figure 3-11c indicates brittle behavior, i.e. failure before yielding.

The micro-mechanisms of the fracture of Zircaloy-4 with radial hydrides at temperatures near the ductile to brittle temperature are as follows:

- First, radial hydrides induce cracks at small strains either in the interior or at the hydride-matrix interface. This crack initiation process is controlled by strain incompatibility between the surrounding deforming matrix and the non-deforming radial hydrides as shown in Figure 3-18a, c and, d.

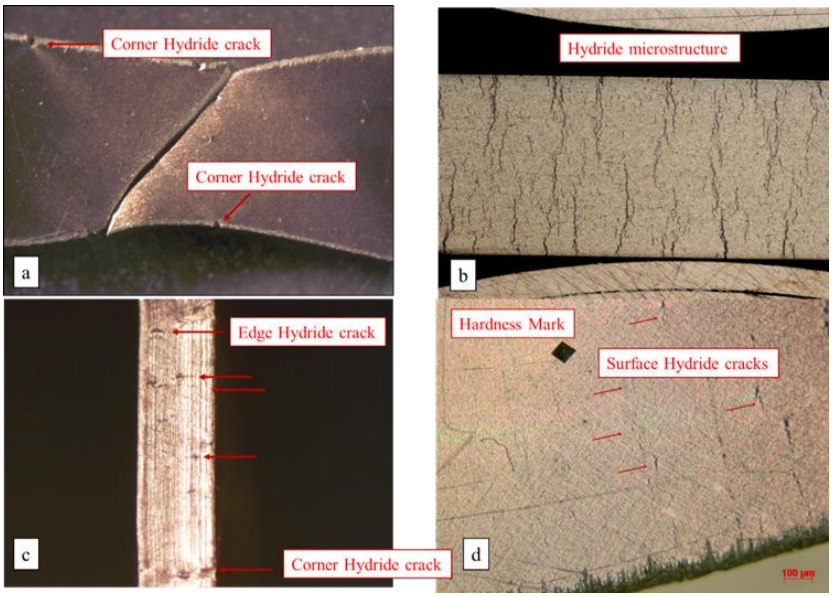

Figure 3-18 (a, b and, c) The radial hydride crack initiations of a sample with 160 wt. ppm of H and RHF=0.9 but the sample failed in a ductile manner at 125°C. (b)Hydride micro structure of the sample that was 1-cycle treated with cooling rate of 12.5°C/min.

Once the crack initiates, two processes are possible:

- While radial hydrides induce cracks at low strains, the cracks may arrest such that unstable crack propagation does not occur; as a result, the specimen exhibits measurable ductility, such as shown in Figure 3-16a. Upon further straining of the material, the cracks blunt and the cladding fails in a ductile manner by a process of void initiation, growth/linking, and coalescence.
- The second possibility is that not only do cracks initiate but also unstable crack growth occurs following a crack path through the population of radial hydrides as governed by the associated radial hydride connectivity. As a result, the crack propagates rapidly along the radial hydride network in the cladding, and the cladding fails in a brittle manner, as shown in Figure 3-17a. This type of process results in low value of the fracture toughness in cladding with extensively reoriented hydrides and a high degree of associated radial hydride connectivity.

The failure process of cladding containing radial hydrides and deformed over a wide range of temperatures can be understood as follows [8]:

$$\epsilon_f = (\epsilon_1)_{ci} + (\epsilon_1)_{cp} \tag{3.10}$$

where ϵ_f is the fracture strain, $(\epsilon_1)_{ci}$ is the major principal strain for crack initiation, and $(\epsilon_1)_{cp}$ is the major principal strain for crack propagation.

At temperatures well above the DBTT, $(\epsilon_1)_{ci}$ is high, because the hydrides themselves become ductile and resist crack initiation, and the crack initiation strain exceeds the strain for ductile failure due to global damage accumulation or localized necking, causing the cladding to be ductile. However, if the crack initiation strain is less than the strain for ductile fracture, crack initiation occurs. If the crack has sufficient stress intensity to propagate (either due to its long length or because of small fracture toughness of the matrix with radial hydrides), the cladding fails in a "brittle manner", resulting in low ductility as seen in Figure 3-17 and failure behavior consistent with temperatures below DBTT.

The fracture toughness of the matrix is a direct function of the temperature, and of the orientation, and connectivity of the hydrides (in-plane and out-of-plane) present. The difference between the behavior of the material at 40°C with 20% and 80% RHF shows that in this case it is the crack *propagation* rather than crack initiation that causes brittle failure in one case and not in the other. This "brittle-like" behavior can be analyzed using linear elastic fracture mechanics and determining the initial crack sizes and the shapes, as shown in the following section.

3.7.2 Fracture Mechanics Analysis of the "Brittle-like" Failure of the Zircaloy-4 in the Presence of Radial Hydrides

Linear elastic fracture mechanics may be used to analyze the failure response of the brittle specimens [94]. Given the nearly linear elastic load-displacement responses observed for brittle material, linear elastic fracture mechanics can be used. In this approach, the stress intensity factor, *K*, is a measure of the stress field near the crack tip caused by the remote stresses acting on a loaded member. For a mode I crack normal to the far-field stress, the stress intensity factor, *K*, is a function of crack geometry, applied stress, and the crack length. The stress intensity factor can be calculated as follows:

$$K = F\sigma\sqrt{\pi a} \tag{3.11}$$

where F is a factor which depends on crack geometry, σ is the applied remote stress normal to the crack, and a is the crack length. When the stress intensity factor K_I reaches the critical fracture toughness, K_{IC}, the sample fails in a macroscopically brittle manner due to unstable crack growth [94].

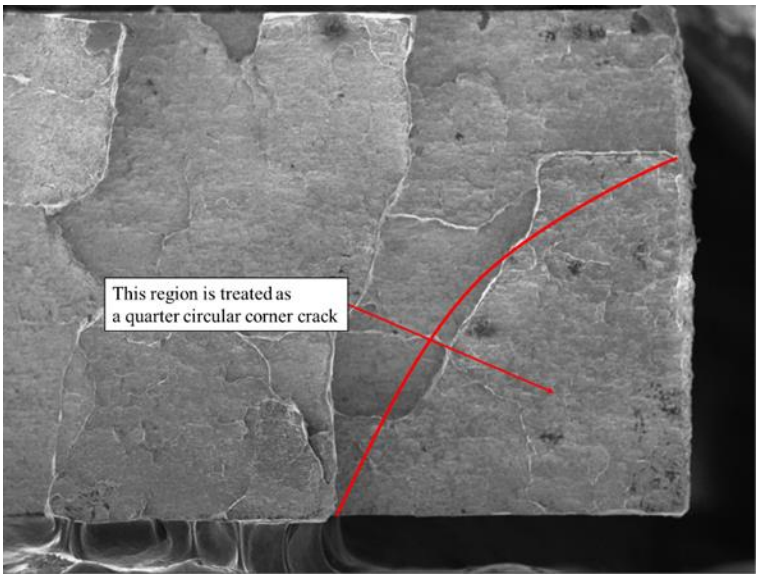

Figure 3-19 Fracture surface of a specimen that has been analyzed using linear elastic fracture mechanics. Fractography suggests crack initiation in the form of a quarter circular corner crack as shown.

For the case of a mode I crack propagating at room temperature through hydride microstructures with varying hydride orientations, Raynaud et al. [101] showed that the fracture toughness of Zircaloy-4 sheet decreases with increasing hydrogen content and with increasing radial hydride fraction. They reported that the fracture toughness of the cladding material with pre-crack that was formed decreased from about 40-50MPa√m to 10-20MPa√m in the presence of radial hydrides, when tested at 25°C.

In the present study, the fracture surfaces of specimens that failed when tested below the DBTT (such as shown in Figure 3-18) were analyzed for fractographic evidence of an initial crack. Based on that crack shape and length as well as the load at failure, the data in Table 3-4 compares the values of the stress intensity factors at failure with the reported fracture toughness values for Zircaloy-4 with radial hydrides; see Raynaud et al. [101]. Importantly, Table 3-4 indicates that in each case the calculated stress intensity values for the cracks were anticipated from SEM fractographs as shown in Figure 3-19 exceed the fracture toughness values reported by Raynaud et al. for the case of radial hydrides. This situation indicates that the creation of the initial crack is

sufficient to cause its rapid propagation and the brittle failure of the specimen for samples listed in Table 3-4. Furthermore, as seen in Table 3-4, the initial crack size inferred from the fracture surface analysis is similar in scale to the largest of the radial hydrides observed. This comparison strongly suggests that the initial crack created at a large radial hydride may indeed be fatal to the material.

Table 3-4 Stress intensities of three brittle specimens based on an initial flaw size interpreted from an examination of the fracture surface

Sample	Hydrogen [wt. ppm]	Radial Hydride Fraction [%]	Test Temp [ºC]	Max. Hydride Length [mm]	Initial Crack Length [mm]	Crack Type	Shape Factors	Stress Intensity [MPa√m]	Fracture Toughness [101] [MPa√m]	%EL
#1	172	60	125	0.23	0.26	Quarter Elliptical Crack	0.99	14	15	0.2
#2	187	85	125	0.40	0.29	Edge Crack	1.23	19	12.5	0.2
#3	173	90	90	0.40	0.56	Quarter Circular Crack	1.00	20	10	0.1

[1]Note that the shape factors in Equation (3.11) for the corner cracks are based on an analysis by Kiciak et al. [143] and the listed shape factors involves the correction from crack shapes. Please see the shape function calculations for relevant crack geometries in the Appendix

3.7.3 Comments on Radial Hydride Connectivity and Fracture Surface

In the previous section, "brittle-like" fracture induced by radial hydrides has been proposed as the result of propagation of a crack the along radial hydride precipitates that likely form micro-

cracks ahead of the main crack. The resulting crack growth generates a non-planar fracture surface as the crack path follows the existing connectivity between radial hydrides. To understand how this non-planar fracture surface is formed during failure, the topography of the fracture surface was characterized by optical profilometry (as discussed in Chapter 2.6) in terms of average facet sizes and height difference between adjacent facets.

The fracture surface of a brittle specimen was examined in order to characterize the topography formed during fracture at 90°C in the Zircaloy-4 specimen with nearly 100% reoriented hydrides. Figure 3-20a shows the fracture surface obtained by optical profilometry. To verify the technique, a specific area of that fracture surface, as shown in Figure 3-20a, is matched to the SEM image of that area as which is shown in Figure 3-20b.

In this procedure, the length of a facet and elevation between two adjacent facets can be determined. Figure 3-20c shows the facet profile corresponding to the scanning path shown in Figure 3-20a. In this case, the maximum height difference between two adjacent facets is about 150 μm. This difference is probably related the distance separating two long radial hydride facets along which the crack propagates during fracture. Also evident in Figure 3-20c is the abrupt change in elevation between neighboring sections of the fracture path. There is no inclined path between two adjacent facets for this brittle specimen; rather, the fracture surface consists of a mesa and cliff topography. Further, regions that appear as single facets are in fact comprised of several smaller facets with similar elevations, if examined at higher magnifications. For example in Figure 3-20b, there appears to be a large facet from 400 to 1200 μm which in fact is formed by four sub-facets (each is approximately 100-150 μm), each about 20 μm apart in elevation. These facet sizes are similar to the macroscopic hydride particles which consist of collection of smaller size hydride platelets. Thus, smaller size cracks (sub facets) initiated and linked at/in the hydride platelets form macro cracks which finally grow and form the non-planar or tortuous fracture surface. Taken as a whole, Figure 3-20 indicates a tortuous fracture path formed by the crack as it propagates through

the specimen. The formation of a tortuous fracture path with abrupt inclinations, such as shown in Figure 3-20c, is a result of cracking along radial hydrides (forming the "mesas") and very likely the linking of the radial hydride facets by the circumferential hydrides (forming the "cliffs").

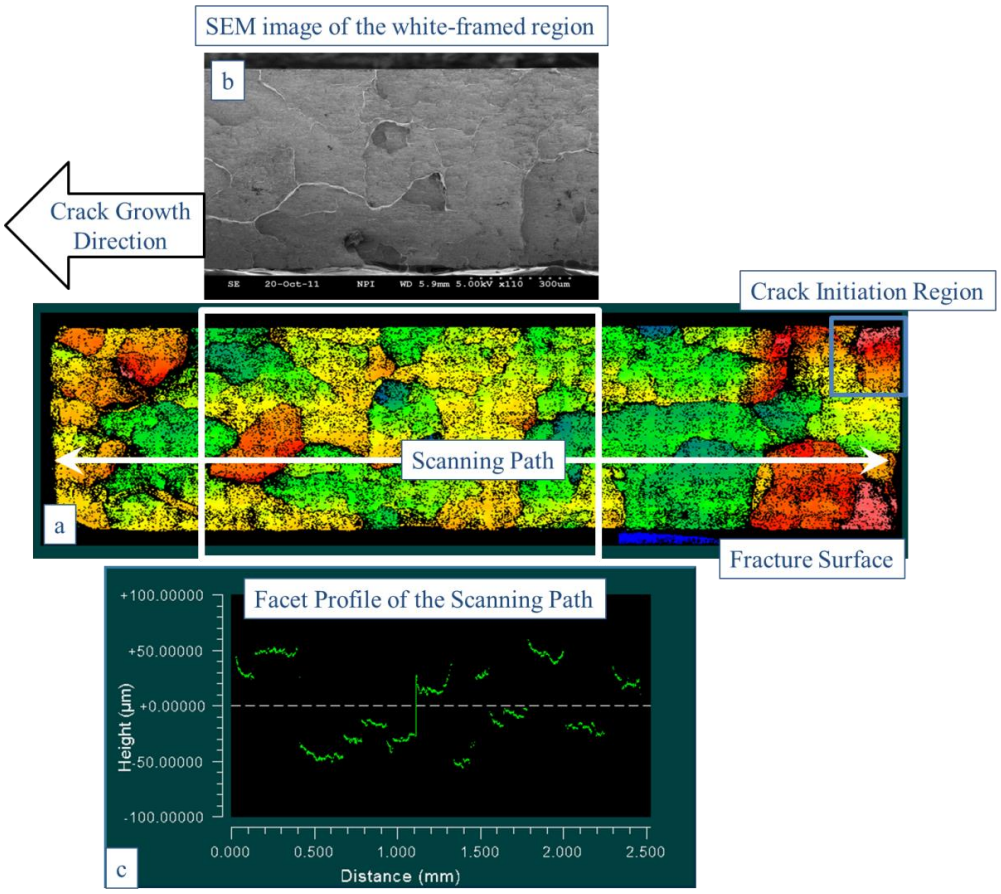

Figure 3-20 Fracture surface topography of uniaxial tensile specimen with 170 wt. ppm and 100% reoriented hydrides at 90^0C (a) the fracture surface topography,(b) scanning electron micrograph image of the white-framed region (c) facet profile of the specimen on the scanning path.

The combination of the radial and circumferential hydrides forming a crack path and including failure has been suggested by M. Billone who defines a metric called radial hydride continuity factor (RHCF) to address this issue [18]. The RHCF is the ratio of the maximum length of the continuous radial and circumferential hydrides in a 150 µm-segment of the cladding divided by the

thickness of the cladding, it can be directly related to the failure behavior of the cladding; Billone showed that as RHCF increases, the DBTT of the cladding increases for the ring compression tested samples [18]. The increase in DBTT with increasing RHCF is likely related to the increased ease of crack propagation after crack initiation. Thus, the cladding can fail in a brittle-like manner as a result of low fracture toughness. A good example of the applicability of the RHCF is shown in Figure 3-17b. For that sample RHCF = 1, and the sample exhibits brittle-like failure as a result of unstable crack propagation after crack initiation.

The RHCF parameter, while a powerful metric to predict the DBTT shift, has limitations. For the sample tested at 125°C and shown in Figure 3-18b, the RHCF can be calculated as close to 1; but the actual hydride microstructure is three-dimensional, and the three-dimensional RHCF may not be necessarily close to 1. This yields that the sample in Figure 3-18b fails in a ductile manner even though many small hydride cracks are formed at the specimen surfaces during deformation. Figure 3-21 illustrates the three dimensional hydride microstructure that has RHCF of 1 when characterized at the TD-ND plane such as the sample shown in Figure 3-18c. According to the Figure 3-21a, even cracks are formed due to the radial hydrides, the three dimensional hydride structure does not permit crack propagation through the ND-RD plane as shown in Figure 3-21b. Thus, Figure 3-18a, c, and, d indicates that that micro-cracks form at radial hydrides but not at locations that have deformed to a significant level of plastic strain. These short cracks could not form a single macro crack to propagate and ductile behavior of the specimen occurs. Thus, the crack initiation by the radial hydrides at small strains appears to be a condition for brittle behavior.

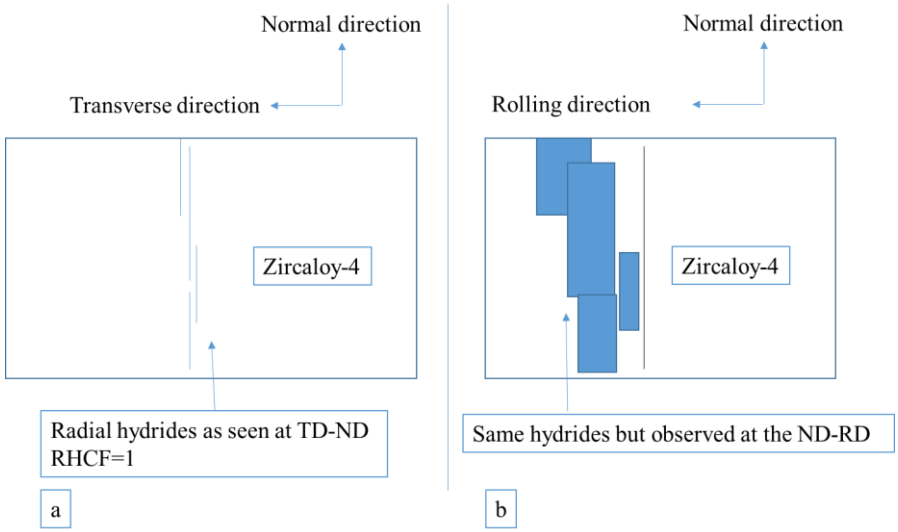

Figure 3-21 Cartoon showing the hydride microstructure (a) that has RHCF of 1 when observed by optical microscope at TD-ND plane as same as Figure 3-18c (b) illustration of the cross sectional view at the ND-RD plane of the same hydride microstructure having RHCF of 1 in (a).

3.7.4 Summary of the Mechanical Behavior Section

If the temperature is sufficiently low for hydrides to initiate cracks, the presence of the radial hydrides and their connectivity with the circumferential hydrides directly affects the fracture toughness of the cladding and in so doing, determines the DBTT. At high radial hydride fractions, the resulting high degree of connectivity can cause the DBTT to increase up to 125°C in this study and to 200°C for high burn-up fuel rods [18]. In contrast, a low radial hydride population and a low degree of hydride connectivity may result in ductile failure of the cladding even at room temperature where radial hydrides can initiate cracks at small strains.

The failure behavior of brittle specimens can be analyzed using linear elastic fracture mechanics based on an initial flaw size determined from careful analysis of the fracture surface. The application of fracture mechanics formulations to determine the critical stress intensity of the initial crack shows stress intensity values that exceed the fracture toughness of the cladding for its radial hydride population and their connectivity. As a result, the sample exhibits unstable crack

propagation after crack initiation, and brittle behavior results. A sample with high radial hydride continuity factor RHCF should have low fracture toughness, resulting a brittle-like failure behavior at elevated temperatures which also results in increase in DBTT. Thus, the presence of radial hydrides and their degree of connectivity can directly affect the cladding mechanical response.

4 HYDRIDE REORIENTATION EXPERIMENTS BY SYNCROTHRON RADIATION

This chapter describes the high energy X-ray diffraction study of the radial hydride precipitation behavior as a result of thermo-mechanical treatments. In order to understand radial hydride precipitation during cooling under tensile stress, experiments were conducted using synchrotron radiation at the Advanced Photon Source at Argonne National Laboratory. Those experiments were performed in situ to observe the dissolution and precipitation behavior of hydrides during the thermo-mechanical treatments. Several companion experiments were also performed that investigated the behavior of the hydrides under various states of stress when subjected to different thermo-mechanical treatments.

4.1 X-ray diffraction Analysis of the As-received Zircaloy-4

To enable a systematic study of the hydride dissolution and precipitation characteristics, it is essential to fit accurately determine the zirconium and zirconium hydride peak locations in as-received Zircaloy-4 is essential To this end, X-ray diffraction patterns of previously hydrided as-received Zircaloy-4 sheet were acquired at room temperature, using the synchrotron radiation X-ray source, in the geometry shown in Figure 2-9.

The orientation of the incoming X-ray beam direction relative to both the “in-plane” (circumferential) and “out-of-plane" (radial) hydrides is shown in Figure 4-1. The incoming X-ray beam direction is perpendicular to the face of the “in-plane” hydride platelets and parallel to the face of the “out-of-plane” hydrides. The “out-of-plane” and “in-plane” hydrides in sheet material

are respectively equivalent to radial and circumferential hydrides in tubular samples, respectively, as stated previously.

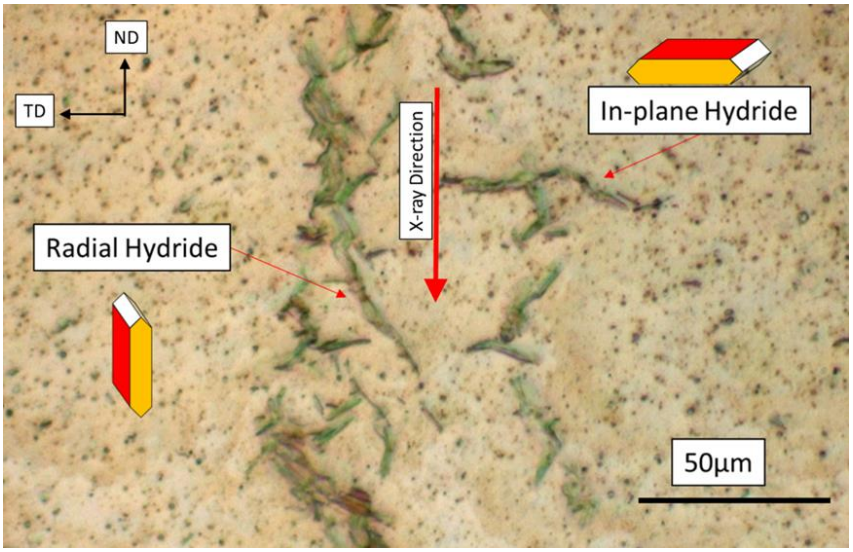

Figure 4-1 In-plane and out-of-plane (radial) hydride microstructures taken on T-N plane and schematics of hydride precipitate orientations relative to the orientation of the X-ray beam. X-ray beam hits the sample on the N-R plane

As stated previously, in the absence of stress, macroscopic hydrides precipitate circumferentially [105, 125]. When cooling down under a sufficiently high applied stress, hydrides will precipitate with a macroscopic orientation perpendicular to the applied stress [105, 125]. The verification of "radial" or out-of-plane macroscopic hydride precipitation under stress is done by low magnification metallographic examination at low temperature (after cooldown).

Figure 4-2 shows a typical diffraction pattern of as-fabricated Zircaloy-4 in CWSR condition after hydriding treatment (180 wt. ppm hydrogen). The X-ray diffraction pattern shown in Figure 4-2 is integrated all around the circumference of the diffraction ring, the chi angle from 0 to 360°, as illustrated in Figure 2-10.

Both α-zirconium and δ-hydride peaks are identified in the diffraction pattern in Figure 4-2. A pseudo-Voigt peak shape is used to fit individual each peak using the program Peak Fit [144]. Table 4.1 shows the calculated d-spacings of some α-zirconium and δ-hydride peaks resulting from the pattern in Figure 4-2. The d-spacing values from the α-zirconium and δ-hydride powder diffraction files (the powder diffraction files (PDF #) of 05-0665 and 34-0649) are respectively also shown in Table 4-1. The fitted values show good agreement with the powder diffraction files, the highest difference being in the 4^{th} significant digit. Four δ -hydride peaks fall within the 2θ range studied: {111}, {200}, {220}, and {311}. For specimens with less than 200 wt. ppm of hydrogen, the most distinguishable δ-hydride peak for accurate fitting is the δ-{111} peak which is convoluted with α-{100} peak, as shown in Figure 4-3. Other δ-hydride peaks such as {200} and {220} are smaller and more difficult to de-convolute from the stronger α-zirconium peaks. The intensity of the δ-hydride {311} diffraction peak is low so that this peak is only usable, but only if the hydrogen contents are high. Because of this, only the δ-{111} hydride peak was used to monitor the hydride dissolution and precipitation in this study.

The α-zirconium pattern showing a deviation from the powder diffraction or non-textured patterns of the α-zirconium is consistent with the crystallographic texture induced by the fabrication process, though which the basal planes preferentially align perpendicular to the normal direction (ND), and thus the diffraction signal intensity from these planes is decreases relative to the prism planes (α- {100} and {101}) in the sample orientation used [145].

Table 4-1 An indexing of the diffraction peaks that represent the alpha zirconium matrix and δ zirconium hydride for the diffraction pattern shown in Figure 4-2.

Peaks	d-spacing calculated from the powder diffraction files [Å][145, 146] (PDF# 05-0665 & 34-0649)	d-spacing from fitting of diffraction pattern [Å]	Percent difference from powder diffraction data [%]
α{100}	2.798	2.798	0.0027
α{002}	2.573	2.577	0.1521
α{101}	2.459	2.459	0.0152
α{110}	1.616	1.616	0.0188
δ{111}	2.76	2.759	0.0004

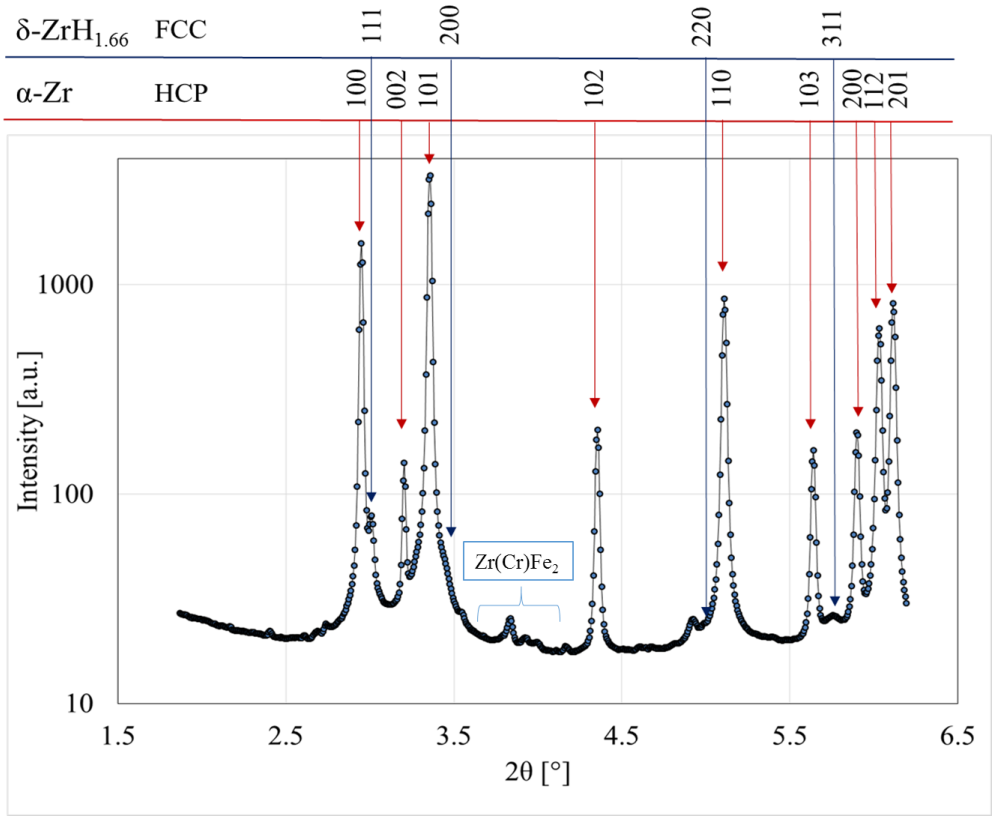

Figure 4-2 Diffraction pattern of hydrided Zircaloy-4 with 180 wt. ppm of hydrogen in the as-received state. The diffraction pattern is integrated over 0-360° in order to determine all zirconium and hydride peaks. $Zr(Cr,Fe)_2$ are second phase particles (SPPs)

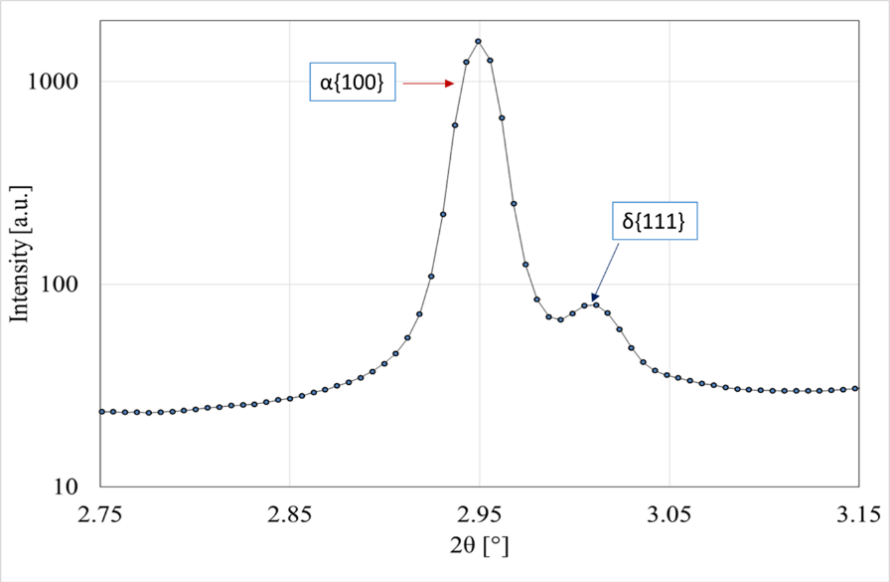

Figure 4-3 Intensity versus two-theta angle, showing the α-Zr {100} peak and the δ-hydride {111} peak which are fitted for the determination of hydride d-spacing.

4.2 Thermo-mechanical Treatments and Determination of Terminal Solid Solubility of Dissolution and Precipitation by X-ray Diffraction

4.2.1 Thermo-mechanical treatments during high energy X-ray diffraction experiments

In order to elucidate hydride precipitation while cooling under hoop tension, previously hydrided Zircaloy-4 samples were subjected to various sequences of thermo-mechanical treatments at various stress levels and at various stress states. Table 4-2 summarizes the temperature and stress histories for the in situ synchrotron radiation experiments conducted, using three different sample geometries, as described in Chapter 2. During the thermo-mechanical treatments, the incoming X-ray beam was diffracted in transmission mode from the samples and the X-ray diffraction data, i.e. the Debye rings, were recorded on an area detector. Using this information, the dissolution and precipitation behavior of hydrides, characterized using the respective X-ray peak intensities was obtained in situ, as done in a previous study [60].

Table 4-2 List of hydrided Zircaloy-4 which were examined during thermo-mechanical treatment by in situ synchrotron X-ray diffraction. For all samples, the maximum temperature during the thermo-mechanical treatments were 450°C, and samples were kept at that temperature for 1 hour.

Test #	Sample Type	H content [wt. ppm]	Thermo-mechanical Treatment	Cooling Rate
1	Plane-Strain Tension	177±5 TSS_d=404°C	3-cycle treatment, No stress was applied during 1st cycle's cool-down. Stress was applied during 2nd and 3rd cycles' cool-down. σ=150MPa	1°C/min for all cycles
2	Plane-Strain Tension	180±20 TSS_d=406°C	5-cycle treatment, No stress was applied during 1st cycle's cool-down. Stress was applied during subsequent cycles cool-down. σ=150MPa	1°C/min for first three cycles. 5°C/min for 4th cycle and 10°C/min for 5th cycle
3	Near-Equibiaxial Tension	172±20 TSS_d=400°C	4-cycle treatment, No stress was applied during 1st cycle's cool-down. Stress was applied during subsequent cycles cool-down. σ=110MPa	1°C/min for all cycles

Figure 4-4 to 4.6 show the evolution of the integrated δ-{111} hydride peak intensity over time during the thermo-mechanical treatments imposed on the samples. In each case the points represent the hydride peak intensity, the solid black line is the temperature and the solid red line is the applied stress in the location considered.

Figure 4-4 shows the hydride peak intensity in an experiment conducted on a plane-strain tension test sample. The overall hydrogen content in the sister sample was 177 wt. ppm. The sample

was subjected to a 3-cycle thermomechanical treatment to dissolve and re-precipitate hydrides. The diffraction patterns systematically taken as a function of time were integrated over an arc of 15° around the TD direction (see Figure 2-10). The result of that integration were plotted in Figure 4-4 The integration around RD and the full 360°C integration showed similar behavior as shown in Figure 4-4.

Figure 4-5 is from an experiment performed on another plane strain tension sample. In this case the average hydrogen content was 180 wt. ppm, and the sample underwent a 5-cycle heat treatment. For the 5-cycle treated samples, the first three cycles were similar to the cycles imposed on the other two samples, whereas in the last two cycles, higher cooling rates 5 and 10 °C/min values were used. Figure 4-6 show the diffracted intensity variation for the α-{100} zirconium peak, for the same sample shown in Figure 4-5.

Finally, Figure 4-7 describes the hydride peak intensity evolution during a test conducted on "near-equibiaxial" sample. For the first two experiments, the hydride peak intensities were acquired from the center of the gauge section where the stress biaxiality ratio is 0.53. In contrast, for the equibiaxial sample, a range of stress biaxiality ratios were examined, namely, 0.84 (near-equibiaxial tension), 0.73, 0.53 (plane strain tension), and 0 (uniaxial tension).

In each case the hydride peak intensity decreases during heat-up until the hydrides completely dissolve, at which point the peak intensity is zero. The peak intensity then increases during cooling when hydrogen precipitation starts and hydride platelets are formed. The places where the intensities go to zero (disappear) or re-appear (present) are used in the next section to determine the hydride dissolution and precipitation temperatures at specific hydrogen contents. When the low temperature dwell (150°C) is reached, the hydride peak intensity reaches a constant value.

The hydride peak intensity in Figure 4-4, 4-5, and 4-7 exhibited some variations in intensity during the test. Normally one would expect that once all precipitation has occurred the hydride peak intensity would then remain constant, then decrease slowly as the temperature increase, etc. In the figures, it is clear that the hydride peak intensity shows intensity variations which cannot be attributed to the normal dissolution and precipitation behaviors caused by temperature changes. Apparently from the Figure 4-6, zirconium intensity also shows an unexpected variation. As will be seen later, the hydride d-spacing was not affected by these intensity variations. The beam intensity was also checked to see if it varied during the experiments but it was not found to be the root cause of such variations. Furthermore, fluctuations in peak intensity were also observed in the α-{100} zirconium peak, the intensity of which should be constant during the entire thermo-mechanical treatment (see Figure 4-4).

Thus, these unexpected variations are unrelated to the thermomechanical treatment and are likely an experimental artifact. It is possible that this unexpected behavior might be caused by a failure in the data collection process, which involved each time acquiring ten frames of X-ray diffraction patterns each for 1 second and adding them up to prevent over-saturation of α-zirconium peaks, and increase the hydride data statistics. If the automated process failed to acquire one of the frames, or imperfectly erased the previous picture before taking the next, the intensities would fluctuate, as observed.

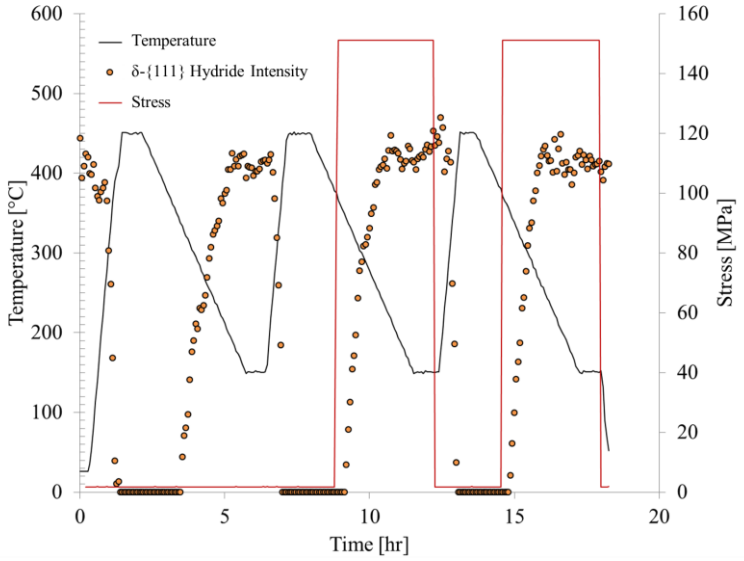

Figure 4-4 The evolution of integrated hydride peak intensity at the center of the gauge section with biaxiality ratio of 0.53 during thermo-mechanical treatment of the plane-strain sample (sample #1 in the Table 4-2) The sample was 3-cycle treated.

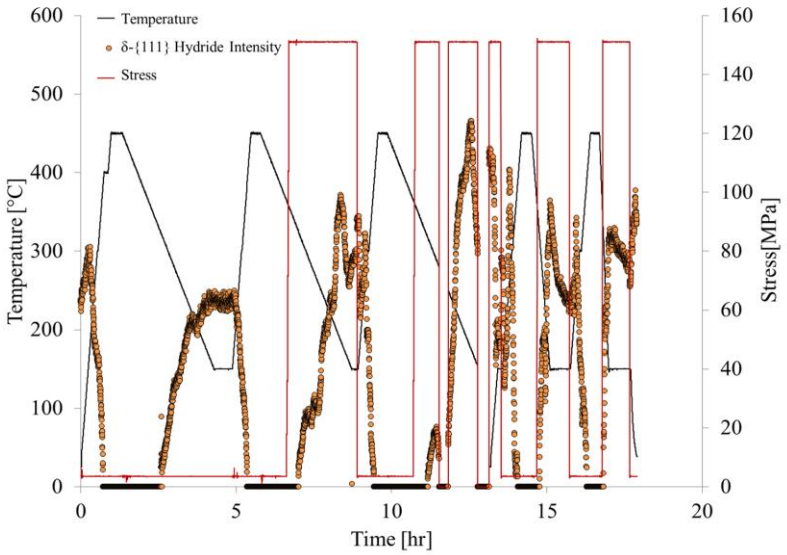

Figure 4-5 The evolution of integrated hydride peak intensity at the center of the gauge section with biaxiality ratio of 0.53 during thermo-mechanical treatment of the plane-strain sample (sample #2 in the Table 4-2) The sample was 5-cycle treated.

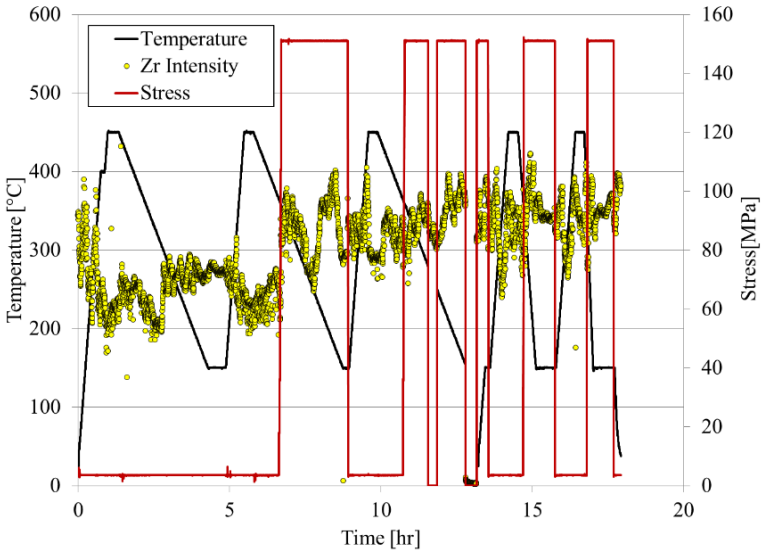

Figure 4-6 The α-{100} Zirconium intensity (/10) behavior and the temperature-stress history over time for the sample #2 which was 5-cycle treated.

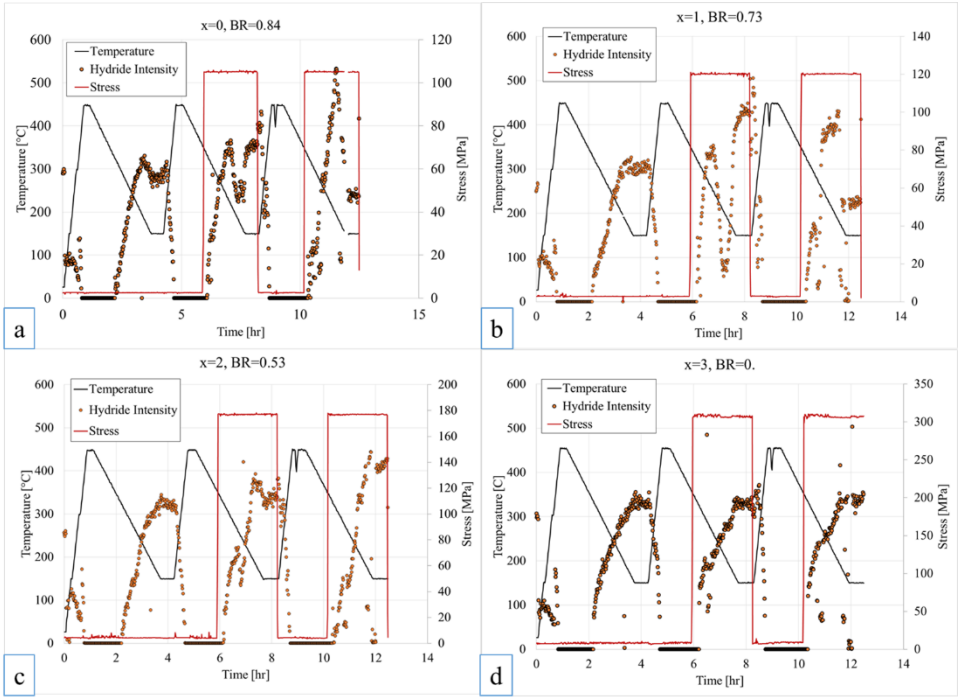

Figure 4-7 The evolution of integrated hydride peak intensity during thermo-mechanical treatment of the near equibiaxial tension sample (sample #3 in the Table 4-2) at different stress biaxialities such as; 0.84 in (a), 0.73 in (b), 0.53 in (c), and 0. in (d)

4.2.2 The Determination of Dissolution and Precipitation Temperatures from the Hydride Diffraction Peak Intensity

Diffraction peaks associated with α-zirconium and δ-hydrides are present in hydrided Zircaloy-4. The intensity of these diffraction signals is related to the volume fraction of the corresponding phase. Therefore, the δ-hydride peak intensity diminishes with increasing temperature because the δ-hydride volume fraction decreases due to hydride dissolution. When, hydrides completely dissolved, the intensity of hydrides disappears. Similarly, the hydride X-ray diffraction intensity increases because hydride volume fraction increases during cool-down as hydrides form. Thus, by following the intensity change of hydride X-ray peaks using high energy X-ray diffraction techniques in transmission, it is possible to study the hydride dissolution and precipitation behavior in situ during heat treatments under applied stress. Thus, tracking the hydride intensity during thermo-mechanical treatments allows to determine the temperatures at which the hydrides are dissolved (disappeared) and precipitated (present) as illustrated in Figure 4-4.

For example, Figure 4-8 shows the hydride peak intensity as a function of temperature during the first cycle of the thermo-mechanical treatment. The hydride intensity decreases while the sample is heating up, and the hydride peak disappears at approximately 380°C. For the hydride peak to disappear at this temperature implies that the hydrogen content is equal to the TSS_d at that temperature, that is, 140 wt. ppm [17]. During cooling, the hydride peak re-appears at about 338°C, which would indicate that the hydrogen content is equal to the TSS_p at that temperature of 147 wt. ppm [17]. The hydrogen content which was measured on the sister samples using hot vacuum extraction technique was 150 wt. ppm. So, the hydrogen contents measured by X-ray diffraction and hot vacuum extraction were in reasonably good agreement, as the differences could be attributed non-uniform distribution of hydrogen in the sample.

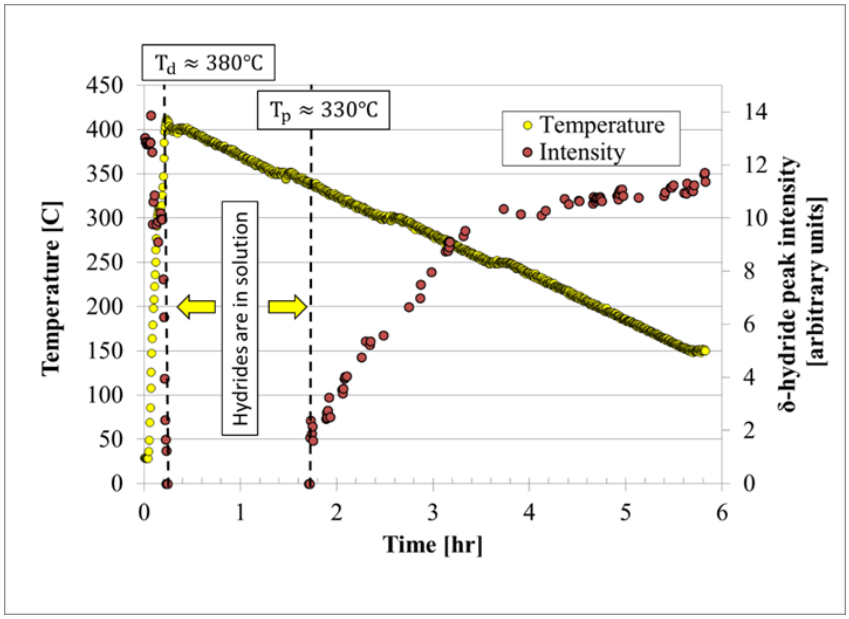

Figure 4-8 The hydride peak intensity at the center of the plane-strain specimen with 177 wt. ppm in the first cycle. The hydride dissolution temperature is 380°C and the hydride precipitation temperature is 338°C.

Figure 4-8 shows a plot of the temperature of a sample having 177 wt. ppm hydrogen, initially at room temperature and taken to 450°C, followed by a hold and several cooling heating cycles. The intensity of the δ-{111} hydride diffraction peak is shown in Figure 4-4. As the temperature increases the hydride peak intensity decreases, indicating the hydrides are progressively dissolved, until at approximately 1 h the intensity goes to zero, indicating complete hydride dissolution. The temperature at the time of dissolution is the temperature for which 177 wt. ppm can be completely dissolved, that is, it is the temperature for which TSS_d is equal to 177 wt. ppm.

Following a short hold at 450°C, the sample temperature is decreased gradually, as shown. At a given temperature the hydride intensity starts to gradually increase. This is then the precipitation temperature for this hydrogen content. This process can be repeated for many

hydrogen concentrations and the results compared to the determinations of TSS_d and TSS_p from McMinn et al. [17], as was done previously [60, 112].

The TSS_d is determined by the process of hydride dissolution into a matrix, and to a first approximation this process does not depend on the sample microstructure (dislocation density grain size or morphology, precipitate microstructure and such). The TSS_d determined in situ in the present work corresponded quite well with the calculation of the TSS_d from the curve determined by McMinn et al. for the amount of hydrogen measured by hot vacuum extraction, as shown in Figure 4-9.

4.2.2.1 Determination of the Hydride Precipitation Temperature (TSS_p)

In contrast, the TSS_p as shown in Figure 4-10, determined by the hydride nucleation process (which is the origin of the dissolution/precipitation hysteresis) depends on factors which influence the process, such as presence of nucleation sites, the grain microstructure, crystallographic texture, cooling rate, pre-existing hydrides, etc. For the latter factor in fact it has been shown that if the hydrides are not completely dissolved during the high temperature treatment, there is no hysteresis [112] as the hydrogen starts coming out of solution as soon as the temperature corresponding to the TSS_d for the amount of hydrogen in the sample is reached during cool down. [105]. To assess the possible influence of applied stress and stress state on the TSS_p, the process of hydride precipitation was systematically studied in different sample configurations and importantly, at different sample locations with different biaxiality ratios.

The results are shown in Table 4-3 and Figures 4-11 and 4-12, and are discussed in detail in the following paragraphs. Table 4-3, derived for a biaxiality ratio of 0.53, shows that the TSS_p values measured in this work are of the same order as those determined by Mc Minn et. al for the

measured hydrogen content [17]. It is also clear that the TSS_p values for circumferential hydrides, formed under no stress, shown in Table 4-3 are consistently lower than those determined by McMinn et al. This is illustrated graphically in Figures 4-11 and 4-12. Figure 4-11 is a plot of TSS_p determined in a sample containing 172 wt. ppm hydrogen for different locations in the sample subjected to different stress levels. The precipitation temperature from McMinn et al. for this hydrogen content is 346°C. It is clear that in addition to the lower precipitation temperature observed under no externally applied stress in Figure 4-11.

For precipitation under external stress, in particular radial hydride precipitation starts, there is a consistent decrease of the precipitation temperature with increasing level of stress, with the exception of the last point at 300 MPa, which exceeds the elastic limit for this temperature. The same behavior can be seen when the precipitation temperature is plotted against the stress biaxiality ratio as shown in Figure 4-12 for Zircaloy-4 specimen containing 172 wt. ppm of hydrogen. A consistent trend of decreasing precipitation temperature is also seen with increasing biaxiality ratio. Although neither of these observations show more than a correlation, they suggest that increasing levels of stress and biaxiality ratios lead to lower precipitation temperature.

The fact that the precipitation temperature is lower than the value obtained from the hydrogen concentration measured in the sister sample and calculated from Mc Minn for the case where no stress is applied case suggests that there could be zirconium alloy microstructure differences between the sample in this study and that studied by Mc Minn et al. [17]. It is also possible that the measured hydrogen content, having been measured from another part of the sample could be slightly different from that actually found on the sample. Note however, that the differences observed were all in the direction of lower precipitation temperature which would indicate a consistently lower hydrogen content in the samples tested than in the sister samples whose hydrogen content was measured; no mechanism suggests that this is the case.

Thus the application of stress during cooling appears to reduce the precipitation temperature compared to the non-stress value. The decrease in precipitation temperature is consistently more pronounced with increasing degree of hydride reorientation (see Figure 4-11), suggesting that precipitation of reoriented hydrides occurs at a lower temperature than that of circumferential ones. One possibility is that the application of stress makes the nucleation process more energetically costly, requiring a lower temperature for precipitation to occur by another path or in another location. This is in agreement with the different microscopic hydride microstructures observed in circumferential or radial hydrides (see Figure 3-3a, b, and c), as different precipitation mechanisms should result in different hydride microstructures. It should also be noted that the dislocation density and the overall amount of cold work can affect hydride nucleation, and those will decrease to a certain extent with increasing number of cycles and increasing dwell time. However the maximum temperature in the thermomechanical cycles in this study was 450°C, which is well below the recrystallization temperature for Zircaloy-4 which likely limited the change in dislocation density during the experiments. More important to this process may be the fact that in the second or third cycles, reoriented hydrides may have already been formed which created favorable dislocation structures to aid hydride precipitation, which would lead to a slight increase in precipitation temperature. The data are too limited to make any conclusions about this.

Table 4-3 The dissolution (TSS_d) and precipitation (TSS_p) temperatures as a function of cycles at which the stress biaxiality is 0.53.

	Temperature [°C]	Cycle number					McMinn [17]
		1st	2nd	3rd	4th	5th	
Plane-Strain Sample (177wt. ppm)	TSS_p	330	330	338			349
Stress Biaxiality is 0.53	TSS_d	383	395	387			404
Plane Strain Sample (180wt. ppm)	TSS_p	330	337	338	338	335	351
Stress Biaxiality is 0.53	TSS_d	390	395	388	400	400	406
Near Equibiaxial Sample (172wt. ppm)	TSS_p	330	325	330			346
Stress biaxiality at this location is 0.53	TSS_d	390	400	400			401

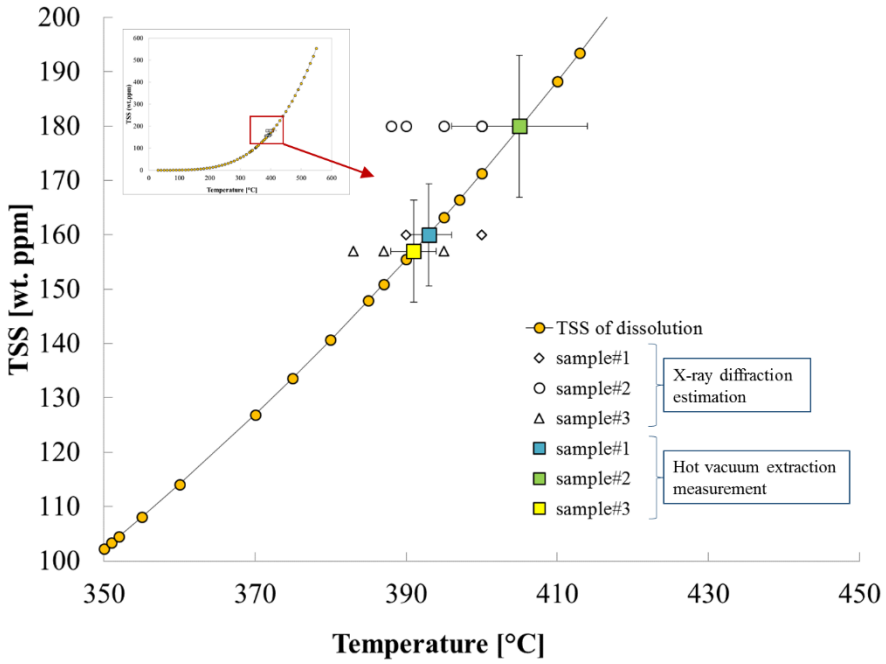

Figure 4-9 The comparison of the TSS_d temperatures obtained by the X-ray diffraction in this study and the Mc Minn's hydride dissolution curve, obtained by differential scanning calorimetry (DSC) [17]. The hydrogen contents of the test samples were measured by hot vacuum extraction.

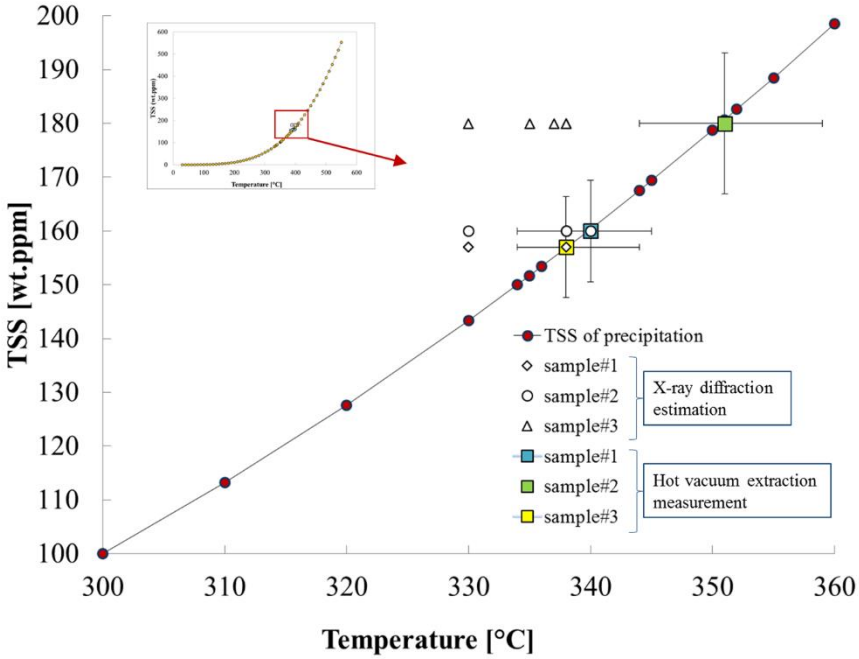

Figure 4-10 The comparison of the TSS_p temperatures obtained by the X-ray diffraction in this study and the Mc Minn's hydride precipitation curve, obtained by the differential scanning calorimetry (DSC) [17]. The hydrogen contents of the test samples were measured by hot vacuum extraction.

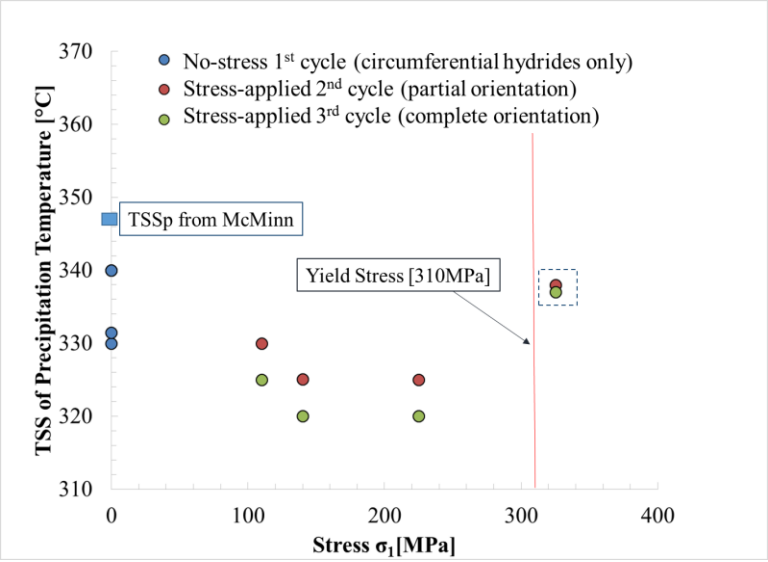

Figure 4-11 TSS of precipitation temperature as a function of major principal stress for the near-equibiaxial tension sample having measured hydrogen content of 172 wt. ppm.

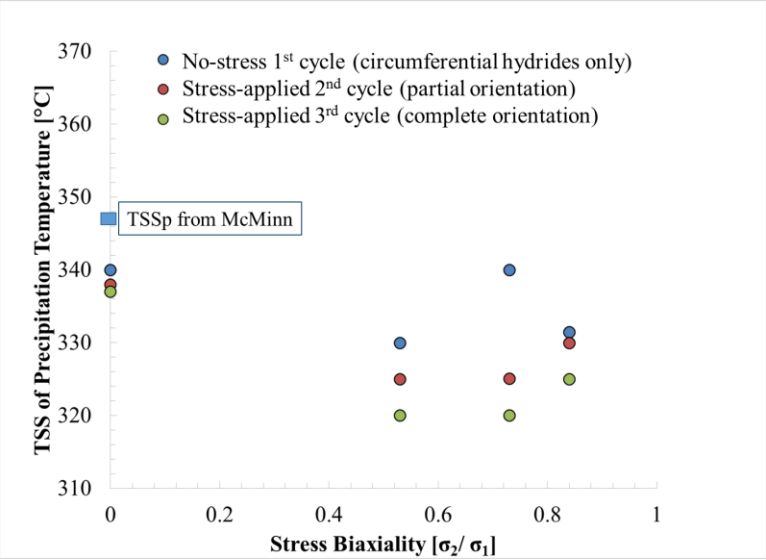

Figure 4-12 TSS of precipitation temperature as a function of stress biaxiality for the near-equibiaxial tension sample having measured hydrogen content of 172 wt. ppm.

4.3 Evolution of α-Zirconium d-spacing during Thermo-mechanical Treatments

As stated previously, while using synchrotron radiation diffraction it is possible to study the d-spacing evolution of the phases present in the sample in situ under temperature and stress. The d-spacings of the phases present in the material, α-zirconium (HCP) and δ-hydride (FCC) are calculated by fitting the X-ray diffraction patterns (Debye rings), which are systematically acquired during the thermo-mechanical cycles. The acquired X-ray diffraction patterns were integrated over a small angular range of ±15° around the TD (applied stress direction) and RD (in plane direction, perpendicular to the TD). The TD represented the major principal stress direction studied and the integration around RD was the minor principal stress direction, both studied across the gauge width from one notch center to the other in a double-edge notch sample.

This section presents the results of the study of the evolution of the α-{100} zirconium d-spacing during thermo-mechanical treatments. Figure 4-13 shows that during heat-up the α-{100}

d-spacing increases linearly with temperature (see red triangles) according to the thermal expansion coefficient of α-zirconium, until the temperature reached up to approximately 250 °C. The slope of the d-spacing with temperature provides an estimate of thermal expansion coefficient of the α-Zirconium, in this case determined to be about 7.5 10^{-6} K^{-1}, as compared to 7.1 10^{-6} K^{-1} for Zircaloy-4 for plate material [130], that is also expected to be in the range of 5 to 7 10^{-6} K^{-1}. As the temperature increases above 250°C the hydride dissolution process has been accelerated, thus the hydrogen to go into solution and changing the d-spacing of the α-zirconium while the dissolution occurs. When all hydrides are dissolved (in this case ~391°C). The zirconium d-spacing returns to its original slope determined by α-zirconium thermal expansion line parallel to the original line. The point at which this occurs gives another estimate of the dissolution temperature, in this case, about 391°C, and the hydrogen content is 170 wt. ppm which compares well with the value of 404°C for a sister sample containing 180 wt. ppm of hydrogen.

As the sample temperature decreases upon cooling (data in circles in Figure 4-6), the zirconium d-spacing contracts again according to the thermal expansion coefficient (the line is parallel to that obtained during heating). Because the TSS_p is lower than TSS_d, the deviation from the straight line happens at a temperature lower than 391°C. Similarly, the deviation from the straight line provides an estimate of the TSS_p, in this case determined to be about 338 °C, which compares well with 349 °C for a sample containing 180 wt. ppm of hydrogen.

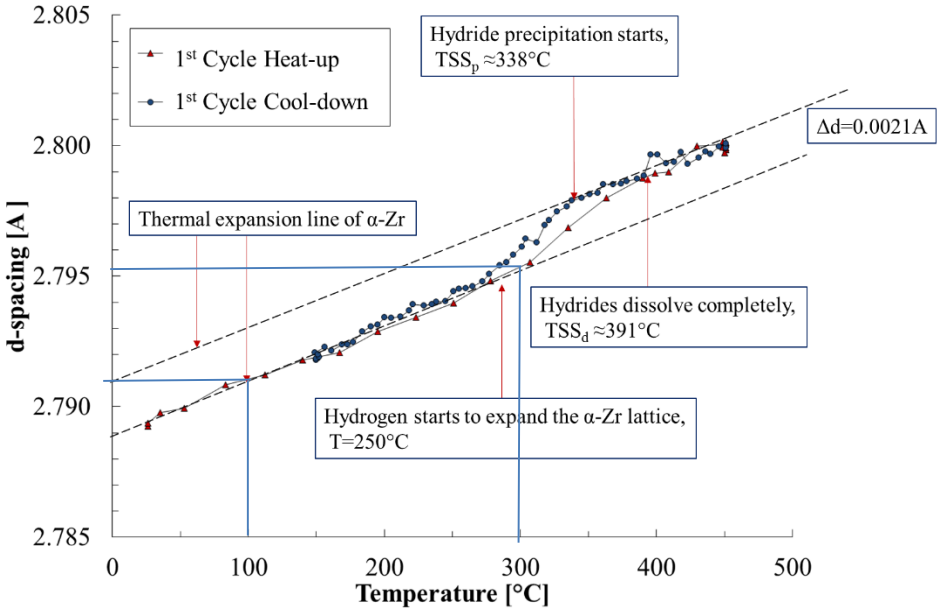

Figure 4-13 The d-spacing variation in RD (non-loading direction) of α-Zr (100) during one cycle thermo-mechanical treatment. The sample had 180 wt. ppm of Hydrogen, and the maximum temperature was 450°C; the cooling rate was 1°C/min.

Figure 4-14 shows the variation of the-{100} zirconium d-spacing both in the TD (applied stress direction or major principal stress direction) and RD (normal to TD or minor principal stress direction) during each cycle of a 5-cycle heat treatment. The stress was applied when the temperature reaches 400°C during cooling in all cycles after the second cycle. When even the stress was applied during cooling, the α-zirconium d-spacing increased immediately in TD. The data in Figure 4-14 was acquired at the gauge center where the stress biaxiality ratio (σ_2/σ_1) was 0.53, close to that of internally pressurized cladding tube under vacuum-drying conditions for dry-cask storage or transportation, as discussed in Chapter 3. In this stress state, no strain in the minor stress direction is expected. This is in fact verified as the zero stress and applied stress lines of d-spacing fall on top of each other.

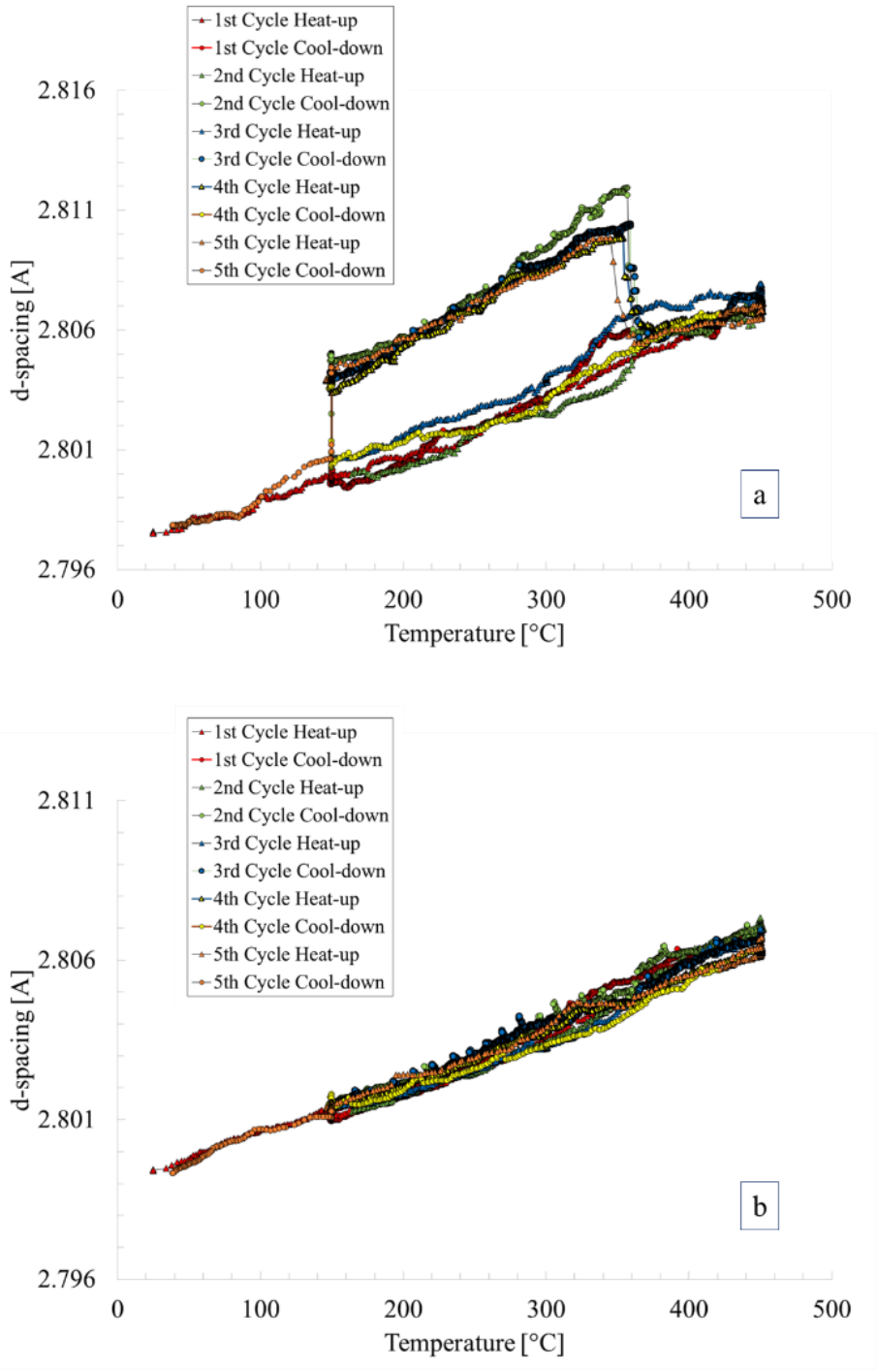

Figure 4-14 The d-spacing variation in (a) the TD (loading direction) and (b) the RD (non-loading direction) of α-Zr (100) during 5-cycle thermo-mechanical treatment. The sample had 150 wt. ppm of Hydrogen, and the maximum temperature was 450°C.

As stated above, the applied far-field stress at 375°C causes increase in the TD d-spacing of α-{100} zirconium and creates 150 MPa according to the finite element analysis at the center of the gauge section where the diffraction data collected. The Hooke's law written in Equations (B-4) and (4-2) can predict the elastic strains as a result of the applied stresses.

$$e_1 = \frac{1}{E}(\sigma_1 - \nu\sigma_2) \tag{4-1}$$

$$e_2 = \frac{1}{E}(\sigma_2 - \nu\sigma_1) \tag{4-2}$$

where the major and minor elastic strains: e_1 and e_2, major and minor principal stresses: $\sigma_1$and σ_2, E is the Young's modulus (82 GPa at 375°C), and ν is Poisson's ratio. For the d-spacing data as shown in Figure 4-14a at TD (applied stress direction), the d-spacing change as a result of tensile stress (164 MPa) is consistent with the FEA-calculated stress (150 MPA), as will be described in the following paragraphs.

Figure 4-14b shows the d-spacing behavior (of 5-cycle treated specimen) at RD (minor principal stress direction). No change in the RD d-spacing was observed in any cycle. The expected d-spacing in RD is constrained by the stress state. For an elastic body, the plane-strain condition is assured by at least minor stress value of +νσ (where ν is Poisson's ratio in α-zirconium, 0.36) to prevent minor strain contraction. In this case, the stress state causes a minor stress of $0.53\sigma_1$ (σ_1 =150MPa according to finite element analysis). Therefore, the net stress to result in a positive minor strain is $\sigma_{net}=0.53\sigma_1-0.36\sigma_1=0.17\sigma_1$. The net stress causes (in this case 25.5 MPa at the minor principal direction) a positive minor strain of $\epsilon = \frac{\Delta d}{d_0} = \frac{\sigma_{net}}{E}$ (where d_0 is the maximum d-spacing of α-{100} zirconium when the stress applied at 375°C). Because of this, the maximum

expected d-spacing change in RD (Δd) is 3.2 10^{-4} Å. The resultant d-spacing change is not significant to the experimental data because it is in the error margin of the acquired α-zirconium d-spacing data, (the fitted d-spacing data has 4-significant digits). Thus, no d-spacing change (or strain) caused by the minor stress is observed experimentally at the stress biaxiality ratio of 0.53.

To facilitate the understanding of the characteristics of α-{100} zirconium d-spacing during thermo-mechanical treatments, the d-spacing behavior of a 3-cycle thermo-mechanically treated sample (sample #1) in Figure 4-15 is explained. Because the minor stress has negligible effect on d-spacing evolution in the RD, only the TD data is shown in Figure 4-15. The Figure 4-15 shows the d-spacing evolution of a sample similar to the results of 5-cycle treated sample, as shown in Figure 4-14. For the 1st cycle, while the sample was heated up to 450 °C with a rate of 5 °C/min, d-spacing increased with a rate of 7.5 10^{-6} /°C which corresponds to the thermal expansion coefficient of α-zirconium (7.1 10^{-6} /°C) [130]. The same variation in α-zirconium during hydride dissolution is also observed. The d-spacing decrease as sample was cooled down. After the 1st cycle under no-stress, the sample was re-heated up to 450 °C at the same rate. Since, no stress was applied during all heat-ups. The d-spacing change was same and followed the thermal expansion line of α-zirconium in each case.

Similar to previous case, for the 2nd cycle cool-down, a tensile stress of 150 MPa at the data acquisition location was applied to the sample at 375°C at which hydrogen was still in solution, causing the d-spacing of α-{100} to increased. The mechanical stress by using the d-spacing data and Hooke's law, in this case, was calculated as 164 MPa; 14 MPa difference between the expected stress from finite element and the calculated from d-spacing data causes 1.7 10^{-4} Å that was in the fitting error. Thus, the experimentally calculated stress is in agreement with the finite element analysis (150 MPa). The same d-spacing difference calculation is also valid for the stress calculation when the applied stress was removed at 150 °C. At 150 °C, the stress is estimated as

173 MPa (E=92 GPa at 150°C). Importantly, it should be noted that the variations between the elastic constants taken from the MATPRO database and the sheet material utilized in this study can cause variation in the calculated stress values.

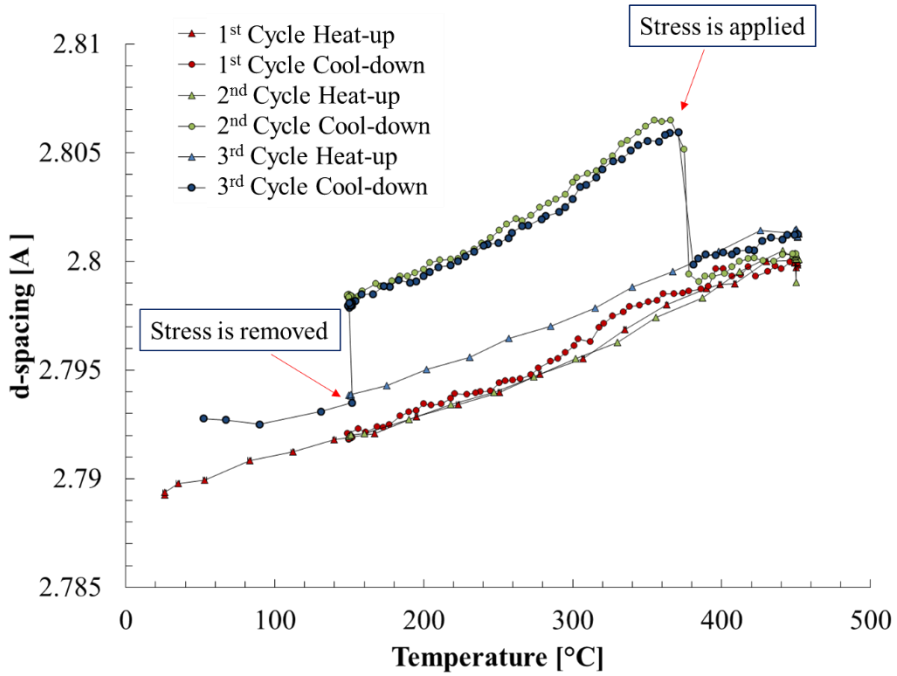

Figure 4-15 The d-spacing variation in TD (loading direction) of α-Zr (100) during 3-cycle thermo- mechanical treatment. The sample had 177 wt. ppm of Hydrogen, and the maximum temperature was 450 °C; the cooling rate was 1 °C/min.

In conclusion, the α-zirconium d-spacing variation was reproducible for all samples. For any cycle, α-{100} d-spacing follows the α-zirconium thermal expansion. During the no stress (1st) cycle, the hydride dissolution causes α-zirconium d-spacing expansion behavior which has a sharp change when the hydride dissolution completed. Thus, the terminal solid solubility of dissolution temperature can also be calculated using the zirconium d-spacing data. For the stress applied cycles, the stress calculations from d-spacing data agrees well with the finite element analysis, considering the ±25 MPa difference causes d-spacing change of $3.2\ 10^{-4}$ Å.

4.4 The Evolution of Hydride d-spacing during thermo-mechanical treatments

In this section, the δ-hydride d-spacing behavior during dissolution and precipitation is investigated. To evaluate the behavior of hydrides during dissolution and precipitation under conditions similar to vacuum drying, the δ-{111} hydride d-spacing was calculated by the fitting of X-ray patterns throughout the process, both in the direction of the stress-applied (TD) and perpendicular to the no-remote-stress-applied direction (RD).

Figure 4-16 and 4-18 depict a 3-cycle thermo-mechanical treatment and the hydride d-spacing evolution of a sample (sample#1) during that 3-cycle treatment. The data was acquired at the center of the gauge section where σ_2/σ_1 =0.53. While heating up the sample, the δ-{111} hydride d-spacing in TD and RD increased until the dissolution temperature of 391 °C was reached for 177 wt. ppm of hydrogen present in the sample, at which temperature the hydride peak disappears. After dwell at the maximum temperature of 450°C for 1 hr, the sample was cooled down to 150°C under zero stress. When the temperature was 331 °C, hydrides started to form, causing the hydride peaks re-appear, as shown in Figure 4-16. The hydride d-spacing decreased at a rate of approximately $3\ 10^{-6}$ /°C while cooling down to 150 °C, at which temperature of the sample was held at 150°C for an hour. This process whole was constituted one cycle. As previously described, the sample was subjected to a 3-cycle treatment and a tensile stress was applied during cool-down periods of the 2nd and 3rd cycles.

For the 2nd cycle cool-down, the d-spacing in the applied stress direction (TD) increased relative to the initial value and then decreased with temperature decreased at a rate of $5\ 10^{-6}$ /°C. In contrast, the d-spacing in RD was at the same d-spacing value of 2.744 Å as the unstressed value, before decreasing at a rate of $5\ 10^{-6}$ /°C. As the temperature decreased the hydride RD d-spacing did not show the effect of the minor principle stress because the change in the RD d-spacing is in the error margin. Using Hooke's law as shown in Equations (B-4) and (4-2) with the elastic

properties of hydrides: the Poisson's ratio of hydrides is approximately 0.35 and the Young's modulus of hydrides are in the range of 110-132 GPa at room temperature [74], it should be noted that the hydride elastic constants are unknown at high temperatures such as 375°C which causes higher d-spacing change calculation. So that, the difference in the d-spacing (Δd) is calculated as 5.5×10^{-4} Å by taking d_0=2.743 Å (the initial d-spacing at the beginning). Assuming that the elastic constant of hydrides are more or less similar, this number also can be considered as the maximum expected d-spacing change at 375°C as well as that of 25°C.

After 2nd cycle cool-down, the applied stress was removed. Interestingly, however, the δ-{111} d-spacing in TD did not decrease to its initial value of 2.745 Å, but it decreased only to 2.750 Å. Considering the hydride microstructure was radial rather than circumferential, this non-matched d-spacing indicated that the radial hydrides were under tension relative to the circumferential hydrides, or the radial hydrides were under less compression than the circumferential hydrides compared to the stress free powder diffraction d-spacing value of hydrides (2.76 Å). In non-intuitive fashion during the subsequent re-heating, the d-spacing in the TD started to decrease, indicating a thermal contraction with increasing temperature. This complex behavior was also observed for the 3rd cycle as well, and discussed in the following.

To understand the behavior of the δ-{111} hydride d-spacing in detail, we analyze it separately for RD and TD as a function of temperature. Figure 4-16 show the variation of the δ-{111} d-spacing with temperature in RD (the minor stress direction) as determined from diffraction patterns located at the center of the gauge section, i.e. where stress biaxiality ratio (σ_2/σ_1) is 0.53. The heat-up stage of the cycles are indicated by triangles while the cool down cycles by circles. In the last two cycles the samples are a 150 MPa of stress is applied when the temperature reaches to 375 °C during cooling, and the stress is removed when temperature reaches 150°C. During (the first heating-cooling cycle under no remote stress), the macroscopic morphology of hydride

microstructure is in-plane (circumferential). However, the hydride microstructure becomes out-of-plane (radial) in the second and third cycles, after cooling under the tensile stress. Hence, Figure 4-16 clearly shows that the hydride d-spacing behavior along the non-loading direction (RD) is identical for both circumferential and radial hydrides.

During the initial heat up phase, the (in-plane) hydride d-spacing increases as a result of thermal expansion, in a manner similar to that seen in zirconium peaks. For temperatures up to about 190°C, the hydrides expand at a rate roughly equal to that of the Zircaloy-4 matrix ≈ 5 to 6 10^{-6} /ºC. However, the d-spacing expansion rate increased to 20-25 10^{-6} /°C at temperatures above 190°C. This increase is roughly equal to the thermal expansion coefficient of hydrides according to data based on X-ray diffraction from Yamanaka [74]. Thus, the thermal expansion of hydrides shows a two-stage behavior: below 190°C, hydride thermal strains due to heat-up are constraint by Zircaloy-4 matrix and above that specific temperature, the constraint of matrix has decreased that the δ-hydride thermal strains are able to increase at the rates of close to the δ-hydride thermal expansion coefficient Importantly, subsequent cycles in which the load induces radial hydrides in RD also show the same bi-linear thermal expansion behavior during heating, as seen in Figure 4-16.

However, the d-spacing behavior changes in TD (load applied direction) when hydride microstructure changes from in-plane to out-of-plane, (as shown in Figure 4-17). During the heating phase of the 1st and 2nd cycles, the hydride microstructure is still in-plane. After the tensile stress is applied during the cool-down phase of the 2nd cycle, hydrides start to precipitate under tension, which causes an immediate increase in hydride d-spacing in TD as a result of tensile stress. This strain is consistent with the level of stress indicated in Figure 4-17. As cooling continues down to 150°C at a rate of 5 x 10^{-6} /°C, the hydride d-spacing decreases. After dwell at 150°C, the sample is heated up under no applied stress. However, the hydride microstructure now consists of out-of-plane hydrides. As discussed previously, the δ-spacing is seen to decrease with increasing

temperature, see the indicator "A" in Figure 4-17. These unexpected results are discussed in the following discussion section.

Figure 4-16 and 4-17 also indicates that both in-plane and out-of-plane hydrides completely dissolve at similar temperatures, i.e. approximately 391°C for 177 wt. ppm of hydrogen. While cooling, the δ-{111} hydride signal re-appears at approximately 337 °C upon reaching the precipitation temperature. When the hydrides first precipitate (under no applied stress), they show slightly lower d-spacing, indicating they precipitate under compression, and they quickly follow the thermal expansion coefficient of the hydrides are similar to that of the matrix, indicating matrix constraint. This is true not only for the 1st cycle without tensile stress (i.e. in-plane hydrides) but also for the 2nd and 3rd cycles in which radial hydrides are present.

Furthermore, Figure 4-16 indicates that the initial hydride d-spacing upon precipitation is significantly less than that of the hydrides at the same temperature during heating-up, thus, the hydrides are in a state of compression upon precipitation, as would be expected from their transformation strains [40, 48, 68]. An average estimate of the magnitude of the compressive stresses within the hydride indicates stresses on the scale of 240 MPa, assuming an elastic modulus of the hydride of 110-120 GPa [130] and a compressive strain of 0.002 indicated in Figure 4-16 at 325 °C. As expected, this stress level is close to the yield stress (≈250-275 MPa) of the Zircaloy-4 matrix at ≈ 325^{0}C.

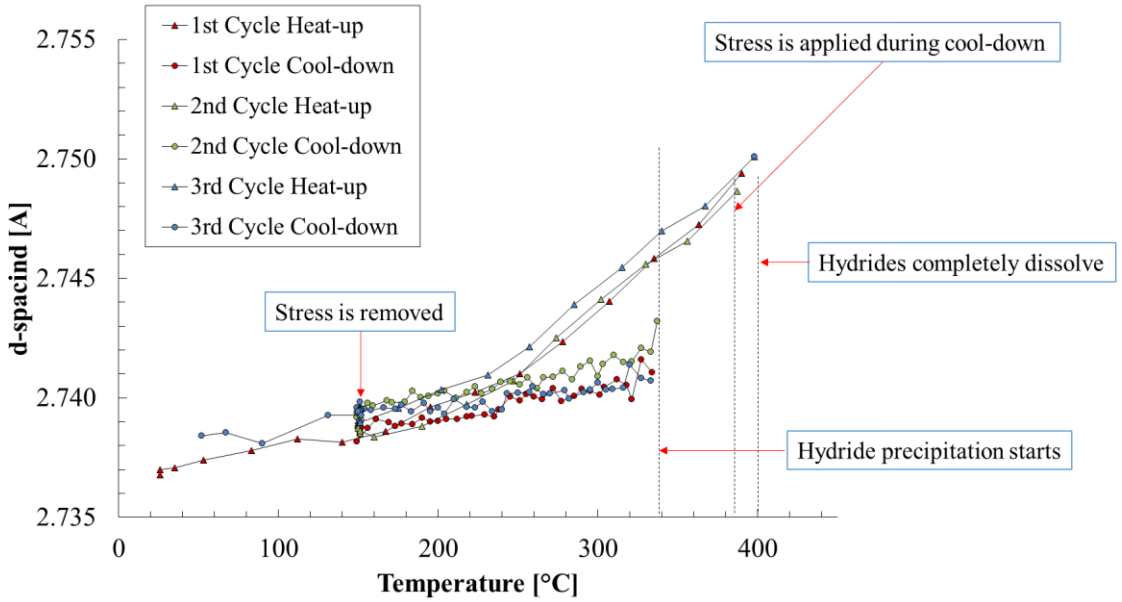

Figure 4-16 The δ-{111} hydride d-spacing in the RD orientation in a sample with 177 wt. ppm of hydrogen. Complete hydride reorientation occurred at that specific location which is the center of the specimen. The stress is 150 MPa at that location, the stress biaxiality ratio is 0.53, and the load is applied during the 2nd and 3rd cycle cool downs.

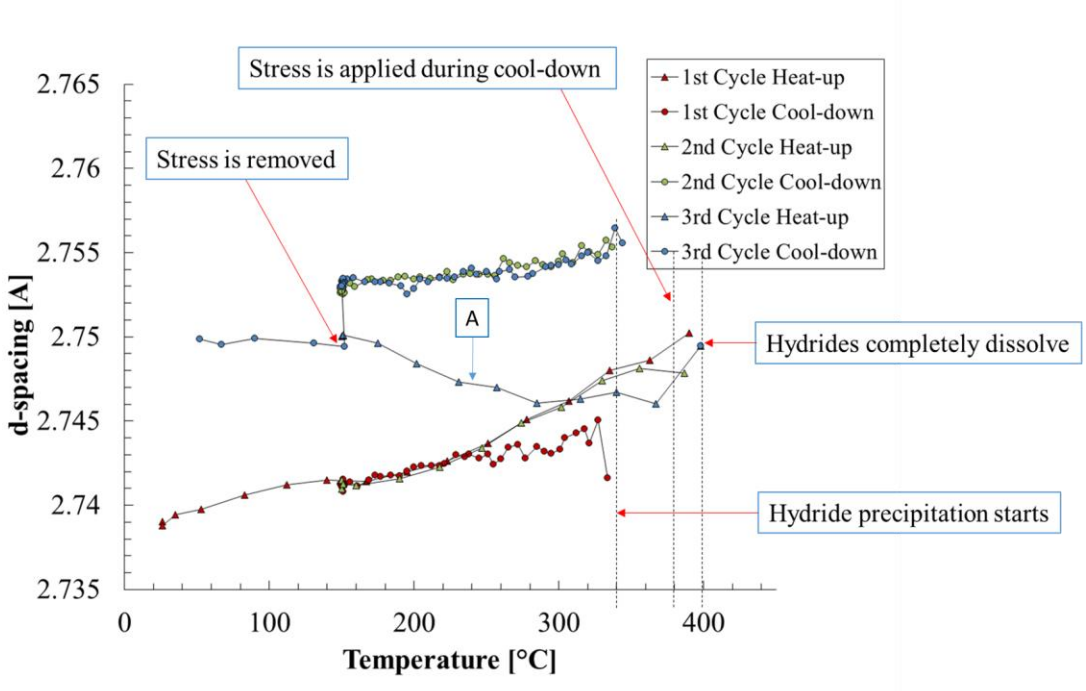

Figure 4-17 The δ-{111} hydride d-spacing in the TD orientation in a sample with 177 wt. ppm of hydrogen. Complete hydride reorientation occurred at that specific location which is the center of the specimen. The stress is 150 MPa at that location and stress biaxiality ratio is 0.53.

For the 5-cycle treated sample, the δ-{111} hydride d-spacing behavior as shown in the RD (Figure 4-18) is similar to the 3-cycle treated sample. Figure 4-18a shows the δ-{111} d-spacing behavior during heat-up and cool-down stages of 5-cycle treated sample. The d-spacing behavior in RD does not change during heating and cooling cycles when a tensile stress is applied. For clarity, Figure 4-18b only shows hydride d-spacing for the 1st cycle heat-up and cool-down. In Figure 4-18b, the RD data (minor stress direction) has bi-linear thermal expansion for both circumferential and radial hydrides. Also, hydrides are initially compressed upon precipitation.

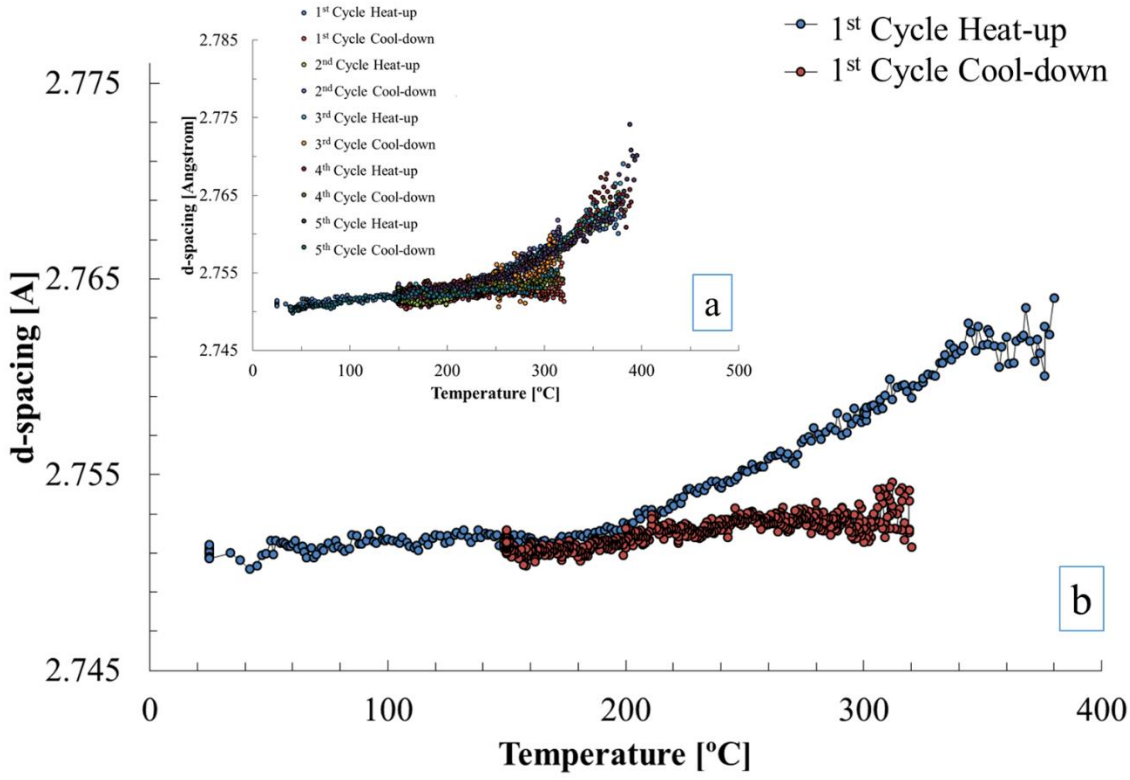

Figure 4-18 (a) δ-{111} hydride d-spacing behavior in the RD (no-stress-applied direction) orientation in a sample with 194 wt. ppm of hydrogen. Complete hydride reorientation occurred at that specific location which is the center of the specimen. The stress is 150 MPa at that location, the stress biaxiality ratio is 0.53, and the stress is applied during the 2nd, 3rd, 4th, and 5th cycle cool downs. (b) δ-{111} hydride d-spacing in the RD as a function of temperature for 1st cycle heat-up and cool-down.

Figure 4-19 shows the TD hydride d-spacing data (applied stress direction). Although the figure is complex, it is clear that bi-linear thermal expansion behavior is seen during the 1st cycle heat-up and thermal contraction of hydrides during 3rd and 4th cycles' heat-up under no-stress. This re-producible data, similar to the 3-cycle treated sample, is complex to analyze in its present form. Therefore, in the following paragraph the d-spacing behavior is analyzed cycle by cycle for the 5-cycle sample.

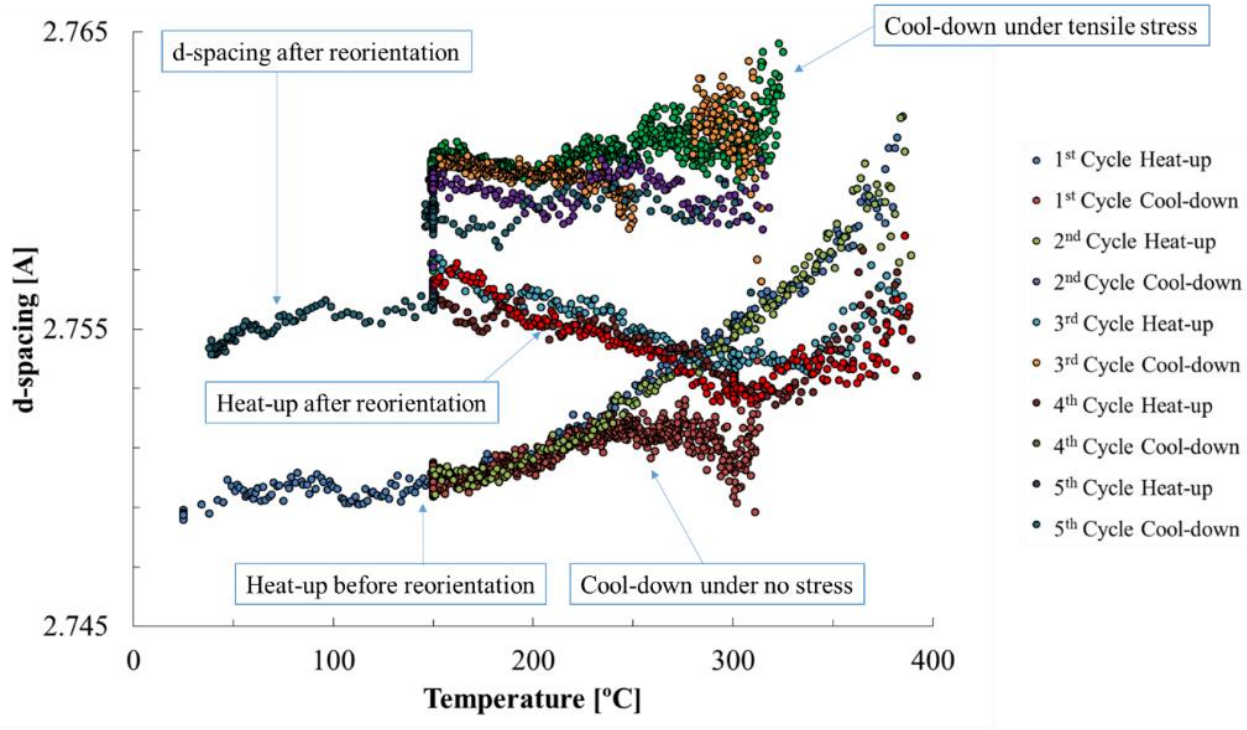

Figure 4-19 The δ-{111} hydride d-spacing behavior in the TD orientation in a sample with 180wt.ppm of hydrogen. Complete hydride reorientation occurred at that specific location which is the center of the specimen. The stress is 150MPa at that location, the stress biaxiality ratio is 0.53, and the load is applied during the 2nd, 3rd, 4th, and 5th cycle cool downs.

The complex hydride d-spacing behavior shown in Figure 4-19 can be described by examining one cycle at a time and recognizing the difference in diffraction conditions between the RD and TD directions. Figure 4-20 shows the detailed behavior of the hydride d-spacing behavior along the TD during the 1st cycle. This data is seen to be similar to the 1st cycle hydride d-spacing behavior in RD. The rate of expansion of δ-{111} hydride d-spacing is ≈3.1 10^{-6} /°C up to a temperature of 200 °C, more or less similar to the thermal expansion coefficient of Zircaloy-4 (5.1 10^{-6} /°C). Thus, the in-plane (circumferential) hydrides expand with a rate of similar to that of the Zircaloy-4 matrix up to the temperature of 200°C. However, above 200°C, hydrides expand with a higher rate of ≈18 10^{-6} /°C, which is much higher than that of the Zircaloy-4 matrix but it is similar to the "hydride thermal expansion" coefficient determined by Yamanaka et al. (25 10^{-6} /°C) [147].

Figure 4-20 also indicates that the hydrides initially nucleate under compressive internal stresses in the range of ≈200 to 240 MPa. The compressive internal stress, internal energy per volume, can be calculated from the amount of undercooling (ΔT) for order check by using a basic formula such as;

$$Q = \frac{1}{V_{hyd}} c_p \Delta T \tag{4-3}$$

where Q is the amount of thermal energy per volume [J/m^3], V_{hyd} is the molar volume of the hydrides (16.7 mol/m^3) [126], c_p is the hydride specific heat (50 J-$mol^{-1}K^{-1}$) [147], and $\Delta T = TSS_d - TSS_p$ for a specific hydrogen content of 194 wt. ppm. ΔT for this case is the difference between hydride dissolution and precipitation temperatures (404 vs 323°C). Inserting the values in Equation (4-3), the amount of thermal energy per volume is estimated as 242.51 MJ/m^3 (MPa). For the circumferential hydride nucleation at approximately 323°C, the amount of thermal energy per volume, at least, has to be converted into internal stress to overcome the nucleation barrier. Thus, the compressive stress, which is limited by the flow stress of Zircaloy-4, to nucleate circumferential

hydrides which is calculated using the hydride d-spacings at the TSS_d and TSS_p should be similar or at the same order to the amount of thermal energy per volume supplied by under cooling.

Since the hydride peak intensity is low at the beginning of precipitation, the uncertainty in d-spacing determination becomes is high. As nucleation proceeds, the hydrides start to grow causing more distinct diffraction peaks and reducing the uncertainty in d-spacing.

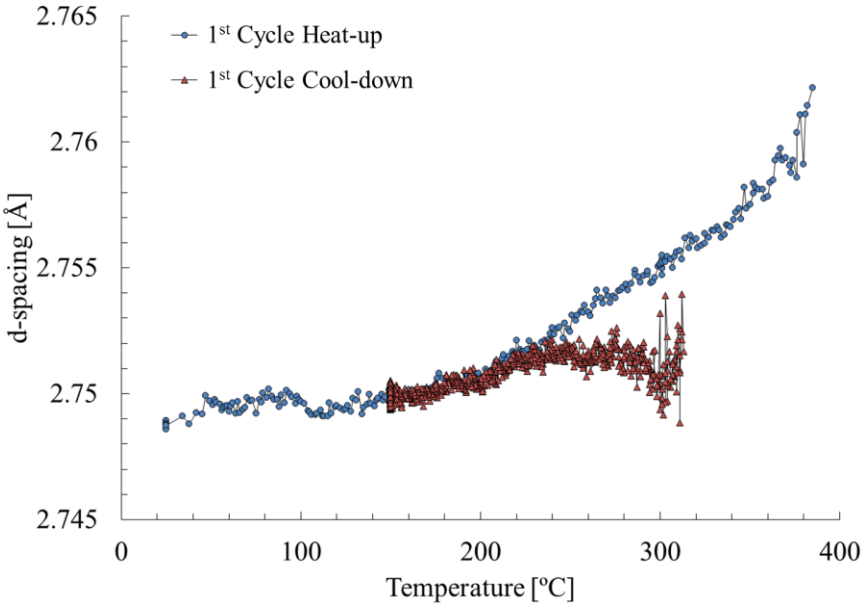

Figure 4-20 The hydride d-spacing in the applied load direction (TD) as a function of temperature for 1st cycle heat-up and cool-down. The sample has 194 wt. ppm of hydrogen, and the data were acquired at a location where biaxiality ratio is 0.53.

Figure 4-21 shows the d-spacing evolution during the 2nd cycle of the thermo-mechanical treatment. The 2nd cycle starts with heating from 150 to 450 °C, and the hydride d-spacing behavior is similar to the 1st cycle heating. This is followed by cooling under far field stress 150 MPa (FEA calculation) to initiate radial hydride precipitation. Thus the initial hydride precipitation starts under far field tensile stress, the δ-{111} hydride d-spacing increases to have tensile strain ($\Delta d/d_o$)

of ≈ 0.0019 corresponding to the stress (calculated from points A to B in Figure 4-21) of ≈209 MPa for δ-hydrides, this calculated stress at the hydrides is higher than the applied on the matrix (173 MPa), indicating two explanations: the elastic constant of hydrides are lower at high temperatures, particularly at the precipitation temperature, and by assuming, hydrides are oblate spheroids that creates a stress concentration of ≈1.25 at the applied stress direction which leads to 173 MPa x 1.1 equals to 190 MPa [148]. As a result, upon initial precipitation, the d-spacing of radial hydrides is greater than that of the previously existed circumferential hydrides. As cooling proceeds, the hydride d-spacing decreases with a slope of $\approx 3\ 10^{-6}\ °C^{-1}$, which is similar to the initial heating slope below 200°C, indicating that the radial hydrides are also under being constrained by the Zircaloy-4 matrix during cooling. Upon removal of the tensile stress at 150°C, the d-spacing of the δ-{111} radial hydrides in the TD (2.76 Å), is *higher* than the initial d-spacing of in-plane hydride phase (2.75 Å). Thus, as described earlier, the δ-{111} planes of out-of-hydrides are under tension in the loading direction (TD) relative to their original in-plane orientation. The scale of the tensile strain is: $\Delta d/d_o \approx 0.0036$ at 150 °C temperature at which the applied stress was removed (from points C to D in Figure 4-21). Such a strain suggests a residual tensile strain (from points D to F in Figure 4-21) within the radial hydrides but confined to the planes responsible for the diffraction signal in this TD orientation. In fact, if the radial hydrides were able to contract by following their expansion line the d-spacing would be 2.754 Å (point E in Figure 4-21) rather than 2.757 Å (point D in Figure 4-21), so that, they would be under more compression relative to their final state (point D in Figure 4-21) but the matrix contraction rate constrained the hydrides. The 3rd cycle begins with the heat-up (heating) shown in Figure 4-21 the d-spacing along the TD orientation *decreases* as temperature increases, indicating that δ-{111} planes of radial hydrides at the TD, where permanent strain exists, contracts as heated-up.

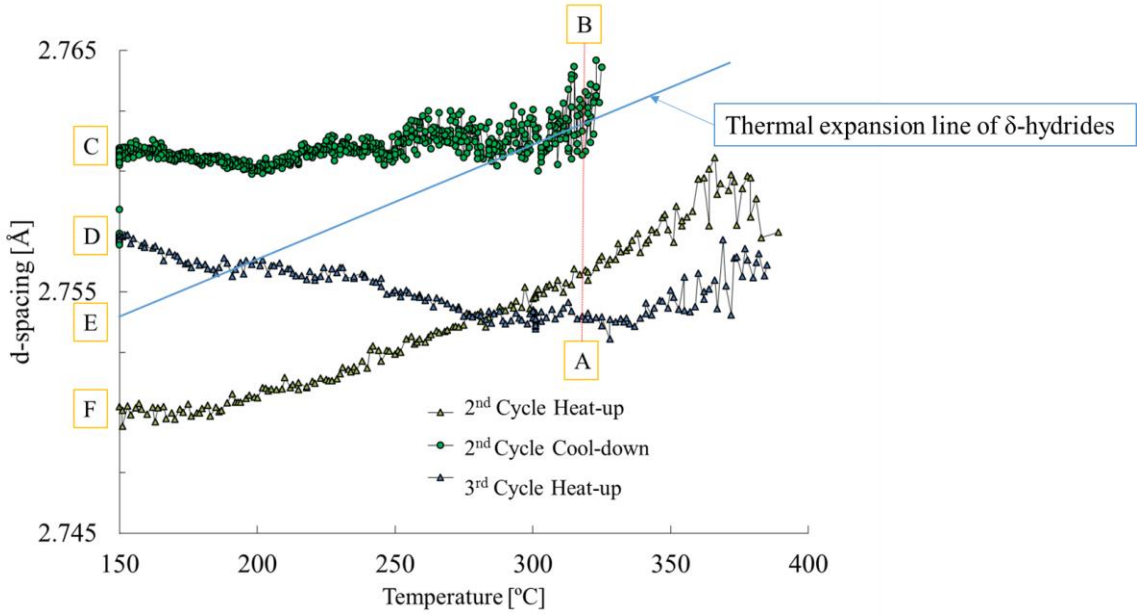

Figure 4-21 Hydride d-spacing in the TD orientation as a function of temperature for 2st cycle heat-up (in-plane hydrides), cool-down (radial hydrides), and 3rd cycle heat-up (radial hydrides). The sample with 194 wt. ppm of hydrogen is 5-cycle treated. Data were acquired at a location where stress biaxiality ratio is 0.53

The same d-spacing behavior as observed during 3rd cycle is also seen for the d-spacing data of 4th and 5th cycles at which higher cooling rates 5 and 10 °C/min (see Figure 4-22a and b) are applied, in fact, the same δ-{111} d-spacing behavior is observed at 3rd, 4th, and 5th cycles: the permanent hydride strain in TD after removing the stress and the thermal contraction as hydrides are heated-up. The permanent strain should be same for 3rd, 4th, and 5th cycles because the applied stress is kept same for these cycles. Also indicated that the thermal contract behavior is independent from cooling rates in the range of 1 to 10 °C/min, so that, these d-spacing behaviors are likely related to the microstructure of the radial hydrides.

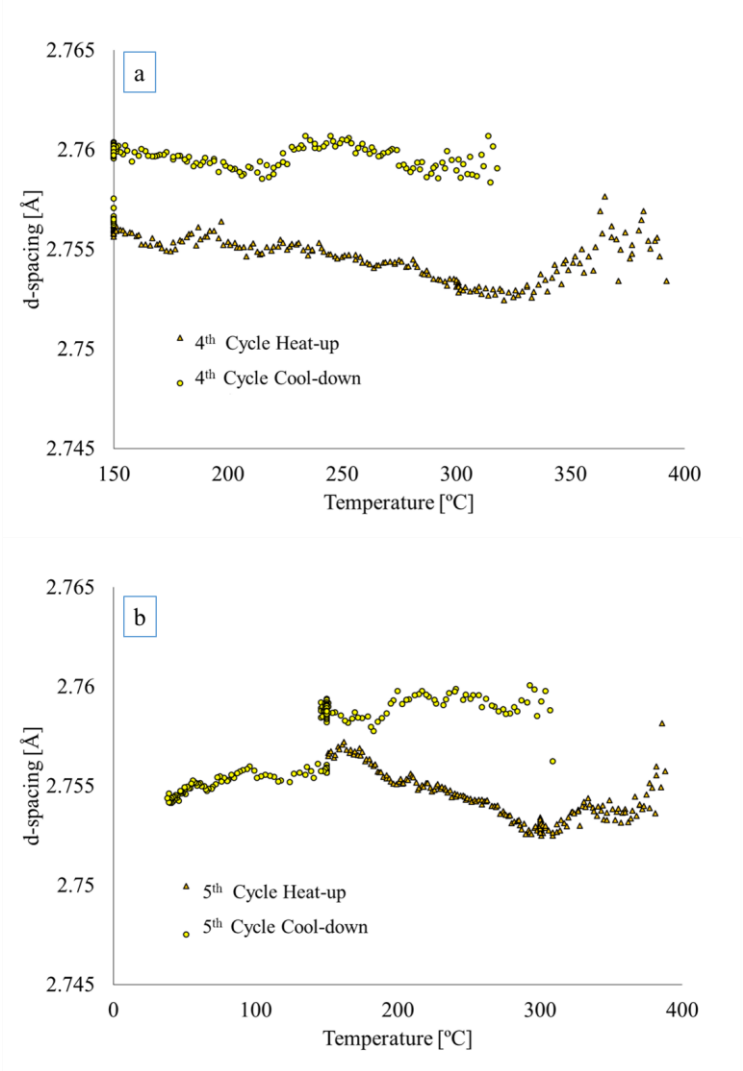

Figure 4-22 Hydride d-spacing in the TD orientation as a function of temperature for 4th (a) and 5th (b) cycles. The sample with 194 wt. ppm of hydrogen is 5-cycle treated. Data were acquired at a location where stress biaxiality ratio is 0.53

4.5 The Stress State Effect on Hydride d-spacing Behavior during Thermo-Mechanical Cycling

The effect of stress state on hydride precipitation can be examined by utilizing the "near-equibiaxial" tension sample geometry. To accomplish this goal, the X-ray beam location was continuously changed during data acquisition from the center of the gauge section to the notch using 1-mm increments during the heating and cooling cycles, as shown in Figure 4-23. Therefore, the X-ray diffraction data were acquired at locations that experience widely different stress biaxiality ratios from 0.84 (near-equibiaxial), to 0.53 (internally pressurized tube conditions), to 0 (uniaxial) as shown in Figure 4-23.

Figure 4-24 shows the hydride d-spacing behavior during the *heating* phase of each of three cycles at the three locations shown in Figure 4-23 different stress biaxiality ratios (σ_2/σ_1). As shown in Figure 4-24, the RD d-spacing behavior during heating is independent of both stress state and of hydride orientation (i.e., in-plane hydrides or radial-type hydrides) since the results are the same in all points and all cycles. As before, the hydride thermal expansion shows bi-linear behavior with a low rate of thermal expansion ($\approx 3.1 \times 10^{-6}\ °C^{-1}$) to about 200°C and a much higher rate of expansion ($\approx 18.0 \times 10^{-6}\ °C^{-1}$) above that temperature. Also, as described earlier, Figure 4-18 shows no thermal contraction of the hydrides in the RD orientation (normal to the applied direction) was observed during the 3rd cycle heat-up when radial hydrides are already formed.

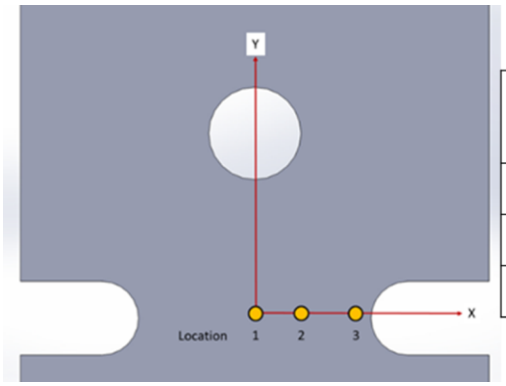

Location	Stress Biaxiality Ratio	Major Principal Stress [MPa]
1	0.84	100
2	0.53	150
3	0.	300

Figure 4-23 X-ray beam locations at which X-ray diffraction patterns obtained. Each location has a different stress state and major principal stress value.

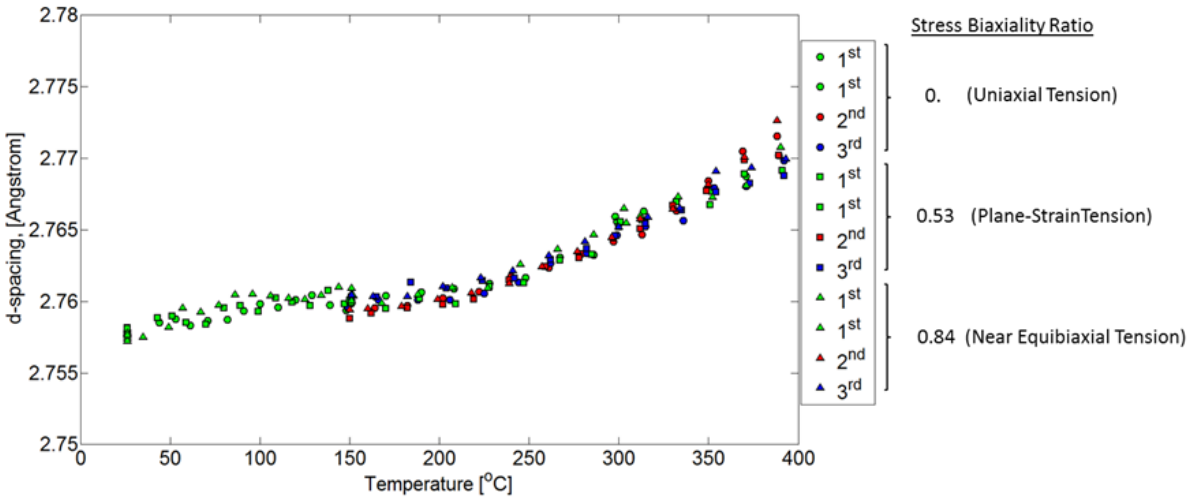

Figure 4-24 δ-{111} hydride d-spacing variation in the RD orientation (normal to the applied load direction) during the heating stages for each cycle as a function of temperature at three different stress biaxiality ratios. The colors represents the cycle numbers, such as green data is for 1st cycle, red is for 2nd cycle, and blue is for 3rd cycle. The circles are for uniaxial tension, squares are for "plane-strain" tension, and triangles are for "near-equibiaxial" tension stress states.

The Figure 4-25 shows the hydride d-spacing variation at different stress state locations during cool-down under an applied stress that is normal to the RD orientation of the diffraction signal. Figure 4-25 indicates that the degree of stress biaxiality has no effect on d-spacing behavior of the radial hydrides as they form during cooling under load. This data from the sample # 3, as

shown in Figure 4-25 and Figure 4-26, is similar to the previously acquired data from sample # 1 and 2, which indicates that the δ-{111} hydride d-spacing behavior in RD and TD are same in all no stress and stress applied cycles for all specimens used in this study.

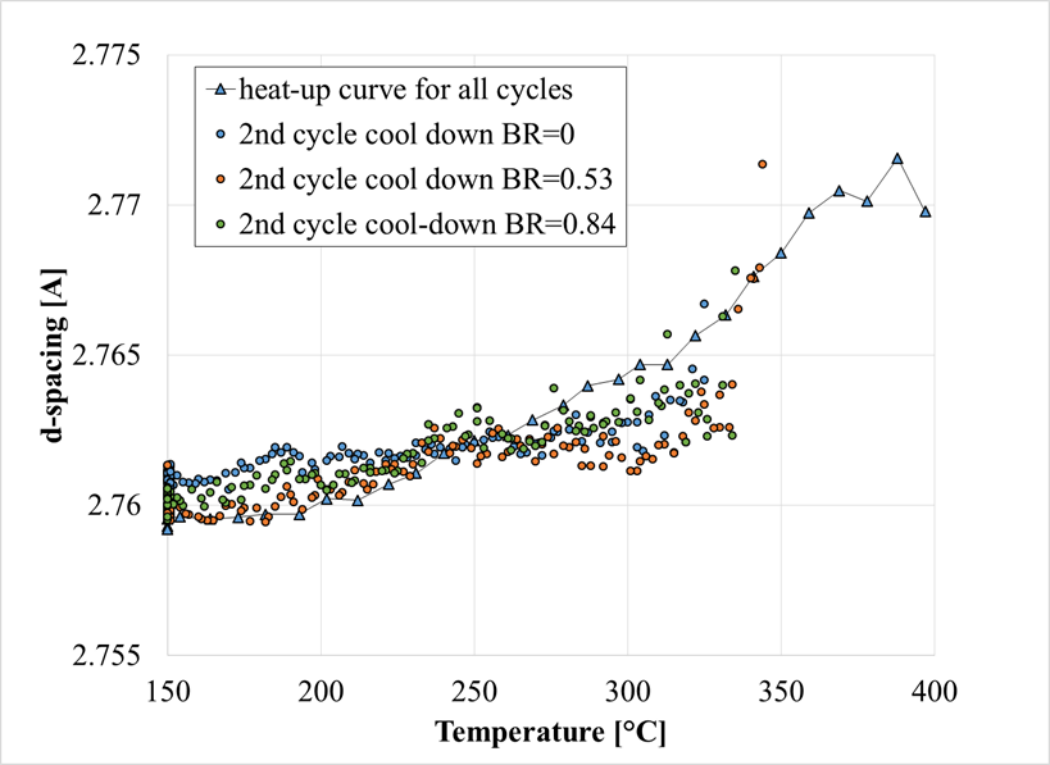

Figure 4-25 The (radial) hydride d-spacing variation along the RD orientation (normal to applied load) as a function temperature at three different stress biaxiality ratios. The sample has 180 wt. ppm of hydrogen.

Because of the sample geometry (notch and hole effects), principal stresses also vary with in the gauge section of the sample. Figure 4-26 shows diffraction data that was acquired in the TD orientation at three different stress state and stress level locations. These data show behavior that is similar that of the previous results obtained from plane-strain tension sample as in Figure 4-21. Hence, the d-spacing variation in both RD and TD orientations are consistent with different samples.

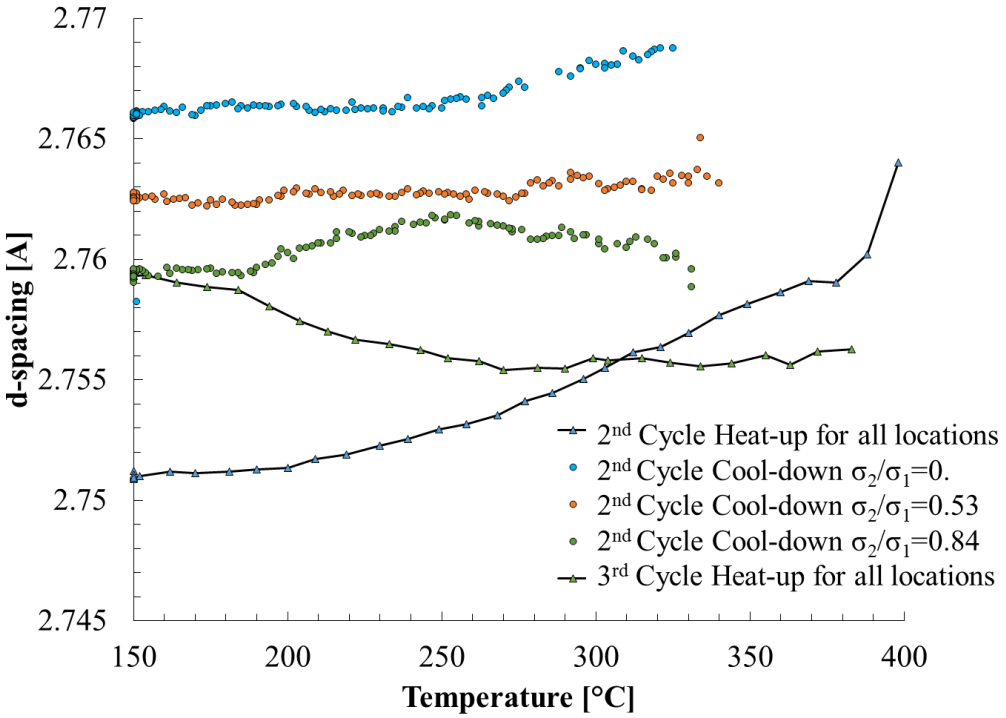

Figure 4-26 The radial hydride d-spacing variation along the TD orientation (normal to applied load) as a function temperature at three different stress biaxiality ratios. The sample has 172 wt. ppm of hydrogen.

Figure 4-26 shows the d-spacing in radial hydrides for 2nd cycle heat-up, hydrides at all of the locations/stress states exhibit the same bilinear thermal expansion behavior as observed previously; see Figure 4-21. For cooling under tensile stress, radial hydrides form at each of the three locations/stress states. The highest principal stress is in the uniaxial tension location (σ_1= 300 MPa, due to the notch effect). Thus, the initial d-spacing at that location when stress is applied is higher than that at the two other locations where the maximum principal stresses are less (100 MPa and 150 MPa at locations where stress biaxiality ratios are 0.84 and 0.53, respectively). In addition, Figure 4-26 shows that the hydrides contract according to similar thermal contraction rates at the three different stress biaxialities, which also follow the matrix thermal contraction rate.

At the beginning of 3rd cycle heat-up, Figure 4-26 shows that radial hydride d-spacings are the same for the three different stress biaxiality locations after the stress is removed. Those d-

spacing values are also similar to the δ-{111} hydride d-spacing values shown in Figure 4-21 for radial hydrides in the TD direction. During heating of the sample under no stress, Figure 4-26 shows that thermal contraction of the δ-{111} planes aligned with the TD occurs. This thermal contraction during heat-up is independent of stress biaxiality, which suggests that once the applied stress is removed, the initial level of residual tensile stress within the hydrides is similar even at three locations though they formed under three different stress biaxiality. Thus, the same effects of stress state effect at different locations has been observed in 3rd cycle heat-up.

4.6 Radial Hydride Signature using Synchrotron Radiation

The tapered tensile specimen described in Section 2 was examined using X-ray diffraction analysis at room temperature after being subjected to the two-cycle thermo-mechanical treatment shown in Figure 4-27.

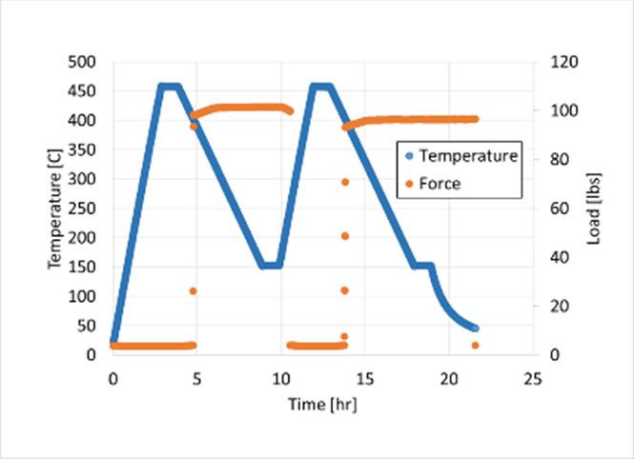

Figure 4-27 Thermo-mechanical treatment to estimate the threshold stress for hydride reorientation. The maximum temperature is 450°C, the heating rate is 5°C/min, and the cooling rate is 1°C/min.

The sample was first heated up to 450°C with a heating rate of 5 °C/min and held for 1hr at this temperature. Then the sample was then cooled down to 150°C at a cooling a rate of 1 °C/min. The stress was applied at 400°C during cool down and kept constant until 150°C. Due to the range of stresses along the tapered gauge section, the radial hydride fraction was equal to 1 at the narrowest part of the gauge section and equal to 0 ("circumferential" or in plane hydrides) at the widest part of the gauge section.

The mating piece shown in Figure 3-5 was examined at the APS as follows. A calibrant material (ceria) with known lattice parameter and crystal structure was pasted on the sample surface to determine precise peak locations. Then, the sample was attached to the sample holder and examined using 80 keV X-ray diffraction in transmission geometry at various locations along the taper (shown in Figure 4-28) to investigate the characteristics of the hydride peaks as a function of hydride orientation.

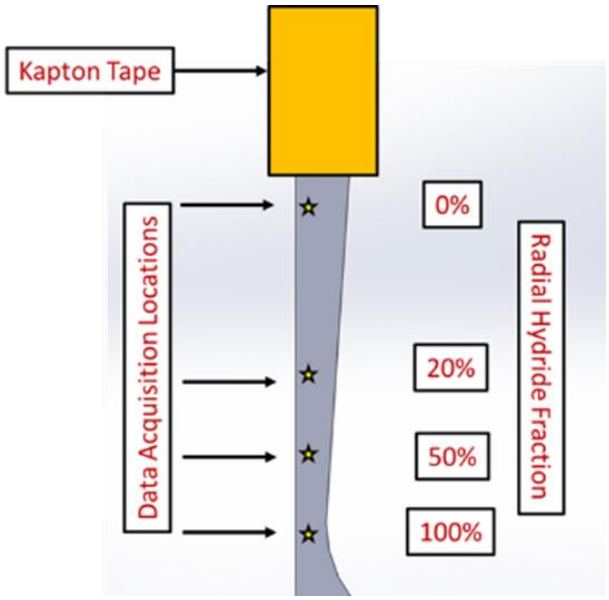

Figure 4-28 The sectioned tapered tensile specimen and data acquisition locations by X-ray diffraction.

The X-ray diffraction data in the form of diffraction rings over a range of 2θ angles were acquired at different locations along the specimen gauge lengths. The diffraction rings were integrated in segments along both the rolling direction (RD) (no-stress direction) and transverse direction (TD) (the applied stress direction). The integrated X-ray data for both directions were fitted as explained in Chapter 2.4, and the δ-{111} hydride peak was selected for detailed study of the hydride. The error in d-spacing estimations are originated by the peak fitting procedures. Since, the hydride peak is mostly convoluted with α-{100} zirconium peak, accuracy in the fitting process is essential. The accuracy of fitting has two important components based on the mathematical operation during fitting: the very first one is the fitting function residue that is at the order of 10^{-6}, on the other hand, having low residue does not verifies the resultant peak shapes; the other parameter is the overall shape of the convoluted δ-{111} hydride and α-{100} zirconium peaks. Therefore, the fitting has been performed very carefully using four different methods to eliminate any systematical errors.

Figure 4-29 shows the intensity of the δ-{111} hydride peaks against d-spacing when integrated along the arc aligned with the TD (applied stress direction) at several locations along the specimen length. These locations correspond to a range of radial hydride fractions (RHF) (as determined by metallographic pictures after thermo-mechanical treatment). The plot shows that the δ-{111} hydride peak d-spacing (given by the peak centroid) increases gradually as the radial hydride fraction of hydride reorientation increases from 0 to 1. Therefore, the planes which give rise to the diffraction of the δ-{111} hydride peak acquired at a location where RHF=0 ("only circumferential hydrides are present") show a *smaller* d-spacing than the δ-{111} hydride peak acquired at a location where RHF=0.2. Similarly δ-{111} hydride planes at a location where RHF 0.2 show a smaller d-spacing compared to hydride planes at a location where RHF=0.5. This result indicates that circumferentially oriented hydrides have a smaller d-spacing than radial hydrides when measured along the loading direction as seen previously by Colas [60, 83, 112]. Thus, the

increase in hydride d-spacing along the loading direction may be considered as a signature of the presence of radial hydrides, and an indication of hydride reorientation.

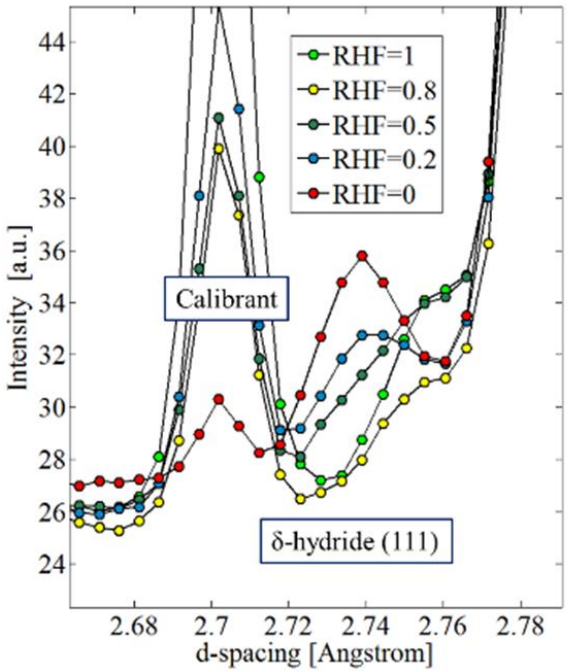

Figure 4-29 The δ-{111} hydride peak behavior as a function of radial hydride fraction (RHF) and as determined in the TD orientation.

Figure 4-30 shows the variation of δ-{111} hydride d-spacing as determined along either the rolling (RD) or the transverse (TD) directions as a function of stress level and radial hydride fraction. The radial hydride fraction increases from 0 to 1 as the applied stress increases, and the hydrides become completely out-of-plane (radial) hydrides at high stress levels of200 MPa. However, the transition from out-of-plane to in-plane hydrides starts at stress levels near 155 MPa.

As shown in Figure 4-30, the change in the hydride microstructure is reflected in the variation of the d-spacing of the δ-{111} hydride peak. The d-spacing integrated over the TD (loading direction) increases rapidly as the radial hydride fraction increases. In contrast, the d-spacing in the RD (the direction normal to the loading direction) changes only slightly. Previous work had seen similar increase of the d-spacing for the δ-{111} planes aligned perpendicular to the

loading direction as the RHF increases [112]. For the in-plane (circumferential) hydrides, d-spacing of δ-{111} hydride planes in TD are smaller than d-spacing of δ-{111} hydride planes in RD. In contrast at higher stresses at which the hydrides have reoriented, the d-spacing of the δ-{111} hydride planes in the TD is higher than that in the RD direction, and the far-field stress state in this case is uniaxial tension, Hooke's law can be applied to the Zircaloy-4 matrix as in Equation (4-4).

$$\sigma = E\varepsilon = E\frac{\Delta d}{d_0} \tag{4-4}$$

Assuming Young modulus [74], E = 120 GPa and the variation in d-spacing at room temperature, $\Delta d/d_o \approx 0.0050$ (see Figure 4-30), the permanent residual strain acting on radial hydride particle relative to circumferential hydrides. This strain level creates a stress level that is similar to Zircaloy-4 matrix's yield stresses (525 to 625 MPa at room temperature [8, 130]. Hence, radial hydride precipitation occurs in a manner that leaves the δ-{111} planes at TD under residual tensile strain compared to δ-{111} planes at TD for circumferential hydrides.

Another perspective to understand radial hydride d-spacing is based on the d-spacing of stress-free hydride, which is based on powder diffraction file PDF value (2.76 Å). Figure 4-30 indicates that as radial hydrides are formed, the d-spacing in the TD orientation increases close to the stress-free d-spacing of δ-hydrides (based on the PDF value). In contrast, the d-spacing values of the circumferential hydrides indicate that they are under compression for both directions relative to the powder diffraction value [146]. The level of compression, $\Delta d/d_o \approx 0.0050$ indicates residual stresses of 500 to 600 MPa (E=100-120 GPa) similar to the yield stress of Zircaloy-4 (525-625 MPa) at room temperature, as was demonstrated above using Equation (4-4).

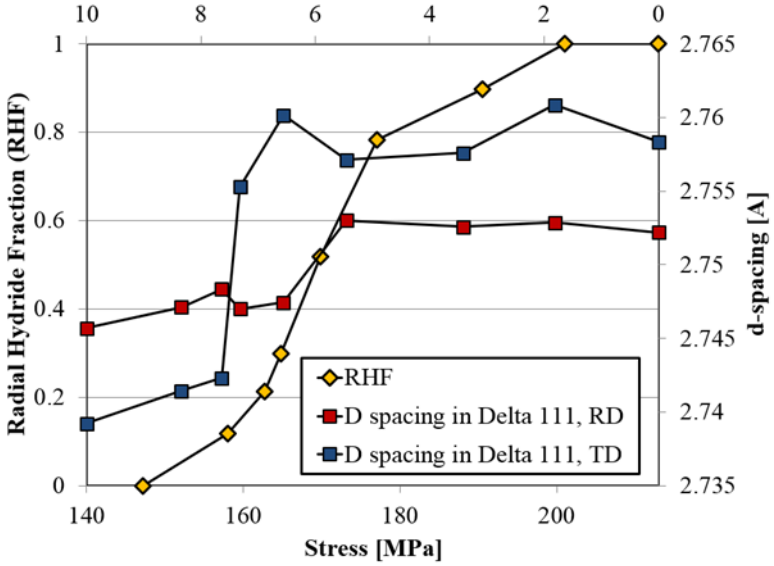

Figure 4-30 The variation of d-spacing of the δ-hydride {111} peak as a function of stress and radial hydride fraction. The uniaxial tapered sample was 2-cycle radial hydride treated. The load was applied parallel to the transverse direction, which is the hoop direction in tube geometry

In order to understand the hydride d-spacings for all orientations, a companion experiment was also conducted to acquire diffraction data from hydride planes which gives diffraction in ND (where 60% of Zr-002 planes oriented). This was accomplished by rotating the sample such that the X-ray beam hits the ND-TD surface of the tapered sample as shown in Figure 4-31, thus, rotating the sample enabled to acquire diffraction data from circumferential hydride faces at ND and the diffraction data from circumferential hydride edges at TD.

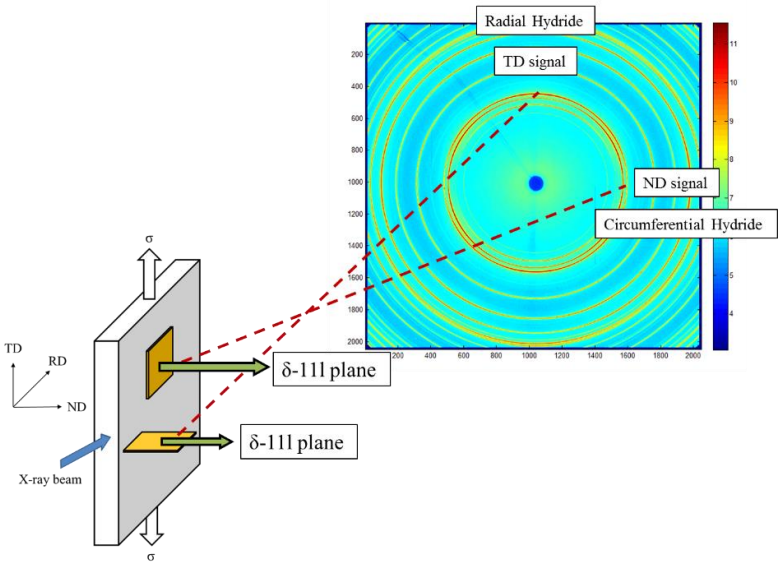

Figure 4-31 The schematic orientation of hydride planes within the tapered sample which was subjected to 2-cycle thermo-mechanical treatment and tested at room temperature. The tapered tensile specimen results in sections which have only circumferential hydrides and those that have only radial hydrides. The sample orientation with respect to the X-ray beam enable acquisition of diffraction signals from hydride planes in the ND orientation.

The data were acquired at two different locations on the tapered tensile sample such that only circumferential hydrides exist at one location and only radial hydrides exist at the other. Table 4-4 shows that the circumferential hydrides are initially under tension in ND relative to TD. Whereas, radial hydrides show the opposite behavior: they are under tension in TD relative to the ND and as well as RD (Figure 4-30).

Table 4-4 Hydride d-spacings within a tapered tensile specimen as examined in Figure 4-31

Macroscopic hydride structure	δ-{111} hydride d-spacing [Å]	
	ND	TD
Circumferential (RHF≈0)	2.763	2.754
Radial (RHF≈1)	2.751	2.759

The above effect can be seen more clearly by examining the diffraction patterns shown in Figure 4-32 for circumferential hydrides and Figure 4-33 for radial hydrides. The diffraction pattern for circumferential hydrides in Figure 4-33 shows that those δ-{111} hydride planes from ND signal have higher d-spacing than the δ-{111} hydride planes from TD orientation. Thus, the δ-{111} hydride planes are under tension relative to the other δ-{111} hydride planes within the circumferential hydrides. For radial hydrides, Figure 4-33 shows that δ-{111} hydride planes in the TD orientation are now in tension relative to the other δ-{111} hydride planes in ND within the hydride. Thus, at room temperature, both circumferential hydrides and radial hydrides show similar tension behavior within those δ-{111} hydride planes parallel to the macroscopic hydride platelet face.

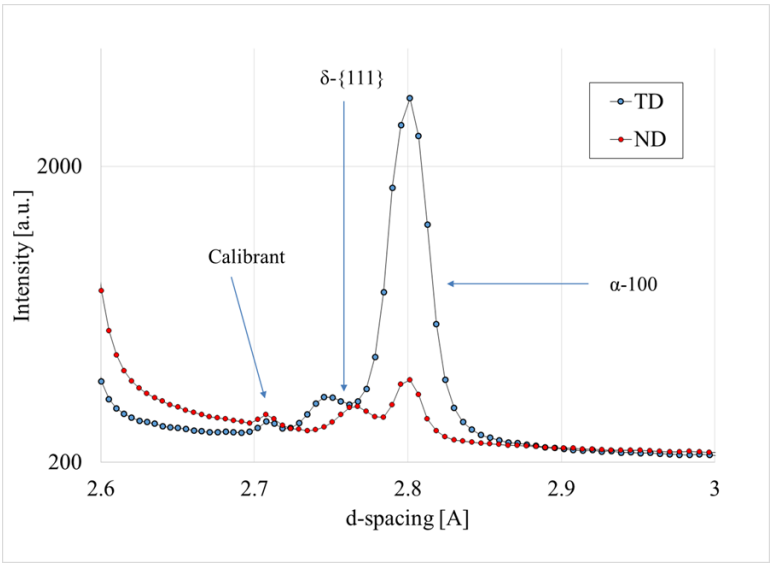

Figure 4-32 X-ray diffraction pattern which is taken from a tapered sample with 180 wt. ppm of hydrogen and 2-cycle treated. Only circumferential hydrides exist at this location. (RHF≈0). Ceria is used as the calibrant.

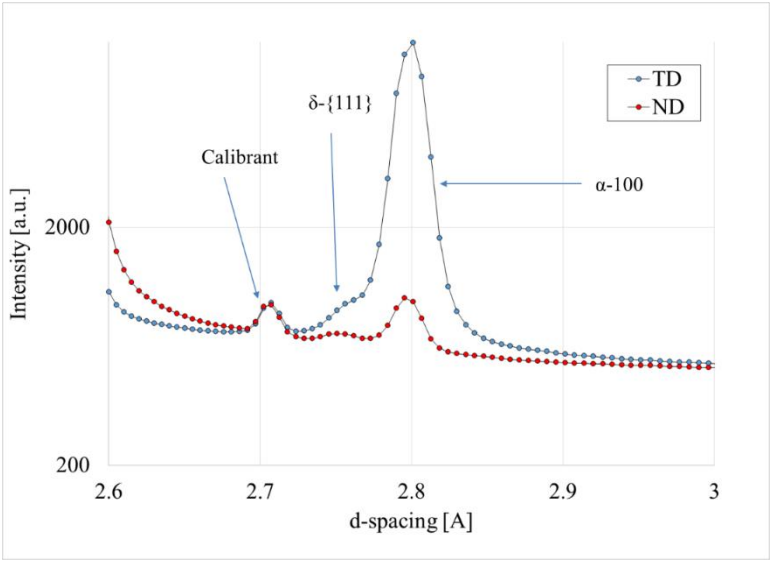

Figure 4-33 X-ray diffraction pattern which is taken from a tapered sample with 180 wt. ppm of hydrogen and 2-cycle treated. Only radial hydrides exist at this location. (RHF≈1). Ceria is used as the calibrant.

4.7 X-ray Diffraction Experiments of Irradiated Cladding Samples

To understand the applicability of unirradiated but pre-hydrided sample tests to irradiated material, some limited examinations were performed using synchrotron radiation of high burn-up samples which had taken previously subjected to various hydride reorientation treatments. For these examination, nuclear power reactor irradiated cladding samples were defueled Zircaloy-4 and M5 spent fuel cladding tubes were utilized. All samples were prepared in the hot cell at ANL under the supervision of M. Billone, as described in Chapter 2.

4.7.1 Examination of Irradiated Zircaloy-4 of H.B. Robinson

The first experiment was designed to determine the presence of the hydride phase in irradiated Zircaloy-4 spent fuel cladding material from H.B. Robinson Nuclear Power Plant at room temperature. The sample, which contained 270 wt. ppm of hydrogen (see Figure 4-34a) was in the

as-irradiated condition, i.e. no thermo-mechanical treatment was applied to it prior to the examination. In this experiment, the X-ray diffraction pattern from the irradiated sample (see Figure 4-34a and b) were acquired at room temperature in the absence of stress at various locations using a 0.1 mm 80 keV beam by an x-y scan of the sample surface. To investigate the differences in the X-ray diffraction signals, a 120°-arc segment of tubular sample with 243 wt. ppm of hydrogen which was pre-hydrided by gaseous diffusion as described in Section 2.5 was also examined at room temperature.

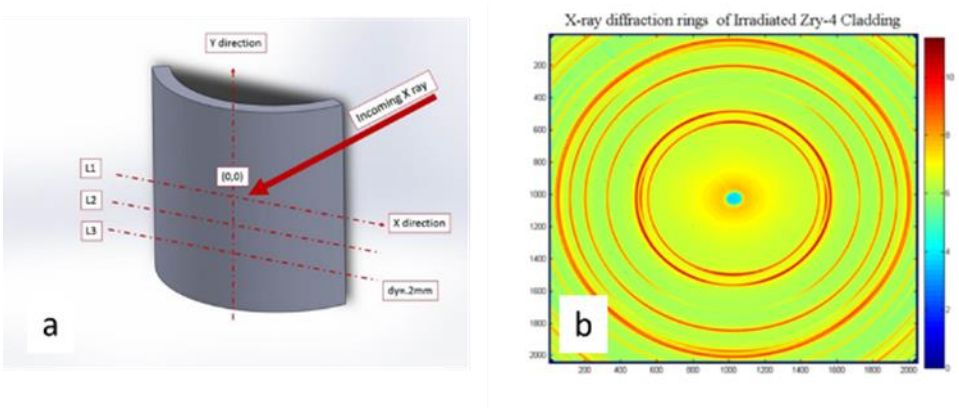

Figure 4-34 (a) A schematic diagram of the irradiated specimen and direction of the x-ray beam and (b) diffraction rings of the irradiated sample

The α-zirconium peaks are observed in the diffraction pattern at the expected two-theta positions and indexed as shown in Figure 4-35. The strongest δ-hydride peak {111} is convoluted with the main α-{100} zirconium peak (Figure 4-35). The positions of the α-zirconium and δ-hydride peaks are shown in Table 4-5 and compared to the peak positions from the Powder Diffraction Files (05-0995 and 34-0649) [145, 146]. The peak positions correspond quite well, as the discrepancy is less than 0.15%.

The intensity of the observed peaks differs significantly from the powder diffraction data due to the crystallographic texture of the cladding tube as a result of manufacturing process. In

particular the intensity of the basal plane reflection is significantly decreased since a majority of the basal planes have their normal parallel to the beam direction (radial direction of the tube).

Table 4-5 An indexing of the diffraction peaks that represent the α-zirconium and the δ-zirconium hydride

Peaks	Expected d-spacing [Å]	Fitted d-spacing [Å]	Relative difference in peak location by fitting [%]
α-{100}	2.798	2.798	0.002702
α-{002}	2.573	2.577	0.152112
α-{101}	2.459	2.459	0.015189
α-{110}	1.616	1.616	0.018764
δ-{111}	2.760	2.759	0.000401

Comparing the diffraction behavior of the irradiated Zircaloy-4 cladding and un-irradiated Zircaloy-4 sheet, the diffraction peaks of α-zirconium are wider in the irradiated Zircaloy-4 sample than in the unirradiated Zircaloy-4 sample, as measured by the full-width-half-maximum (FWHM) shown in Figure 4-35b. This peak broadening is likely caused by the lattice defects formed as a result of radiation damage. As discussed in the literature, neutron irradiation of zirconium alloy at reactor operating temperatures causes the formation of defects and defect clusters which coalesce into <a> dislocation loops, both interstitial and vacancy in nature, and <c> component loops. The high concentration of these defects after irradiation causes peak broadening. In both cases the δ-{111} hydride peak is easily noticeable and appears to have similar d-spacings of 2.760 (PDF values) and 2.759 Å (irradiated), although the broadening of the α-{100} zirconium peak causes the hydride peak to be more convoluted with α-{100} zirconium peak in the unirradiated sample.

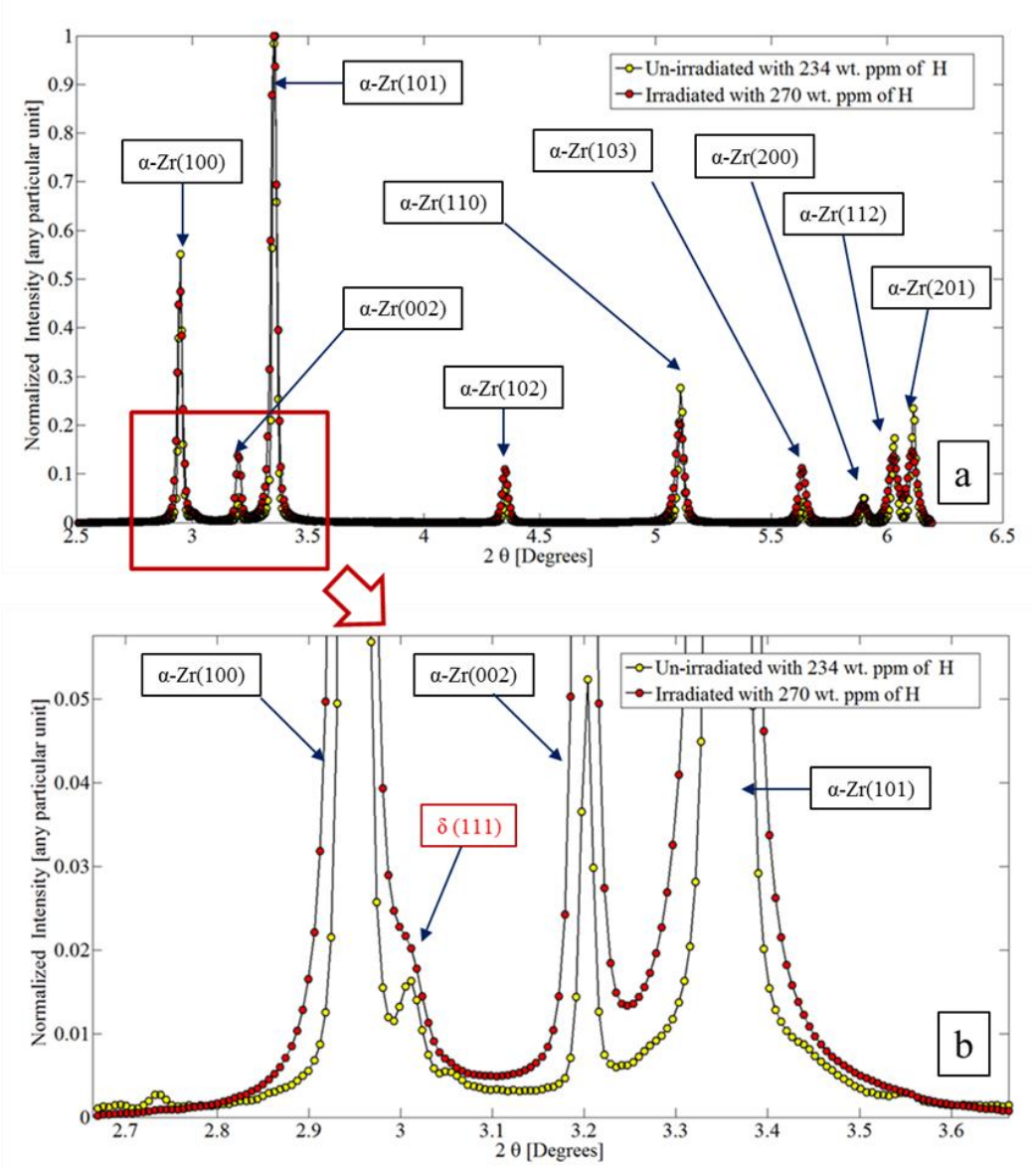

Figure 4-35 (a)X-ray diffraction pattern of both irradiated tubing and un-irradiated sheet Zircaloy-4.(b) Magnification of X-ray diffraction pattern shown in (a) in the region near the hydride peak.

4.7.2 Examination of High Burn-up Irradiated M5 Cladding

A more in-depth study of the effect of thermo-mechanical treatments in hydride precipitation was conducted in which different samples were prepared with different radial hydride continuity factors (RHCF). Four M5 spent fuel cladding segments having similar burn-up values and hydride contents but different radial hydride continuity factors (RHCF) as a result of different post-irradiation thermo-mechanical treatments were examined at the APS/ANL facility. The samples were subjected to the 1-cycle thermo-mechanical treatment under supervision of M. Billone [18]. Table 4-6 shows the list of the M5 cladding samples tested at APS at ANL and their properties. Sample number 1 was examined in the as-irradiated state, while samples 2 to 4 were subjected to different stress levels in the thermo-mechanical treatment to achieve different radial hydride continuity factors (RHCF) as indicated in Table 4-6 [18]. Sample 5 was the unirradiated control sample.

Table 4-6 List of M5 cladding samples tested at APS at ANL

Sample Designation (ANL Designation)	H content [wt. ppm]	Oxide Thickness [μm]	Burn-up [GWd/MTU]	Stress applied during treatment [MPa]	Resulting RHCF after treatment [%]
1 (652E6J)	76±5	8	72	0	0
2 (651E3H)	58±15	9	68	90	31±13
3 (651E5F)	72±10	8	68	110	61±10
4 (645D5)	94±4	13	63	140	72±10
5 (as received)	0	0	0	0	0

Figure 4-36 shows the initial hydride microstructure of the as-irradiated sample (Sample number 1 in the Table 4-6). The M5 cladding, which is a Zr-1%Nb alloy, has a similar texture to that of Zircaloy-4 material but it is in the recrystallized stress relief (RXA) state. Figure 4-37 shows the hydride microstructures of irradiated and radial hydride treated samples which were tested by X-ray diffraction.

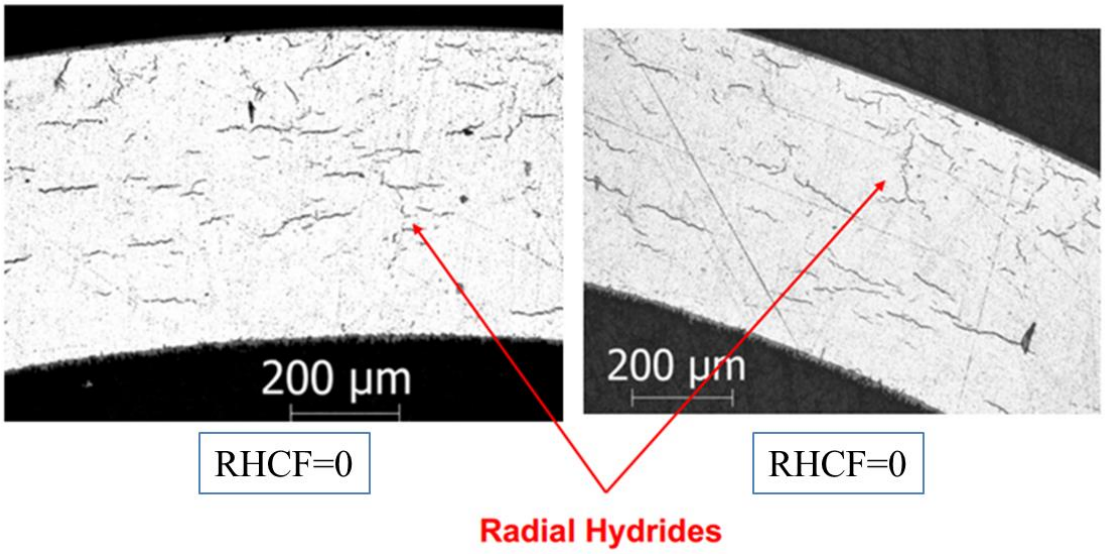

Figure 4-36 The hydride microstructure of the as irradiated M5 cladding material (Sample number 1). Micrographs were provided by M. Billone and T. Burtseva (ANL).

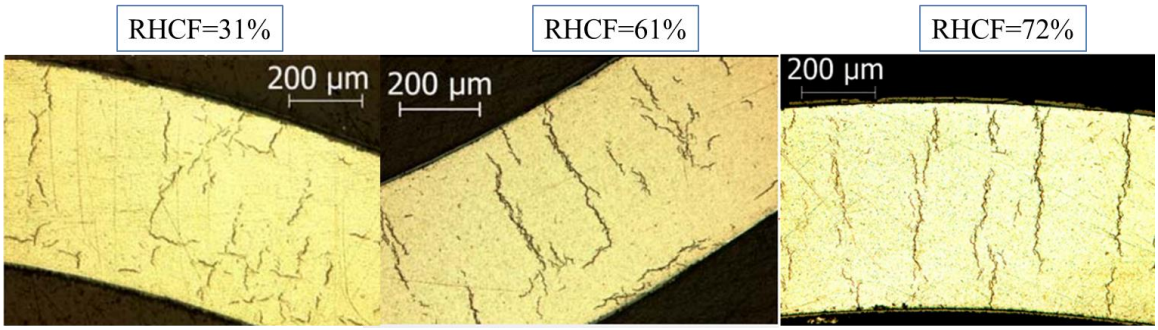

Figure 4-37 (a) Hydride microstructure of sample with RHCF of 31%(Sample 2), (b) Hydride microstructure of sample with RHCF of 61% (Sample 3), (c)Hydride microstructure of sample with RHCF of 72% (Sample 4). Micrographs were provided by M. Billone and T. Burtseva (ANL).

X-ray diffraction patterns of the samples were acquired using a beam energy of 86keV and a beam size of 100x100μm. These X-ray diffraction patterns M5 cladding tube were indexed, and the main phases were determined as shown in Figure 4-38. In the unirradiated sample in addition to α-zirconium peaks, β-niobium peaks were also observed as expected since M5 contain niobium alone the solubility. Figure 4-38 also shows the comparison of the X-ray diffraction of as-irradiated and the as-received M5 cladding tubes. As increase of the FWHM in the irradiated samples was observed as a result of microstructural evolution under irradiation as seen in Zircaloy-4.

Figure 4-38 shows the diffraction patterns obtained for the five samples resulting from the integration of the Debye rings over both circumferential (hoop) direction and axial direction. The expected variation in α-zirconium peak locations due to texture are observed. Notably, the α-{002} peak was observed in the diffraction pattern of the axial direction with low intensity compared to that seen in the circumferential direction. In general, M5 cladding's texture is similar to the Zircaloy-4, such that Kearns' factor on the axial direction is low, (~ 0.1). Therefore, α-{002} peaks usually are not observed in that orientation. Another important observation of α-zirconium peak in Figure 4-38 was the peak broadening, induced by the defect creation by neutron irradiation, as a result of radiation damage. The peak broadening of M5 cladding is also similar to that of observed in Zircaloy-4 that all samples had similar burn-ups and zirconium phases. The FWHM change of α-zirconium peaks of all samples are similar since their burn-ups are similar as shown in Table 4-6. Thus similar burn-up values indicates that all samples were experienced similar irradiation damage conditions during reactor operation.

The most notable change in the diffraction patterns of the as-received state to the as-irradiated state is the significant decrease or disappearance of two β- {110} and {200} niobium peaks which were visible before irradiation. This behavior was observed in X-ray diffraction patterns of both circumferential and axial direction. For the as-irradiated samples, small diffuse

shoulders near the α-{101} and {102} zirconium peaks were observed near the expected β niobium peak locations (~2.4 A), i.e. a slightly large lattice spacing than that of the β niobium. This could be caused by the dissolution of the β phase, with the migration of niobium atoms into the α-zirconium phase and the precipitation as small β niobium rich precipitates of different lattice spacing. Bechade et al. observed the formation of nanometer-sized, needle-shaped niobium rich precipitates after irradiation of M5 [149].

Regarding the δ-{111} hydride peak, the overall hydrogen contents in these samples are relatively low, so it is difficult to distinguish the hydride peaks from the α-zirconium peaks and the background. Thus, the δ-{111} peak appears as a small shoulder on the α-{100} peak, becoming just a little more noticeable after the highest stress thermo-mechanical treatment, especially in the circumferential direction. As a result, no conclusion can be gathered regarding to the behavior of hydrides and hydride reorientation signature. To obtain this information sample with higher hydrogen contents would be required.

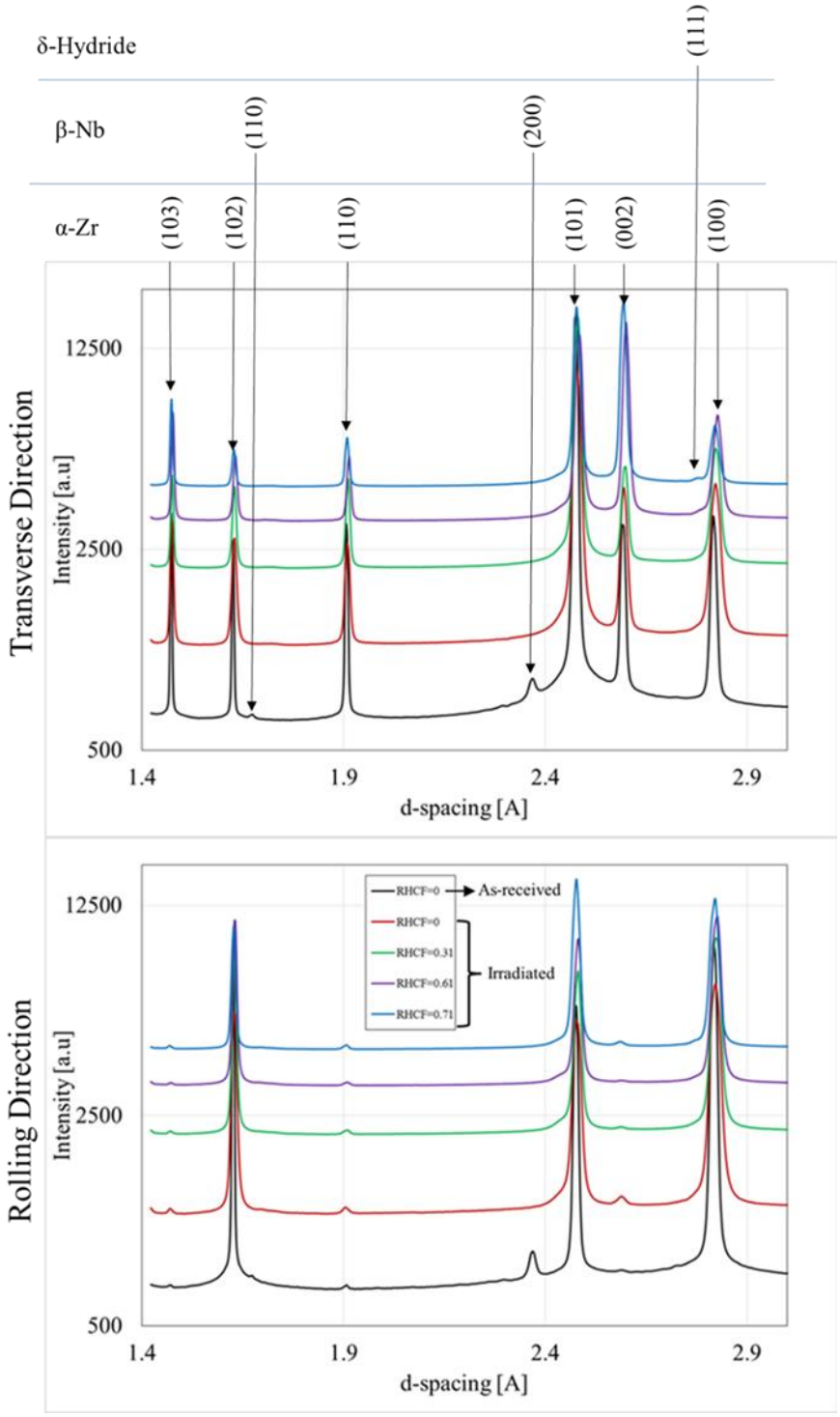

Figure 4-38 Comparison of the X-ray diffraction patterns of M5 unirradiated, as-irradiated and after different heat treatments as specified in Table 4-6.

4.8 Discussion of the Experimental Results of X-ray Diffraction Tests

In this chapter, the hydride reorientation phenomenon as a result of precipitation under tensile stress was investigated using synchrotron X-ray diffraction technique. First, the hydride phase formation and dissolution was studied in a pre-hydrided sample. Secondly, the dissolution and precipitation behavior of hydrides were investigated. Then, the variation in the d-spacing of the α-zirconium and δ-hydride phases during thermo-mechanical treatments at different stress states and cooling rates was studied. A radial hydride signature was determined from the d-spacing data of the tapered uniaxial tension sample. Finally, irradiated cladding samples having different radial hydride fractions were characterized using X-ray diffraction.

The main discussion topics in this section can be listed as follows;

- The difference between the dissolution and precipitation temperatures caused by the undercooling for both circumferential and radial hydrides.
- The effect of stress and stress state on radial hydride precipitation temperature
- The α-Zirconium lattice expansion as a result of hydride dissolution
- The bi-linear hydride thermal expansion behavior for circumferential and radial hydride edge planes during heating up under no far field stress.
- The hydride d-spacing obtained from the hydride faces for circumferential and radial hydrides are under tensile strain compared to the circumferential and radial hydride d-spacing at the platelet edges. This behavior is denoted as radial hydride signature for the hydride reorientation experiments.
- The thermal contraction of radial hydride face planes due to heating. The radial hydride d-spacing at the hydride faces that are under tensile strain decreases as temperature increases to remove those tensile strains caused by the stress state within the hydride, thermal-expansion mismatch, and the transformation strains.

The difference between the observed hydride dissolution and precipitation temperatures shows a hysteresis because of the energy barrier of nucleation during hydride precipitation. The undercooling supplied a certain amount of thermal energy in order to create the hydride interface and to supply the strain energy associated with the transformation, for both circumferential and radial hydrides.

The circumferential hydride precipitation temperature observed in this work was systematically lower than the observed previously [17] for similar hydrogen contents. The reason for this difference is not clear but could be related to difference in the sample microstructure between this and other studies.

The precipitation temperature also appeared to be decreased with increasing stress and biaxiality ratio, with the exception of where the sample has yielded. The reason for this decrease is not clear, but could be related to the different precipitation mechanisms of hydrides, including the circumferential and radial hydrides.

The expansion of the Zirconium lattice is caused by hydrogen dissolution while temperature increases. Barrow et al. observed the lattice expansion for Zircaloy-2 with 131 wt. ppm of hydrogen as a result of heating and cooling cycles [34]. Since, the hydrogen contents are similar to Barrow's analysis, the lattice expansion was determined similar 0.001. Further analysis can be applied as a function of hydrogen content to relate lattice expansion to the hydrogen content but this study aims to establish an understanding of hydride reorientation.

Another important result was the final radial hydride d-spacing along TD orientation (the load applied) is independent of the applied stress, the thermo-mechanical cycles, stress states, and the cooling rate. For all the samples including the tapered sample, there was a residual tensile strain in the stress applied direction relative to other directions. One speculation may be possible with the inspection of the hydride d-spacing in ND. For circumferential hydrides, the d-spacing in ND

could be similar to the d-spacing of radial hydrides in TD that may suggest that the radial hydride δ-{111} planes at TD have the same closed-packed orientation relationship with the circumferential hydride δ-{111} planes at ND.

The thermal expansion behavior shown in Figure 4-18 is unexpected since mechanical behavior of hydrided Zircaloy-4 (specifically the ductile to brittle transition behavior) indicates that the hydrides are *softer* than the matrix at elevated temperatures [8]. Thus, it could be expected that the "soft" hydrides would be constrained by the harder matrix at high temperature, and their thermal expansion rate would be that of the matrix at high temperatures. Conversely, at low temperatures where the hydrides should be the harder constituent, this reasoning would predict that their expansion rate might approach that of an unconstrained hydride. The reverse is seen in Figure 4-18 where the hydride expands at the unconstrained rate only at *high* temperatures.

The bi-linear d-spacing expansion as a function of temperature in Figure 4-18 can be explained by the change of the local stress state near hydride platelets during dissolution. Puls [39] and Singh [86] calculated stresses acting on the hydride platelet edges and face that are highly compressive when hydrides precipitate surrounded by the zirconium matrix and become tensile during dissolution as shown Figure 4-39. Thus, as dissolution starts, the triaxial compressive stress state within the hydrides becomes tensile which enables hydrides to expand at higher expansion rates as will be explained in next paragraph.

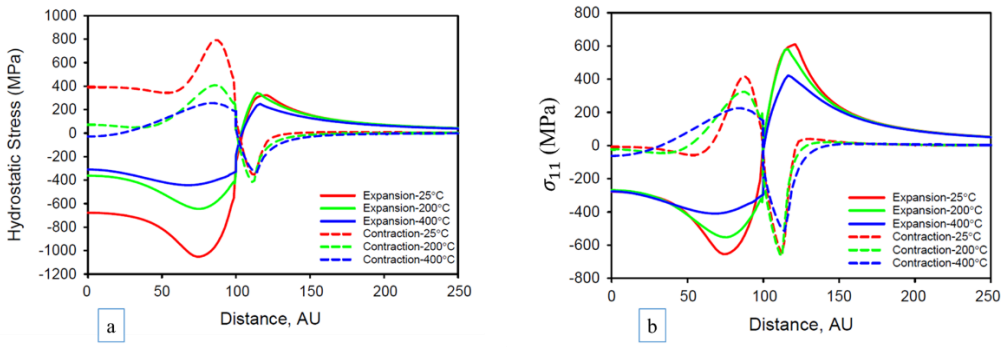

Figure 4-39 (a) the hydrostatic stress distributions within the hydride platelet during precipitation (expansion) and dissolution (contraction) (b) the stress normal to the hydride platelet face during precipitation and dissolution [86].

By using Hooke's law, Singh's finite element analysis shows that as the temperature increases, the compressive stresses at the edge direction of hydrides as shown in Figure 4-40 (initially higher than the compressive stresses at the face direction of hydride) is removed at a higher rate than the stresses on the hydride face and becomes tensile as shown in Figure 4-41 [86]. As hydrides dissolve in the matrix during heat-up, the hydride expands and matrix contracts because of the loss of hydrogen volume near the hydride platelet tip that the matrix shrinks into. Therefore, dissolution removes the compressive stress state that precipitated hydride experiences at low temperatures. Thus, the reversal of the local stress state from compression to tension removes the constraint of the Zircaloy-4 matrix, and hydride can expand its thermal expansion coefficient which is higher than the Zircaloy-4.

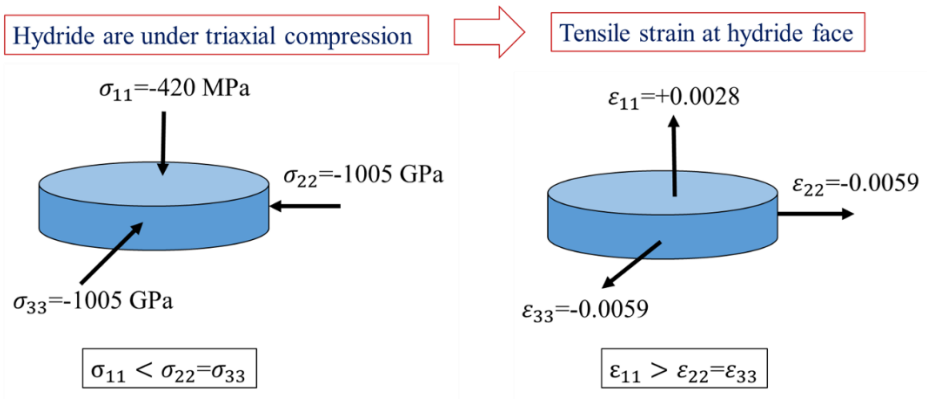

Figure 4-40 The hydride stress and strain states according to Singh's finite element results [86] while they are precipitated in zirconium matrix. The strains are predicted using generalized Hooke's law.

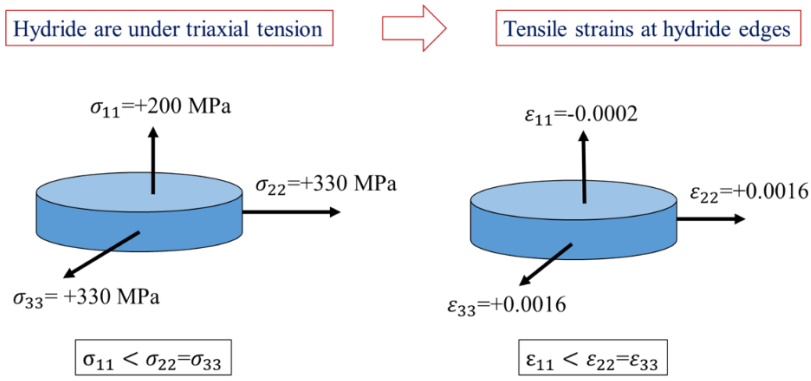

Figure 4-41 The hydride stress and strain states at 200 °C at which temperature the bi-linear thermal expansion behavior starts during dissolution from Singh finite element analysis [86]. The strains are predicted using generalized Hooke's law.

Also, they calculated that the compressive stresses acting on the hydride edges are higher than those acting on the hydride face as shown in Figure 4-40. The analysis done by Singh indicated that the hydride face will be under tensile strain (according to the Hooke's law). Thus, considering the hydride face is aligned perpendicular to the applied stress direction after hydride reorientation, the δ-{111} d-spacing at the hydride face will apparently be higher than the d-spacing values at the hydride edges as observed during the room temperature X-ray diffraction experiments (see Figure 4-30).

The thermal expansion behavior of radial hydrides in RD shows the same bi-linear behavior as in circumferential hydrides. However, the d-spacing behavior during heating for TD is distinctive, since as the temperature increases the d-spacing decreases; thermal contraction happens. This thermal contraction may be speculated in terms of the change of stress state and thermal mismatch strain between hydrides and zirconium matrix which cause decrease in the large residual tensile strains accumulated in the hydrides normal to their flat faces (considering earlier described anomalous thermal expansion behavior of the hydrides upon heating). The residual tensile strain for out-of-plane hydrides (see Figure 4-17) has now two parts: the tensile hydride face strain, which is caused by the triaxial compressive stress state and the thermal expansion mismatch strain between hydride and zirconium matrix which also depends on the anisotropic misfit strains to accommodate the excessive volume of the hydride. Thus, the residual tensile strain is removed during heating by thermal contraction as observed in Figure 4-17. This thermally induced contraction of the radial hydrides continues upon heating from 150°C to about 330°C at which temperature the hydride begins to expand at a rate roughly similar to that of the unconstrained case seen in the in-plane hydrides during heat up ($\approx 20\ 10^{-6}/°C$). At about 330 °C, it may be inferred that residual hydride strain relaxation due to the differential of thermal expansion rates between hydride and matrix is completed. Furthermore, this same behavior can be observed in the 4^{th} (and 5^{th} cycles) with cooling rates of 5°C/min and 10°C/min.

5 CONCLUSIONS

The main goal of this study was to investigate hydride reorientation behavior in Zircaloy-4 alloy for nuclear fuel cladding material as influenced by thermo-mechanical history and far-field stress state. In order to elucidate the stress state effect, mechanical test experiments were performed using a novel mechanical tensile test sample design that created a range of tensile biaxial stresses within the specimens. Matching the stress state calculated by finite element analysis at a specific location within a specimen to the hydride microstructure at that location was then used to identify the effect of stress state on hydride reorientation. In situ high energy X-ray diffraction experiments using synchrotron radiation were performed to investigate the dissolution-precipitation behavior of both in-plane and radial hydrides as well as the misfit strain characteristics of the hydride platelets during thermo-mechanical treatment of samples. The major conclusions obtained from this study are as follows:

1- The presence of a minor stress in addition to the major principal stress enhanced the hydride reorientation. Mechanical tests using novel specimen configurations that induce stress states ranging from uniaxial to "near-equibiaxial" tension showed that as stress biaxiality ratio increased, the threshold stress for radial hydride formation decreased. The threshold stress was determined as 150 MPa for uniaxial tension, 115 MPa for "plane-strain" tension, but only 85 MPa for "near-equibiaxial" tension.

2- The degree to which multi-axial tensile stresses assisted the nucleation of radial hydrides was theoretically modelled using the Gibbs free energy differences of transformation that include the effect of far-field tensile stress. The (major principal) threshold stress for radial hydride formation was predicted to be linearly related to the magnitude of the *minor* principal stress, such that increasing the minor stress decreased, the threshold stress decreased with a rate that depended on the hydride transformation strain. The

experimental results agree well with the theoretical predictions of the model, assuming recently predicted values of the transformation strains.

3- Room temperature X-ray diffraction data showed that the d-spacing of those δ-hydride {111} planes oriented perpendicular to the tensile stress increased with increasing radial hydride fraction (RHF). This increased δ-{111} d-spacing is a radial hydride signature that can be observed using high energy X-ray diffraction.

4- The d-spacing of in-plane δ-{111} planes for all orientations showed "bi-linear" expansion behavior while heating-up such that the rapid thermal expansion rate of the δ-hydrides was observed only at elevated temperatures. Based on a computational analyses of stresses within precipitating and dissolving hydrides, the bi-linear behavior can be explained in terms of a change in stress state within the hydrides from compression to tension as hydrides dissolve, enabling a more rapid rate of thermal expansion (characteristic of hydrides) at elevated temperatures.

5- The presence of radial hydrides increased the ductile to brittle transition temperature (DBTT) observed during tensile testing. If the temperature was sufficiently low for radial hydrides to initiate cracks, the radial hydrides and their connectivity with the circumferential hydrides increased the DBTT and decreased the fracture resistance of the cladding.

6- The failure behavior of brittle-like specimens was consistent with linear elastic fracture mechanics based on an initial flaw size determined by a cluster of radial hydrides that have a high degree of interconnectivity. Based on the application of fracture mechanics formulations to determine the stress intensity of the initial crack, the stress intensity values exceeded the expected fracture toughness of the cladding for its radial hydride population and their connectivity. Thus, the samples exhibited unstable crack propagation after crack initiation, and "brittle-like" behavior resulted.

6 RECOMMENDATIONS FOR FUTURE WORK

This study investigates the mechanisms of hydride reorientation as influenced by the far-field stress state acting on hydride precipitates using in situ high energy X-ray diffraction techniques which enables to track hydride d-spacing variation from diffraction signals during dissolution and precipitation. This study mostly involved hydride d-spacing variations on directions (TD and RD) which represents the loading conditions similar to vacuum drying conditions. However, the diffraction data obtained from normal direction (ND) is also essential to complete understanding of strain variation during phase transformations. Also, the failure criterion for radial hydrides should be established considering the change in failure mode as hydride microstructure changes. The main points of research activities on zirconium hydride dissolution and precipitation which will support the model developments can be proposed as follows:

The dissolution and precipitation behavior of hydrides under tensile stress:

The d-spacing behavior of pre-hydrided samples that incoming X-ray beam hits the TD-ND plane of the sample which allows to obtain diffraction data from δ-hydride planes that are oriented perpendicular to the ND plane where 60% of basal planes of α-zirconium on the average present. Hydrogen contents of samples should be higher than 250 wt. ppm; samples with 300 wt. ppm of hydrogen enable to acquire δ- {220}, {200}, and {301} peak, in addition to δ-{111} peak. Particularly, the δ-{220} family of planes involve planes that are perpendicular to the {111} family of planes. Thereby, acquiring {220} family peaks allow to predict strain evolution at closed-packed planes and those planes that are perpendicular to the closed-packed planes. To prevent and assure any peak saturation and bleeding, or unpredicted responses from detector, diffraction data should be acquired at 0.5 sec for 20 frames and each data point should have at least 2 sec lag-time (in total a data should be acquired at least in 3 seconds.)

Understanding the hysteresis on hydride precipitation:

According to the strain energy accommodation theory, the hysteresis is caused by partial relaxation of the plastic strain energy which is directly related to the dislocation density and dislocation structure. To investigate this effect for a given material such as Zircaloy-4, pre-hydrided material in the conditions of: as-hydrided, annealed out at 400, 500, and 600°C should be subjected to identical heat treatments. In addition, extra pre-hydrided materials should be plastically deformed to various levels prior to thermo-mechanical treatments. The hydride dissolution and precipitation behavior from X-ray diffraction should be acquired by X-ray beam size of at least 200x200μm up to 1x1mm to ensure the local hydrogen variations are not important.

Hydride rim formation

A procedure should be developed to create hydride rim microstructure that are observed in cladding materials after operation. This goal may be achieved as follows: the tubular or flat samples are hydrided to 500 wt. ppm. Then, one side of the flat sheet will be attached to a heating element and insulated from outside environment. Other side will be open to a coolant (oil, water, or high velocity air stream). At first, samples will be heated up and hydrogen will be dissolved. Then, the temperature gradient will be applied to the sample that should cause rim formation. After then, the sample will again be hydrogen charged, but this time the charging temperature will be less than the dissolution temperature of the hydrogen content of 500 wt. ppm. Then, the sample will again be subjected to temperature gradient. This successive process will continue until the desired rim structure is obtained.

APPENDIX A

THE CALCULATION OF MISFIT STRAINS BY ITS FORMAL DEFINITION AND COMMENT ON ATOMIC RADII METHOD

The Carpenter's and Singh's analyzes are based on the closed-packed plane orientation relationship of δ-{111} parallel to α-(002) and volumetric accommodation of stress-free, isotropic, and cubic FCC (without distortion) δ-hydride crystal into the anisotropic HCP α-zirconium crystal by atomic radii method. Carpenter also states that the anisotropy of the misfit is caused by the entirely the anisotropy of the α-zirconium crystal and is independent of the relative orientation of the hydride[40].

However, the d-spacing of hydrides, in particular for circumferential hydrides, shows difference to the α-zirconium materials axis such as normal (radial for tubes) and transverse (hoop) directions, please see Table 4-4 in Section 4.6. Thus, the misfit estimation, in particular for circumferential hydrides embedded in CWSR zirconium matrix only shows the maximum possible misfit accommodation, the actual transformation strains in CWSR Zircaloy-4 will be lower due to the grain boundaries and dislocations.

As will be discussed in Section 4.6, when only the radial hydride microstructure is present, the hydride {111} d-spacing in normal direction, that is 2.751Å, (ND) which gets closer to hydride {111} d-spacing in the transverse direction, that is 2.759Å, (TD, the stress applied direction), please see Table 4-4. Thereby, the d-spacing difference at normal and transverse directions for radial hydrides can be thought as similar. Thus, the same procedure of the transformation strain calculation based on atomic radii could be applied to the radial hydrides only, considering the radial hydride precipitation is dictated by nucleation process. Noting cautiously again, for circumferential hydrides, the d-spacing difference between ND (2.763Å) and TD (2.754Å) is more significant than

the radial hydrides. Thus, the Singh's procedure will fail in case of circumferential hydrides because the importance of the orientation relationship constrain increases and the correct lattice parameters of hydrides must be involved in analysis. Thus, it is essential to include misfit strain calculation by the formal definition of misfit strain using the d-spacings of hydrides and matrix as:

$$\varepsilon_{[hkl]} = \frac{d_H - d_\alpha}{d_\alpha} \tag{A.1}$$

where $\varepsilon_{[hkl]}$ is the misfit (transformation strain) at relevant direction due to the orientation relationship d_H and d_α are the d-spacing of corresponding planes in hydride and α-zirconium matrix. Hence, the dilatation transformation strain (e_1^T) can be directly written as:

$$e_1^T = \frac{d_{\delta 111} - d_{\alpha 002}}{d_{\alpha 002}} \tag{A.2}$$

where $d_{\delta 111}$ is the d-spacing of hydride in <111> direction (closed packed direction) and $d_{\alpha 002}$ is the d-spacing of α-zirconium in <002> direction (normal to the basal plane). Equation (3.5) is based on the closed packed plane orientation relationship of δ-hydride {111} plane parallel to α-zirconium (002) plane

On the other hand, the second component of misfit can be calculated by considering the corresponding planes that are perpendicular to the δ-{111} or α-(002) which is δ-$(2\bar{2}0)$ or δ-{220} and α-{100}. Thus the minor transformation strain is written as:

$$e_1^T = \frac{d_{\delta 2\bar{2}0} - d_{\alpha 100}}{d_{\alpha 100}} \tag{A.3}$$

The Equations (3.5) and (3.6) describes the amount of strain that is accommodated as a result of hydride precipitation. For Singh's procedure, the stress-free conditions yields that the hydride lattice spacing is unique, that is the powder diffraction value, and the transformation strain

calculated at stress-free hydride crystal represents the maximum misfit if the hydride crystal ideally fit into zirconium crystal which is basically valid for homogenous nucleation of hydrides. Actually, hydride precipitation initiates at grain boundaries, stacking-faults, or dislocations for CWSR Zircaloy-4 material. Thus, the expected transformation strain that accommodates the volume difference caused by fitting the hydride in matrix could be lesser than the stress-free misfit strains.

As mentioned above such a misfit calculations is valid only if the orientation relationship described above is maintained in the reoriented hydride. As described in Chapter 3.5, the d-spacings of the δ-hydrides and α-zirconium obtained by high energy X-ray diffraction are as follows

Table A-1 d-spacing data of both α-Zirconium and δ-hydrides at room temperature

	d-spacing [Å]
Zirconium α(002)	2.5859
In-plane (circumferential) hydrides δ{111}	2.763
Out-of-plane (radial) hydrides δ{111}	2.759

By using the d-spacings as shown in Table 3-2, Equation (3.5) indicate that the dilatational transformation strains at room temperature in the orientation normal to the hydride platelet are

e_1^T = 0.0685 for circumferential hydrides and

e_1^T = 0.0669 for radial hydrides.

These room temperature values, which are obtained by the X-ray diffraction experiments, are similar to Carpenter's value (0.072) but smaller than the e_1^T = 0.077 which was estimated at 300°C calculated by Singh et al. based on the lattice parameters of stress-free pure α-zirconium single crystal. However, the lattice parameters of CWSR Zircaloy-4 alloy differ from those of pure α zirconium because of cold-work and because of the presence of alloying elements. Importantly,

the d-spacing of δ-($2\bar{2}0$) was not fittable because of its low intensity and convolution with α-zirconium peak. So, the minor transformation strain could not be calculated.

APPENDIX B

THE CALCULATION OF STRESS INTENSITY FACTORS THAT ARE USED IN FRACTURE MECHANICS ANALYSIS OF "BRITTLE-LIKE" SAMPLES

I. CORNER CIRCULAR CRACK [150]

The stress intensity factor is written as

$$K_I = 1.12^2 \frac{2}{\pi} \sigma \sqrt{\pi a} \tag{B-1}$$

where σ is the tensile stress and a is the radius of quarter circular crack

II. SINGLE EDGE CRACK [150]

$$K_I = f(\frac{a}{W}) \sqrt{\frac{\pi a}{W}} \sigma \sqrt{\pi a} \tag{B-2}$$

$$f\left(\frac{a}{W}\right) = \frac{\sqrt{2\tan(\frac{\pi a}{2W})}}{\cos(\frac{\pi a}{2W})} [0.752 + 2.02\left(\frac{a}{W}\right) + 0.37(1 - sin\frac{\pi a}{2W})^3] \tag{B-3}$$

where σ is the tensile stress, a is the crack length, and W is the specimen width

III. CORNER ELLIPTICAL CRACK [143]

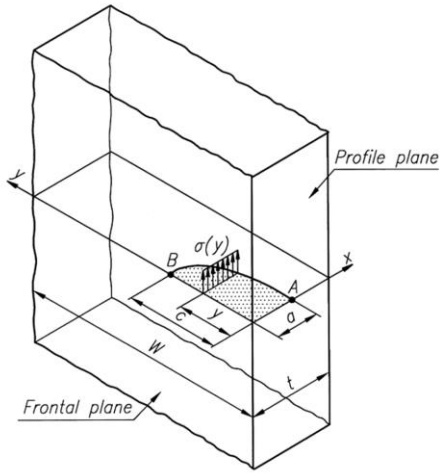

Figure B-1 Corner quarter elliptical crack in a finite thickness plate subjected to a uniform loading [143]

The stress intensity at front A:

$$K_I^A = \sigma \sqrt{\frac{\pi a}{Q}} Y_0 \tag{B-4}$$

The stress intensity at front B:

$$K_I^B = \sigma \sqrt{\frac{\pi a}{Q}} F_0 \tag{B-5}$$

$$Q = \begin{cases} 1 + 1.464\,(a/c)^{1.65} & a/c \le 1 \\ 1 + 1.464\,(c/a)^{1.65} & a/c > 1 \end{cases} \tag{B-6}$$

$$Y_0 = A_0 + A_1(a/t)^{A_2} \quad \text{(B-7)}$$

$$F_0 = D_0 + D_1(a/t)^{D_2} \quad \text{(B-1)}$$

Please see paper called *"Weight functions and stress intensity factors for corner quarter-elliptical crack in finite thickness plate subjected to in-plane loading"* by Kiciak et al. for constants A and D [143].

BIBLIOGRAPHY

1. Lemaignan, C. and A.T. Motta, Zirconium Alloys in Nuclear Applications, in Materials Science and Technology, A Comprehensive Treatment, B.R.T. Frost, Editor. 1994, VCH: New York. p. 1-51.
2. Kass, S. The Development of the Zircaloys. in Symposium on Corrosion of Zirconium Alloys, ANS Winter meeting, 1963. 1964. New York: ASTM.
3. Brachet, J.C., et al., Influence of hydrogen content on the alpha/beta phase transformation temperatures and on the thermal-mechanical behavior of Zy-4, M4 (ZrSnFeV), and M5 (ZrNbO) alloys during the first phase of LOCA transient. Zirconium in the Nuclear Industry: Thirteenth International Symposium, ASTM STP 1423, 2002: p. 673-701.
4. Sabol, G.P. ZIRLO an Alloy Development Success. in 14th ASTM INternational Symposium on Zr in the Nuclear Industry. 2005. Stockholm.
5. Sabol, G.P., et al. Development of a Cladding Alloy for High Burnup. in Eighth International Symposium on Zirconium in the Nuclear Industry. 1989. San Diego: ASTM.
6. Douglass, D.L., The Metallurgy of Zirconium. 1971, Vienna: International Atomic Energy Agency Supplement.
7. Tenckhoff, E., Deformation Mechanisms, Texture and Anisotropy in Zirconium and Zirconium Alloys. STP. Vol. 966. 1988, Philadelphia: ASTM.
8. Raynaud, P., Crack Growth Through the Thickness of THin-Sheet Hydrided Zircaloy-4, in Materials Science2009, Penn State University.
9. Zinkle, S.J. and G.S. Was, Materials challenges in nuclear energy. Acta Materialia, 2013. 61(3): p. 735-758.
10. Cox, B., Pellet-clad interaction (PCI) failures of zirconium alloy fuel cladding — A review. Journal of Nuclear Materials, 1990. 172(3): p. 249-292.
11. Edsinger, K. and K.L. Murty, LWR pellet-cladding interactions: Materials solutions to SCC. JOM, 2001. 53(7): p. 9-13.
12. Motta, A.T., A. Couet, and R.J. Comstock, Corrosion of Zirconium Alloys Used for Nuclear Fuel Cladding. Annual Review of Materials Research, 2015. 45(1): p. 311-343.
13. Pierron, O.N., D. A. Koss, ,A. T. Motta, and K. S. Chan, The influence of hydride blisters on the fracture of Zircaloy-4. Journal of Nuclear Materials, 2003. 322: p. 21-35.
14. Couet, A., A.T. Motta, and R.J. Comstock, Hydrogen pickup measurements in zirconium alloys: Relation to oxidation kinetics. Journal of Nuclear Materials, 2014. 451(1–3): p. 1-13.
15. Kearns, J.J., Terminal solubility and partitioning of hydrogen in the alpha phase of zirconium, Zircaloy-2 and Zircaloy-4. Journal of Nuclear Materials, 1967. 22(3): p. 292-303.
16. Kearns, J.J., Dissolution kinetics of hydride platelets in Zircaloy-4. Journal of Nuclear Materials, 1968. 27: p. 64-72.
17. McMinn, A., E.C. Darby, and J.S. Schofield, The terminal solid solubility of hydrogen in zirconium alloys. Zirconium in the Nuclear Industry: Twelfth International Symposium, ASTM STP 1354, 2000: p. 173-195.
18. Billone, M.C., T.A. Burtseva, and R.E. Einziger, Ductile-to-brittle transition temperature for high-burnup cladding alloys exposed to simulated drying-storage conditions. Journal of Nuclear Materials, 2013. 433(1–3): p. 431-448.

19. Commision, U.S.N.R., Standard Review Plan for Spent Fuel Dry Storage Systems at a General License Facility -Final Report (NUREG-1536, Revision 1), in NUREG-15362013.
20. Anatech, Spent Fuel Transportation Applications—Assessment of Cladding Performance, in A Synthesis Report 1015048 A. Machiels, Editor 2007, EPRI.
21. IAEA, Spent Fuel Performance Assessment and Research, in IAEA-TECDOC-13432003, Nuclear Fuel Cycle and Materials Section.
22. Aomi, M., T. Baba, T.Miyashita,K. Kamimura, T. Yasuda, Y. Shinohara, andT. Takeda, Evaluation of Hydride Reorientation Behavior and Mechanical Properties for High-Burnup Fuel-Cladding Tubes in Interim Dry Storage. Journal of ASTM International, 2008. 5(9): p. Paper ID JAI101262.
23. Chu, H.C., S. K. Wu, K. F. Chien, and R. C. Kuo Effect of radial hydrides on the axial and hoop mechanical properties of Zircaloy-4 cladding. Journal of Nuclear Materials, 2007. 362(1): p. 93-103.
24. Zuzek, E., Abriata, J. P., San-Martin, A., and Manchester, F. D., The H-Zr (hydrogen-zirconium) system. Bulletin of Alloy Phase Diagrams, 1990. 11(4): p. 385-395.
25. Dupin, N., I. Ansara, C. Servant, C. Toffolon, C. Lemaignan, and J. C. Brachet, A thermodynamic database for zirconium alloys. Journal of Nuclear Materials, 1999. 275(3): p. 287-295.
26. Cassidy, M.P. and C.M. Wayman, Crystallography of hydride formation in zirconium: the delta yields epsilon transformation. Metallurgical Transactions A, 1980. 11A(1): p. 57-67.
27. Daum R. S., S.C.Y., and A. T. Motta, Identification and Quantification of hydride phases in Zircaloy-4 cladding using Synchrotron Radiation Diffraction. Journal of Nuclear Materials, 2009. 392 (3): p. 453-463.
28. Puls, M.P., The Effect of Hydrogen and Hydrides on the Integrity of Zirconium Alloy Components in Delayed Hydride Cracking2012, Springer.
29. Bradbrook, J.S., G.W. Lorimer, and N. Ridley, The precipitation of zirconium hydride in zirconium and Zircaloy-2. Journal of Nuclear Materials, 1972. 42: p. 142-160.
30. Cassidy, M.P. and C.M. Wayman, Crystallography of hydride formation in Zirconium: The delta yields gamma transformation. Metallurgical Transactions A, 1980. 11A(1): p. 47-56.
31. Setoyama, D. and S. Yamanaka, Phase diagram of Zr–O–H ternary system. Journal of Alloys and Compounds, 2004. 370(1–2): p. 144-148.
32. Moore, K.E., Phase relationships in the $\alpha + \delta$ region of the Zr-H system. Journal of Nuclear Materials, 1969. 32(1): p. 46-56.
33. Beck, R.L., Zirconium-Hydrogen phase system. Transactions of the ASM, 1962. 55: p. 542-555.
34. Barrow, A.T.W., C. Toffolon-Masclet, J. Almer, M. R. Daymond, The role of chemical free energy and elastic strain in the nucleation of zirconium hydride. Journal of Nuclear Materials, 2013. 441(1–3): p. 395-401.
35. Carpenter, G.J.C., J.F. Watters, and R.W. Gilbert, Dislocations generated by zirconium hydride precipitates in zirconium and some of its alloys. Journal of Nuclear Materials, 1973. 48: p. 267-276.
36. Westlake, D.G., The habit planes of zirconium hydride in zirconium and zircaloy. Journal of Nuclear Materials, 1968. 26(2): p. 208-216.
37. Carpenter, G.J.C., The precipitation of gamma-zirconium hydride in zirconium. Acta Metallurgica, 1978. 26: p. 1225-1235.
38. Chung H. M., R.S.D., J. M. Hiller, and M. C. Billone, Characteristics of hydride precipitation and reorientation in spent-fuel cladding. Zirconium in the Nuclear Industry: Thirteenth International Symposium, ASTM STP 1423, 2002: p. 561-582.

39. Leitch, B. and M. Puls, Finite element calculations of the accommodation energy of a misfitting precipitate in an elastic-plastic matrix. Metallurgical Transactions A, 1992. 23(3): p. 797-806.
40. Carpenter, G.J.C., The dilatational misfit of zirconium hydrides precipitated in zirconium. Journal of Nuclear Materials, 1973. 48: p. 264-266.
41. Nath, B., G.W. Lorimer, and N. Ridley, Effect of hydrogen concentration and cooling rate on hydride precipitation in alpha-zirconium. Journal of Nuclear Materials, 1975. 58: p. 153-162.
42. Mishra, S., K.S. Sivaramakrishnan, and M.K. Asundi, Formation of the gamma phase by a peritectoid reaction in the zirconium-hydrogen system. Journal of Nuclear Materials, 1972. 45: p. 235-244.
43. Cann, C.D. and A. Atrens, A metallographic study of the terminal solubility of hydrogen in zirconium at low hydrogen concentrations. Journal of Nuclear Materials, 1980. 88: p. 42-50.
44. Nath, B., G.W. Lorimer, and N. Ridley, The relationship between gamma and delta hydrides in zirconium-hydrogen alloys of low hydrogen concentration. Journal of Nuclear Materials, 1973. 49: p. 262-280.
45. Lanzani, L. and M. Ruch, Comments on the stability of zirconium hydride phases in Zircaloy. Journal of Nuclear Materials, 2004. 324: p. 165-176.
46. Kiran Kumar, N.A.P., J.A. Szpunar, and Z. He, Preferential precipitation of hydrides in textured zircaloy-4 sheets. Journal of Nuclear Materials, 2010. 403(1–3): p. 101-107.
47. Mani Krishna, K.V., A. Sain, I. Samajdar, G. K. Dey, D. Srivastava, S. Neogy, R. Tewari, and S. Banerjee, Resistance to hydride formation in zirconium: An emerging possibility. Acta Materialia, 2006. 54(18): p. 4665-4675.
48. Qin, W., Kiran Kumar, N. A. P.,Szpunar, J. A., and J. Kozinski, Intergranular δ-hydride nucleation and orientation in zirconium alloys. Acta Materialia, 2011. 59(18): p. 7010-7021.
49. Z. Zhao, M.B.-Y., J.P. Morniroli, A. Legris, L. Thuinet, Y. Kihn, A. Ambard, and L. Legras. Characterization of zirconium hydrides and phase field approach to a mesoscopic-scale modeling of their precipitation. in 15th International Symposium on Zirconium in the Nuclear Industry, June 24, 2007 - June 28, 2007. 2009. Sunriver, OR, United states: American Society for Testing and Materials.
50. Pierron, O., Influence of hydride blisters on failure of Zircaloy-4 sheet, in Msc. Thesis in Intercollegiate Graduate Program in Materials 2002, The Pennsylvania State University: University Park, PA. p. 98.
51. Hellouin de Menibus, A., A. Quentin, D. Ousmane, P. Berger, S. Bosonet, E. Foy, V. Macdonald, J. Besson, and J. Crépin, Formation and characterization of hydride blisters in Zircaloy-4 cladding tubes. Journal of Nuclear Materials, 2014. 449(1–3): p. 132-147.
52. Singh, R.N., S. Mukherjee, A. Gupta, and S. Banerjee, Terminal solid solubility of hydrogen in Zr-alloy pressure tube materials. Journal of Alloys and Compounds, 2005. 389(1–2): p. 102-112.
53. Tang, R. and X. Yang, Dissolution and precipitation behaviors of hydrides in N18, Zry-4 and M5 alloys. International Journal of Hydrogen Energy, 2009. 34(17): p. 7269-7274.
54. Une, K. and S. Ishimoto, Terminal solid solubility of hydrogen in unalloyed zirconium by differential scanning calorimetry. Journal of Nuclear Science and Technology, 2004. 41(9): p. 949-952.
55. Une, K. and S. Ishimoto, Dissolution and precipitation behavior of hydrides in Zircaloy-2 and high Fe Zircaloy. Journal of Nuclear Materials, 2003. 322: p. 66-72.

56. Khatamian, D., Solubility and partitioning of hydrogen in metastable Zr-based alloys used in the nuclear industry. Journal of Alloys and Compounds, 1999. 293–295(0): p. 893-899.
57. Khatamian, D. and V.C. Ling, Hydrogen solubility limits in α- and β-zirconium. Journal of Alloys and Compounds, 1997. 253–254(0): p. 162-166.
58. Khatamian, D., et al., Hydrogen solubility limits in Excel, an experimental zirconium-based alloy. Journal of Alloys and Compounds, 1995. 231(1–2): p. 488-493.
59. Khatamian, D. and J.H. Root, Comparison of TSSD results obtained by differential scanning calorimetry and neutron diffraction. Journal of Nuclear Materials, 2008. 372(1): p. 106-113.
60. Colas, K.B., A. T. Motta, M. R. Daymond, and J. D. Almer, Effect of thermo-mechanical cycling on zirconium hydride reorientation studied in situ with synchrotron X-ray diffraction. Journal of Nuclear Materials, 2013. 440(1–3): p. 586-595.
61. Blackmur, M.S., J. D. Robson, M. Preuss, O. Zanellato, R. J. Cernik, S. Q. Shi, F. Riberio, and J. Andrieux, Zirconium hydride precipitation kinetics in Zircaloy-4 observed with synchrotron X-ray diffraction. Journal of Nuclear Materials, 2015. 464(0): p. 160-169.
62. Zanellato, O., M. Preuss, J. Y. Buffiere, F. Riberio, A. Steuwer, J. Desquines, J. Andrieux, and B. Krebs, Synchrotron diffraction study of dissolution and precipitation kinetics of hydrides in Zircaloy-4. Journal of Nuclear Materials, 2012. 420(1–3): p. 537-547.
63. Santisteban, J.R., M. A. Vicente-Alvarez, P. Vizcaíno, A. D. Banchik, and J. D, Almer, Hydride precipitation and stresses in zircaloy-4 observed by synchrotron X-ray diffraction. Acta Materialia, 2010. 58(20): p. 6609-6618.
64. Kammenzind, B.F., Hydrogen pickup and redistribution in alpha-annealed Zircaloy-4. Zirconium in the Nuclear Industry: Eleventh International Symposium, ASTM STP 1295, 1996: p. 338-370.
65. Slattery, G.F., The terminal solubility of hydrogen in the zirconium/2 at % chromium/0.16 at % iron alloy. Journal of Nuclear Materials, 1969. 32(1): p. 30-38.
66. Sawatzky, A. and B.J.S. Wilkins, Hydrogen solubility in zirconium alloys determined by thermal diffusion. Journal of Nuclear Materials, 1967. 22(3): p. 304-310.
67. Erickson, W.H. and D. Hardie, The influence of alloying elements on the terminal solubility of hydrogen in α-zirconium. Journal of Nuclear Materials, 1964. 13(2): p. 254-262.
68. Puls, M.P., The effects of misfit and external stresses on terminal solid solubility in hydride-forming metals. Acta metallurgica, 1981. 29(12): p. 1961-1968.
69. Kim, J.-S. and Y.-S. Kim, Effect of thermal history on the terminal solid solubility of hydrogen in Zircaloy-4. International Journal of Hydrogen Energy, 2014. 39(29): p. 16442-16449.
70. Puls, M.P., On the consequences of hydrogen supersaturation effects in Zr alloys to hydrogen ingress and delayed hydride cracking. Journal of Nuclear Materials, 1989. 165(2): p. 128-141.
71. Puls, M.P., Elastic and plastic accommodation effects on metal-hydride solubility. Acta Metallurgica, 1984. 32(8): p. 1259-1269.
72. Barnett, D.M., On nucleation of coherent precipitates near edge dislocations. Scripta Metallurgica, 1971. 5(4): p. 261-266.
73. Lee, J.K. and W.C. Johnson, Re-examination of the elastic strain energy of an incoherent ellipsoidal precipitate. Acta Metallurgica, 1978. 26(4): p. 541-545.
74. Yamanaka, S., K. Yoshioka, M. Uno, H. Anada, T. Matsuda, and S. Kobayashi, Thermal and mechanical properties of zirconium hydride. Journal of Alloys and Compounds, 1999. 293-295: p. 23-29.

75. Kempter, C.P., R.O. Elliot, and K.A. Gschneidner, Thermal expansion of delta and epsilon zirconium hydrides. Journal of Chemical Physics, 1960. 33(3): p. 837-840.
76. Buccafurni, A., E. R. Carlson, R. Chambers, S. V. Chmielewski, D. L. Hagrman, N. L. Hampton, J. K. Hohorst, E. T. Laats, R. E. Mason, M. L. McComas, K. A. McNeil, M. A. Morgan, C. S. Olsen, and G. A. Reymann, SCDAP/RELAP5/MOD2 Code Manual, Volume 4: MATPRO - A library of materials properties for light-water-reactor accident analysis, NUREG/CR-5273 (EGG-2555), U.S.N.R. Commission, Editor 1990, EG&G Idaho, Inc.
77. Cheadle, B.A., Physical Metallurgy of Zr alloys, in CRNL-12081975, Chalk River National Laboratory.
78. Lloyd, L.T., Thermal Expansion of Alpha-Zirconium Single Crstals, in Metals, Ceramics, and Materials1963, Argonne National Laboratory.
79. Skinner, G.B. and H.L. Johnston, Thermal expansion of zirconium between 298 K and 1600 K. Journal of Chemical Physics, 1953. 21: p. 1383-1384.
80. SCDAP/RELAP5/MOD2, Code Manual volume 4: MATPRO: "A Library of Materials Properties for Light Water Reactors Accident Analysis", NUREG/CR-5273, EG-2555, chapter 4.9. 1990.
81. Beck, R.L. and W.M. Mueller, Mechanical properties of solid zirconium hydride. Nuclear Metallurgy, Vol. VII, A Symposium on Metallic Moderator and Cladding Materials, 1960: p. 63-66.
82. Nakatsuka, M., Elastic anisotropy of zirconium alloy fuel cladding. Nuclear Engineering and Design, 1981. 65(1): p. 103-112.
83. Colas, K., Fundamental Experiments on hydride Reorientation in Zircaloy, in PhD. in Nuclear Engineering2012, The Pennsylvania State University. p. 314.
84. Flanagan, M.E., Effect of Hydrogen on Deformation Behavior of Zircaloy-4, in MSc in Nuclear Engineering2008, Penn State University.
85. Link, T.M., Failure of Zircaloy Cladding under Severe Loading Conditions, in MSc in Materials1997, Penn State University: University Park, PA.
86. Singh, R.N., H. K. Khandelwal, A. K. Bind, S. Sunil, and P. Ståhle, Influence of stress field of expanding and contracting plate shaped precipitate on hydride embrittlement of Zr-alloys. Materials Science and Engineering: A, 2013. 579(0): p. 157-163.
87. Link, T.M., D.A. Koss, and A.T. Motta, Failure of Zircaloy Cladding under transverse plane-strain deformation. Nuclear Engineering and Design, 1998. 186: p. 379-394.
88. Daum R. S., S.M., D. W. Bates, A. T. Motta, D. A. Koss, and M. C. Billone, On the embrittlement of Zircaloy-4 under RIA-relevant conditions. Zirconium in the Nuclear Industry: Thirteenth International Symposium, ASTM STP 1423, 2002: p. 702-718.
89. Glendening, A., et al., Failure of hydrided Zircaloy-4 under equal-biaxial and plane-strain tensile deformation. Journal of ASTM International, 2005. 2(6): p. 1-16.
90. Le Saux, M., J. Besson, S. Carassou, C. Poussard, and X. Averty, Behavior and failure of uniformly hydrided Zircaloy-4 fuel claddings between 25°C and 480°C under various stress states, including RIA loading conditions. Engineering Failure Analysis, 2010. 17(3): p. 683-700.
91. Prat F. , M.G., J. Besson, and E. Andrieu, Behavior and rupture of hydrided Zircaloy-4 tubes and sheets. Metallurgical and Materials Transactions A, 1998. 29A(June 1998): p. 1643-1651.
92. Daum, R.S., D. W. Bates, D. A. Koss, and A. T. Motta. The influence of a hydrided layer on the fracture of Zircaloy-4 cladding tubes. in International Conference on Hydrogen Effects on Material Behaviour and Corrosion Deformation Interactions, Sep 22-26 2002.

2003. Moran, WY, United States: Minerals, Metals and Materials Society, Warrendale, PA 15086, United States.
93. Yunchang, F. and D.A. Koss, The influence of multiaxial states of stress on the hydrogen embrittlement of zirconium alloy sheet. Metallurgical Transactions A, 1985. 16A(April 1985): p. 675-681.
94. Raynaud, P.A., D.A. Koss, and A.T. Motta, Crack growth in the through-thickness direction of hydrided thin-wall Zircaloy sheet. Journal of Nuclear Materials, 2011. 420(1-3): p. 69-82.
95. Glendening, A., et al., The Influence of Stress State on the Failure of Hydrided Zircaloy-4. Journal of ASTM International, 2004.
96. Link, T.M., D.A. Koss, and A.T. Motta, Strain Localization in Sheet Metal Containing a geometric Defect. Metallurgical and Materials Transactions, 2000. 31A(7): p. 1883-1886.
97. Puls, M.P., The influence of hydride size and matrix strength on fracture initiation at hydrides in zirconium alloys. Met. Trans. A, 1988. 19(6): p. 1507-1522.
98. Grigoriev, V., B. Josefsson, and B. Rosborg. Fracture Toughness of Zircaloy Cladding Tubes. in Zirconium in the Nuclear Industry: Eleventh International Symposium, ASTM STP 1295. 1996. Garmisch-Partenkirchen, Germany: ASTM.
99. Hsu, H.-H. and L.-W. Tsay, Effect of hydride orientation on fracture toughness of Zircaloy-4 cladding. Journal of Nuclear Materials, 2011. 408(1): p. 67-72.
100. Flanagan, M.E., D.A. Koss, and A.T. Motta. The Influence of Hydrogen on the Deformation Behavior of Zircaloy-4. in Proceedings of the 2008 Water Reactor Fuel Performance Meeting. 2008. Seoul, Korea.
101. Raynaud, P.A., M. J. Meholic , D. A. Koss, A. T. Motta, and K. S. Chan. Influence of Hydride Microstructure on Through-Thickness Crack Growth in Zircaloy-4 Sheet. in Proceedings of the 13th International Conference on Environmental Degradation of Materials in Nuclear Systems-Water Reactors. 2007. Whistler, Canada: TMS.
102. Louthan, J.M.R. and C.L. Angerman, Influence of stress on hydride habit plane in Zircaloy-2. Metallurgical Society of American Institute of Mining, Metallurgical and Petroleum Engineers -- Transactions, 1966. 236(2): p. 221-222.
103. Louthan Jr, M.R. and R.P. Marshall, Control of hydride orientation in zircaloy. Journal of Nuclear Materials, 1963. 9(2): p. 170-184.
104. Marshall, R.P. and M.R. Louthan, Tensile properties of Zircaloy with oriented hydrides. Transactions of the ASM, 1963. 56: p. 693-700.
105. Kearns, J.J. and C.R. Woods, Effect of texture, grain size, and cold work on the precipitation of oriented hydrides in Zircaloy tubing and plate. Journal of Nuclear Materials, 1966. 20(3): p. 241-261.
106. Hardie, D. and M.W. Shanahan, Stress reorientation of hydrides in zirconium−2.5% niobium. Journal of Nuclear Materials, 1975. 55(1): p. 1-13.
107. Hardie, D. and M.W. Shanahan, The effect of residual stresses on hydride orientation in a zirconium-2.5% niobium alloy. Journal of Nuclear Materials, 1974. 50(1): p. 40-46.
108. Ells, C.E., The stress orientation of hydride in zirconium alloys. Journal of Nuclear Materials, 1970. 35: p. 306-315.
109. Chu, H.C., S.K. Wu, and R.C. Kuo, Hydride reorientation in Zircaloy-4 cladding. Journal of Nuclear Materials, 2008. 373(1–3): p. 319-327.
110. Sakamoto, K. and M. Nakatsuka, Stress reorientation of hydrides in recrystallized Zircaloy-2 sheet. Journal of Nuclear Science and Technology, 2006. 43(9): p. 1136-1141.
111. Desquines, J., D. Drouan, M. Billone, M. P. Puls, P. March, S. Fourgeaud, C. Getrey, V. Elbaz, and M. Philippe, Influence of temperature and hydrogen content on stress-induced

radial hydride precipitation in Zircaloy-4 cladding. Journal of Nuclear Materials, 2014. 453(1–3): p. 131-150.
112. Colas K., A.T.M., M. R. Daymond, M. Kerr, J, Almer, Hydride Platelet Reorientation in Zircaloy studied with Synchrotron Radiation Diffraction. Journal of ASTM International, 2011. 8(No. 1): p. Paper ID JAI103033.
113. Singh, R.N., R. Kishore,S. S. Singh, T. K. Sinha, and B. P. Kashyap, Stress-reorientation of hydrides and hydride embrittlement of Zr–2.5 wt% Nb pressure tube alloy. Journal of Nuclear Materials, 2004. 325(1): p. 26-33.
114. Alam, A.M. and C. Hellwig, Cladding tube deformation test for stress reorientation of hydrides. 2008. 5(2): p. JAI101110 (15 pp.).
115. Vicente Alvarez, M.A., J. R. Santisteban, P. Vizcaino, A. V. Flores, A. D. Banchik, and J. Almer, Hydride reorientation in Zr2.5Nb studied by synchrotron X-ray diffraction. Acta Materialia, 2012. 60(20): p. 6892-6906.
116. Bai J. B., N.J., D. Gilbon, C. Prioul, and D. Francois, Hydride embrittlement in Zircaloy-4 plate. Part II: Interaction between the tensile stress and hydride morphology. Metallurgical and Materials Transactions A, 1994. 25A: p. 1199-1208.
117. ASTM, B811-97,Standard specification for wrought zirconium alloy seamless tubes for nuclear reactor fuel cladding, 1997: West Conshohocken, PA. p. 920-935.
118. Marshall, R.P., Influence of fabrication history on stress-oriented hydrides in zircaloy tubing. Journal of Nuclear Materials, 1967. 24(1): p. 34-48.
119. Daum, R.S., S. Majumdar, Y. Y. Liu, and M. C. Billone, Radial-hydride embrittlement of high-burnup Zircaloy-4 fuel cladding. Journal of Nuclear Science and Technology, 2006. 43(9): p. 1054-1067.
120. Singh, R.N., R. L. Mikin, G. K. Dey, D. N. Sah, I. S. Batra, P. Ståhle, Influence of temperature on threshold stress for reorientation of hydrides and residual stress variation across thickness of Zr–2.5Nb alloy pressure tube. Journal of Nuclear Materials, 2006. 359(3): p. 208-219.
121. Valance, S. and J. Bertsch, Hydrides reorientation investigation of high burn-up PWR fuel cladding. Journal of Nuclear Materials, 2015. 464(0): p. 371-381.
122. Cha, H.-J., J-J Won, K-N Jang, J-H An, and K-T Kim, Tensile hoop stress-, hydrogen content- and cooling rate-dependent hydride reorientation behaviors of Zr alloy cladding tubes. Journal of Nuclear Materials, 2015. 464(0): p. 53-60.
123. Hong, S.I. and K.W. Lee, Stress-induced reorientation of hydrides and mechanical properties of Zircaloy-4 cladding tubes. Journal of Nuclear Materials, 2005. 340(2-3): p. 203-208.
124. Kese, K., Hydride re-orientation in Zircaloy and its effect on the tensile properties, S.N.P. Inspectorate, Editor 1998, Department of Materials Science and Engineering, Royal Institute of Technology: Stockholm, Sweden. p. 1-37.
125. Ells, C.E., Hydride precipitates in zirconium alloys (A review). Journal of Nuclear Materials, 1968. 28(2): p. 129-151.
126. Qin, W., J.A. Szpunar, and J. Kozinski, Hydride-induced degradation of hoop ductility in textured zirconium-alloy tubes: A theoretical analysis. Acta Materialia, 2012. 60(12): p. 4845-4855.
127. Daum, R.S., et al., Radial-hydride Embrittlement of High-burnup Zircaloy-4 Fuel Cladding. Journal of Nuclear Science and Technology, 2006. 43(9): p. 1054–1067.
128. Danielson, P., Zirconium and Hafnium and their Alloys, in ASM Handbook. 1980. p. 497-501.
129. Pierron, O.N., D.A. Koss, and A.T. Motta, Tensile Specimen Geometry and the Constitutive Behavior of Zircaloy 4. Journal of Nuclear Materials, 2003. 312: p. 257-261.

130. Siefken, L.J., E. W. Coryell, E. A. Harvego, and J. K. Hohorst, MATPRO - A Library of Materials Properties for Light-Water-Reactor Accident Analysis, SCDAP/RELAP5/MOD 3.3 Code Manual Vol.4, Rev. 2, 2001.
131. Link, T.M., Failure of Zircaloy cladding under severe loading conditions, in Intercollege Graduate Program in Materials1997, The Pennsylvania State University: University Park, PA. p. 81.
132. Colas, K.B., A. T. Motta, J. D. Almer, M. R. Daymond, M. Kerr, A. D. Banchik, P. Vizcaino, and J. R. Santisteban, In situ study of hydride precipitation kinetics and re-orientation in Zircaloy using synchrotron radiation. Acta Materialia, 2010. 58(20): p. 6575-6583.
133. Colas, K.B., A. T. Motta, M. R. Daymond, J. D. Almer, and Z. Cai. Hydride Behavior in Zircaloy-4 during Thermomechanical Cycling. in 15th International Conference on Environmental Degradation of Materials in Nuclear Power Systems—Water Reactors. 2011. Colorado Springs.
134. Larson, A.C. and R.B. Von Dreele, General Structure Analysis System (GSAS), 2000, Los Alamos National Laboratory.
135. Ruzauskas, E.J. and K.N. Fardell, Design, operation, and performance data for high burnup PWR fuel from H. B. Robinson plant for use in the NRC experimental program at Argonne National Laboratory, 2001, Electric Power Research Institute.
136. Mitchell D., A.G., and D. Davis. Optimized ZIRLO Fuel Performance in Westinghouse PWRs. in Top Fuel. 2010. Orlando, FL.
137. Brach, E.W., Interim Staff Guidance - 11, Rev. 3, Cladding considerations for the transportation and storage of spent fuel, 2003, U. S. Nuclear Regulatory Commission, Spent Fuel Project Office.
138. Schneider, C.A.R., W. S. & Eliceiri, K. W., ImageJ, 2012: Nature methods 9(7): 671-675. p. "NIH Image to ImageJ: 25 years of image analysis
139. Sauthoff, G., The influence of external forces on precipitation. Scripta Metallurgica, 1976. 10(6): p. 557-559.
140. Singh, R.N., P. Ståhle, A. R. Massih, and A. A. Shmakov, Temperature dependence of misfit strains of δ-hydrides of zirconium. Journal of Alloys and Compounds, 2007. 436(1–2): p. 150-154.
141. Perovic, V., G.C. Weatherly, and C.J. Simpson, The role of elastic strains in the formation of stacks of hydride precipitates in zirconium alloys. Scripta Metallurgica, 1982. 16: p. 409-412.
142. Barrow, A.T.W., A. Korinek, and M.R. Daymond, Evaluating zirconium–zirconium hydride interfacial strains by nano-beam electron diffraction. Journal of Nuclear Materials, 2013. 432(1–3): p. 366-370.
143. Kiciak, A., G. Glinka, M. Eman, and M. Shiratori, Weight functions and stress intensity factors for corner quarter-elliptical crack in finite thickness plate subjected to in-plane loading. Engineering Fracture Mechanics, 1998. 60(2): p. 221-238.
144. Seasolve Software, I. PeakFit Version 4.12. 2003.
145. 05-0665, R.C., The Powder Diffraction File, 2001, International Center for Diffraction Data: Newton, PA.
146. 34-0649, R.C., The Powder Diffraction File, 2006, International Center for Diffraction Data: Newton, PA.
147. Yamanaka S., K.Y., K. Kurosaki, M. Uno, K. Takeda, H. Anada, T. Matsuda, and S. Kobayashi, Thermal properties of zirconium hydride. Journal of Nuclear Materials, 2001. 294: p. 94-98.

148. Tandon, G.P. and G.J. Weng, Stress Distribution in and Around Spheroidal Inclusions and Voids at Finite Concentration. Journal of Applied Mechanics, 1986. 53(3): p. 511-518.
149. Béchade, J.L., D. Menut, S. Doriot, S. Schlutig, and B. Sitaud, X-ray diffraction analysis of secondary phases in zirconium alloys before and after neutron irradiation at the MARS synchrotron radiation beamline. Journal of Nuclear Materials, 2013. 437(1–3): p. 365-372.
150. Anderson, T.L., Fracture Mechanics Fundamentals and Applications. 2005: Taylor and Francis/CRC press.

Vita

Mahmut Nedim Cinbiz

PERSONAL SUMMARY

- A multidisciplinary background of nuclear engineering, materials science, and mechanics of materials.
- Experience in synchrotron radiation X-ray diffraction, scanning electron microscopy, optical profilometry and metallography, evaporative physical vapor deposition, thermo-mechanical treatments, mechanical testing, fracture analysis, fracture mechanics.
- Experience in finite element and finite volume methods, Fortran 90, MATLAB, ANSYS, ANSYS/fluent, CATIA, SolidWorks, and Linux-based operating systems.

EDUCATION AND RESEARCH

Ph.D. Candidate in Materials Science and Engineering, The Pennsylvania State University, PA, USA

- **Thesis:** The effect of stress state on the dissolution and precipitation behavior of zirconium hydrides and their effects on the mechanical behavior in Zircaloy-4.

M.S. in Nuclear Engineering, Hacettepe University, Ankara, Turkey (2008).

- **Thesis:** Numerical Modelling of Thermal and Kinetic Phenomena in Reactive Systems.

B.S. in Nuclear Engineering, Hacettepe University, Ankara, Turkey (2005).

PROFESSIONAL EXPERIENCE

Aug 2010 – Present: Ph.D. Candidate and Research Assistant, Department of Mechanical and Nuclear Engineering. My Advisors are Prof. Arthur Motta, and Prof. Donald Koss.

Aug 2006– July 2010: Research Assistant (Hacettepe University, Nuclear Energy Engineering Department, Ankara, Turkey). During this time, I worked on three projects listed below.